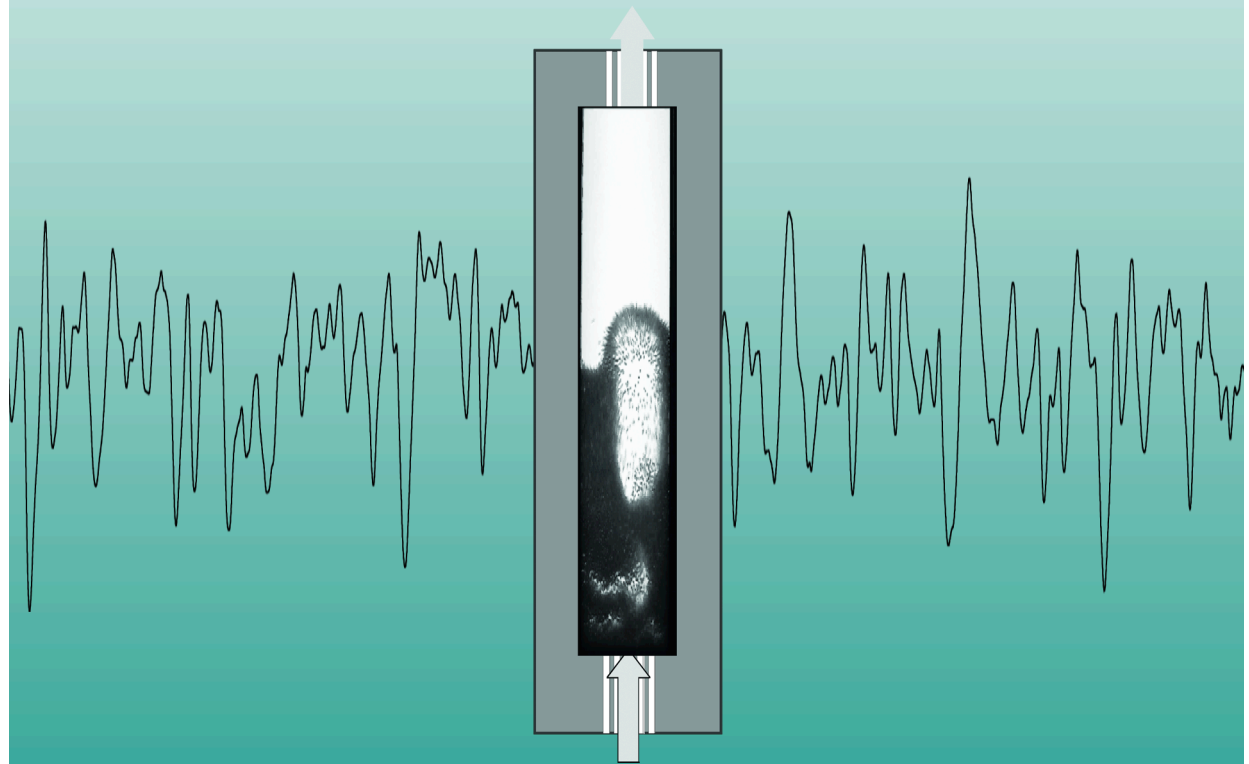


CONCEPTUAL DESIGN OF A FLUIDIZED BED NUCLEAR REACTOR

Statics, Dynamics and Safety-related Aspects



Alexander Agung

Propositions accompanying the thesis

“Conceptual design of a fluidized bed nuclear reactor: statics, dynamics and safety-related aspects”

Alexander Agung

1. In a nuclear reactor with fissile material in the form of a fluidized bed, radial redistribution of particles and the presence of large bubbles in the bed cause a large change in reactivity.
[Chapter 3 of this thesis]
2. Developing safety culture must be the paramount concern in any nuclear engineering curriculum.
3. The term “exergy crisis” is preferable to “energy crisis” as in real processes exergy is always consumed while energy is always conserved.
4. Since many last names are based on occupations, a name such as “Fletcher” should be abandoned and be replaced by a name reflecting modern occupations.
5. The number of female professors in technical universities cannot be used to represent the level of emancipation of women in a country.
[“Sisters doin' it for themselves”, Delta, jaargang 38, nr.34, 2006]
6. The education method home-schooling should be abolished because children raised by this method suffer from a lack of socialization.
7. To supply electricity by means of nuclear power in rural and remote areas of developing countries where the electrification ratio is low, nuclear reactors must have the following features: modular, low power, total passive safety system, long operation time without refueling and competitive with local renewable energy resources.

8. Despite a long relationship between the two countries, the influence of Indonesia on the Netherlands is only in supplementing culinary vocabularies.
9. The development of neutron radiography is driven by solutions, not by problems.
10. Life is much more complicated with children. But, once you have them, everything is meaningless without them.

These propositions are considered defendable and as such have been approved by the supervisors, prof. (em). dr. ir. H. van Dam and prof. dr. ir. T.H.J.J. van der Hagen.

Stellingen
behorende bij het proefschrift

“Conceptual design of a fluidized bed nuclear reactor: statics, dynamics and safety-related aspects”

Alexander Agung

1. Radiale herverdeling van deeltjes en de aanwezigheid van grote bellen veroorzaken grote veranderingen in de reactiviteit in een fluïde-bed kernreactor.
[Hoofdstuk 3 van dit proefschrift]
2. Het ontwikkelen van een veiligheidscultuur zou de hoogste zorg moeten krijgen in ieder “nuclear engineering” curriculum.
3. De term “exergiecrisis” heeft de voorkeur boven “energiecrisis” omdat in praktische processen exergie altijd verminderd terwijl energie altijd behouden is.
4. Aangezien veel achternamen gebaseerd zijn op beroepen, zou een naam als “Fletcher” afgeschaft dienen te worden en vervangen door een naam die een modern beroep vertegenwoordigt.
5. Het aantal vrouwelijke hoogleraren aan technische universiteiten kan niet gebruikt worden om de mate van emancipatie weer te geven in een land.
[“Sisters doin' it for themselves”, Delta, jaargang 38, nr.34, 2006]
6. De opvoedmethode gebaseerd op thuisscholing dient te worden afgeschaft omdat het kinderen die volgens deze methode zijn opgevoed ontbreekt aan sociale vaardigheden.

7. Om elektriciteit geproduceerd d.m.v. kernenergie aan te bieden op het platteland en in afgelegen gebieden van ontwikkelingslanden met een lage elektrificatie ratio dienen kernreactoren de volgende eigenschappen te hebben: modulair, laag vermogen, compleet passief veilig, een lange levensduur zonder brandstofherlading en competitief met lokale hernieuwbare energiebronnen.
8. Ondanks een lange relatie tussen de twee landen is de invloed van Indonesië op Nederland beperkt tot een uitbreiding van het culinaire taalgebruik.
9. De ontwikkeling van neutronenradiografie wordt gedreven door oplossingen, niet door problemen.
10. Het leven is ingewikkelder met kinderen. Maar als je ze eenmaal hebt, is alles zonder ze zonder betekenis.

Deze stellingen worden opponeerbaar en verdedigbaar geacht en zijn als zodanig goedgekeurd door de promotoren, prof. (em). dr. ir. H. van Dam and prof. dr. ir. T.H.J.J. van der Hagen.

Conceptual Design of A Fluidized Bed Nuclear Reactor

Statics, Dynamics and Safety-related Aspects

The research described in this thesis was performed in the section of Physics of Nuclear Reactor of the department of Radiation, Radionuclides and Reactors, faculty of Applied Sciences, Delft University of Technology, Mekelweg 15, 2629 JB Delft, The Netherlands.

Conceptual Design of A Fluidized Bed Nuclear Reactor

Statics, Dynamics and Safety-related Aspects

Proefschrift

ter verkrijging van de graad van doctor
aan de Technische Universiteit Delft,
op gezag van de Rector Magnificus prof. dr. ir. J. T. Fokkema,
voorzitter van het College voor Promoties,
in het openbaar te verdedigen
op maandag 11 juni 2007 om 12.30 uur

door

Alexander AGUNG

Sarjana Teknik in Nuclear Engineering
Universitas Gadjah Mada, Indonesië

Master of Science in Energy Engineering
Royal Institute of Technology, Zweden

geboren te Pekalongan, Indonesië

Dit proefschrift is goedgekeurd door de promotoren:

Prof. (em). dr. ir. H. van Dam

Prof. dr. ir. T. H. J. J. van der Hagen

Samenstelling promotiecommissie:

Rector Magnificus,	voorzitter
Prof. (em). dr. ir. H. van Dam,	Technische Universiteit Delft, promotor
Prof. dr. ir. T. H. J. J. van der Hagen,	Technische Universiteit Delft, promotor
Dr. ir. D. Lathouwers,	Technische Universiteit Delft
Prof. dr. R. F. Mudde,	Technische Universiteit Delft
Prof. dr. C. C. Pain,	Imperial College London, U.K.
Prof. dr. ir. J. A. M. Kuipers,	Universiteit Twente
Dr. ir. J. C. Kuijper,	NRG Petten

Copyright ©2007 Alexander Agung and IOS Press

All rights reserved. No part of this book may be reproduced, stored in a retrieval system, or transmitted, in any form or by any means, without prior permission from the publisher.

ISBN 978-1-58603-759-8

Keywords: Fluidized Bed Nuclear Reactor, gas-cooled high temperature reactor, inherent safety, dynamics modeling, stability analysis, passive removal of decay heat

Published and distributed by IOS Press under the imprint Delft University Press

Publisher

IOS Press

Nieuwe Hemweg 6b

1013 BG Amsterdam

The Netherlands

Tel: +31-20-688 3355

Fax: +31-20-687 0019

Email: info@iospress.nl

www.iospress.nl

www.dupress.nl

LEGAL NOTICE

The publisher is not responsible for the use which might be made of the following information.

PRINTED IN THE NETHERLANDS

*Where the mind is without fear and the head is held high;
Where knowledge is free;
Where the world has not been broken up into fragments by narrow domestic
walls;
Where words come out from the depth of truth;
Where tireless striving stretches its arms towards perfection;
Where the clear stream of reason has not lost its way into the dreary desert sand
of dead habit;
Where the mind is led forward by thee into ever-widening thought and action—
Into that heaven of freedom, my Father, let my country awake.*

“Gitanjali”
Rabindranath Tagore (1861–1941)

This thesis is dedicated to
⊗ Zidah, Naufal, Rian ⊗

Contents

List of Figures	xi
List of Tables	xv
1. Introduction	1
1.1. Background	1
1.2. Gas-cooled fluidized bed nuclear reactor	3
1.3. Objective of the research	4
1.4. Outline of the thesis	5
2. The concept of Fluidized Bed Nuclear Reactor (FLUBER)	7
2.1. Overview of related concepts	7
2.2. Review of fluidization processes	8
2.2.1. Flow regimes of fluidization	8
2.2.2. Classifications of particles	10
2.2.3. Mapping of fluidization regimes	10
2.2.4. Advantages and drawbacks of fluidized beds	13
2.3. General features of FLUBER	13
2.3.1. Materials of FLUBER	13
2.3.2. Overview of the previous FLUBER design	16
2.4. Summary	17
3. Static behavior of FLUBER	19
3.1. Design modifications of FLUBER	20
3.1.1. Design targets	20
3.1.2. Design parameters	21
3.1.3. Computational procedure	22
3.1.4. Results	26
3.2. Behavior of homogeneous bed	31

3.3.	Influence of particle distribution on reactivity	32
3.3.1.	Influence of axial particle distribution	32
3.3.2.	Influence of radial particle distribution	34
3.4.	Influence of bubbles on reactivity	37
3.4.1.	Single-bubble model	37
3.4.2.	Two-bubble model	38
3.4.3.	Multi-bubble model	43
3.5.	Summary	45
4.	Space-independent dynamics of FLUBER	47
4.1.	Introduction	47
4.2.	Dynamics model description	48
4.2.1.	Fluidization model	48
4.2.2.	Heat transfer model	49
4.2.3.	Neutronics model	51
4.2.4.	Thermophysical properties of gas and particles	53
4.2.5.	Computational methodology	55
4.3.	Steady state behavior of the reactor	55
4.4.	Linear stability analysis	57
4.4.1.	Eigenvalue evaluation	57
4.4.2.	Frequency response	59
4.5.	Operational transients	62
4.5.1.	Change in the inlet flow rate	62
4.5.2.	Change in the helium inlet temperature	64
4.6.	Influence of particle redistribution on power	64
4.7.	Summary	67
5.	Space-dependent dynamics of FLUBER	71
5.1.	Introduction	71
5.2.	Description of the codes	72
5.3.	Governing equations	73
5.3.1.	Neutronics model	73
5.3.2.	Multiphase model	76
5.4.	Implementation	79
5.5.	Static calculations	81
5.6.	Dynamic simulations	83
5.7.	Comparison with the point dynamic model	101
5.8.	Summary	102
6.	Passive removal of post-shutdown decay heat	103
6.1.	Introduction	103
6.2.	The mathematical model	104
6.2.1.	Continuity equation	104
6.2.2.	Momentum equation	106
6.2.3.	Energy equations	106

6.2.4. Turbulent kinetic energy and dissipation-rate equations	107
6.2.5. Radiative transfer equation	109
6.2.6. Decay heat model	110
6.2.7. Boundary conditions	111
6.3. Material properties	112
6.3.1. Thermal properties	112
6.3.2. Radiative properties of particles	113
6.4. Numerical treatment	114
6.4.1. Discretization and solution method for the flow model	114
6.4.2. Numerical treatment for the RTE	115
6.4.3. Implementation	118
6.5. Results and discussions	119
6.5.1. Assessment of the numerical methods for the RTE	119
6.5.2. Results for different cases	121
6.5.3. Discussion	128
6.6. Summary	130
7. Concluding remarks	135
7.1. General discussion	135
7.2. Remarks on computational tools	137
7.3. Future work	138
Bibliography	139
Nomenclature	149
Summary	155
Samenvatting (Summary in Dutch)	157
Ringkasan (Summary in Bahasa Indonesia)	159
List of relevant publications	161
Acknowledgments	163
Curriculum Vitae	165

List of Figures

1.1. Schematic view of FLUBER at collapsed and fluidized state.	3
2.1. Various conditions of fluid-solids interaction in a bed.	9
2.2. Geldart's particle classification.	11
2.3. General flow regime diagram for the whole range of gas-solid fluidized bed.	11
2.4. A micrograph of a typical TRISO fuel particle.	15
2.5. Reactivity of the old design as a function of void fraction for different fuel temperature.	17
3.1. The ideal reactivity curve at cold condition (293 K).	20
3.2. The INAS code system employed in this research.	24
3.3. Rhombohedral arrangement of fuel particles in a lattice cell.	24
3.4. FLUBER models for KENO-V.a calculations, i.e. (a) the model with porous reflector, (b) with bottom absorber and (c) with a ring of side absorber.	25
3.5. The influence of various modifications to the reactivity.	27
3.6. The reactivity behavior of the bed as a function of MFR	27
3.7. Reactivity as a function MFR at 140 kg, 180 kg, 220 kg and 260 kg of fuel inventory.	29
3.8. Reactivity as a function of MFR at 10 ppm, 30 ppm and 50 ppm of side absorber concentration.	30
3.9. The static reactivity of the new design for different fuel temperature as a function of bed expansion.	32
3.10. Thermal, epithermal and fast neutron flux at packed bed conditions, normalized to 1 fission neutron per second.	33
3.11. Thermal, epithermal and fast neutron flux at expanded bed conditions, normalized to 1 fission neutron per second.	33
3.12. Front view of axially inhomogeneous core for KENO-V.a model and density distribution.	35

3.13. Reactivity of the homogeneous and the axially inhomogeneous core.	35
3.14. Front view of radially inhomogeneous core for KENO-V.a model.	36
3.15. Reactivity of a homogeneous and radially inhomogeneous core.	36
3.16. Side and top view of the single-bubble model.	39
3.17. Reactivity as a function of axial position of bubble for the single-bubble model.	39
3.18. Front and top view of the two-bubble model.	40
3.19. An example of bubble arrangements in the many-bubble model.	44
3.20. The reactivity as a function of number of bubble layers and its corresponding height of the topmost layer.	44
4.1. Reactivity as a function of void fraction at fuel temperature of 993 K and the fitted reference reactivity curve to be used in the dynamic model.	54
4.2. Fuel temperature and total power as a function of the coolant mass flow rate in steady state condition and power density and specific power as a function of core expansion.	56
4.3. Root-locus plot of the roots of the characteristic polynomial as a function of the coolant mass flow rate.	59
4.4. Magnitude and phase of the transfer function from coolant mass flow rate variations to reactor power fluctuations.	61
4.5. Magnitude and phase of the transfer function from inlet helium temperature variations to reactor power fluctuations.	61
4.6. Bed height, reactivity, fuel temperature and total power after a step change in inlet flow rate from its initial condition of 33 kg/s.	63
4.7. Bed height, reactivity, fuel temperature and total power after a step change in inlet coolant temperature from its initial condition of 543 K.	65
4.8. Time traces of total reactivity influenced by external reactivity.	68
4.9. Trace of total power as a function of time for a steady system subject to external noise on the reactivity (150 pcm standard deviation).	68
4.10. Trace of bed height as a function of time for a steady system subject to external noise on the reactivity (150 pcm standard deviation).	69
4.11. Trace of fuel temperature as a function of time for a steady system subject to external noise on the reactivity (150 pcm standard deviation).	69
5.1. An outline of the FETCH code, representing the flow of information among different modules.	72
5.2. (a) The 2D schematic and (b) the finite element mesh for FLUBER used for the time-dependent simulation, the left boundary is the central axis.	80
5.3. The effective multiplication factor as a function of expanded bed for EVENT and KENO-V.a.	84
5.4. The difference in multiplication factor between EVENT and KENO-V.a using AMPX-converted library.	84
5.5. The effective multiplication factor as a function of expansion, calculated by EVENT with the 6-group WIMS8A library. The inventory of uranium is 152 kg. .	85

5.6. Power, mean gas temperature, maximum particle temperature, concentration of the longest, 3rd longest and shortest living delayed neutron precursors for a uranium inventory of 120 kg and an input gas velocity of 120 cm/s.	86
5.7. Gas temperature at bottom right (Detector 1) and top center (Detector 14) of the cavity for a uranium inventory of 120 kg and an input gas velocity of 120 cm/s.	89
5.8. (a) Particle volume fraction, (b) gas temperature (°C), (c) the longest living delayed neutron precursor concentration (cm^{-3}), (d) the shortest living delayed neutron precursor concentration (cm^{-3}), for a uranium inventory of 120 kg and an input gas velocity of 120 cm/s at 50 seconds after the initial transient. The left boundary in these figures is the central axis.	90
5.9. Power, mean gas temperature and maximum particle temperature for a uranium inventory of 120 kg and an input gas velocity of 180 cm/s.	91
5.10. (a) Particle volume fraction and (b) gas temperature (°C) for a uranium inventory of 120 kg and an input gas velocity of 180 cm/s at 50 seconds after the initial transient.	92
5.11. Power, mean gas temperature and particle temperature for uranium inventory of 152 kg and input gas velocity of 120 cm/s.	94
5.12. The particle volume fraction at various time level after start-up for a uranium inventory of 152 kg and an input gas velocity of 120 cm/s and their corresponding power and temperature.	95
5.13. The particle volume fraction at various time level for a uranium inventory of 152 kg and an input gas velocity of 120 cm/s and their corresponding power and temperature.	96
5.14. Power, mean gas temperature and particle temperature for a uranium inventory of 152 kg and an input gas velocity of 180 cm/s.	98
5.15. The particle volume fraction at various time level after start-up for a uranium inventory of 152 kg and an input gas velocity of 180 cm/s and their corresponding power and temperature.	99
5.16. (a) Particle volume fraction, (b) gas temperature (°C), (c) the longest living delayed neutron precursor concentration (cm^{-3}), (d) the shortest living delayed neutron precursor concentration (cm^{-3}) for a uranium inventory of 152 kg and an input gas velocity of 180 cm/s at 50 seconds after the initial transient.	100
5.17. Total power and fuel temperature as a function of time calculated using the point dynamics code. Uranium inventory is 170 kg and mass flow rate is 11 kg/s. The graphs are reproduced from (Lathouwers <i>et al.</i> , 2003).	101
6.1. Percentage of decay power to the initial total power after shutdown of the reactor as a function of time.	105
6.2. Fuel temperature during a loss of mass flow.	105
6.3. Thermal conductivity of unirradiated graphite (left) and irradiated graphite (right). The conductivity of irradiated graphite is given for various level of fast fluence (in $\text{neutron}/\text{cm}^2$).	113

6.4. Heat transferred to the surface of the bottom reflector, calculated by using P_1 and S_N methods with a particle volume fraction in the bed of 0.6.	119
6.5. Heat transferred to the surface of the top reflector, calculated by using P_1 , S_N and VF (as comparison) with a particle volume fraction in the cavity of 10^{-3} and 10^{-12}	120
6.6. The maximum fuel temperature as a function of time calculated by different methods. Multimode heat transfer is applied in these simulations.	121
6.7. The time evolution of the maximum fuel temperature for different initial operating power using the S_6 model for the pressurized, fresh graphite system.	123
6.8. Percentage of heat surface at various locations of interface between the core and reflector in a pressurized system.	124
6.9. Temperature distribution in the reactor after shutdown.	125
6.10. Plot of various fields in the core cavity.	127
6.11. The time evolution of the maximum fuel temperature for different initial operating power using S_6 model for the pressurized, irradiated graphite system.	128
6.12. Percentage of heat surface at various locations for an pressurized, irradiated graphite system.	129
6.13. The time evolution of the maximum fuel temperature for different initial operating power using S_6 model for the depressurized, fresh graphite system.	130
6.14. Percentage of heat surface at various locations for a depressurized, fresh graphite system.	131
6.15. The time evolution of the maximum fuel temperature for different initial operating power using S_6 model for the depressurized, irradiated graphite system.	132
6.16. Percentage of heat surface at various locations for a depressurized, irradiated graphite system.	133

List of Tables

2.1. Characteristics of FLUBER.	16
2.2. Characteristics of fuel particles.	16
3.1. Parameter comparisons of the previous designs and the current design.	31
3.2. The position of bubble #2 of Type I – Type IV model.	41
3.3. Reactivity difference ($\Delta\rho$) of the type I two-bubble model relative to the homogeneous core.	41
3.4. Reactivity difference ($\Delta\rho$) of the type II two-bubble model relative to the homogeneous core.	42
3.5. Reactivity difference ($\Delta\rho$) of the type III two-bubble model relative to the homogeneous core.	42
3.6. Reactivity difference ($\Delta\rho$) of the type IV two-bubble model relative to the homogeneous core.	43
5.1. Structure of energy groups and their corresponding group collapsing in WIMS and AMPX libraries.	80
5.2. Physical properties of particles and gas for the simulations.	82
5.3. The initial and boundary conditions for the simulations.	82
5.4. Position of the fourteen detectors in the bed.	82
5.5. Time-averaged, minimum and maximum values of power and temperature, excluding the first 20 seconds after initial transient, for a uranium inventory of 120 kg and an input gas velocity of 120 cm/s.	85
5.6. Time-averaged, minimum and maximum value of power and temperature, excluding the first 20 seconds after initial transient, for a uranium inventory of 120 kg and an input gas velocity of 180 cm/s.	89
5.7. Time-averaged, minimum and maximum value of power and temperature, excluding the first 20 seconds after initial transient, for a uranium inventory of 152 kg and an input gas velocity of 120 cm/s.	94

5.8. Time-averaged, minimum and maximum value of power and temperature, excluding the first 20 seconds after initial transient, for a uranium inventory of 152 kg and an input gas velocity of 180 cm/s.	97
5.9. Time-averaged power and gas temperature for a uranium inventory of 170 kg and a mass flow rate of 11 kg/s calculated by the point dynamics and multidimensional dynamics model.	102
6.1. Initial values of the temperatures.	119
6.2. The CPU time and the time-disadvantage factor for simulating 3-hour real time using various methods.	122

1

CHAPTER

Introduction

1.1. Background

The demand for energy increases dramatically. By the year 2050, the world population is predicted to increase from 6 billion to 10 billion people (U.S. DOE and GIF, 2002) and the global electricity consumption is projected to increase by 160% (Deutch and Moniz, 2006). To satisfy the demand, all options of energy production are needed. Intensive consumption of fossile fuel, however, evidently increases the concentration of CO₂, SOx and NOx in the atmosphere, leading to a global climate change. The technology of clean fossile fuel is not proven yet. On the other hand, contribution of renewable energy increases too slowly while the oil and gas resources are depleting. On this account, the role of nuclear energy will be vital in the future.

In order to successfully deploy nuclear power plants in the future, the developers of nuclear power plants are faced with challenges in the following issues (Ansolabehere *et al.*, 2003): (i) safety, (ii) economics, (iii) proliferation and (iv) waste.

Some proposals have been put forward to address those challenges by implementing either evolutionary designs or innovative designs. The evolutionary design comprises gradual development and improvements of the power plant to be deployed in near-term future based upon the results of the operational records and the implementation of the defense-in-depth and the probabilistic safety analysis. The innovative design emphasizes on radical advances in design and safety features of the plant for the long-term future deployment (IAEA, 1997b). Here passive safety features and intensive means to prevent core damage are stressed.

One of the innovative reactor concepts that has been widely investigated is that of small modular reactors. Small modular reactors are desirable (Mourogov *et al.*, 2002; Ohashi *et al.*, 2000) for the following reasons:

- *Flexibility to develop, plan and construct the plant.*

Being modular in design, any reactor size can be built from the basic module.

- *Increased safety level based on passive features.*

By adopting a smaller reactor, the inventory of the fissile material in the core becomes smaller, leading to a safer situation in case of a core disruptive accident. Moreover, by enhancing the inherent and passive safety features, the reactor becomes more simple and the need for a large number of redundancies in control and safety system can be reduced. It is also possible that a safety system such as Emergency Core Cooling Systems (ECCS) may not be necessary.

- *Easy operation and maintenance.*

As the reactor is more simple and strongly reliant on inherent and passive safety features, the operation and maintenance of the reactor can be performed more easily.

- *Economic competitiveness.*

With safer design as described above, together with smaller, more simple and modularized plants, the initial investment cost becomes smaller.

- *Easier plant siting close to industrial or populated areas.*

Due to the inherent safety, the plant can be located near industrial or populated areas, hence reducing the electricity transmission cost.

- *Suitable for use in areas with or without grids.*

Due to the flexibility and the low transmission cost, the reactor can also be installed on inlands or dispersed demand areas where an electricity grid is unavailable. This possibility is very interesting for developing countries where the demands are not concentrated or for remote islands such as in Indonesia where access to the grid is limited.

The high temperature gas-cooled reactor (HTGR) is considered to be one of the best candidates to be deployed as a small modular reactor (Tsuchie, 2000) because it can be adapted to satisfy the aforementioned features. From the safety point of view, the design choice of fuel material enables to contain the fission products inside the coated fuels. Combined with a low power density of the small reactor, the fuel integrity can be maintained even if the most severe accident occurs. It is now possible to produce electricity via a direct gas turbine cycle. This means that the need for a steam turbine can be eliminated and the efficiency of the plant can be higher, implying economic competitiveness of the plant. Furthermore, as the output temperature of this reactor is high, it is possible to diversify the use of the reactor not only for electricity production but also for hydrogen production and as co-generating plant. The reactor can be operated using various nuclear fuel compositions such as U, Th or Pu, so it can be designed as a proliferation-free reactor by choosing a proper fuel cycle. As for the radioactive waste, the spent fuel from the HTGR can be vitrified before being deposited in a waste repository.

1.2. Gas-cooled fluidized bed nuclear reactor

Several “old” concepts have been revisited, and one of them is based on the concept of fuel fluidization. In this project a new type of nuclear reactor based on gas-solid fluidization principle is proposed. This fluidized bed nuclear reactor (FLUBER) consists of a graphite-walled tube partially filled with TRISO-coated fuel particles. In contrast with other HTGRs where the TRISO particles are encased within a graphite pebble or rods, the particles in FLUBER are laid in the bottom part of the cavity of the tube, forming a packed bed. Helium is used as a coolant that flows from bottom to top through the tube, thereby fluidizing the particle bed. During the fluidization process, the bed of solid particles is transformed into something closely resembling a liquid. Fig. 1.1 shows a schematic view of FLUBER in a packed bed and in a fluidized state. When the flow is absent or at low rate, the bed remains packed as indicated in Fig. 1.1 (left). When the flow rate is increased, the bed expands and forms a fluidized state; see Fig. 1.1 (right). Only when the coolant flow is large enough does the reactor become critical because of the surrounding graphite that moderates and reflects the neutrons.

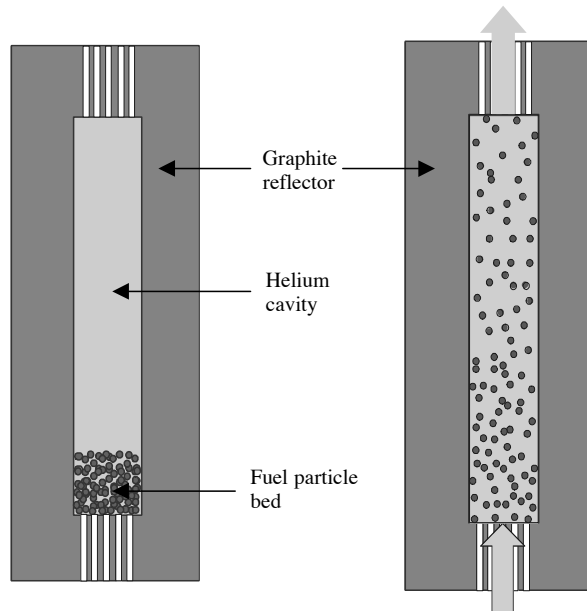


Figure 1.1. A schematic view of FLUBER at collapsed/packed condition (left) and at fluidized state when the gas flows into the reactor (right). The size of fuel particles is not to scale.

Fluidized beds have several features that are advantageous for a nuclear reactor, such as a uniform temperature distribution due to rapid particle mixing and a high transfer rate between particles and fluid. The high heat transfer rate between particles and fluid yields a

high temperature of fluid without leading to an excessive fuel temperature. This offers the advantages of a high core outlet temperature and the use of a highly efficient direct-cycle gas turbine. The excellent mixing properties guarantee a uniform power distribution and consequently a uniform fuel burnup.

Another possible advantage of using a fluidized bed for nuclear reactors is that the bed height increases when the gas flow increases. The change in geometry of the bed affects the neutronics of the reactor and consequently the power produced will change as well. In this manner the power generation can be controlled by altering the inlet flow rate, thus reducing dependencies on control rod mechanisms.

1.3. Objective of the research

The objective of this research is *to obtain a preliminary design of a high temperature gas-cooled fluidized bed fission nuclear reactor*. The reactor in question should satisfy the following requirements:

1. *Modular and low power.*

The reactor should be constructed from a modular basis and be simple in design. It is also low in power and due to its modularity the number of basic module can be extended to fulfill larger demands.

2. *Large shutdown margin.*

From a neutronics point of view, an inherently safe operation requires that the system is strongly subcritical in the packed state since active control rods are absent in this reactor. This implies that the cold shutdown margin should be large enough so that fresh fuel particles can be safely filled into the cavity.

3. *Able to produce power when the bed of particles expands and stop as soon as the coolant flow is lost.*

This requirement implies that the reactor is critical when the bed expands and in the case that the flow of fluid into the reactor is suddenly absent, either intentionally or by accident, the reactor becomes subcritical. In this sense the consequence of a Loss-of-Coolant Accident can be minimized.

4. *Stable from the reactivity point of view.*

Stability in a nuclear power plant is very important as it determines whether the fission process may go uncontrollable. The key parameter is the temperature feedback coefficient. A negative value of this coefficient is necessary as this will restrain an excessive increase of fission reaction.

5. *Resistant to inherent fluctuations in the fluidization regime.*

The hydrodynamics of gas-solid fluidized beds are a complex phenomenon. Particles in fluidized beds are not distributed uniformly and even move rather chaotically. The presence of bubbles in a gas-solid fluidized bed is common and depending on the fluidization regime the bubbles may grow very large. This situation leads to fluctuations in reactivity and in turn to power and temperature. Thus the reactor should be operated within acceptable safety margin under such circumstances.

6. *Able to remove post-shutdown decay heat by passive means without compromising the safety margin.*

Safety criteria must be applied not only during the operation of the reactor but also when the reactor has been shutdown. In the latter case although fission reactions are absent, the decay of the fission products continues. The decay heat should be transferred from the fuel in order to prevent an excessive temperature increase which leads to a fuel/core damage. This requirement is stringent especially when LOFA or LOCA occurs. Here the cooling capability has deteriorated and an additional system such as ECCS to cool the reactor is thus required. The coolant in this system is driven by pumps. If these pumps malfunction or if a total site-blackout occurs, the decay heat cannot be removed effectively.

A better solution to handle the decay heat is to rely on a passive system. Here the removal of decay heat from the core takes place without any intervention of human operators or active systems such as pumps. To increase the possibility of passive removal of the decay heat, the reactor should have a low power density (power per unit volume).

The research project consists of three parts. The first part is concerned with the static properties of the reactor. This includes deciding the design targets and parameters, upon which a preliminary design is then proposed. The behavior of this reactor at low and high void fraction as well as with inhomogeneous distribution of fuel particles is further investigated. The aim of these investigations is to satisfy requirements no. 1 and 2.

The subject of the second part is related to the behavior of the reactor under dynamic conditions. Numerical models of the neutronics and fluid dynamics are developed and used to investigate whether requirements no. 3–5 can be fulfilled.

The third part of this project deals with the decay heat removal in absence of the forced cooling system. With this investigation an answer can be found to the question what the maximum power is that can be produced. The aim of this part is to satisfy requirement no. 6.

1.4. Outline of the thesis

In Chapter 2 the concept of the fluidized bed nuclear reactor (FLUBER) is discussed. A concise description of the underlying fluidization process is also presented along with the advantages and the drawbacks of fluidized beds. Furthermore, the general features of FLUBER are described and an overview of the FLUBER design available at the time of starting this PhD project is presented in this chapter.

The description of the static behavior of the modified FLUBER design is presented in Chapter 3. Some neutronic calculations have been performed to satisfy the design targets and the results are presented in this chapter. The influence of inhomogeneous particle distribution as well as the influence of bubble on reactivity is reported.

Chapter 4 discusses the time dependent behavior of FLUBER as well as a linear stability analysis using a zero-dimensional (point) dynamics model. The dynamic behavior investigated in this chapter comprises operational transients and the influence of particle redistribution —modeled as a noise term in the reactivity— on power.

The point dynamics model is not able to capture the phenomenon of bubble formation and movement of fuel particles. For this purpose a multidimensional dynamics model is required. In Chapter 5, the multidimensional dynamics of FLUBER using coupled neutronics and multiphase flow models is described. The behavior of the reactor for different operational conditions is presented and the resistance of FLUBER under large disturbances is also discussed. Finally, a comparison to the zero-dimensional dynamic model is evaluated to justify the use of the two models.

Chapter 6 describes the development of the multimode heat transfer model for assessing the possibility of removal post-shutdown decay heat by passive means. Several situations that might occur were simulated and the results of the simulation are given in this chapter.

In Chapter 7 the final conclusions are drawn and some recommendations for future work are presented.

CHAPTER 2

The concept of Fluidized Bed Nuclear Reactor (FLUBER)

2.1. Overview of related concepts

The concept of using non-rigid fuels in a reactor core is not new and dates back to the earliest period of nuclear reactor development. An early concept was the molten-salt reactor wherein the homogeneous fuel circulated in a closed core and heat exchanger loop. Another concept involves fuel suspended in fluid and it has been proposed by several authors. Sefidvash (1985, 1996, 2002) proposed a fluidized bed using uranium dioxide as fuel cladded by zircaloy or stainless steel and using supercritical water as coolant. This reactor is modular in design so that any power plant size can be constructed from the basic module.

Taube *et al.* (1986) proposed a design using uranium carbide macro fuel spheres floating in a molten lead coolant. In the event of a coolant pump failure, the fuel spheres will descend and settle on the collector trays which are located below the core. The fuel spheres inside the trays form a subcritical assembly with sufficient cooling.

A new type of BWR plant design that combines the fluidized bed concept and the “density-lock” mechanism was introduced by Mizuno *et al.* (1990). This reactor involves ~1 cm spherical fuels suspended in a water coolant that is allowed to boil. In the event of coolant pump failure, the fuel sphere would descend through a so-called “density lock” into a liquid holding tank to remove residual decay heat.

The possibility of using micro fuel spheres (<1 mm) was also explored (Harms and Kingdon, 1994; Kingdon, 1998). In this reactor, the fuel is suspended in an upward moving helium flow within cylindrical columns separated by an appropriate moderator material such as graphite or low pressure D₂O into which control rods may be inserted for control

and shutdown. Below the core is a conically divergent dry annulus surrounded by light water to provide both nuclear subcriticality and perpetual cooling by packed-bed heat transfer in case of pump failure.

All concepts have in common that they provide a “fail-safe” mechanism. In the case of a loss-of-coolant accident, the core collapses and becomes subcritical, which is an important safety aspect because it stops the fission process.

2.2. Review of fluidization processes

2.2.1. Flow regimes of fluidization

Fluidization is a process whereby a bed of solid particles is transformed into something closely resembling a liquid. In general fluidized beds show a number of liquid-like properties, for example lighter objects float on top of the bed, the surface stays horizontal even in tilted beds and the solids can flow through an opening in the vessel.

The transport behavior of a fluidized bed can be characterized from the flow regimes and the properties of fluidized particles. Regime classification is based upon bubble behavior (Fan and Zhu, 1998), while the fluidized particles are classified based on the size and density of the particles.

At a low flow rate, fluid moves through the pores between the particles without disturbing the bed. This situation is called a *fixed bed* or a *packed bed*; see Fig. 2.1(a). An increase in the fluid flow rate will lead to a critical condition at which the drag force on the particles balances the gravity force and the particles are suspended. The bed is referred to as an *incipiently fluidized bed* or a bed at *minimum fluidization*; see Fig. 2.1(b). The corresponding superficial fluid velocity is then called the minimum fluidization velocity, u_{mf} . A further increase in the fluid flow rate will accelerate the particles upwards and the bed expands.

The bed behavior along an increase of the fluid flow rate depends on whether the fluidizing agent is liquid or gas. In a liquid-solid fluidized bed, an expansion of the bed takes place in a smooth manner. Instabilities and heterogeneities of solids distribution are normally not observed. This kind of bed is called a *homogeneous fluidized bed* or a *particulate fluidized bed*; see Fig. 2.1(c).

The behavior of gas-solid fluidized beds is quite different. As the flow rate increases, large instabilities occurs, creating bubbles and inducing vigorous motion of particles. The bed does not expand much beyond its volume at minimum fluidization and bubble coalescence and break up take place in the bed. This kind of bed is called a *bubbling fluidized bed* or an *aggregative fluidized bed*; see Fig. 2.1(d). The superficial gas velocity at the incipient of the bubbling regime is called the minimum bubbling velocity, u_{mb} .

As the flow increases bubble coalescence is enhanced and in a small-diameter bed, the size of the bubbles can be large. For fine particles this situation will form *axial slugs*; see Fig. 2.1(e); while for coarse particles it will form a *flat slug*; see Fig. 2.1(f).

The *turbulent fluidized bed*, as shown in Fig. 2.1(g) occurs when the gas velocity increases beyond the bubbling fluidization regime and the *terminal velocity*, u_t , of the particles is reached. The bubble and emulsion phases in this regime becomes indistinguishable, the surface of the bed disappears, and the tendency of bubble breakup is enhanced,

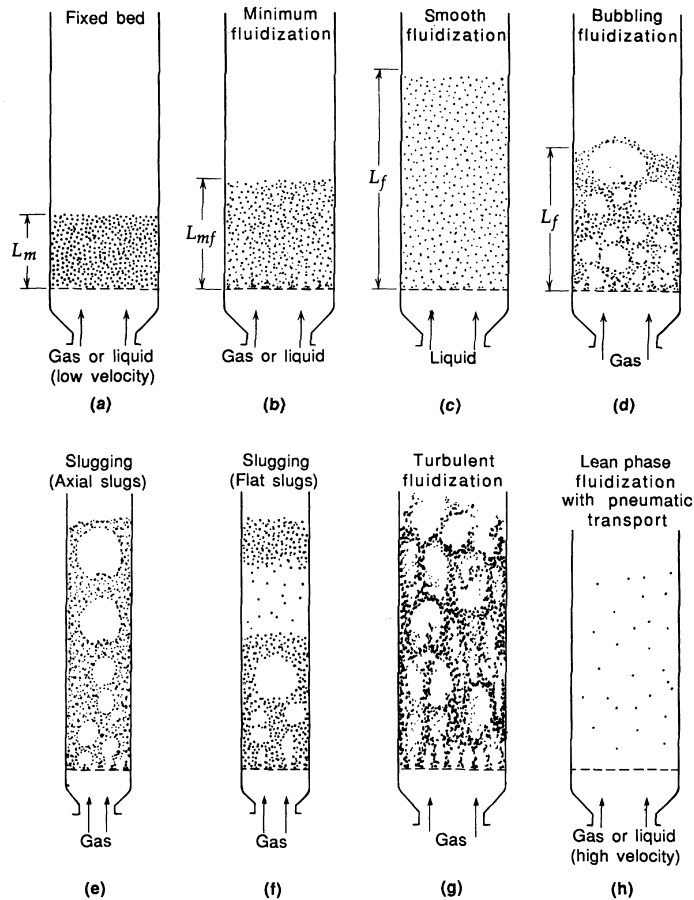


Figure 2.1. Various conditions of fluid-solids interaction in a bed (Kunii and Levenspiel, 1991).

resulting in reduced presence of large bubbles. One might observe as well a turbulent motion of solid clusters. With an even further increase in gas velocity, solid particles are carried out of the bed and this situation gives a *disperse-* or *lean-phase* fluidized bed; see Fig. 2.1(h).

2.2.2. Classifications of particles

According to Geldart (1972), particles can be classified into four groups, i.e. groups A, B, C and D, depending on their average diameter and the density difference between the particles and the gas. Figure 2.2 shows the particle classification which was obtained empirically. This classification is important in understanding the fluidization behavior of solid particles, as under similar operating conditions particles of different groups may behave entirely differently. The Geldart's classification has been widely adopted in the design of gas-solid fluidized beds. A brief description of these particle groups is given below.

Group C consists of small particles with a particle diameter, d_p , smaller than 20 μm . Fluidization of these particles is very difficult as they are very cohesive, in the sense that the inter-particle forces are comparable to the gravitational forces on these particles. The bed expansion may be very high when these particles are fluidized.

Group A consists of particles having a diameter of 30–100 μm and/or a low particle density ($\lesssim 1400 \text{ kg/m}^3$). When these particles are fluidized, the bed expands before bubbles appear (hence $u_{mf} < u_{mb}$). Thus a fluidized bed with Group A particles can be operated in both particulate and bubbling fluidization regime. In the bubbling fluidization regime, gas bubbles coalesce frequently as they move upward, although there exists a maximum stable bubble size (usually less than 10 cm).

In beds of Group B particles, the particulate fluidization regime does not exist. Thus, $u_{mb}/u_{mf} \approx 1$. The bubble size increases with the bed height and it is roughly independent of the mean particle size. There is no maximum stable bubble size for this group.

Group D consists of coarse particles ($d_p > 1 \text{ mm}$). Similar to Group B particles, bubbles appear as soon as u_{mf} is reached. Bubbles coalesce rapidly and grow to large size. The dense phase has a low voidage and when the bubble size approaches the magnitude of the bed diameter, flat slugs as shown in Fig. 2.1(f) appear. Particle mixing is not as good as that of Group A or B particles and to fluidize these solids a large flow rate of gas is required.

2.2.3. Mapping of fluidization regimes

The properties of the particles and the velocity of the fluidizing gas now can be used to determine the regime of fluidization. Figure 2.3 shows the map of fluidization regimes. This type of map is useful for engineering applications and is representing experimental data of many researchers for various conditions as follows (Kunii and Levenspiel, 1991):

<i>Gases</i>	: air, N ₂ , CO ₂ , He, H ₂ , CCl ₄ , Freon-12
<i>Temperature</i>	: 20 – 300 °C
<i>Pressure</i>	: 1 – 85 bar

Two dimensionless numbers are used for the axes in the fluidization map, i.e. the dimensionless particle size, d_p^* , and the dimensionless superficial gas velocity, u^* , defined

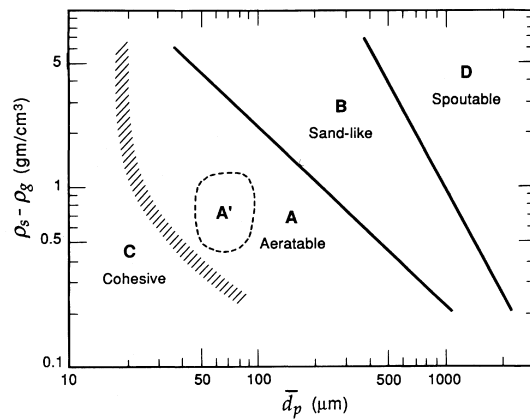


Figure 2.2. Geldart's particle classification (Geldart, 1972).

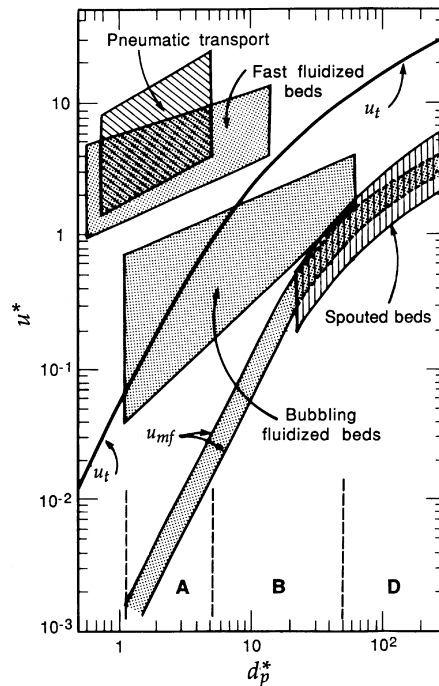


Figure 2.3. General flow regime diagram for the whole range of gas-solid fluidized bed as a function of dimensionless particle size, d_p^* , and dimensionless gas velocity, u^* . Letters A, B, and D refer to the Geldart's classification of solids.

as:

$$d_p^* \equiv d_p \left[\frac{\rho_g(\rho_p - \rho_g)g}{\mu^2} \right]^{1/3} = \text{Ar}^{1/3} \quad (2.1)$$

$$u^* \equiv u \left[\frac{\rho_g^2}{\mu(\rho_p - \rho_g)g} \right]^{1/3} = \frac{\text{Re}_p}{\text{Ar}^{1/3}} \quad (2.2)$$

where d_p is the particle diameter, u is the superficial velocity of the gas, ρ_g and ρ_p are the gas and particle density, respectively, and μ is the viscosity of the gas. Ar is the Archimedes number and its expression is obvious from Eq. (2.1), while Re_p is the Reynolds number ($\equiv d_p \rho_g u / \mu$).

The minimum fluidization velocity, u_{mf} and the terminal velocity, u_t , are also presented in Fig. 2.3. The minimum fluidization velocity occurs when the drag force by the upward moving gas balances the buoyancy force of the particle. By using Ergun's formulation (Ergun, 1952), an expression for the minimum fluidization velocity can be written concisely in terms of the Reynolds and Archimedes number as

$$\frac{1.75}{\alpha_{g,mf}^3 \phi_s} \text{Re}_{p,mf}^2 + \frac{150(1 - \alpha_{g,mf})}{\alpha_{g,mf}^3 \phi_s^2} \text{Re}_{p,mf} = \text{Ar} \quad (2.3)$$

where $\alpha_{g,mf}$ is the void fraction at minimum fluidization, $\text{Re}_{p,mf}$ is the Reynolds number at minimum fluidization ($= d_p u_{mf} \rho_g / \mu$) and ϕ_s is the sphericity of the particles, describing the departure of the particle from a spherical shape, defined as the ratio of a surface area of a sphere with the volume same as the particle to an actual surface area of the particle. In this thesis it is assumed that the particles are spherical, thus having $\phi_s = 1$.

The problem to apply Eq. (2.3) in practice is to estimate the value of the void fraction at minimum fluidization, $\alpha_{g,mf}$, as this value is not necessarily the same as the one at packed condition. An empirical relation is often used instead:

$$\text{Re}_{p,mf} = \sqrt{K_1^2 + K_2 \text{Ar}} - K_1 \quad (2.4)$$

Many investigations have been performed to evaluate the values of K_1 and K_2 . For example, based on 284 data points Wen and Yu (1966) proposed $K_1 = 33.7$ and $K_2 = 0.0408$. Similar approaches have been performed by Babu *et al.* (1978) and Grace (1982). Extension to high pressures (up to 64 bar) for coarse particles has been recommended by Chitester *et al.* (1984), giving $K_1 = 28.7$ and $K_2 = 0.0494$, while a recent investigation conducted by Formisani *et al.* (1998) extends to high temperature systems (up to 800 °C).

As mentioned earlier, Fig. 2.3 shows a curve of the particle terminal velocity, u_t . This velocity is reached when the gravity force and drag force become equal. This value can be estimated from fluid mechanics by the expression

$$u_t = \sqrt{\frac{4(\rho_p - \rho_g)gd_p}{3C_D \rho_g}} \quad (2.5)$$

where C_D is the drag coefficient which can be determined experimentally.

In a fluidized bed having D-group particles, bubbles appear as soon as u_{mf} is reached. Bubbles develop in the lower part of the bed and grow as they rise to the surface. Several correlations to estimate bubble growth in fluidized beds have been developed from experiments. For Geldart B and D particles, Mori and Wen (1975) proposed the following correlation

$$\frac{d_{bm} - d_b}{d_{bm} - d_{b0}} = e^{-0.3z/D} \quad (2.6)$$

where d_b is the bubble diameter, d_{bm} is the maximum (limiting) bubble size, d_{b0} is the initial bubble size formed near the bottom of the bed, z is height in the fluidized bed and D is the diameter of the bed.

The limiting size of the bubble, d_{bm} , can be calculated as

$$d_{bm} = 0.65 \left[\frac{\pi}{4} D^2 (u - u_{mf}) \right]^{0.4} \quad (2.7)$$

and the initial bubble size, d_{b0} , is (Kunii and Levenspiel, 1991)

$$d_{b0} = \frac{2.78}{g} (u - u_{mf})^2 \quad (2.8)$$

2.2.4. Advantages and drawbacks of fluidized beds

Fluidized beds have been widely used in many industrial applications due to their properties such as:

- uniform temperature distribution due to rapid particle-fluid mixing,
- good gas-to-particle and bed-to-wall heat transfer
- large particle-fluid area due to the small size of the particles,
- smooth transport of particles due to liquid-like behavior of fluidization, and
- applicability to large and small scale operations.

However, although the aforementioned advantages are encouraging, some drawbacks also present in the fluidized beds such as:

- attrition of particles,
- erosion of vessel walls because of collisions by particles,
- difficulty in scaling-up fluidized bed reactors, and
- the bed exhibits a complex hydrodynamics behavior when bubbling occurs.

2.3. General features of FLUBER

2.3.1. Materials of FLUBER

The materials employed in FLUBER are similar to those in other high temperature gas cooled reactors. TRISO particles, containing UO_2 , are used as fuel. Unlike in pebble bed reactors where the TRISO particles are contained in pebbles with a graphite matrix, fuel particles in FLUBER are dispersed in a core cavity to form a particle bed. This corresponds to the main objective is to produce power by means of fluidization.

TRISO particles

In the design of a HTGR (and also valid for FLUBER) it is very important to retain fission products within the particles so that their release to the primary coolant does not exceed an acceptable limit (Sawa *et al.*, 2001). The use of coated particles has made possible the development of HTGR technology. The coated particle fuel is characterized by low defect fractions during fabrication ($< 10^{-5}$) and a high degree of leak tightness with respect to fission products (Chapelot *et al.*, 2001; Porta *et al.*, 2001; Nickel *et al.*, 2002). Another advantage in using coated particles fuel is the high flexibility with regards to the core design (IAEA, 1997a). For example by varying the moderator-to-fuel ratio (MFR) the neutronics of the core can easily be influenced. Further the high surface-to-volume ratio (SVR) of coated particles in combination with the relatively high thermal conductivity of SiC and graphite provides an efficient heat transfer.

Each TRISO particle consists of a spherical kernel containing enriched uranium dioxide covered with a concentric porous carbon buffer layer, an inner pyrolytic carbon layer (I-PyC), a silicon carbide (SiC) layer, and an outer pyrolytic carbon layer (O-PyC). Fig. 2.4 shows a micrograph of a typical TRISO particle.

The porous carbon buffer layer is intended to accommodate swelling of the fuel kernel and to provide free volume for the storage of gaseous fission products and CO gas (Minato *et al.*, 1994). This buffer layer also mitigates stress on other coating layers and protects the I-PyC layer from the damage caused by recoil of fission fragments. In comparison to conventional fuel assemblies, the use of a porous carbon buffer layer enables a higher fuel burnup.

The second layer is the I-PyC layer which prevents corrosion of the UO_2 kernel in the SiC layer. This layer can be regarded as a *mini pressure vessel* because it withstands high internal pressures (> 500 bar) at very high temperatures (≈ 1873 K). Furthermore, I-PyC layer is a reliable barrier for fission products as it almost completely retains short-lived fission gasses. However, Miller *et al.* (2001) reported that the I-PyC layer is the first part to fail caused by the shrinkage that this layer endures during irradiation time of the particle.

The SiC layer is the strongest layer and provides mechanical strength. It also acts as a barrier against metallic fission products such as Cs, Sr and Ag (Ogawa *et al.*, 1985; Minato *et al.*, 1993; Sawa *et al.*, 1997) due to the lower diffusion coefficient than that in I-PyC. A greater thickness of the porous carbon and SiC layers always reduces the probability of failure of the coating (Golubev *et al.*, 2002).

The outer layer, the O-PyC layer, protects the inner SiC layer from mechanical failure during handling of coated fuel particles. Similar to the I-PyC layer, this layer retains short-lived fission gases. The O-PyC layer also experiences irradiation-induced shrinkage as a result of fast neutron exposure and it reduces the SiC tensile stress due to internal pressure. With all these layers, TRISO particles are able to retain more than 99.9% of all fission products within the particle themselves at high burnup (Ahlf *et al.*, 1990) and high temperature conditions (Kugeler and Phlippen, 1996).

Helium

When choosing a cooling gas for a nuclear reactor, several factors need to be considered, such as thermodynamic effectiveness, chemical stability, neutronic properties,

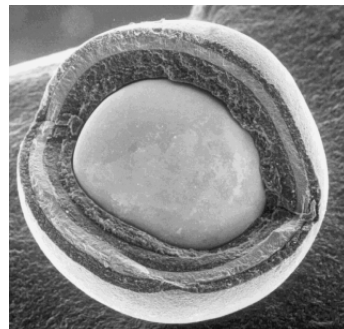


Figure 2.4. A micrograph of a typical TRISO fuel particle. In the center is the UO_2 kernel, surrounded by a cladding of four layers: porous carbon, I-PyC, SiC and O-PyC. The outer diameter of this particle is 1 mm.

structural material compatibility, availability and cost. From a thermodynamic point of view, helium allows operation at high temperature, providing high thermal efficiency. In addition, the absence of a phase change of helium is advantageous as it ensures a uniform cooling. Some measures of merit are used to compare the thermal performance of gas coolants (Melese and Katz, 1984), such as the required heat transfer area for a fixed flow area and pressure change for a given system pressure. The first criterion indicates the complexities of mechanical design, while the latter relates to pressure loads on grid plates (if any). Using these figures of merit, the choice of gas coolants usually reduces to CO_2 and helium. However, on the basis of turbomachinery design, helium is preferred over carbon dioxide. Helium needs e.g. a smaller frontal area for the same blade efficiency and lower exit diffuser losses. On the other hand, helium requires more blade rows than a turbomachine using carbon dioxide for large pressure ratio turbomachinery.

Besides the above, helium is also chemically inert and does not react with carbon of O-PyC layers, reducing the possibility of particle fuel failures. From a neutronics point of view, the total cross-section of helium is small, so neutrons do hardly interact with helium.

Graphite

Graphite is employed as a moderator as well as a structural material. Desirable properties of graphite are minimal dimensional changes, high thermal conductivity – ensuring a good heat transfer behavior during operation and accidental events (IAEA, 2001), low thermal expansion, low elastic modulus, high tensile strength, low impurity content, and acceptable oxidation resistance (Melese and Katz, 1984). Being solid, graphite ensures a constant moderating behavior as opposed to the liquid moderator in water-cooled reactors. The MFR in HTRs generally is higher than in LWRs, resulting a larger fraction of thermal fission over total fission. Massimo (1976) showed that in HTRs 85% of the fuel absorptions take place below 1 eV, while in LWRs this figure is only 70%. However, irradiation effects by fast neutrons cause dimensional changes, changes in thermal conductivity and irradiation-induced creep (IAEA, 2000).

2.3.2. Overview of the previous FLUBER design

The development process of FLUBER dates back to 1996 and is continuously performed to get better performance (Van Dam *et al.*, 1996; Van der Hagen *et al.*, 1997; Kloosterman *et al.*, 1999, 2001). The design available at the time of starting this PhD project is given in Table 2.1 and 2.2.

Table 2.1. Characteristics of FLUBER (Kloosterman *et al.*, 2001).

Radius of the core cavity [cm]	56.4
Height of the core cavity [cm]	600
Height of the whole reactor [cm]	800
Thickness of the radial reflector [cm]	100
Thickness of the axial reflector [cm]	100
Collapsed-bed height [cm]	136
Uranium inventory [kg]	120
Enrichment [% weight]	16.76
Helium pressure [bar]	60

Table 2.2. Characteristics of fuel particles (Kloosterman *et al.*, 2001).

Material	Density, [g/cm ³]	Outer diameter, [mm]
UO ₂ kernel	10.88	0.26
Porous carbon buffer layer	1.1	0.77
I-PyC coating	1.9	0.85
SiC coating	3.2	0.92
O-PyC coating	1.9	1.00

In packed bed conditions, the core is subcritical as a result of a lack of moderation. As the flow rate increases, the core expands and neutrons leak away to the graphite reflector where they are moderated and are possibly reflected back to the core. In this event we can say that the effective MFR increases. Increasing the flow leads to an increase in the number of neutrons scattered back into the core, hence increasing reactivity. The situation where the reactivity increases as the bed height increases is called *undermoderation*. At higher flow rates, however, the reactor core becomes increasingly more transparent (from a neutronic point of view) and consequently the probability of neutron leakage increases, thus decreasing the reactivity. The situation where the reactivity decreases as the bed height increases is called *overmoderation*. With a proper choice of system parameters, the reactor can be critical within a certain range of coolant flow rates as discussed by Kloosterman *et al.* (2001).

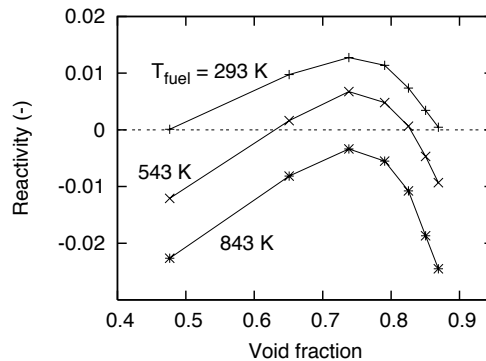


Figure 2.5. Reactivity of the old design as a function of void fraction for different fuel temperature. The total mass of uranium is 120 kg, cross-section area of the core is 1 m^2 .

Fig. 2.5 shows the reactivity of the previous design as a function of void fraction for three different core temperatures, which were chosen for the purpose of calculating the temperature coefficient. Throughout this thesis, the void fraction is defined as the fraction of the total volume accounted for by the volume of the gas in the gas-solid mixture, excluding the void cavity above the bed surface. At room temperature (293 K), in a packed condition, the reactor is close to critical. When the bed expands, by increasing the flow rate, the reactivity increases accompanied with power generation and an increase in core temperature. The negative fuel temperature coefficient, however, will keep the reactor critical at a new equilibrium point. If we proceed further to expand the bed (enlarge the void fraction) by increasing the helium flow rate, we will follow the horizontal line of zero reactivity. In this situation the reactor produces power (undermoderated region). At a void fraction of about 0.74 (corresponding to 274 cm of bed height), the core temperature reaches a maximum of about 663 K. If the gas flow rate increases further, then we reach the overmoderated region. In this case the reactor is critical at lower power and core temperature.

Lathouwers *et al.* (2003) improved on the design by using natural boron of 20 ppm as an absorber at the bottom of the side reflector and increasing the fuel inventory to 170 kg. This resulted in a higher outlet temperature (about 850 K) and a higher total power of about 40 MW. The reactivity at packed bed condition is -1.8%, rising to a maximum value of 0.5%.

2.4. Summary

It has been discussed in this chapter that nuclear reactors operated based on fluidization are quite attractive thanks to the excellent mixing and heat transfer properties. We have had proposed such a reactor based on gas-solid fluidization and improvements to the design have been performed. However some questions are still open such as the stability and the performance of the reactor in operation.

CHAPTER 3

Static behavior of FLUBER*

In Chapter 2 an overview of the fluidization process was described followed by the design concept of FLUBER and some features of the preceding designs. From a neutronic point of view, the reactor is feasible as it becomes critical when the bed expands and sub-critical when the bed collapses.

However, some drawbacks about this design are as follows: (i) the reactivity margin of the packed bed condition is too narrow for safe operation, see for example Fig. 2.5, (ii) the maximum attainable power is rather limited, and (iii) the maximum outlet gas temperature is too low to obtain high thermal efficiency.

In this chapter it will be shown that some modifications of the design may solve the aforementioned issues. Section 3.1 describes the design target and parameters of the modified FLUBER, as well as its computational method and the results of such modifications. Section 3.2 discusses the behavior of homogeneous FLUBER after being modified, while the influence of particle distribution on reactivity is discussed in Section 3.3. During operation, bubbles or void regions are always present in a fluidized bed. The influence of such bubbles in a core on reactivity is discussed in Section 3.4. Finally, a summary in Section 3.5 concludes this chapter.

*This chapter is adapted from the following papers:

Agung, A., Lathouwers, D., van der Hagen, T.H.J.J., van Dam, H., Pain, C.C., de Oliveira, C.R.E., and Goddard, A.J.H. (2003). Influence of Bubbles on Reactivity and Power in a Fluidized Bed Nuclear Reactor. *Proc. GENES4/ANP-2003*, Kyoto, Japan.

Agung, A., Lathouwers, D. , van der Hagen, T.H.J.J. , van Dam, H., Pain, C.C., Goddard, A.J.H., Eaton, M.D., Gomes, J.L.M.A., and Miles, B. (2006). On an Improved Design of a Fluidized Bed Nuclear Reactor. Part I: Design Modifications and Steady State Features. *Nuclear Technology*, **153**, 117.

3.1. Design modifications of FLUBER

3.1.1. Design targets

An example of an ideal reactivity curve at cold conditions (room temperature of 293 K) is shown in Fig. 3.1, where ρ_{sm} denotes the cold shutdown margin and represents the minimum value of reactivity at packed bed condition and ρ_{ex} is the excess reactivity that is the maximum value of reactivity. The ideal reactivity curve does not exhibit an intermediate maximum and the excess reactivity is reached at the maximum bed expansion, implying that the maximum gas temperature and power will be reached at full bed expansion and therefore at the maximum coolant flow.

The slope of the reactivity curve determines the sensitivity of the reactor power against the change of void fraction. The steeper the slope ($d\rho/d\alpha_g$; α_g being void fraction), the more sensitive the reactor. At a constant helium flow rate, the reactor is theoretically stationary at a certain power level, but the nature of the fluidization process creates bubbles (void regions) within the bed (especially in the bubbly and slug flow regime). Any disturbances originating from local bubble generation may lead to large reactivity fluctuations. Having a larger shutdown margin (at a constant excess reactivity) is desirable from a safety point of view, but it also leads to a more sensitive reactor. A similar situation applies to the excess reactivity. However, too flat a curve is not desirable because the reactivity swing between packed bed and fully expanded bed becomes small.

The excess reactivity is required to compensate for the negative reactivity feedback from the fuel temperature. Previous results (Kloosterman *et al.*, 2001; Lathouwers *et al.*, 2003) indicate that the fuel reactivity coefficient is about -4 pcm/K. Thus, to ensure operation at 1000 K above room temperature, a (cold) excess reactivity of at least 4% is required. This margin will be higher if build-up of fission products is taken into account. To ensure

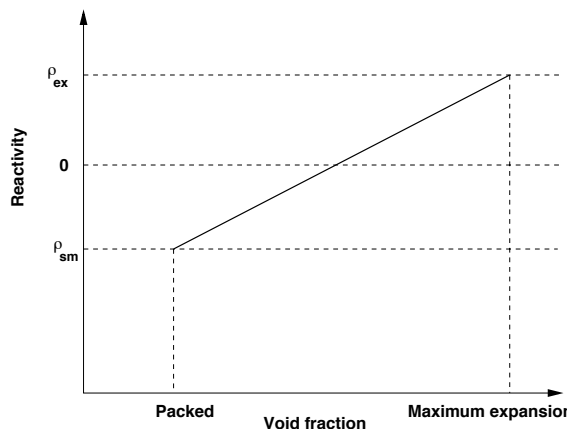


Figure 3.1. The ideal reactivity curve at cold condition (293 K). ρ_{ex} and ρ_{sm} are the excess reactivity and shutdown margin, respectively. The maximum reactivity is achieved at full bed expansion.

a safe shutdown in the absence of active controls, the reactor is required to have a large shutdown margin. It is reasonable to require about 4% – 5% of cold shutdown margin at packed bed conditions.

3.1.2. Design parameters

Several modifications are proposed to achieve the ideal reactivity curve, and they can be categorized into two parts, i.e. to obtain a reactivity curve with the intended shape and to achieve the required values of the shutdown margin and excess reactivity. Because there are many degrees of freedom, the modifications are concentrated on the following items:

- *Use of a porous bottom reflector*

By installing a porous reflector at the bottom of the reactor, the thermalization of neutrons by the graphite is less effective. Therefore, at packed bed conditions, the reactivity will be lower but at larger bed expansion the influence of the porous reflector becomes less and re-entrance of thermal neutrons has a stronger influence. In this work the porosity of the graphite bottom reflector is varied to a maximum of 40%.

- *Adding absorber at the bottom of the reflector*

The key point to achieve a larger shutdown margin is to increase the neutron absorption when the bed is collapsed. Boron is added to the bottom reflector, which will absorb more neutrons at the bottom of the core. As the bed height increases, this absorption effect decreases, and moderation by the side reflector will dominate. A region with natural boron absorber of 50 cm thick is located at the bottom of the reflector and the absorber concentration is varied up to 20 ppm.

- *Adding absorber at the bottom of the side reflector*

An absorber ring consisting of a mixture of graphite and natural boron is embedded in the lower part of the side reflector. In principle the process is similar to that of adding the bottom absorber. When the bed collapses, more neutrons are absorbed in the absorber region. As the bed expands, the absorption becomes less pronounced. The higher the concentration of absorber, the higher the reactivity swing it can produce. Adding a side absorber ring is expected to give a better result compared to an absorber at the bottom. The surface area of the bottom absorber is fixed at a certain value, in this case the cross-section area of the core. In the case of a side absorber, the surface area can be varied depending on the height of the absorber. Furthermore, the ratio of the absorber surface area to the total side surface area changes during fluidization which increases the reactivity swing.

- *Increasing the uranium inventory*

A higher excess reactivity can be achieved effectively by increasing the mass of uranium in the core, in this case by altering the number of fuel particles. However, increasing the uranium inventory also gives a smaller shutdown margin. Hence it is obvious that there should be a compromise based on this issue. The uranium inventory is varied here from 140 kg to 260 kg.

- *Changing the core cross-section area*

Changing the core cross-section area also influences the reactivity of the system. With a constant fuel inventory, enlarging the cross-section reduces the height of the packed bed. This situation leads to a smaller probability of neutron capture in the core, but it may lead to a larger leakage. Further with a lower packed bed, void fraction at the maximum bed height becomes larger. As long as the reactor operates in the undermoderated region, the reactivity at maximum bed expansion will be higher.

Incorporating either a bottom absorber or a side absorber in combination with the change in the core cross-section is also useful to obtain a larger shutdown margin. When the cross-section area is enlarged, the surface area of absorber obviously becomes larger. In either situations, a larger SVR is achieved and more absorption takes place. In the present work, variation of core cross-section is from 1 m^2 to 2 m^2 .

- *Modifying the moderator-to-fuel ratio (MFR)*

Changes in the MFR can be achieved by altering the diameter of either the fuel kernel or the fuel particle. Although it is possible to fabricate particles with a fuel kernel diameter up to 6 mm (Brandau, 2002), in the present work only the kernel diameter was altered and the particle diameter was kept constant at 1 mm. The reason of doing so is related to the fluidization process: increasing the size of the fuel particles makes the particles more difficult to fluidize.

Throughout this thesis, the MFR is defined as the ratio of the number of carbon atoms to the number of uranium atoms of the particles. In this study, the variation of the kernel diameter is from 0.2 mm (MFR of 354) to 0.3 mm (MFR of 103). For a core with fixed cross-section area and fuel inventory, enlarging the size of fuel kernel reduces the height of a packed bed and vice versa.

3.1.3. Computational procedure

FLUBER has unconventional aspects which require special attention in terms of neutronic calculations, such as the variation of geometry under operational conditions, the presence of a large void volume above the core, and a strong spectral variation in the core. A multigroup diffusion or transport code should be used to handle such problems. However, during the first stages of the calculations it became clear that the physical conditions in FLUBER lie outside the range of applicability or acceptable accuracy of standard methods (Van Dam *et al.*, 1996). The Bold-Venture two-dimensional diffusion code (ORNL, 1989) was used with 49-group data library and a special treatment should be performed to handle the diffusion coefficient for the cavity by using a formalism developed by Gerwin and Scherer (1987). It was found that at low bed expansion, the k_{eff} is very sensitive to the diffusion coefficient, while at high expansion, the result is almost independent of the diffusion coefficient. Calculations using a transport code were also performed, i.e. by using the two-dimensional discrete ordinates code DORT (Rhoades and Childs, 1988) with 16-group data library. The results however were not of high quality, even with high order ordinates, because of the possible occurrence of ray effects in the cavity. Hence, for our subsequent calculations, the Monte Carlo code was used to obtain more accurate results.

All static calculations have been carried out using the INAS (IRI – NJOY – AMPX – SCALE) code system with nuclear data libraries based on the JEF-2.2 data file (de Leege, 1994). A schematic graph of the INAS code system is given in Fig. 3.2.

The master library is processed by NJOY91.128 and NSLINK42 and is weighted by hard spectrum, producing a 172-group AMPX-format library. The built-in fine group master library available in SCALE is not used because of the use of soft-spectrum weight.

DANCOFF-MC (Feher *et al.*, 1994) is a Monte Carlo code for calculating the Dancoff factor, which by definition is the probability of a neutron being emitted isotropically from a surface of a fuel lump for having the next interaction in another fuel lump. This factor is used as a correction to the neutron escape probability in a lattice cell calculation.

For our purpose, a special code based on DANCOFF-MC is used, i.e. DCMC3Q. This code is developed for specific purposes such as for pebble bed reactors and other reactors with similar fuel arrangements. The DCMC3Q has an additional capability to calculate Dancoff factor for quasi-regular array. For FLUBER calculations, particles are modeled in a rhombohedral arrangement (see Fig. 3.3). Calculations were performed for each void fraction value corresponding to a specific bed height. Each calculation was running until either a maximum of 1 million cycles or a deviation smaller than 10^{-5} had been reached, whichever came first.

CSAS (Landers and Petrie, 2000) is an automatic driver for preparing cross-sections and for criticality analysis. The purpose of CSAS in our calculations is to create microscopic cell-weighted working format cross-section libraries (or working libraries) for subsequent use. The result of the Dancoff correction factor obtained from DCMC3Q is used as an input in CSAS. Several functional modules are employed in CSAS to generate a working library, i.e. BONAMI (Greene, 2000a), NITAWL-II (Greene *et al.*, 2000) and XSDRNPM (Greene and Petrie, 2000). The BONAMI module calculates resonance-shielded cross-sections by the use of the Bondarenko method in the unresolved region, while the NITAWL-II calculates the resonance-shielded cross-sections by using the integral Nordheim method in the resolved region. The cell-weighted cross-section is then computed by weighting the cross-section by the flux generated from the one-dimensional transport code XSDRNPM.

Some assumptions are used for creating the working libraries in FLUBER calculation. The carbonous layers in the fuel particle (i.e. the buffer, I-PyC, SiC and O-PyC layers) are lumped into one layer because the total thickness of those layers is much smaller than the neutron mean free path. Impurities in the carbonous layer are assumed to be 1 ppm of natural boron. The fuel particles are assumed to be uniform and are arranged in a regular lattice.

The values of the Dancoff factor are obtained by assuming the fuel as a black absorber. The correction to the Dancoff factor considering a grey effect is performed in the NITAWL-II module. This special treatment is employed because NITAWL-II has a built-in procedure to treat the greyness of the fuel (Petrie, 2001).

The major part of the criticality calculations is carried out by the three-dimensional Monte Carlo code KENO-V.a (Petrie and Landers, 2000) with the library created by the preceding CSAS calculation. Figure 3.4 shows the model of FLUBER for KENO-V.a calculations. FLUBER is modeled as a cylinder with four material zones, three of which are common for all static models, i.e. fuel particle bed (zone A), helium cavity (zone B) and graphite

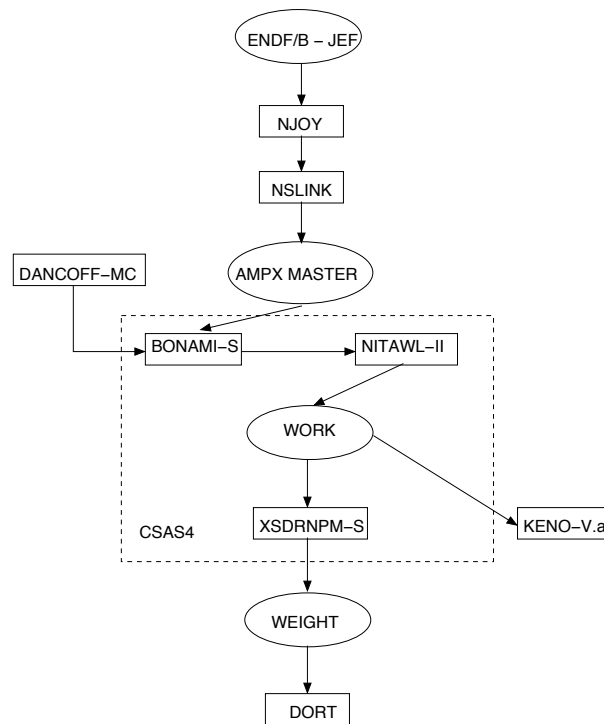


Figure 3.2. The INAS code system employed in this research (de Leege, 1994).

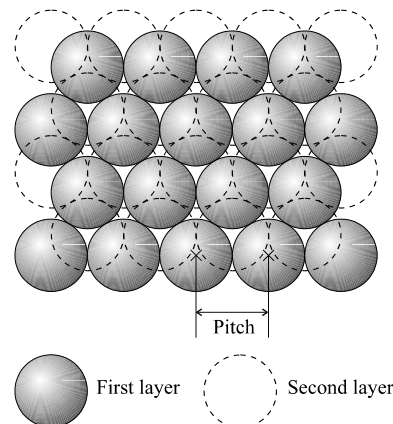


Figure 3.3. Rhombohedral arrangement of fuels in a lattice cell (Feher et al., 1994).

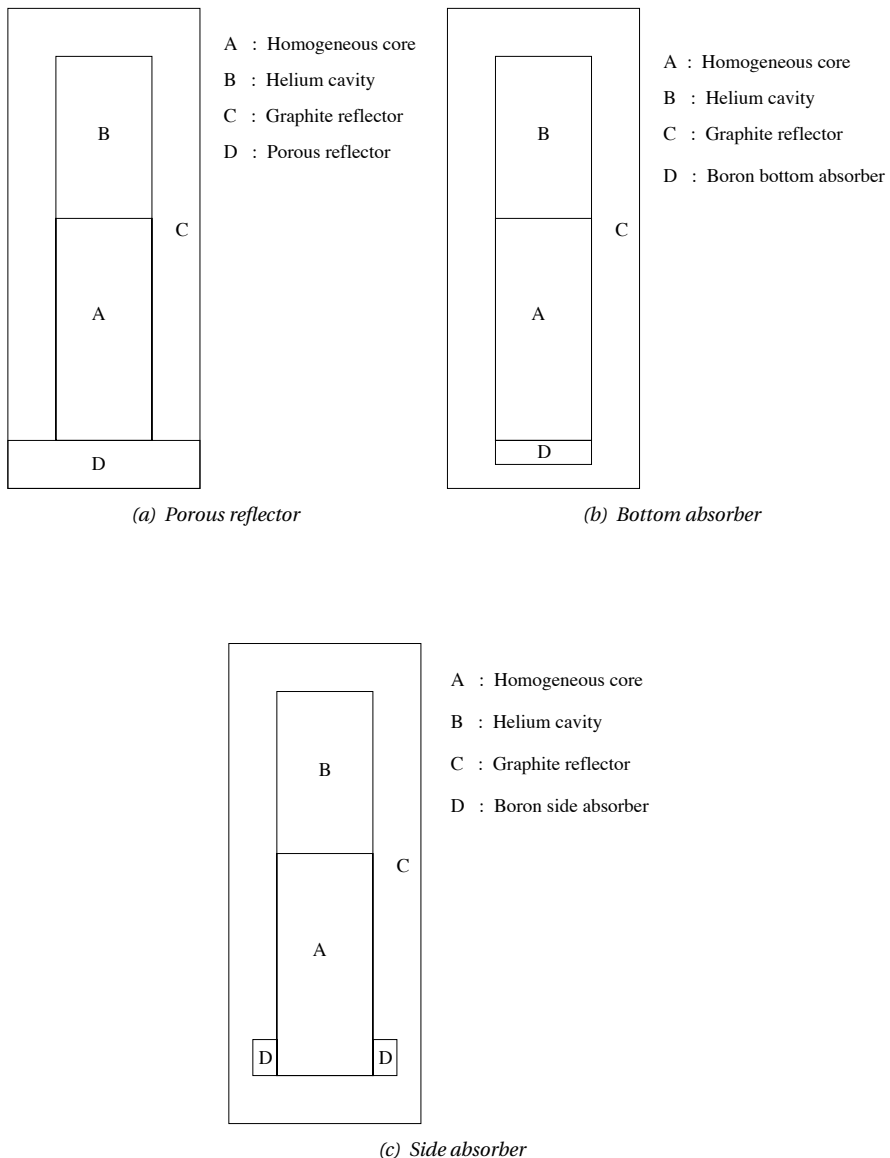


Figure 3.4. FLUBER models for KENO-V. a calculations, i.e. (a) the model with porous reflector, (b) with bottom absorber and (c) with a ring of side absorber.

reflector (zone C). The fourth material zone (zone D) is specific for each model, namely the bottom absorber, the porous reflector and the natural boron side absorber.

Within the current model, the particles are assumed to have a uniform distribution with a minimum void fraction of 0.4 (Cumberland and Crawford, 1987). The assumption of a uniform particle distribution is justified by the fact that the neutron mean free path in the core is much larger than the pitch among fuel kernels. Calculations were performed for different states of the bed (from collapsed bed until full expansion) for each model. The results of KENO-V.a have a standard deviation of k_{eff} about 0.0005 (not shown in the subsequent graphs for reasons of clarity).

3.1.4. Results

In Fig. 3.5 the results of modifications are compared by using, respectively, a porous bottom reflector, a bottom absorber and a side absorber at a bed cross-section area of 1 m^2 . The figure shows that installing a porous axial reflector does not lead to a substantial improvement. For example, when the thickness of the porous reflector is 50 cm, increase in the porosity up to 40% will give a slight decrease in reactivity. Enlarging the thickness of the porous reflector and increasing the porosity up to 80% could result in the reactivity going down to -2% for the packed bed; however, this effort in fact deteriorates the maximum reactivity that can be achieved.

Adding boron absorber to the bottom reflector gives a better result compared to the small porous bottom reflector. In this case an absorber concentration of only 20 ppm natural boron will give a decrease in reactivity of about 1% at packed bed conditions. The reactivity at higher void fractions does not change significantly, which is advantageous. However, the reactivity curve exhibits an intermediate maximum.

With 50 cm in height and width of the side absorber ring, the absorption sensitivity at a lower void fraction for this arrangement is larger than that of a bottom absorber. An absorber concentration of 20 ppm gives a reactivity decrease to -4%. Furthermore the reactivity curve does not exhibit a maximum, which is desirable. However, the reactivity at higher void fraction is strongly affected, and the decrease of reactivity reaches about 0.5% in this arrangement.

Comparing these results to the previous design (Fig. 2.5), the curve corresponding to side absorber apparently has a shifted shape towards the bottom-right side of the plane. This means that a larger shutdown margin can be achieved as well as the requirement of no-intermediate-maximum. Thus, the reactor with a side absorber ring is chosen for the subsequent step, which is meant to adjust the criticality.

The reactivity curve can also be presented in terms of MFR. As the maximum reactivity is achieved at fully expanded conditions, in presenting the results, we concentrate on two states, i.e. the packed bed and the fully expanded bed, and investigate whether these points meet the required ρ_{sm} and ρ_{ex} , respectively. A typical graph of such a representation is shown in Fig. 3.6. The dash-dotted line corresponds to the packed bed (minimum void fraction) and the solid line corresponds to the fully expanded bed (maximum void fraction). These curves intersect at a point, dividing the plane into two regions: the undermoderated region and the overmoderated region. In this thesis, the intersection is called a *transition point*. Because of the requirement of no-intermediate-maximum in the reac-

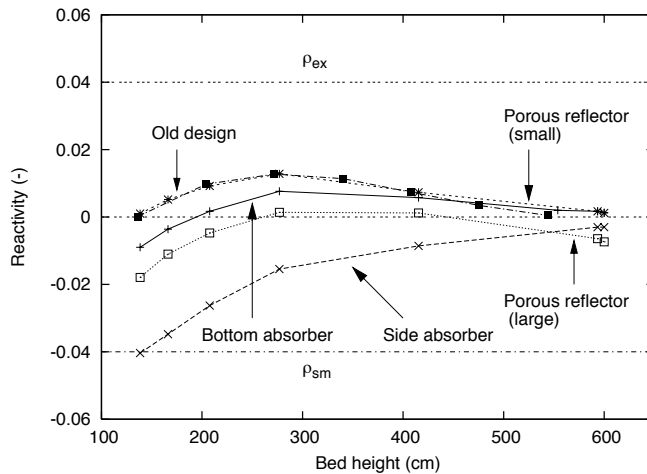


Figure 3.5. The influence of various modifications to the reactivity. The mass of uranium is 140 kg with uniform core temperature of 293 K. The bottom reflector has a porosity of 40% and thickness of 50 cm in the case of small porous bottom reflector and 80% in porosity and 100 cm in thickness for the large porous bottom reflector. The ring in the side absorber has a dimension of 50 cm in both width and height. The layer of bottom absorber is 50 cm thick. The concentration of boron is 20 ppm for both side absorber and bottom absorber.

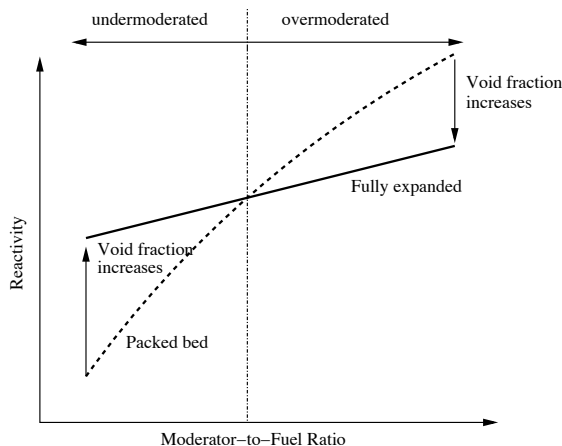


Figure 3.6. A typical graph showing the reactivity behavior of the bed as a function of MFR. The dash-dotted line represents the bed at packed condition and the solid line represents the bed at full expansion. The plane is divided by a transition point into two regions, i.e. the undermoderated region where the reactivity increases as the void fraction (or bed height) of the core increases and the overmoderated region where the reactivity decreases as the void fraction of the core increases.

tivity curve, we are interested in the undermoderated region (left of the transition point in the MFR-reactivity plane).

In Figs. 3.7–3.8 the reactivity curves for three modification parameters are shown, i.e. for the side absorber, the fuel inventory and the MFR. The core cross-section area is fixed at 2 m^2 . The curve of minimum void fraction is indicated with + markers (packed conditions), while that of maximum void fraction is given with \times markers (fully expanded condition). A vertical dashed line is also present, showing the transition point, defined earlier.

In Fig. 3.7, the side absorber is set at 50 ppm of concentration and 50 cm of height and width. The variation of kernel radius is 0.1 (rightmost in the graph), 0.11, 0.12, 0.125, 0.13, 0.14 and 0.15 (leftmost in the graph) mm. The fuel inventory is varied from 140 kg (Fig. 3.7(a)) to 260 kg (Fig. 3.7(d)) with increments of 40 kg. These graphs can be interpreted as follows. Reducing the fuel kernel radius at a constant fuel inventory will lead to an increase in packed bed height. In this event the influence of the side absorber becomes weaker and consequently the reactivity increases. If we take a constant fuel kernel radius, increasing the fuel inventory gives a higher packed bed height, which reduces the influence of the side absorber, thus leading to an increase in reactivity as well.

When the inventory is 140 kg (see Fig. 3.7(a)), the minimum void fraction line crosses the shutdown margin at a higher MFR (in this case when the kernel radius is ≈ 0.102 mm), or in other words, the packed bed is higher. This is not surprising, as the bed has to be higher to compensate for the influence of the side absorber. This situation gives a small reactivity swing and is therefore not preferable. At the other extreme when the fuel inventory is 260 kg (see Fig. 3.7(d)), the minimum void fraction line intersects the shutdown margin at about 0.131 mm of kernel radius. The reactivity at maximum bed expansion in this case is about 2% higher than the intended excess reactivity, resulting in a steep reactivity slope. At 220 kg of inventory (see Fig. 3.7(c)), the curves give the required result as at kernel radius of 0.125 mm both the minimum void fraction line and maximum expansion lines intersect the shutdown margin and over-reactivity margin at the intended values.

In Fig. 3.8 the fuel inventory is fixed at 220 kg. The concentration of the side absorber is varied from 10 to 50 ppm in a fixed geometry of 50 cm height and 50 cm width. Variations of the fuel kernel diameter are the same as in Fig. 3.7(a). At a constant MFR (or in this case at a constant packed bed height) it is clear that the higher the absorber concentration, the lower the reactivity at packed bed conditions. At low MFR (or larger kernel size) the influence of the side absorber is larger than that at high MFR (or smaller kernel size) as already described above. In order to achieve the intended shutdown margin, particles with a larger kernel size require less absorption from the side absorber. At maximum expansion, the influence of the side absorber is less when compared to the influence to packed bed. At maximum expansion, the reactivity differences are about 2%, but at packed bed the differences are in the order of 8%. As shown in Fig. 3.8(c), the kernel with 0.13 mm of radius, 20 ppm of side absorber and the kernel with 0.125 mm radius, 50 ppm of side absorber are candidates. However, the kernel with 0.125 mm radius is preferable. The reason is that while the radius of the kernel is varied, the outer radius of the buffer layer, whose main purpose is to accommodate kernel swelling and fission gas release, is kept constant. With a smaller kernel size (and consequently higher ratio of buffer layer volume to kernel volume), higher burnup of the fuel in the reactor is possible, as compared to particles with larger kernel size.

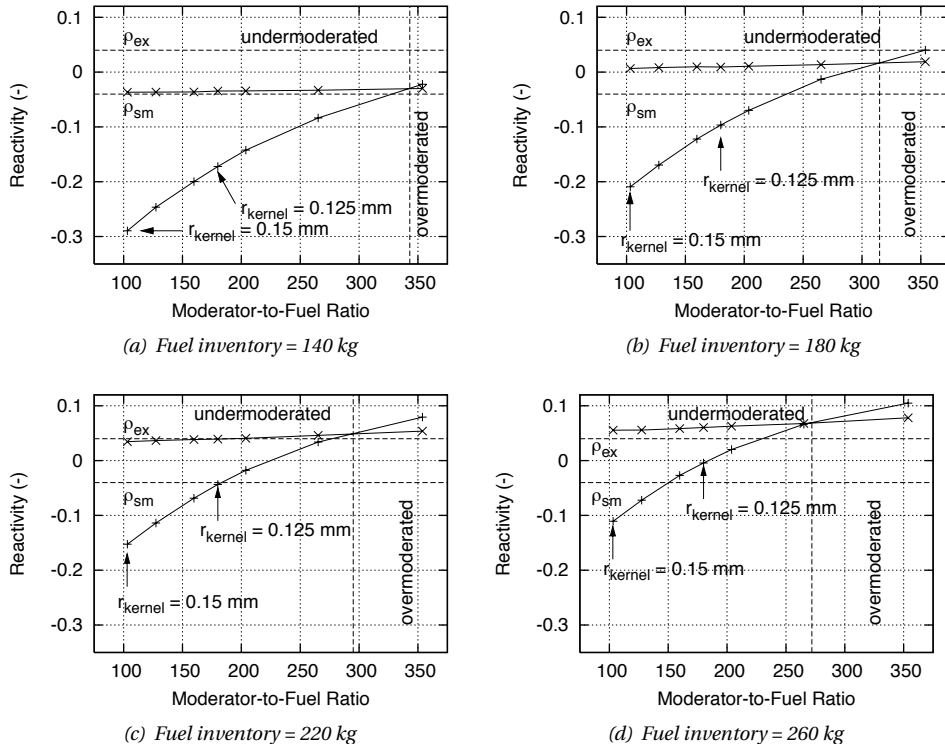


Figure 3.7. Reactivity as a function of MFR at 140 kg, 180 kg, 220 kg and 260 kg of fuel inventory. The side absorber is 50 cm thick and width and its concentration is 50 ppm. The core cross-section area is 2 m^2 . The variation of kernel radius is 0.1 mm (rightmost), 0.11 mm, 0.12 mm, 0.125 mm, 0.13 mm, 0.14 mm and 0.15 mm (leftmost). A vertical dashed line in the right part of the graph is connecting the transition point, dividing the plane into an undermoderated region and a overmoderated region. The graph basically shows two types of bed conditions, i.e., the packed bed situation (with + markers) and the fully expanded bed situation (with x markers).

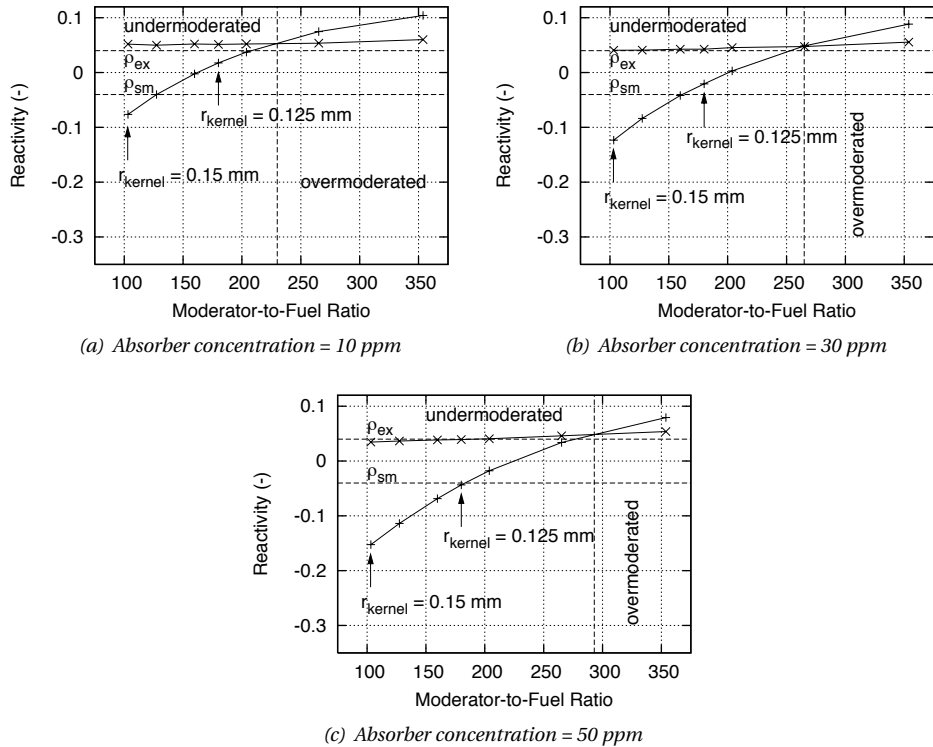


Figure 3.8. Reactivity as a function of MFR at 10 ppm, 30 ppm and 50 ppm of side absorber concentration. Fuel inventory is fixed at 220 kg. Other parameters are the same as in Fig. 3.7.

These results show that increasing the fuel inventory is effective to achieve the required excess reactivity, while enlarging the core cross-section area in combination with installing a side absorber is effective to get a larger reactivity shutdown margin. Based on the results given in Figs. 3.7–3.8, a new design is proposed and the various modifications to accommodate the new over-reactivity and shutdown margin are summarized in Table 3.1.

Table 3.1. Parameter comparisons of the previous designs and the current design.

Parameters	Old design ¹	1st Revision ²	2nd Revision ³
Thickness of radial absorber [cm]	-	50	50
Height of radial absorber [cm]	-	50	50
Natural boron concentration in radial absorber [ppm]	-	20	50
Cross-section area of the core [m ²]	1	1	2
Uranium inventory [kg]	140	170	220
Fuel kernel diameter [mm]	0.26	0.26	0.25

¹ Kloosterman *et al.* (2001)

² Lathouwers *et al.* (2003)

³ This thesis

3.2. Behavior of homogeneous bed

Fig. 3.9 shows the reactivity as a function of bed expansion for the finally selected design. The bed is packed at 122 cm of height and is subcritical at room temperature. The bed expands as the gas flows into the reactor. When the bed height reaches about 325 cm, the reactor becomes critical. Increasing the gas flow gives a supercritical situation, but as the power generation increases, the fuel temperature also increases and introduces a negative reactivity feedback, keeping the reactor critical. Further expansion enables the reactor to be critical at higher temperature. At maximum bed expansion the highest possible temperature is 1193 K.

Neutron flux distributions in FLUBER are shown in Fig. 3.10 and 3.11 for the packed bed and the expanded bed, respectively. The energy boundary for epithermal neutrons has been chosen as 1.1 eV, while that for fast neutrons is 2.25 keV. Fast neutrons are produced as products of fission process in the fuel, thus the population of the fast neutrons is high in the core (see Fig. 3.10(c) and 3.11(c)). Neutron thermalization process takes place mostly in the graphite reflector. When the bed is packed, this process occurs mainly in the side and bottom reflector (see Fig. 3.10(a)). When the bed is expanded, thermalization also occurs in the top reflector (see Fig. 3.11(a)). Observe as well the presence of a depression region in the lower part of side absorber. This depression is caused by the embedded natural boron in the side reflector.

KENO-V.a also calculates the effective neutron generation time (Λ). For the collapsed bed the generation time is about 1.3 ms, increasing with increasing bed height to about

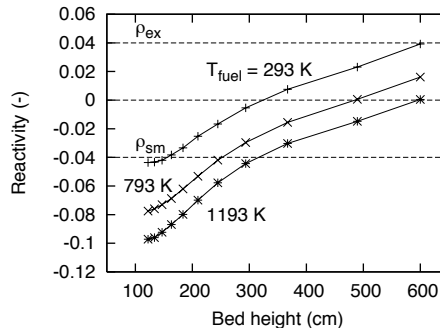


Figure 3.9. The static reactivity of the new design for different fuel temperature as a function of bed expansion. ρ_{ex} and ρ_{sm} are the excess reactivity and shutdown margin, respectively. The temperature of helium gas is the same as the temperature of fuel particles, while the temperature of graphite reflector is given as an arithmetic average between the temperature of fuel particles and room temperature (293 K).

2.6 ms at maximum bed expansion. The increase of Λ is caused by the increasing influence of the reflector on the neutron chain reaction, which tends to slow down the dynamics the system.

3.3. Influence of particle distribution on reactivity

In a gas-solid fluidized bed it is quite difficult to have a homogeneous fluidization. Depending on the fluidization regime, it may exhibit small or large bubbles (void surrounded by particle clusters). In the current section, the influence of inhomogeneities of particle distribution on the reactivity is investigated and will be compared to the reactivity of the homogeneous core. The objective of such a simulation is to understand whether a particular fluidization regime might influence the reactivity significantly. In Section 3.3.1 we will discuss the reactivity change if the core has an axial inhomogeneity, followed by discussion about radial inhomogeneities in Section 3.3.2.

3.3.1. Influence of axial particle distribution

To study the influence of an axial particle distribution on reactivity, a so called jet model is introduced. This model simulates a condition where the upper part of the particle bed is ejected from the core into the freeboard (cavity). In this model, 85% of the fuel particles in the lower part of the active core has a uniform distribution and the remaining 15% of the particles is distributed into 10 material zones with decreasing density (see Fig. 3.12). The fuel inventory is kept constant. The height of the particle bed in the jet model is 1.15 times of its initial homogeneous core.

The results of the jet model are shown in Fig. 3.13 for both 293 K and 993 K. The reactivity is plotted in the graphs as a function of the height of the corresponding homoge-

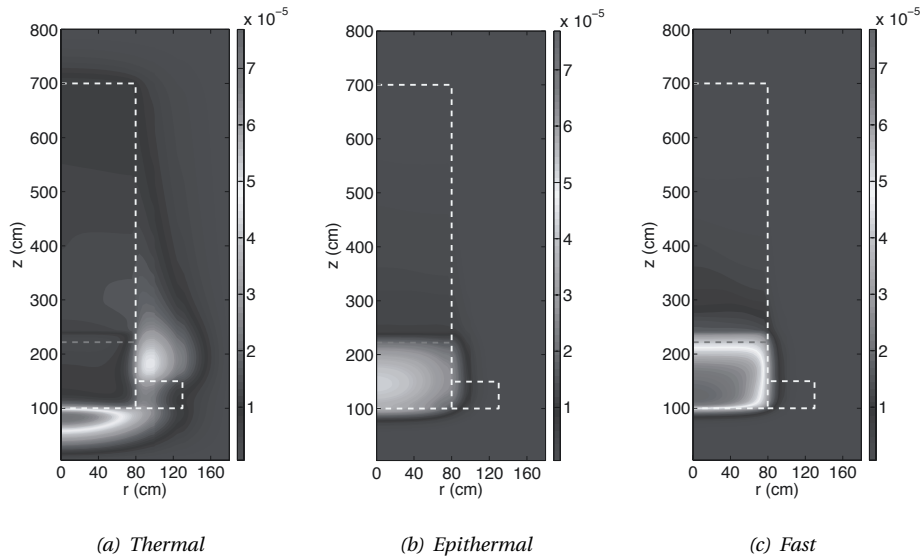


Figure 3.10. Thermal (left), epithermal (middle) and fast (right) neutron flux at packed bed conditions, normalized to 1 fission neutron per second.

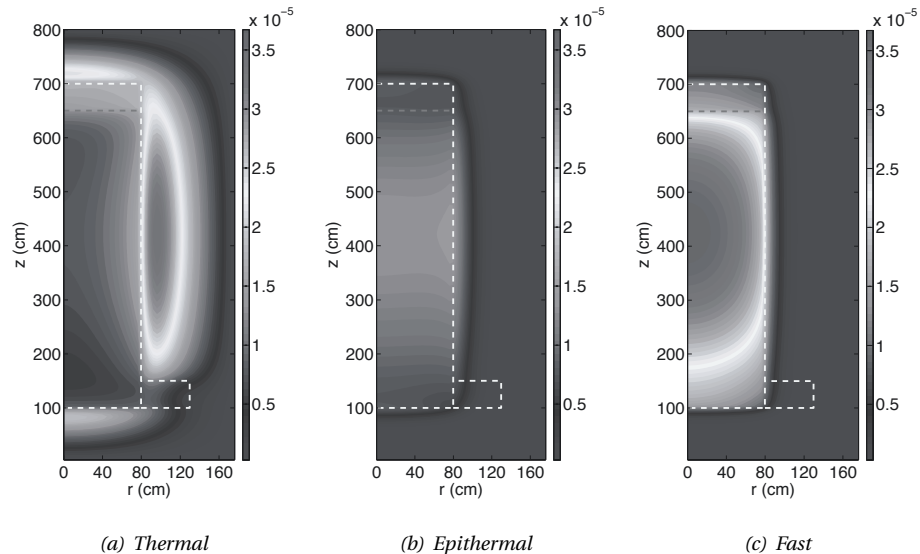


Figure 3.11. Thermal (left), epithermal (middle) and fast (right) neutron flux at expanded bed conditions, normalized to 1 fission neutron per second.

neous bed, instead of the bed height. This is more convenient for making comparison, as the bed in the jet model is always higher than in the homogeneous model.

The reactivity of the jet model is always smaller than that of the homogeneous model. This is in agreement with the fact that the importance function decreases with height (Van der Hagen *et al.*, 1997). Redistributing particles in the upper part of the active core indicates particle movement to a lower importance region, hence decreases the reactivity.

The reactivity change, ($\Delta\rho_{jet} = \rho_{jet} - \rho_{hom}$), spans from -56 pcm to -246 pcm for fuel temperature of 293 K, while for 993 K the range is between -98 pcm and -257 pcm. These results, however, do not give any clear trends on how $\Delta\rho_{jet}$ would behave as a function of bed height. For different bed heights, the importance function is not the same. Hence an *a priori* knowledge of reactivity change would be difficult as the bed expands.

3.3.2. Influence of radial particle distribution

Mudde *et al.* (1999) reported that radial void fraction profiles obtained from a tomographic reconstruction are not flat. The time-averaged voidage in the center is higher than the voidage close to the wall. This is reasonable as the large void tends to move upward in the central region, while particles that are thrown up return to the bed via the wall region. From neutronics point of view, particles that are close to the wall have a higher importance than those in the central region (Van der Hagen *et al.*, 1997). These facts suggest that radial particle distribution will affect the value of reactivity. In this section we investigate the extent of the reactivity change caused by radial particle distribution.

Two kinds of particle distributions were investigated, i.e. voidage is higher close to the wall than in the center region and voidage is higher in the center region than close to the wall. For these two distributions, the core is divided into five material zones of equal volume (see Fig. 3.14). For simplicity, we name these regions as region I (which is in the central region) to region V (which is close to the wall). The total number of fuel particles and the height of the particle bed are kept constant. In the case of increasing particle volume fraction to the wall, the particle volume fraction of each region is given as

$$\begin{aligned}\alpha_{p,I} &= 0.5\alpha_{p,hom}; \alpha_{p,II} = 0.75\alpha_{p,hom}; \alpha_{p,III} = \alpha_{p,hom}; \\ \alpha_{p,IV} &= 1.25\alpha_{p,hom}; \alpha_{p,V} = 1.5\alpha_{p,hom}\end{aligned}$$

where $\alpha_{p,hom}$ is the particle volume fraction of the related homogeneous bed at a specific bed height.

In the case of increasing volume fraction to the central region, the volume fraction of each region is

$$\begin{aligned}\alpha_{p,I} &= 1.5\alpha_{p,hom}; \alpha_{p,II} = 1.25\alpha_{p,hom}; \alpha_{p,III} = \alpha_{p,hom}; \\ \alpha_{p,IV} &= 0.75\alpha_{p,hom}; \alpha_{p,V} = 0.5\alpha_{p,hom}\end{aligned}$$

Simulations were performed for various heights of the particle bed, from 184 cm up to the maximum bed expansion of 600 cm. For each bed height, calculations were performed at 293 K and 993 K.

Figures 3.15(a) and 3.15(b) show the reactivity value of the bed with radially distributed particle and its corresponding homogeneous state at 293 K and 993 K, respectively.

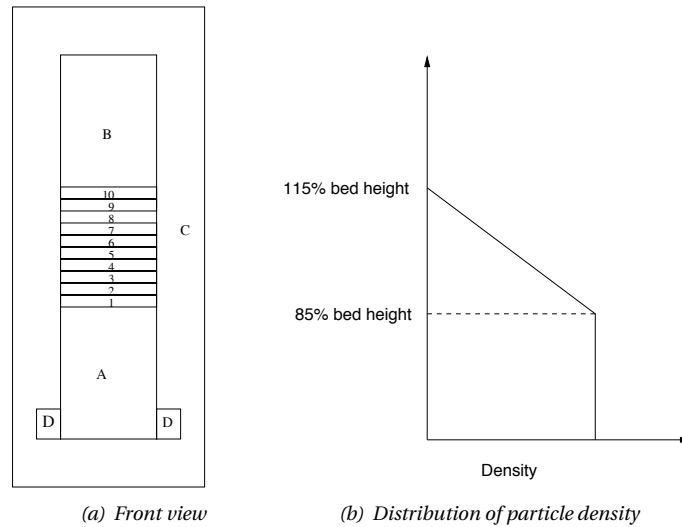


Figure 3.12. Front view of axially inhomogeneous core for KENO-V. a model (left). 85% of the core volume has the same initial particle density, while particles in the other 15% of the core volume are distributed linearly decreasing. For computational purposes, this linearly inhomogeneous part of the core is divided into ten material zones. A = homogeneous core; B = helium cavity; C = graphite reflector; D = boron side absorber; 1, 2, ..., 10 = layers of fuel (decreasing in density). The distribution of the particle density is shown in the right figure.

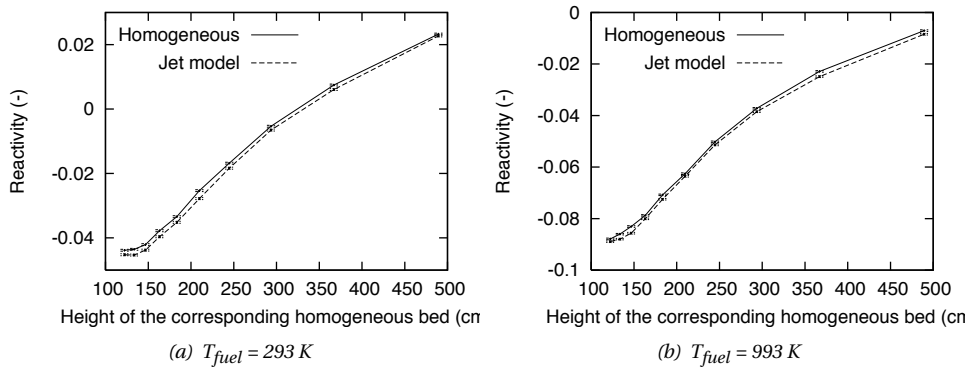


Figure 3.13. Reactivity of homogeneous and axially inhomogeneous core. The left figure shows the reactivity at a fuel temperature of 293 K and the right figure shows the reactivity at a fuel temperature of 993 K.

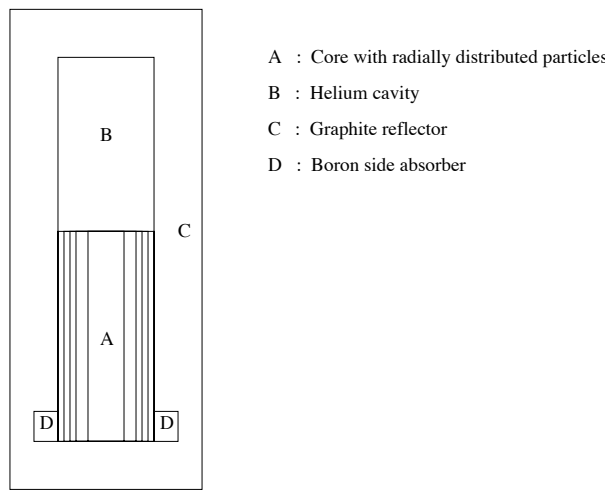


Figure 3.14. Front view of radially inhomogeneous core for KENO-V.a model. The core is divided into 5 material zones of equal volume. Fuel particles are linearly distributed with increasing number of particles either to the side reflector or to the center of the core.

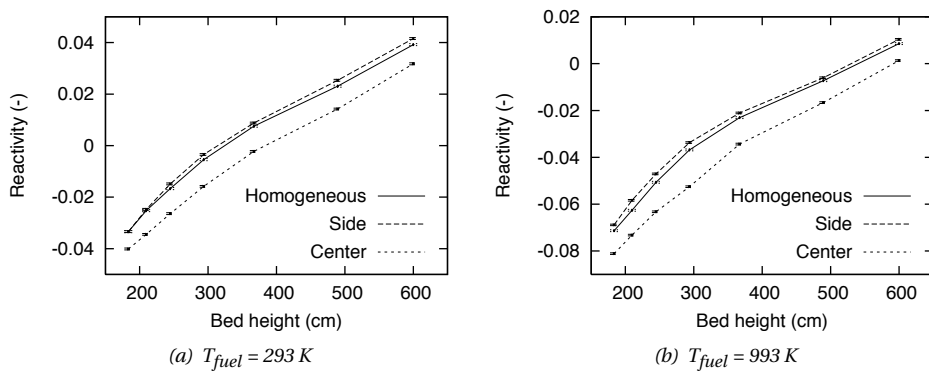


Figure 3.15. Reactivity of a homogeneous and radially inhomogeneous core. The left figure shows the reactivity at a fuel temperature of 293 K and the right figure shows the reactivity at a fuel temperature of 993 K.

When particles are concentrated close to the wall or periphery, the reactivity becomes higher (shown as a dashed line) than its corresponding homogeneous state (solid line). The fuel importance in the periphery is higher than in the central region, hence the particles are experiencing an increase in importance value when they move from the central part to the periphery. The effect is a positive reactivity change. The largest reactivity change for this model is 235 pcm at 293 K and 424 pcm at 993 K.

An opposite effect occurs when particles move from the periphery to the central region, as now particles move from a high importance region to a low importance region. The result is a negative reactivity change, as shown clearly in dotted lines in the graphs. The largest reactivity change for this model is -1000 pcm at 293 K and -1800 pcm at 993 K.

These results imply that movements of particles in radial direction would give a strong effect on reactivity.

3.4. Influence of bubbles on reactivity

It has been described in Chapter 2 that a gas-solid fluidized bed may experience different flow regimes and large bubbles/void regions may appear in the bed. The presence of void regions in the core may induce a change in reactivity, hence it is interesting to understand the extent of this change. For this purpose we set up static calculations using KENO-V.a. The objectives of such simulations are to answer whether (i) different fluidization regimes will exhibit different behavior in reactivity change and (ii) such reactivity changes are acceptable for operational of FLUBER.

For the simulations we will use the following assumptions: (i) the maximum reactivity is achieved when the bed is fully expanded, hence all calculations are performed at the fully expanded bed, (ii) the total mass is constant and particles are redistributed homogeneously when bubbles occur, and (iii) each calculation represents a snapshot of a specific state of the bed.

To simulate the occurrence of bubbles in the reactor, some void regions were implemented into the KENO-V.a model. These void regions are regarded as bubbles. Three types of bubble models were used, i.e. one large bubble, two intermediate size bubbles and many small size bubbles. Each type of bubble represents a different fluidization regime. In Section 3.4.1, the single-bubble model is discussed, followed by the two-bubble model in Section 3.4.2. Section 3.4.3 finalizes this section by introducing the many-bubble model.

3.4.1. Single-bubble model

The single-bubble model is intended to represent the condition of the axial slugging regime where large bubbles are present in the bed (see Fig. 2.1). A single rising bubble in a fluidized bed behaves like a bubbling liquid of low viscosity (Kunii and Levenspiel, 1991). For example, the shapes of bubbles are close to spherical when they are small and spherical cap-shaped when they are large.

The size of bubbles can be calculated from Eq. (2.6) as a function of height from the bottom of the bed and the superficial velocity. For the superficial velocity of 50 to 150 cm/s, the bubble sizes vary up to 170 cm around the top reflector. The bubble in our calculations

is modeled as a sphere with a diameter of 100 cm. This model is justified to represent a slug regime because the ratio of bubble diameter to bed diameter is larger than 0.6 (Fan and Zhu, 1998). The bubble is assumed to move upward and not to break up along its way to the bed surface.

In the KENO-V.a model, the center of the bubble coincides with the axis of the core. The axial position of the bubble center is varied for 11 different positions, with 50 cm increments. Figure 3.16 is an example of the arrangement of the bubble in the core.

Fig. 3.17 shows the reactivity of the one-bubble model. The x-axis represents axial positions of the bubble center from the bottom of the core. The reactivity value of a homogeneous core is shown for comparison. All calculations are performed at fuel temperature of 993 K. As each of the simulations represents a snapshot of an upward movement of the bubble, this graph can also be interpreted as the variation of reactivity over time.

When the position of the bubble is low enough (for example when the center of the bubble is 50 cm above the bottom reflector as shown in Fig. 3.16), fuel particles of low importance value which were previously occupying the space of the current bubble are distributed over the rest of the core. It means that the particles now become more important and introduce a large increase of reactivity. On the other hand, a large decrease of reactivity will occur whenever particles move from a more important region into a less important one. Previous calculations as discussed in Section 3.2 indicated the presence of a thermal neutron peak around a height of about 350 cm (see Fig. 3.11). A bubble present in this region will inevitably perturb the neutron distribution and at the same time more fuel particles are moved to the region next to the side absorber (a low important region) as well. Hence, the reactivity in this case will be largely decreased. When the bubble moves upward to this height, the reactivity obviously decreases.

The same situation also applies to the region close to the upper axial reflector where a thermal neutron peak occurs. This situation can be seen in Figure 3.17 when the bubble position reaches 550 cm.

It can be inferred that a slugging fluidization gives a high reactivity deviation from the homogeneous state within a magnitude of 278 pcm. A fluidized bed reactor operated in this regime then may experience large reactivity oscillations.

3.4.2. Two-bubble model

The two-bubble model is intended to represent the situation of the bubbling regime, where relatively large bubbles (though smaller than those in a slugging regime) occur in the bed.

Two spherical bubbles are modeled with a diameter of 50 cm. To represent various radial positions of the two bubbles, four types of this model are used, i.e. Type I – type IV, as shown in Fig. 3.18. For convenience we refer to the bubble that is always located adjacent to the wall/periphery as bubble #1 and the other bubble as bubble #2. The radial and angular positions of the bubble #2 are given in Table 3.2. The axial positions of the center of the bubbles are varied for four different heights, i.e. 25 cm (corresponding to the height of side absorber), 75 cm, 325 cm (corresponding to the height of thermal neutron peak in the radial reflector) and 575 cm (the bubbles coincide with the surface of the top reflector).

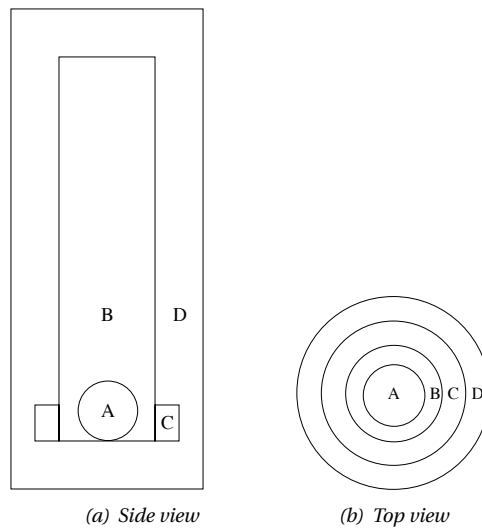


Figure 3.16. Side view (left) and top view (right) of the single-bubble model, showing the lowest position of the bubble as an example. “A” is the bubble, “B” is the homogeneous bed, “C” is the side absorber and “D” is the reflector.

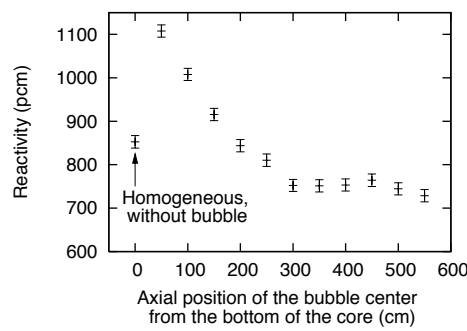


Figure 3.17. Reactivity as a function of axial position of bubble for the single-bubble model.

The results of static calculations for this model are given in Table 3.3–3.6, where the reactivity as a function of axial position of the bubbles is presented as well as its corresponding reactivity change from a homogenous core. The reactivity of the homogeneous core is 853 pcm which is calculated at fuel temperature of 993 K.

The following findings can be drawn from the tables:

- For all types, the largest positive reactivity change in each type is found when both bubbles are located at 25 cm from the core bottom. This result is quite predictable as the region at the core bottom has a low importance value due to the influence of the side absorber. When bubbles appear in this region, fuel particles are pushed from a low importance region to a high importance region, inducing a positive reactivity change. Type I gives the largest positive reactivity change (80 pcm) among other types as the particles that were in the center bottom core (having low importance both radially and axially) are distributed to another region of the core.
- For type I, the largest negative reactivity change is found when both bubbles are located at 325 cm, while for type II–IV at 575 cm.
- For type II–IV, bubbles at the same height and travelling upward together will give a decrease in reactivity change.
- For all types, in a fixed height of 325 cm for bubble #1, the largest negative reactivity change is achieved when bubble #2 is at 325 cm.

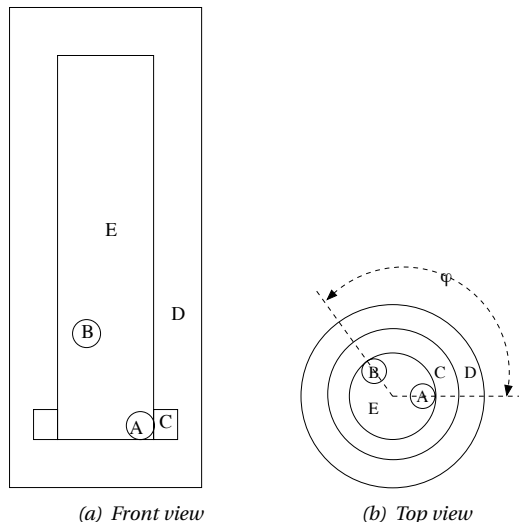
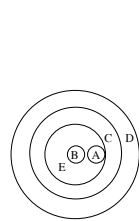


Figure 3.18. Front view (left) and top view (right) of the two-bubble model. “A” is the bubble #1, “B” is the bubble #2, “C” is the side absorber, “D” is the reflector and “E” is the homogeneous bed.

Table 3.2. The position of the bubble # 2 of Type I – Type IV model. The radial distance (r) is calculated from the center of the cylinder to the center of the respective bubble. The angular location (φ) is calculated as the difference in position between the center of bubble #1 and #2 as indicated in Fig. 3.18.

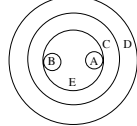
	Type I	Type II	Type III	Type IV
r (cm)	0	54	54	54
φ (°)	0	180	90	135

Table 3.3. Reactivity difference ($\Delta\rho$) of the type I two-bubble model relative to the homogeneous core.



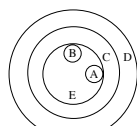
Axial position of bubble #2 (cm)	Axial position of bubble #1 (cm)			
	25	75	325	575
	$\Delta\rho$ (pcm)	$\Delta\rho$ (pcm)	$\Delta\rho$ (pcm)	$\Delta\rho$ (pcm)
25	80	36	32	56
75	20	15	-13	26
325	40	31	-63	36
575	21	-3	-24	37

Table 3.4. Reactivity difference ($\Delta\rho$) of the type II two-bubble model relative to the homogeneous core.



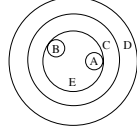
Axial position of bubble #2 (cm)	Axial position of bubble #1 (cm)			
	25	75	325	575
	$\Delta\rho$ (pcm)	$\Delta\rho$ (pcm)	$\Delta\rho$ (pcm)	$\Delta\rho$ (pcm)
25	51	36	12	-36
75	35	16	21	-19
325	47	7	-33	-16
575	-5	6	-84	-55

Table 3.5. Reactivity difference ($\Delta\rho$) of the type III two-bubble model relative to the homogeneous core.



Axial position of bubble #2 (cm)	Axial position of bubble #1 (cm)			
	25	75	325	575
	$\Delta\rho$ (pcm)	$\Delta\rho$ (pcm)	$\Delta\rho$ (pcm)	$\Delta\rho$ (pcm)
25	70	52	17	16
75	43	70	-13	-8
325	51	-19	-51	-46
575	23	52	-50	-96

Table 3.6. Reactivity difference ($\Delta\rho$) of the type IV two-bubble model relative to the homogeneous core.



Axial position of bubble #2 (cm)		Axial position of bubble #1 (cm)			
		25	75	325	575
		$\Delta\rho$ (pcm)	$\Delta\rho$ (pcm)	$\Delta\rho$ (pcm)	$\Delta\rho$ (pcm)
25	25	87	31	1	-7
	75	20	65	3	-26
	325	61	18	-27	-69
	575	31	10	-17	-71

3.4.3. Multi-bubble model

This model represents a condition of turbulent fluidization where the distribution of particles and bubbles tend to be homogeneous. In this model it is assumed that bubble formation occurs continuously at the bottom of the core or bed and that the bubbles propagate upward to the top of the bed. Once the bubbles move upward, new bubbles are created at the bottom of the bed. Hence there are two regions present in the bed, i.e. the bubble region and the homogeneous region above the bubble region. This situation occurs only until the upper part of the bubble region reaches the top of the bed. The bubbles break up once they reach the top of the bed.

Bubbles in this model are further assumed to be spherical with a diameter of 5 cm. This value is assumed to be small enough to represent small bubbles, but large enough to cause a significant reactivity change.

For the purpose of KENO-V.a modeling, bubbles are contained in layers. Each layer has 212 bubbles arranged in triangular arrays. Layers of bubbles are further stacked on top of each other in a staggered way, starting from the bottom of the core, giving a rhombohedral arrangement of bubbles. The bed height is kept constant, while the number of layers is increasing (see Figure 3.19). In this way an upward movement of bubbles can be simulated. The distance between two midplanes of the layers is 10 cm.

Figure 3.20 shows the result of a static simulation of the many-bubble model. The result of this simulation is slightly different from that of the one-bubble or two-bubble model. In this multi-bubble model, the ratio of void/bubble volume to the core increases as the number of layers increases, while in the one-bubble/two-bubble model, the ratio is constant. It can be inferred that as the number of layers increases, fuel particles become more packed, hence reducing the mean free path of neutrons at the upper part of the active core. However, when the number of layers increases even more, the situation of

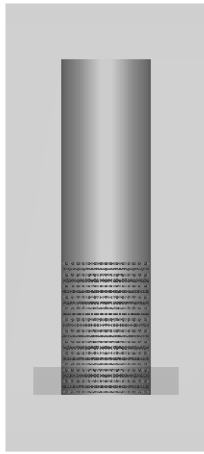


Figure 3.19. An example of bubble arrangements in the many-bubble model. This side-view shows twenty-four layers of bubbles extending from the bottom of the core. The bubbles are arranged in a staggered triangular array, creating a rhombohedral arrangement which is similar to Fig. 3.3.

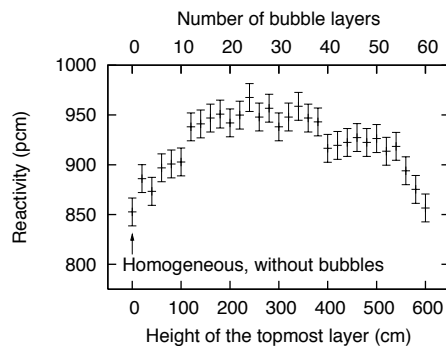


Figure 3.20. The reactivity as a function of number of bubble layers and its corresponding height of the topmost layer.

the active core becomes more homogeneous, and the effects of particle migration from a low-importance zone to a high-importance zone are compensated by the migration from a high-importance zone to a low-importance zone.

The reactivity deviation from the homogeneous bed in this model is smaller than the one-bubble model (about 150 pcm vs. 278 pcm). In operation, this model would be more likely for the operational range of FLUBER.

3.5. Summary

In this chapter an assessment of the design of FLUBER has been performed. Some modifications have been done to get the necessary shutdown margin and excess reactivity. These include enlarging the core cross-section, modifying the fuel kernel diameter, increasing the fuel inventory and adding boron absorber in the bottom part of the side absorber. By doing so, the desired shutdown margin and excess reactivity can be achieved. Static calculations (without feedback effects from fluidization or heat transfer process) further show that the maximum fuel temperature where FLUBER can still achieve criticality is about 1200 K.

Static calculations using a three-dimensional Monte Carlo code have been done as well to simulate particle redistribution in the core, either in axial or radial direction. Such simulations show that the reactivity change is strongly dependent on the particle position. It has been shown that radial redistribution of particles may give a large change in reactivity. The presence of bubbles in the bed has also been simulated for small, medium and large bubbles. The results show that large bubbles perturb the reactivity. During operational of the reactor, the occurrence of such large bubbles may induce a large reactivity oscillation, resulting in a large power oscillation. This oscillation can be prevented by doing some measures during the design or/and operational stage. In the design stage, the geometry of FLUBER should be adjusted that the influence of particle distribution to the reactivity becomes less dominant. In the operational stage, the occurrence of large bubbles should be minimized by e.g. controlling the flow rate.

CHAPTER 4

Space-independent dynamics of FLUBER*

4.1. Introduction

Reactor dynamics is concerned with the analysis of the time-dependent behavior of the reactor. The kinetics of the reactor can be described by a set of equations connecting variables such as neutron density or power and temperature, together with the parameters that may influence these quantities, such as coolant mass flow rate and neutron cross-sections. As most of the properties are temperature dependent, coupling to a heat transfer equation is obviously required to solve the kinetics of the reactor.

A zero-dimensional model can be regarded as a simple approach to understand the dynamics of the system. In relation to FLUBER, a zero-dimensional dynamics (or point dynamics) model comprising coupled neutronics, heat transfer and fluidization can be used to estimate the time-dependent behavior of the system. Since the real system is more complicated due to moving of particles and the occurrences of bubbles in the bed and the point dynamics model can not capture these phenomena accurately, the zero-dimensional method is supported by incorporating the results of three-dimensional static calculations as described in Chapter 3. The results are thus expected to be close to the real multi-dimensional model.

*This chapter is an adapted version of the following papers:

Agung, A., Lathouwers, D., van der Hagen, T.H.J.J., van Dam, H., Pain, C.C., Goddard, A.J.H., Eaton, M.D., Gomes, J.L.M.A., and Miles, B. (2006). On an Improved Design of a Fluidized Bed Nuclear Reactor. Part I: Design Modifications and Steady State Features. *Nuclear Technology*, **153**, 117.

Agung, A., Lathouwers, D., van der Hagen, T.H.J.J., van Dam, H., Pain, C. C., Goddard, A.J.H., Miles, B., Ziver, K.A., Eaton, M.D., and de Oliveira, C.R.E. (2007). On an Improved Design of a Fluidized Bed Nuclear Reactor. Part II: Linear Stability and Transient Analysis. submitted to *Nuclear Technology*.

The objectives of this study are to investigate whether: (i) the results of static calculations as described in Chapter 3 can be realized in operation, by considering the interaction between neutronics, fluidization and heat transfer, (ii) the system is stable and (iii) responses of the system to the operational transients are acceptable.

The results of investigations on steady and unsteady behavior of FLUBER as well as its stability are presented. The organization of this chapter is as follows. Section 4.2 gives a description of the related models, comprising neutronics, fluidization and heat transfer. These models are further implemented in an in-house code, DYNFLUB. It is used to study the behavior of the FLUBER design under steady conditions, which is discussed in Section 4.3. Section 4.4 discusses the linear stability by means of eigenvalue evaluations. It is shown in that the reactor is always stable against small perturbations, as indicated by negative real values of the eigenvalues. Section 4.5 elaborates operational transients in which case the mass flow rate and the helium inlet temperature are varied. In Section 4.6 a stochastic model is introduced to the reactivity feedback to account for redistribution of particles in the bed due to bubbles. The resulting behavior of FLUBER under the influence of random particle movements is described. Finally, a summary is given in Section 4.7.

4.2. Dynamics model description

A dynamic model was developed for describing the coupled hydrodynamics and kinetics of the fluidized bed reactor. The model is based on a zero-dimensional description of the system, neglecting essentially all spatial dependence. The heat transfer model uses separate equations for the conservation of thermal energy of each phase. The neutronics is described by the well-known point kinetics model. To improve the accuracy of the point kinetics model, the results obtained from 3D static calculations as described in Chapter 3 are applied. The coupling between heat transfer and neutronics is obtained through the reactivity feedback due to bed expansion/compression and temperature fluctuations.

4.2.1. Fluidization model

The fluidization flow is described by using the Richardson-Zaki correlation (Fan and Zhu, 1998) which relates the superficial velocity, $u_{g,s}$, to the average bed porosity, α_g ,

$$u_{g,s} = u_t \alpha_g^n \quad (4.1)$$

where u_t is the particle terminal velocity and n equals 2.4 for Reynolds numbers (based on the particle) over 500 which is valid for the whole operational regime of FLUBER.

The particle terminal velocity is reached when the gravity force and drag force become equal. The gravity force is proportional to the mass of fluid displaced by the particle. For a spherical particles it is given as

$$F_g = \frac{\pi d_p^3}{6} g (\rho_p - \rho_g) \quad (4.2)$$

while the drag force is given as

$$F_d = C_D \frac{\pi d_p^2}{4} \frac{\rho_g u^2}{2} \quad (4.3)$$

where d_p is the particle diameter, C_D is the drag coefficient, g is the gravity acceleration, ρ_g and ρ_p are the gas and particle density, respectively.

Hence by equating Eq. (4.2) and Eq. (4.3) the terminal velocity can be written as

$$u_t = \sqrt{\frac{4(\rho_p - \rho_g)gd_p}{3C_D\rho_g}} \quad (4.4)$$

The drag coefficient depends in fact on the Reynolds number (Cheremisinoff and Cheremisinoff, 1984),

$$C_D = \begin{cases} \frac{24}{Re} & \text{for } Re < 2 \\ \frac{18.5}{Re^{0.6}} & \text{for } 2 < Re < 500 \\ 0.44 & \text{for } Re > 500 \end{cases} \quad (4.5)$$

In the Richardson-Zaki relation the void fraction depends algebraically on the fluidization velocity and therefore reacts instantaneously to changes in the flow rate. This is clearly unrealistic because the bed expansion or compression is a convective phenomenon with an associated time scale. To improve the model the void fraction is assumed to relax towards the steady state value as given by the RZ relation with a time constant τ . Hence we assume

$$\frac{d\alpha_g}{dt} = \frac{1}{\tau}(\alpha_{g,\infty} - \alpha_g) \quad (4.6)$$

and the asymptotic value is given by the Richardson-Zaki correlation

$$\alpha_{g,\infty} = \left(\frac{u_{g,s}}{u_t} \right)^{1/n} \quad (4.7)$$

Specification of the time constant is based on the physical notion that disturbances in void fraction propagate at approximately the gas velocity through the dense bed. Thus the time constant is proportional to the bed height, H , and inversely proportional to the average gas velocity

$$\tau = \frac{H(\alpha_g)}{u_g} = \frac{\alpha_g H(\alpha_g)}{u_{g,s}} \quad (4.8)$$

4.2.2. Heat transfer model

Fission heat that is generated in the particles is transferred to the gas phase and convected upwards to the exit of the fluidized bed. Above the plane separating the dense bed and the freeboard (the gas cavity), the gas will no longer heat up, and is simply convected without further thermal consequences. Hence we do not consider the fluidized bed as a whole as the system of interest, but restrict the investigation to the solids and gas present in the region termed as dense.

The energy equation for the fuel particles is

$$m_p C_{p,p} \frac{dT_p}{dt} = P_t + Q \quad (4.9)$$

where m_p is the mass of the particles, $C_{p,p}$ is the specific heat capacity of the particles, T_p is the temperature of the particles, P_t is the total power and Q is the interfacial heat transfer.

The fundamental energy equation in terms of enthalpy for a gas written in conservative form is

$$\frac{dm_g h_g}{dt} = G_{in} h_{in} - G_{out} h_{out} - Q \quad (4.10)$$

where m_g is the mass of the gas, G_{in} and G_{out} are the inlet and outlet mass flow rate of the helium, h_{in} and h_{out} are the helium enthalpy at the inlet and outlet, respectively. Here we have neglected viscous dissipation and pressure changes due to low Mach number in the system (see further below). Using the system mass balance for the gas phase

$$\frac{dm_g}{dt} = G_{in} - G_{out} \quad (4.11)$$

we can write the enthalpy equation in nonconservative form as

$$m_g \frac{dh_g}{dt} = G_{in} (h_{in} - h_{out}) - \frac{dm_g}{dt} (h_{out} - h_g) - Q \quad (4.12)$$

The gas is assumed to be ideal and the specific heat capacity at constant pressure to be constant. The energy equation can then be rewritten in terms of the gas temperature

$$m_g C_{p,g} \frac{dT_g}{dt} = G_{in} C_{p,g} (T_{in} - T_{out}) - \frac{dm_g}{dt} (T_{out} - T_g) - Q \quad (4.13)$$

where T_{in} and T_{out} are the inlet and outlet temperature of the helium.

The mass of helium in the core equals

$$m_g = A_b \rho_g (\alpha_{g,0} - 1) H_0 \frac{\alpha_g}{\alpha_g - 1} \quad (4.14)$$

where A_b is the bed cross-section area, H_0 and $\alpha_{g,0}$ are the height and void fraction of the packed bed, and the following identity is used

$$H(1 - \alpha_g) = H_0(1 - \alpha_{g,0}) \quad (4.15)$$

There are two possibilities on how to relate T_{in} , T_{out} and T_g in Eq. (4.13). One possibility is to assume a linear relation between T_{in} and T_{out} and thus T_g will be an arithmetic average of those parameters. However this assumption is unrealistic for the upper part (outlet) of the reactor, since the outlet temperature would be higher than the fuel temperature. Another possibility, which is used in our calculations, is to set T_g equal to T_{out} (well-mixed approximation) and in this case the second term of the RHS of Eq. (4.13) vanishes.

The interfacial heat transfer, Q , is based on the Nusselt relation for a single particle:

$$Q = \frac{\lambda_g \text{Nu}(\text{Re}_p, \text{Pr}_g)}{d_p} A_i (T_g - T_p) \quad (4.16)$$

The total interfacial area, A_i , equals the interfacial area per unit volume, $a_i = 6(1 - \alpha_g)/d_p$, times the volume of the dense region, $A_b H(t)$. The total exchange area then becomes

$$A_i = \frac{6(1 - \alpha_g)}{d_p} A_b H = \frac{6(1 - \alpha_{g,0})}{d_p} A_b H_0 \quad (4.17)$$

For forced convective heat transfer over a sphere in a uniform flow, the Ranz correlation (Fan and Zhu, 1998) is used

$$\text{Nu} = 2 + 0.66 \text{Re}_p^{1/2} \text{Pr}_g^{1/2} \quad (4.18)$$

where the Reynolds number of the particles is $\text{Re}_p = G_{in} d_p / \alpha_g A_b \mu$ (steady state relation) with μ is the viscosity of the gas and the Prandtl number of the fluidization gas is essentially a constant (taken as 0.71).

4.2.3. Neutronics model

Neglecting the spatial dependence of the system, we use the point kinetics equation to describe the kinetic behavior of the reactor. The point kinetics constitutes a highly simplified but useful model to analyze the kinetics of neutron multiplying systems.

The basic point kinetics model

The basic equation for the point kinetics model (Duderstadt and Hamilton, 1976) is

$$\frac{dP_{pr}}{dt} = \frac{[\rho - \beta]}{\Lambda} P_{pr} + \sum_{i=1}^{N_{pc}} \lambda_i C_i + \frac{S}{\Lambda} \quad (4.19)$$

and the precursors satisfy

$$\frac{dC_i}{dt} = \frac{\beta_i}{\Lambda} P_{pr} - \lambda_i C_i, \quad i = 1 \dots N_{pc} \quad (4.20)$$

where P_{pr} is the prompt power, C_i is the i th precursor (in terms of power units), ρ is the time dependent reactivity, β_i is the i th delayed neutron fraction, and $\beta = \sum_{i=1}^{N_{pc}} \beta_i$ is the total delayed neutron fraction. In addition, Λ is the neutron generation time, λ_i is the decay constant of the i th group delayed neutron precursors and S is the neutron source (also in terms of power). In the present work 6 precursor groups are employed (Hetrick, 1993).

The decay heat model

In the present model, we include the decay power. The delayed heat release of a particular isotope as a function of time resulting from one fission reads

$$f(t) = \sum_{n=1}^{N_d} \gamma_n e^{-\lambda_n t} \quad (4.21)$$

where γ_n and λ_n is the decay heat yield and the decay constant for fission product of group n .

The prompt fission power, P_{pr} , is

$$P_{pr}(t) = Q_f \Psi(t) \quad (4.22)$$

where Q_f is the prompt recoverable energy release per fission of the isotope of interest, and $\Psi(t)$ is the fission rate.

The delayed heat release from an arbitrary fission rate is then expressed in terms of a convolution integral

$$P_d(t) = f(t) * \Psi(t) = \sum_{n=1}^{N_d} \gamma_n \int_0^t e^{-\lambda_n(t-\tau)} \Psi(\tau) d\tau \quad (4.23)$$

Focusing on one delay group (dropping index n) and differentiating with regards to time gives,

$$\frac{dP_d(t)}{dt} = -\lambda P_d + \gamma \Psi(t) = -\lambda P_d + \frac{\gamma}{Q_f} P_p(t) \quad (4.24)$$

Reverting back to the general case of N_d delayed groups, Eq. (4.24) can be written as

$$\frac{dP_{d,n}}{dt} = \frac{\gamma_n}{Q_f} P_p - \lambda_n P_{d,n}, \quad n = 1 \dots N_d \quad (4.25)$$

In the present work a condensed set of 15 decay heat groups is employed from the original data given in (DIN-25485, 1990). Fourteen groups of the original data are intact while groups numbering 15 to 23 are condensed by using the following relation

$$\gamma_{N_d} = \sum_{n=15}^{23} \gamma_n \quad (4.26)$$

$$\lambda_{N_d} = \left(\frac{1}{\gamma_{N_d}} \sum_{n=15}^{23} \frac{\gamma_n}{\lambda_n} \right)^{-1} \quad (4.27)$$

The total power is the sum of prompt and all decay power component,

$$P_t = P_{pr} + \sum_{n=1}^{N_d} P_{d,n} \quad (4.28)$$

The reactivity feedback model

There are two components of reactivity feedback modeled in the fluidized bed fission reactor: (a) feedback due to variation of the void fraction (or height), ρ_{ref} , and (b) feedback from temperature effects, ρ_T :

$$\rho(\alpha_g, T_p) = \rho_{ref}(\alpha_g) + \rho_T(\alpha_g, T_p) \quad (4.29)$$

To obtain the reference value of $\rho_{ref}(\alpha_g)$, three-dimensional static calculations were performed (as discussed in Chapter 3) at a reference temperature of 993 K for various bed expansions and subsequently fitted by a third order polynomial,

$$\rho_{ref}(\alpha_g) = \sum_{i=0}^3 a_i \alpha_g^i \quad (4.30)$$

In these static calculations, the reflector temperature was assumed as an arithmetic mean between the temperature of the core and that of room temperature. The resulting reactivity curve is shown in Fig. 4.1(a).

The second term of the RHS of Eq. (4.29) is a way to account for the feedback arising from departure of the temperature from the reference value. Two situations are distinguished: (a) steady state operation and (b) transients. In the steady state the reactor has reached its equilibrium temperature and the reflector temperature is again assumed to be an arithmetic mean of the core and room temperature. A special term is used for this kind of reactivity feedback, i.e. *steady state temperature reactivity feedback* and the temperature coefficient in the steady state condition using the total temperature coefficient, $\alpha_{d,t}$. The formulation of the steady state temperature feedback then reads

$$\rho_{T,ss} = \alpha_{d,t}(\alpha_g)(T_p - T_{ref}) \quad (4.31)$$

During a transient, the core temperature might change to a new value of T_p . However, due to its high thermal inertia, the reflector is assumed to stay at its initial temperature corresponding to the fuel temperature of T_i , at the start of the transient. The temperature coefficient related to this transient behavior is called the core temperature coefficient, $\alpha_{d,c}$, which in principle is a measure of reactivity deviation from the steady state and its corresponding reactivity feedback is called *transient temperature reactivity feedback*. This feedback is formulated as

$$\rho_{T,tr} = \alpha_{d,t}(\alpha_g)(T_i - T_{ref}) + \alpha_{d,c}(\alpha_g)(T_p - T_i) \quad (4.32)$$

Figure 4.1(b) shows the curves of both $\alpha_{d,t}$ and $\alpha_{d,c}$. The reactivity decreases as the fuel temperature increases, thus giving a negative temperature coefficient. The contribution due to the reflector temperature is positive because of the decrease in absorption rate of the reflector and the increase in the number of reflected neutrons as the reflector temperature increases. However, the total temperature coefficient is negative.

4.2.4. Thermophysical properties of gas and particles

The specific heat capacity of the helium is almost independent of pressure and temperature (Lemmon *et al.*, 2003) and its value is 5193 J/kg K, which is the value at standard

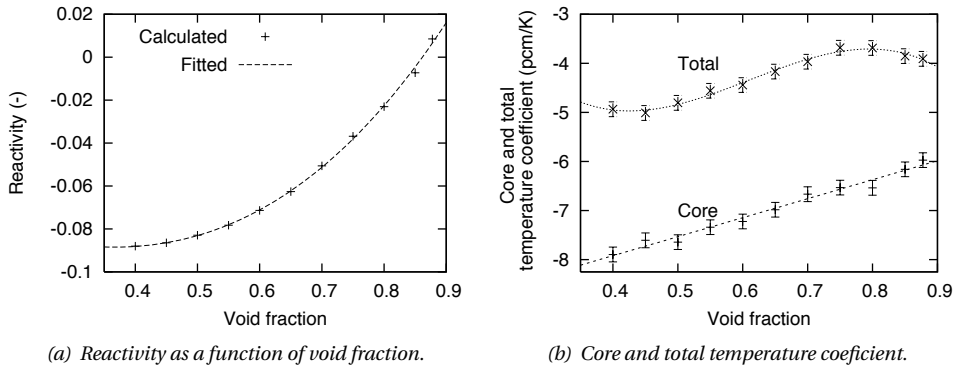


Figure 4.1. (a) Reactivity as a function of void fraction at fuel temperature of 993 K (cross) and the fitted reference reactivity curve (dash line) to be used in the dynamic model. (b) The core and total temperature coefficient as a function of void fraction and their fitted lines. The total temperature coefficient represents the temperature coefficient whereby the temperature of the reflector is given as an arithmetic average between the core temperature and room temperature (to be used for steady state calculations). The core temperature coefficient represents the temperature coefficient whereby the temperature of the reflector is corresponding to the initial value at the incipient of transient.

conditions. The deviations from this value are within 0.75% in the range (300 K $< T_g <$ 1500 K; 1 bar $< p_g <$ 60 bar) and are considered negligible.

The viscosity and the thermal conductivity of helium are given as (Yan, 1990)

$$\mu_g = 3.5953 \cdot 10^{-7} T_g^{0.687} \quad (4.33)$$

$$\lambda_g = 2.774 \cdot 10^{-3} T_g^{0.701} \quad (4.34)$$

within the range of 273 K $\leq T_g \leq$ 1500 K and 1 bar $\leq p_g \leq$ 100 bar.

Data and correlations on the heat capacity of UO₂ are available, for example as reported by Fink *et al.* (1981), Matzke *et al.* (1997) and Ronchi *et al.* (1999). Recommendations are also provided by IAEA (1997c), in which the correlations for material properties are based from MATPRO equations (SCDAP/RELAP5, 1997). However, a review given by Carabao *et al.* (2001) concludes that correlations given recently by Fink (2000) provide the best fit to all the available experimental data for low and high temperature. For our model, the recent Fink correlation will be used.

The specific heat capacity of UO₂ for 298.15 K $\leq T \leq$ 3120 K is written as:

$$C_{p,UO_2} = \frac{1}{M_{UO_2}} (52.1743 + 87.951\theta - 84.2411\theta^2 + 31.542\theta^3 - 2.6334\theta^4 - 0.71381\theta^{-2}) \quad (4.35)$$

where $\theta = T/1000$, T is the temperature and M_{UO_2} is the molecular mass of UO₂.

The specific heat capacity of graphite is given as (Dinsdale, 1991):

$$C_{p,C} = 2.023145 + 7.8645 \cdot 10^{-5} T - 4.26709 \cdot 10^5 T^{-2} + 1.3203 \cdot 10^8 T^{-3} - 1.199 \cdot 10^{10} T^{-4} \quad (4.36)$$

In this model, the buffer and carbonous layers in the fuel particle are lumped into one layer and the presence of Si and other impurities is neglected (only for thermal modeling, not neutronics). The heat capacity of the particle satisfies

$$m_p C_{p,p} = m_{UO_2} C_{p,UO_2} + m_C C_{p,C} \quad (4.37)$$

The ideal gas law is used as the equation of state in the point dynamics model,

$$p_g = \frac{R_u}{W_{He}} \rho_g T_g \quad (4.38)$$

where p_g is the gas pressure, R_u is the universal gas constant and W_{He} is the molecular weight of helium.

Comparing the ideal gas law with NIST data for helium (Lemmon *et al.*, 2003), the difference between the ideal gas law and the NIST data amounts to approximately 2.9% at 300 K and even less at higher temperature (to below 1% above 800 K) at 60 bar. This error is acceptable for our purpose and thus the ideal gas law is used throughout.

Note that p_g is approximated as constant at 60 bar. This assumption is valid, as the perturbations of the mean pressure in the system are expected to be of the order of $\rho_{mix}gh$, amounting to perturbations much less than 1% in magnitude. Further this assumption is justified by the fact that the helium velocity (< 10 m/s) is much lower than the velocity of sound (Lemmon *et al.*, 2003).

4.2.5. Computational methodology

The model as described in Eqs. (4.6), (4.9), (4.13), (4.19), (4.20) and (4.25) consists of a system of $4 + N_{pc} + N_d$ ODE's for α_g , T_g , T_p , P_f , $C_1, \dots, C_{N_{pc}}$, and $P_{d,1}, \dots, P_{d,N_d}$. Due to large range in the related timescale (especially for the delayed neutron precursors and decay heat groups), the system is stiff from computational point of view. In our calculation, this stiff system is solved by the VODE package (Brown *et al.*, 1989). This ODE solver is based on the backward difference technique and has proven reliable in many problems. The initial conditions for the system are obtained from the steady solutions by long-term time integration succeeded by a Newton-method.

4.3. Steady state behavior of the reactor

Figure 4.2(a) shows the steady state conditions for the fuel temperature and the total power based on a helium inlet temperature of 543 K. The reactor starts to produce power at a flow rate of about 19 kg/s (corresponding to a superficial gas velocity of 1.79 m/s) while at 21 kg/s (corresponding to 1.97 m/s) the power reaches the order of megawatt and rises towards its maximum at about 37 kg/s (corresponding to 3.48 m/s). Around 37 kg/s, the porosity of the bed reaches its maximum value (when the height of the bed equals the height of the cylinder) and beyond that the model becomes invalid.

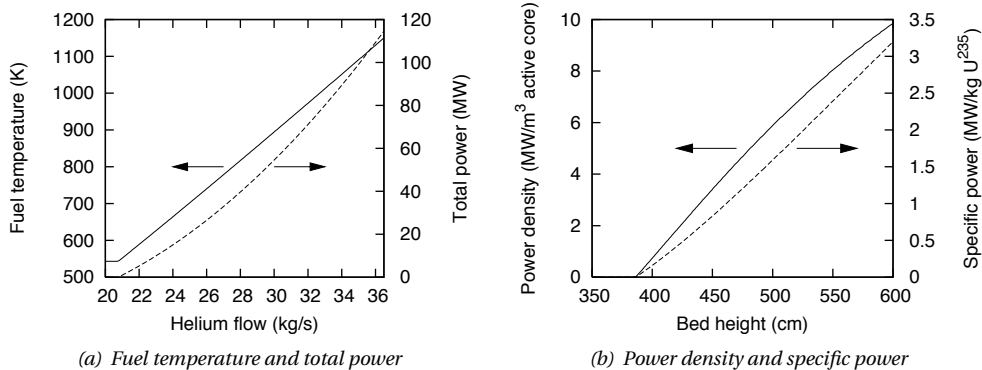


Figure 4.2. Fuel temperature and total power as a function of the coolant mass flow rate in steady state conditions (left). Power density and specific power as a function of core expansion (right).

The maximum total power obtained from this new design is 120 MW which is much higher than could previously be achieved (previously 16 MW (Kloosterman *et al.*, 2001) and 40 MW (Lathouwers *et al.*, 2003)). Further, unlike the previous designs, the new design has an increasing power level for the whole range of operation. These results are consequences of the larger maximum reactivity that can be achieved and the slope of the reactivity curve (see Fig. 3.9).

Although the maximum achievable power is higher, the maximum fuel temperature is 1163 K, which is still below the maximum permissible value of TRISO particle (IAEA, 2001). Hence, a safe steady state operation is ensured in this case. The temperature of the coolant (not shown) is only about 5 K lower than that of the fuel particle thanks to the excellent heat transfer.

The figure also indicates the method of changing the power level of the reactor. By adjusting the flow rate of helium in the core, the intended power level can be achieved without active control mechanisms (control rods). Further, no fission power is generated by the reactor when the helium flow ceases either on purpose or by accident, only the decay heat is of concern.

The nature of fluidization also implies that the power density and specific power varies with the bed expansion. Figure 4.2(b) shows that at maximum bed expansion, the power density equals about 10 MW/m³, which is about 10 times smaller than in a conventional PWR or BWR of 3600 MWt with an average enrichment of 4% (Stacey, 2001). Having a small power density, FLUBER may survive an initial high fuel temperature if the coolant ceases while the reactor shuts itself down, implying an inherent safety.

The maximum specific power of FLUBER is larger than that of conventional PWRs and BWRs. Given in kW/kg of uranium, FLUBER reaches a value about 14 times larger, while given in kW/kg of U²³⁵, FLUBER reaches a value about 3.5 times larger (Duderstadt and Hamilton, 1976). This result demonstrates a prospect of economic competitiveness of FLUBER against conventional reactors.

4.4. Linear stability analysis

4.4.1. Eigenvalue evaluation

The dynamics of FLUBER is characterized by a strong interaction between the bed height, which is determined by coolant mass flow rate, and the core neutronics. This is quite different from conventional fixed solid fuel reactors. In this section we will study the stability of the reactor by means of linear stability analysis. This analysis is valid only for small deviations from equilibrium operational states. Large perturbations to the system will be discussed in Section 4.5.

The system of ODE's describing the coupled fluidization-neutronics model as given in Section 4.2 can be written as

$$\frac{d\mathbf{x}}{dt} = f(\mathbf{x}, \mathbf{g}) \quad (4.39)$$

with the vector \mathbf{x} containing the state variables of the system, i.e. the temperatures, the prompt and delayed power components and the precursor concentrations, and where \mathbf{g} represents the vector containing the independent input variables of the system, i.e. the He mass flow rate, feed temperature and external reactivity. The steady state of the system, denoted as \mathbf{x}_0 (of size n), corresponding to a particular input signal \mathbf{g}_0 (of size m) is calculated from

$$f(\mathbf{x}_0, \mathbf{g}_0) = 0 \quad (4.40)$$

Linearization of the system around the steady state gives

$$\frac{d\delta\mathbf{x}}{dt} = J_x \delta\mathbf{x} + J_g \delta\mathbf{g} \quad (4.41)$$

where the Jacobian matrices, J_x and J_g are given by the following expressions

$$\begin{aligned} J_x &= \frac{\partial f(\mathbf{x}_0, \mathbf{g}_0)}{\partial x} \\ J_g &= \frac{\partial f(\mathbf{x}_0, \mathbf{g}_0)}{\partial g} \end{aligned} \quad (4.42)$$

Performing Laplace transformation we obtain

$$(s\mathbf{I} - J_x)\mathbf{X}(s) = J_g \mathbf{G}(s) \quad (4.43)$$

where $\mathbf{X}(s)$ and $\mathbf{G}(s)$ are the Laplace transformation of $\delta\mathbf{x}$ and $\delta\mathbf{g}$, respectively. The transfer functions of the system, $H_{ij}(s)$, thus can be written as

$$\mathbf{X}_i(s) = \sum_j H_{ij}(s) G_j(s) \quad (4.44)$$

From Eq. (4.43) and (4.44) it is shown that the poles of the transfer functions, and hence the stability of the system, are given by the eigenvalues of the matrix J_x .

The eigenvalues of the Jacobian are, in general, complex numbers. The complex part of the eigenvalue contributes an oscillatory component to the solution. The real part of the eigenvalue is the most important for stability. The system is stable if *all* eigenvalues of

\mathbf{J}_x have negative real parts. In addition, the ratio of real part to the imaginary part is also important as it determines the damping of the impulse response. The ratio between two consecutive maxima of the impulse response is called the *decay ratio* and can be formulated as

$$DR = \exp\left(2\pi \frac{\text{Re}}{|\text{Im}|}\right) \quad (4.45)$$

Having a strongly negative ratio of Re and Im is then very desirable as the oscillation on the exponentially decaying trend is strongly damped.

This method of finding eigenvalue of \mathbf{J}_x is equivalent to finding the poles of the transfer functions through a block diagram connecting the respective components of the system. The present method is preferred as the system is too complicated for an analysis using the block diagram method.

To obtain the eigenvalues numerically, the elements of Jacobian matrix are first calculated by perturbing the solutions of the steady state. In our calculations, the perturbation is taken as 10^{-6} times the steady state solutions. Solutions to the perturbed values are calculated and the differences between the new solutions and the steady state solutions divided by the magnitude of the perturbation form the elements of the Jacobian matrix. The eigenvalues are then computed using the DGEEVX routine from the LAPACK package (Anderson *et al.*, 2000).

For simplicity we consider the system with one precursor group and one decay heat group. The composite decay constants for the delayed neutrons are obtained by using the following weighting scheme,

$$\bar{\lambda} = \left(\frac{1}{\beta} \sum_{i=1}^{N_{pc}} \frac{\beta_i}{\lambda_i} \right)^{-1} \quad (4.46)$$

where the number $1/\bar{\lambda}$ is called *abundance-weighted mean decay time* (Hetrick, 1993). A similar weighting procedure (see Eq. (4.27)) is also applied for the decay heat constants, but all decay groups are now condensed into one. Hence the system now consists of 6 ODE's and consequently 6 eigenvalues. Although we use a condensed set of precursors and decay heat groups, the method is by no means restricted to a single precursor/decay group. Because the reactor power is to be controlled by varying the mass flow rate of helium through the core, the linear stability is studied in terms of coolant mass flow rate variations.

The eigenvalues are plotted in Fig. 4.3(a) for the range of mass flow rate of 19 – 37 kg/s. This range is chosen because the minimum flow rate at the incipient of fluidization is about 19 kg/s while at about 37 kg/s the bed is fluidized up to the maximum expansion. These loci differ several orders of magnitude due to a large variation of the parameter values in the model. Each eigenvalue starts from a certain value and as the coolant mass flow rate increases, the loci move. This is in accordance to the root-locus theory (Hetrick, 1993) that the loci coincide with the poles of the open-loop transfer function when the gain is very small and approach the zeros of the open loop transfer function when the gain is very large.

Three out of six eigenvalues (λ_1 , λ_2 and λ_4) are always real and the other 3 (λ_3 , λ_5 and λ_6) form complex conjugate pairs for a range of flow rates. The most critical eigenvalue is λ_6 because its real value is closest to the origin. However, as the mass flow rate

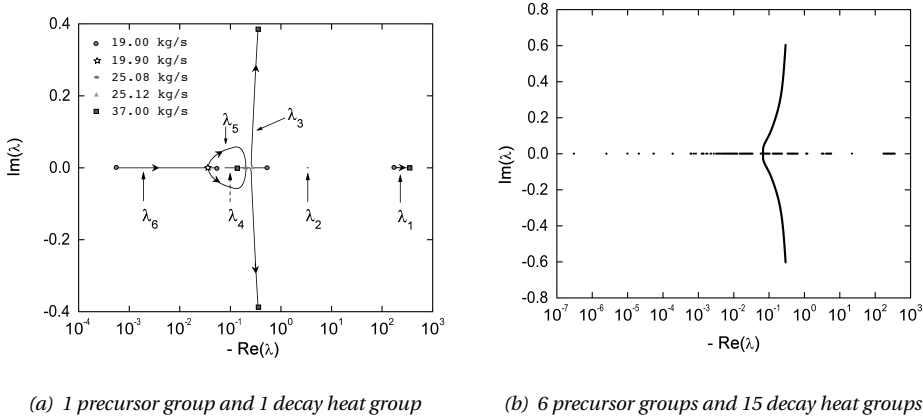


Figure 4.3. Root-locus plot of the roots of the characteristic polynomial as a function of the coolant mass flow rate.

increases λ_6 becomes more negative. When the mass flow rate is about 19.9 kg/s, λ_5 and λ_6 coincide and start to form a complex-conjugate pair. This complex pair later breaks up when the mass flow rate is 25.08 kg/s. λ_5 continues to be real while λ_6 coincides again with λ_3 at 25.12 kg/s of mass flow rate and they form a complex-conjugate pair beyond 25.12 kg/s of mass flow rate. It implies that the system has a non-oscillatory response when the flow rate is less than 19.9 kg/s and within the narrow range of 25.08 – 25.12 kg/s, while between 19.9 kg/s and 25.08 kg/s and beyond 25.12 kg/s the system exhibits an exponentially decreasing sinusoidal behavior against small disturbances. As can be verified from the figure, all eigenvalues have negative real parts, hence the reactor exhibits linear stability. By observing the ratio of $|\text{Re}/\text{Im}|$, we notice that the decay ratio is small, implying strongly damped responses.

As mentioned earlier, the method of finding eigenvalues is not restricted to a single group of precursor and decay heat. The eigenvalues of the system with 6 precursor groups and 15 decay heat groups are shown in Fig. 4.3(b). It is shown that the use of full set of precursor groups and decay heat groups does not change the stability behavior significantly. All loci still have negative real values. The differences between the two figures, however, can be found due to the use of different time constants which are widely spread.

4.4.2. Frequency response

From the relation between input and output (Eq. (4.44)), it is possible to determine the response of the linearized system against any input. In this section, a frequency response which characterizes the system against sinusoidal input is discussed. The behavior of the transfer function describing the system is evaluated at frequency $s = j\omega$. The gain, $G_{ij}(\omega)$,

and phase, $\theta(\omega)$, of the transfer function are defined as

$$G_{ij}(\omega) \equiv |H_{ij}(j\omega)| \quad (4.47)$$

$$\theta(\omega) \equiv \tan^{-1} \frac{\text{Im}(H_{ij})}{\text{Re}(H_{ij})} \quad (4.48)$$

In our calculation the frequency is varied from 0.001 rad/s to 100 rad/s for various steady coolant flow rates of 25, 28, 30, 33 and 36 kg/s (corresponding to an equilibrium reactor power of 21, 40, 55, 80 and 109 MW). Figures 4.4(a) and 4.4(b) show the gain and phase of the total power, respectively. For low frequency (< 0.01 rad/s) the magnitude of the transfer function should be in agreement with the results of steady state calculations, i.e. the slope of the power change. However, this is not the case in our calculations. For example for a mass flow rate of 33 kg/s, the asymptotic power change is about 10 MW/(kg/s) (see Fig. 4.2(a)), while in the frequency response we obtain 8 MW/(kg/s). These differences are caused by the use of different formulation in the model for the temperature feedback to the reactivity. For the purpose of steady state calculations, a steady state temperature reactivity feedback, i.e. Eq. (4.31), is applied. A formulation of this reactivity feedback is based upon an assumption that the reactor has reached its equilibrium temperature and the reflector temperature is assumed to be an arithmetic mean of the core and room temperature. A different formulation is used for the frequency response, i.e. transient temperature reactivity feedback (viz. Eq. (4.32)). The basis for this reactivity feedback is that during a sinusoidal transient, the core temperature might change from an initial temperature of T_i to a new value of T_p , but, due to its high thermal inertia, the reflector is assumed to stay at its initial temperature corresponding to the initial core temperature of T_i . If the steady state temperature reactivity feedback is used for the frequency response, the asymptotic power change for the frequency response will correspond to the power change given in the steady state calculations. This is in fact one limitation of the current code that no mechanism is available to adjust the proper reactivity feedback formulation as a function of frequency. However, such problem arises only for low frequencies.

The gain of this system is quite similar to those of a second order system. Here the gains increase and reaches their maximum (resonance peaks) at natural frequencies, ω_0 , ranging from 0.3 to 0.5 rad/s. The magnitudes of the resonance peaks differ and span from 28 to 94 MW kg⁻¹ s depending on the flow rate. Beyond the natural frequency the magnitude decreases and for coolant mass flow rate variations at higher frequency (> 10 rad/s), the reactor power variations are much smaller. The oscillation in the input flow rate affects the bed height and eventually the reactivity through the void fraction (or bed height) feedback, $\rho_{ref}(\alpha_g)$. At a finite range of frequency of the oscillation, a prompt reactivity feedback occurs, leading to a large power increase. Another interpretation of this gain plot is that to increase the power level of FLUBER by changing the flow rate of the fluidizing gas, one has to do it very slowly.

These plots are also an indication that within the range of 25 kg/s to 36 kg/s a pair of complex conjugate poles present in the left half of the complex plane. Further the phase plot also indicates that the system being investigated is minimum phase, where no zeros and poles can be found in the right half of the complex plane. Hence, the system is asymptotically stable by definition.

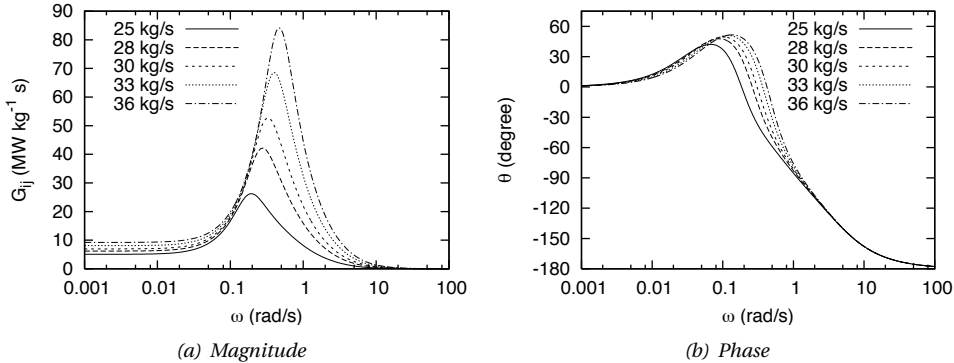


Figure 4.4. Magnitude (left) and phase (right) of the transfer function from coolant mass flow rate variations to reactor power fluctuations.

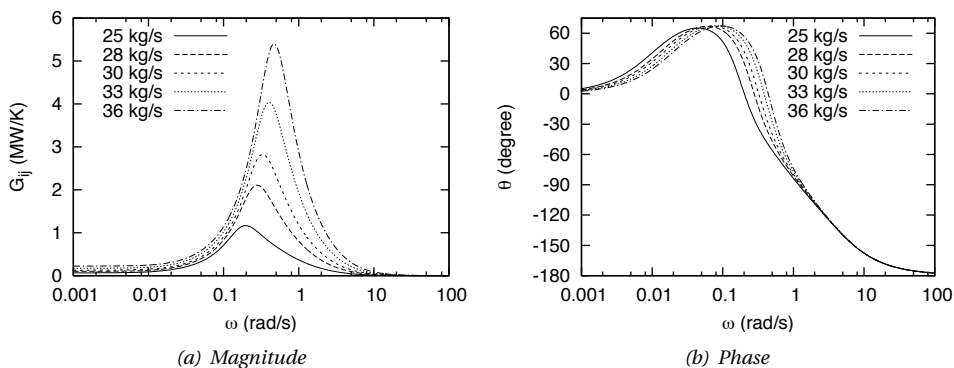


Figure 4.5. Magnitude (left) and phase (right) of the transfer function from inlet helium temperature variations to reactor power fluctuations.

The response of the system against a sinusoidal transient in the inlet temperature is shown in Fig. 4.5. At low inlet flow rate, for example 25 kg/s, the maximum magnitude of the oscillation is about 1 MW/K. At higher inlet flow rate the maximum oscillation is higher than 5 MW/K. All these maximum values take place when the frequency of oscillation is between 0.1 and 1 rad/s. At lower frequency, the magnitude of the transfer function is lower than 0.5 MW/K.

4.5. Operational transients

The linear stability analysis presented in the previous section is valid only for small perturbations from the equilibrium operational point. In this section we will analyze the behavior of the system against large perturbations using a full non-linear model as described in Section 4.2. Two input parameters can be varied in this model, i.e. the coolant mass flow rate, G_{in} and the coolant inlet temperature, T_{in} , which apply as well in reality. Hence, two kinds of operational transients were simulated to investigate the effect to the fluidized bed nuclear reactor, i.e. a change in the inlet flow rate and a change in the helium inlet temperature. For both transients we are considering a step change. Step disturbances are in fact not realistic considering the inertia of the gas circulators, however such simulations are conservative. The initial operational conditions for every simulation are inlet mass flow rate, G_{in} , of 33 kg/s and helium inlet temperature, T_{in} , of 543 K. At this situation, the reactor is assumed to be in steady state with a power level of 80 MW, fuel and gas temperature of 1012 and 1010 K, respectively, and a bed height of 536 cm. These values were obtained by performing steady state calculations as mentioned in Section 4.3. Please note that the difference between fuel temperature and gas temperature is less than 3 K (even during the transients), hence the gas temperature will not be shown in subsequent graphs. During the transient the pressure of the system is kept constant at 60 bar.

4.5.1. Change in the inlet flow rate

The inlet flow rate in the step change simulation is either decreased to 32 kg/s or increased to 34 kg/s. The results of these transients are shown in Fig. 4.6.

As the flow rate decreases, the average porosity of the core (or the bed height) decreases very rapidly. The negative feedback coming from the change in bed porosity (i.e. the first term of the RHS of Eq. (4.29)) becomes dominant and affects the reactivity that further decreases the total power. As the heat generated in the core decreases, the fuel temperature begins to drop. At a later stage the temperature term of Eq. (4.29) will dominate, giving a positive feedback through the Doppler effect. Hence, it is clear that the reactivity (and consequently the total power) will increase and will stabilize to a new steady state. The final states are 72 MW of power, 979 K of fuel temperature and 516 cm of bed height.

A similar event but in reverse order occurs when the inlet flow rate is increased to 34 kg/s. The final total power stabilizes at a higher value, preceded by an overshoot. Although this power overshoot is relatively high (ca. 50 MW), the overshoot in the fuel temperature (and gas temperature) is only about 5 K. The final states of this transient are 88 MW of power, 1045 K of fuel temperature and 556 cm of bed height.

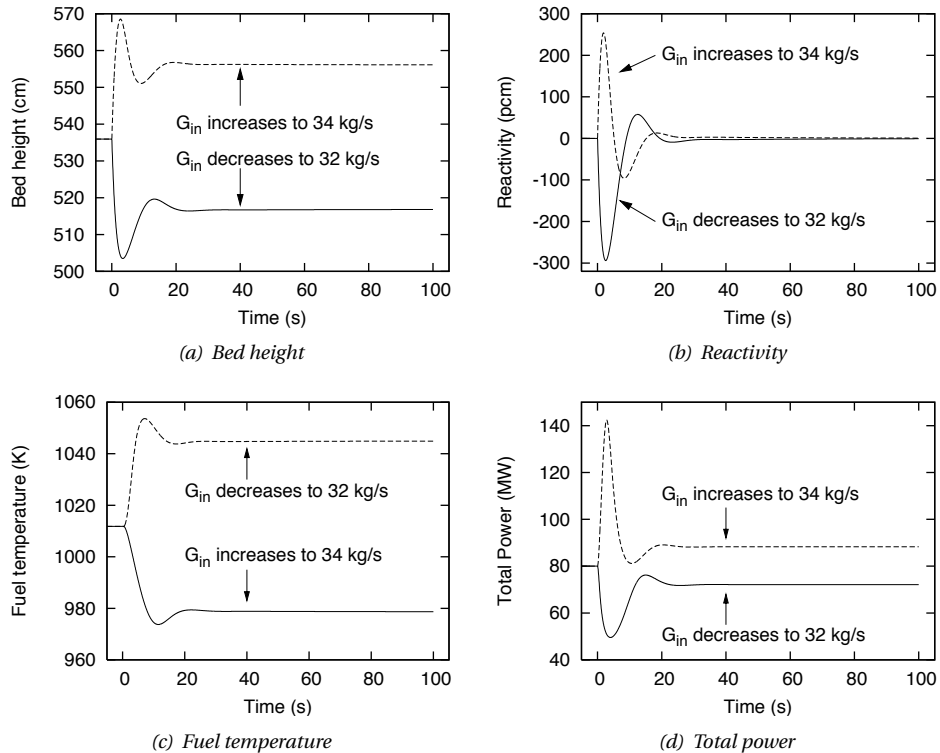


Figure 4.6. (a) Bed height, (b) reactivity, (c) fuel temperature and (d) total power after a step change in inlet flow rate from its initial condition of 33 kg/s .

Note that these final values are slightly different from the expected result of the steady state. For instance, Fig. 4.2(a) shows that the power slope at 33 kg/s is about 10 MW/(kg/s), giving the output power of 90 MW for an increase in mass flow rate to 34 kg/s and 70 MW for a mass flow rate decrease to 32 kg/s. Similar to the frequency analysis, these differences are caused by the use of a different formulation in the model for the temperature feedback to the reactivity, i.e. Eq. (4.31) for the steady state calculations and Eq. (4.32) for the transient calculations. Within the time scale of the transient calculations presented in this section, the final temperature of the reflector is the same as the initial state. However, the reflector temperature in fact gradually increases (or decreases, depending on the kind of the transients). It has been shown by Kloosterman *et al.* (2001) that the reflector has a positive temperature feedback to reactivity (although the total temperature feedback is still negative), leading the power to increase gradually as the reflector temperature increases. The asymptotic power change for such transient in the end will correspond to the power change given in the steady state analysis.

4.5.2. Change in the helium inlet temperature

The results of an instantaneous change of helium inlet temperature are shown in Fig. 4.7. In this case, the inlet temperature is decreased or increased at time 0 by 10 K after the reactor has reached the steady state condition at 33 kg/s.

As the coolant temperature decreases, the helium density increases and consequently the drag force increases as well. So intuitively we may say that the bed becomes higher and the reactor produces more power. However, in our model the mass flow rate is kept constant, giving a decrease in the superficial velocity. Consequently the bed starts to contract, resulting in a sudden decrease in reactivity due to the void fraction feedback. This leads to a decrease in the total generated power and fuel temperature. After some time, however, the decrease of the fuel temperature causes a rise in reactivity due to the negative temperature feedback, creating a rise in power. Similar to the change in gas inlet flow rate, this temperature change also exhibits an overshoot before settling down to a steady condition. The maximum fuel temperature, however, does not increase excessively. In the final state, the change in power is about 1.7 MW, 20 K in fuel temperature and 12 cm in bed height.

4.6. Influence of particle redistribution on power

It has been observed experimentally (Mudde *et al.*, 1999) that if the flow velocity of the fluid is increased, particles in a gas-solid fluidized bed move chaotically and the flow structure is characterized by the occurrence of void regions (or bubbles). The bubble formation and accompanying fuel particle movement present an inhomogeneous state of fuel particle distribution in the core. Several flow regimes may occur in a fluidized bed and in general it can be based on bubble behavior. For type-D Geldart particles, such as TRISO particles, bubbles appear as soon as the minimum fluidization velocity is achieved (Kunii and Levenspiel, 1991), hence within the operational range of the reactor, bubbles may be observed.

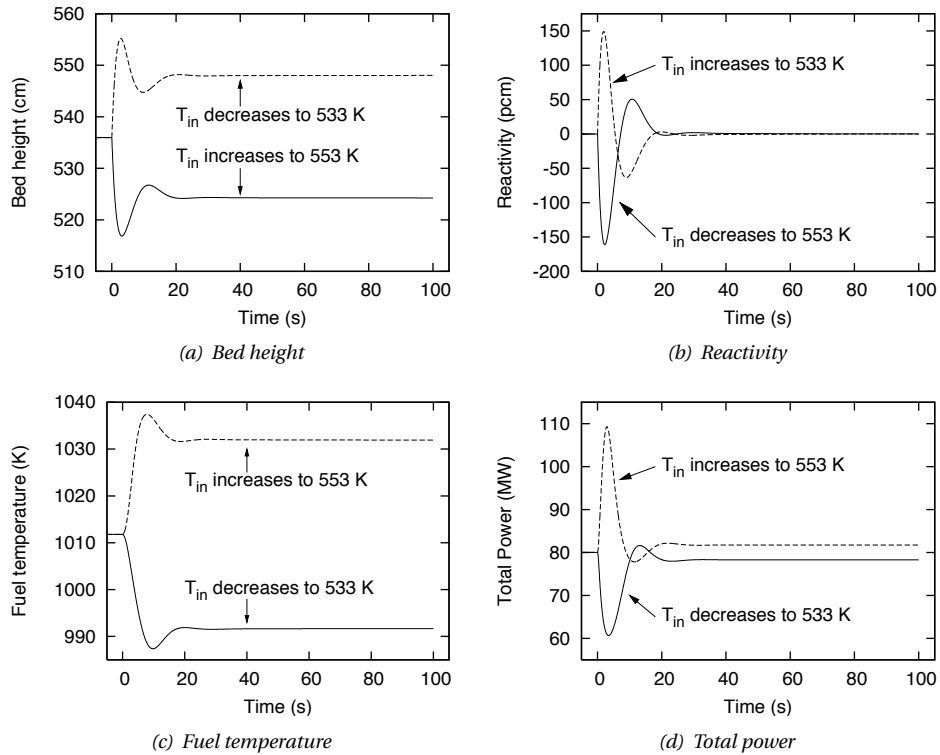


Figure 4.7. (a) Bed height, (b) reactivity, (c) fuel temperature and (d) total power after a step change in inlet coolant temperature from its initial condition of 543 K.

The spatial distribution of particles in the bed will vary as a function of time. As particles close to the reflector have a higher importance than those in the vicinity of the central axis of the bed, this spatial redistribution of particles will have an effect on the reactivity and therefore on the power of the reactor. As mentioned in Section 3.4, some Monte Carlo simulations were performed to quantify the magnitude of the reactivity change due to void/bubbles occurrence in the bed. Bubbles of various sizes were simulated to occur at various positions of the bed. The resulting reactivity changes are further compared to the corresponding homogeneous bed. To account for a stochastic redistribution of the fuel particles, an additional term is included to the reactivity feedback and modeled as a time-dependent external reactivity, $\rho_{ext}(t)$. Equation (4.29) thus becomes

$$\rho(\alpha_g, T_p, t) = \rho_{ref}(\alpha_g) + \rho_T(\alpha_g, T_p) + \rho_{ext}(t) \quad (4.49)$$

This external reactivity is here computed from an AR(1) model (Kendal and Ord, 1990; Chatfield, 1996) as follows:

$$\rho_{ext}(t_k) = \alpha \rho_{ext}(t_{k-1}) + Z(t_k) \quad (4.50)$$

where α is the autoregressive coefficient and Z is a random process with zero mean. The autoregressive coefficient is given by the following relation,

$$\alpha = e^{-t_{int}/\tau_{ar}} \quad (4.51)$$

where τ_{ar} is the correlation time and t_{int} is the sampling interval time. In this model the correlation time is specified at 1 second, which is quite realistic as it relates to the time scale of bubble propagation along the bed height.

The variance of the external reactivity, σ_{ρ}^2 , is given by the following relation,

$$\sigma_{\rho}^2 = \frac{\sigma_z^2}{(1 - \alpha^2)} \quad (4.52)$$

where σ_z^2 is the variance of the random process. The required variance of the external reactivity is obtained from the results of static calculations mentioned in Section 3.4. On the basis of these calculations, the standard deviation was fixed to 150 pcm. The value of σ_z^2 along with randomly generated numbers are subsequently used to determine the value of $Z(t_k)$.

A time trace (with a flow rate of 33 kg/s) was simulated with a duration of 15 minutes and the observed fuel temperature together with the power output and bed height are shown in Figs. 4.8 – 4.10. Figure 4.8 shows the (total) reactivity trace for the first 100 seconds where some large dips or large surges of reactivity occur among smaller ripples. These high frequency ripples are mainly caused by the random movements of particles, while large reactivity changes are induced by changes in the height of the bed.

Fluctuations of the bed height (Fig. 4.10) have a magnitude of about 30 cm and are slowly varying. This behavior can be understood as within the point model, changes in the bed height (or particle void fraction) are influenced by the gas temperature feedback. Temperature changes influence properties of materials which in turn influence the fluidization process. As shown in Fig. 4.11, the temperature of particles (and gas) evolves slowly in time, inducing a low-frequency change of bed height.

The total power (Fig. 4.9) is shown to be highly fluctuating with a time-averaged value of 80.4 MW and a standard deviation of 17.9 MW. The maximum output power is about twice the average. On the other hand, fluctuations of the gas temperature (Fig. 4.11) are in fact more important from an electricity generation point of view. The time-averaged value of gas temperature is 1013 K with a standard deviation of 8.1 K. The maximum gas temperature is about 1043 K. Figure 4.11 shows that the response of the fuel temperature to the external reactivity change is less sensitive.

Although the current design has a large variance of external noise (and consequently a large output power variation), the maximum fuel temperature remains below the maximum permissible temperature of TRISO particles.

4.7. Summary

A point dynamics model comprising coupled neutronics, heat transfer and fluidization has been applied to investigate the stability, the steady state and transient behavior of FLUBER. The following findings are reported:

1. The maximum steady state power produced by this new design is 120 MW, which is higher than that of the previous designs.
2. The maximum steady state fuel temperature is 1163 K, which is still below the maximum permissible value of TRISO particles of 1873 K.
3. Adjusting the helium flow through the core can be used to control the power level of the reactor, thus no active control mechanisms are required for this purpose.
4. The stability of the system has been investigated by a root-locus analysis as a function of the coolant flow rate. The eigenvalues are found to have negative parts for all mass flow rate thus implying linear stability.
5. Transient simulations have been performed for step changes in coolant flow rate and inlet temperature and for external reactivity changes due to stochastic movements of fuel particles. In all cases, the total power might experience a large overshoot, while the fuel temperature, thanks to the negative reactivity feedback, stays still far below the maximum permissible limit.

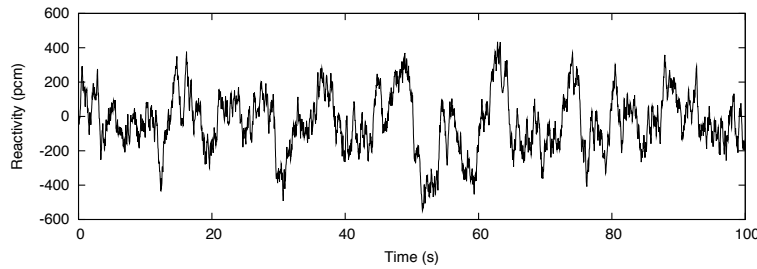


Figure 4.8. Time traces of total reactivity influenced by external reactivity.

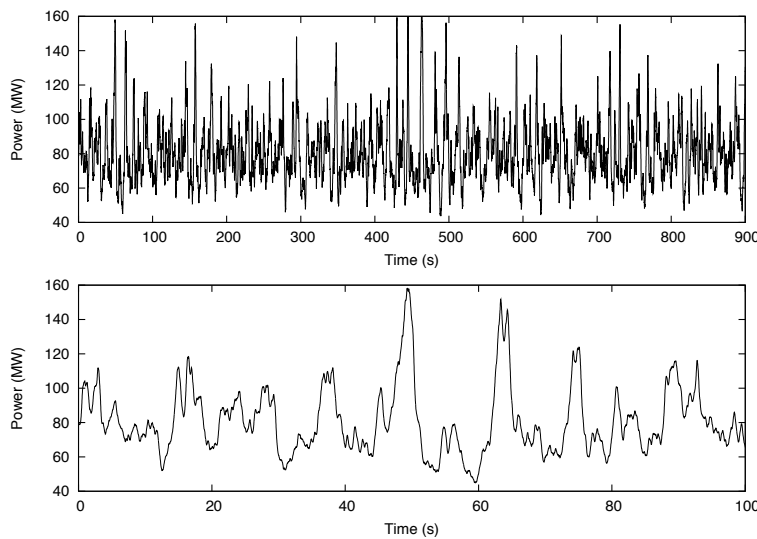


Figure 4.9. Trace of total power as a function of time for a steady system subject to external noise on the reactivity (150 pcm standard deviation). The lower figure shows the power during the first 100 seconds.

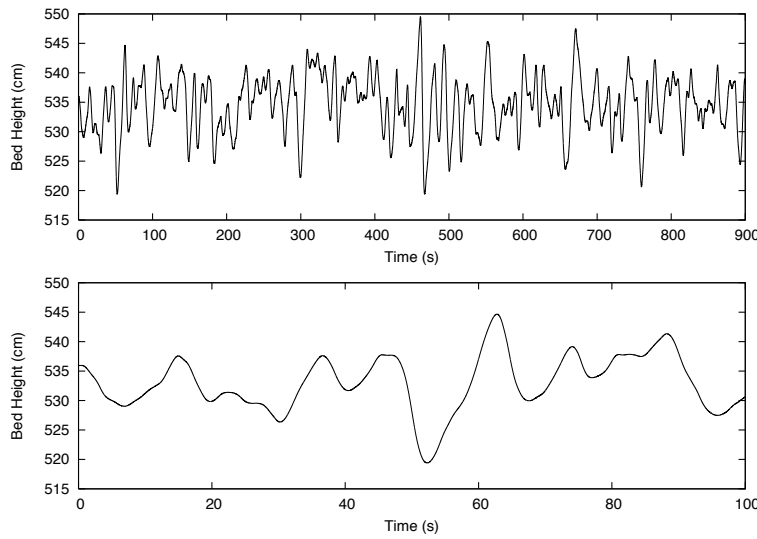


Figure 4.10. Trace of bed height as a function of time for a steady system subject to external noise on the reactivity (150 pcm standard deviation). The lower figure shows the bed height during the first 100 seconds.

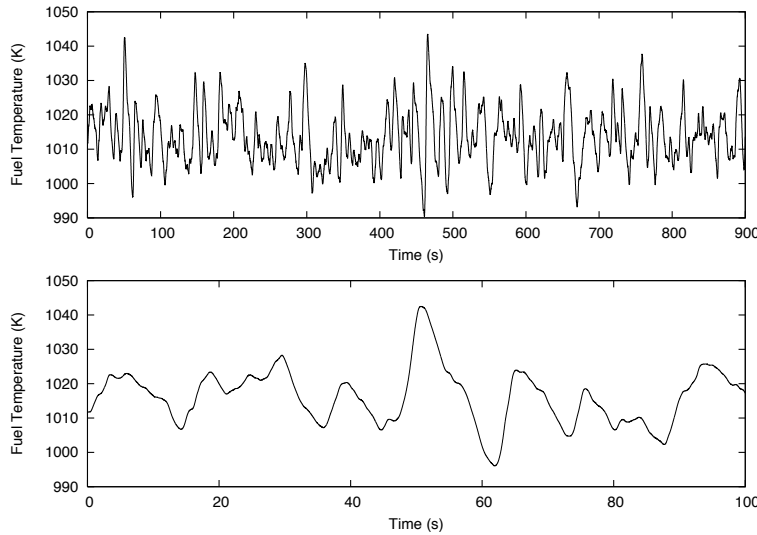


Figure 4.11. Trace of fuel temperature as a function of time for a steady system subject to external noise on the reactivity (150 pcm standard deviation). The lower figure shows the fuel temperature during the first 100 seconds.

CHAPTER 5

Space-dependent dynamics of FLUBER

5.1. Introduction

In Chapter 4 the zero-dimensional (point) dynamics of FLUBER has been discussed, neglecting the influence of spatial dependence. The neutronic parameters applied in the point dynamic model are obtained from the static calculations by assuming a uniform distribution of fuel particles. In reality, particles in fluidized beds are not distributed uniformly and even move rather chaotically. The hydrodynamics of gas-solid fluidized beds are a complex phenomenon, determined by the combined effects of formation, motion and interactions of bubbles as well as by the solids behavior (Van der Stappen, 1996). The time dependent behavior of a fluidized bed is thus important.

We have seen in Chapter 3 that the neutronic behavior of FLUBER is strongly affected by spatial changes in void fraction. Movement of particles from one region to another region having different importance value will give fluctuations in the reactivity, which in turn affect the power generated. This situation differs from “conventional” reactors such as BWRs and PWRs, where fuel elements remain in their fixed position. The time-dependent neutronics of FLUBER is also different from “conventional” as the delayed neutron precursors in FLUBER are also advected with the particles. This problem combined with the nature of fluidization poses a demanding task in terms of computation.

In this chapter the space-dependent dynamics with coupled neutronic and fluid dynamic of FLUBER is described. The influence of different inlet flow rates to the evolution of particle distribution, temperature and power is treated. Of particular interest is the question whether FLUBER can be operated within acceptable safety margins.

5.2. Description of the codes

The simulations of time- and space-dependent dynamics have been performed by using the FETCH code which was developed at Imperial College, London. The FETCH code is comprised of three modules: (i) a radiation transport code EVENT (De Oliveira, 1986), (ii) a computational fluid dynamics code FLUIDITY (Mansoorzadeh *et al.*, 1998) and (iii) an interface module which couples the neutronics and fluid dynamics code. A pictorial representation of the flow of information in the FETCH code is shown in Fig. 5.1. The radiation transport calculation will yield the spatial dependence of energy and delayed neutron source fields, which are input to the fluids module. The fluids module solves the advection/diffusion equations. Delayed neutron precursors are also advected with the fluid and the information regarding the concentration of delayed neutron precursors is returned to the neutronics module. The feedback from the fluids module, in terms of temperature, density and void fraction, is processed by the interface module to obtain the spatial distribution of multi-group neutron cross-sections which are fed back to the neutronics module. For a given element of the finite element mesh, a cross-section set is obtained by interpolating a cross-section database in temperature and void fraction.

The EVENT code solves the Boltzmann transport equation using a second order even-parity variational principle. The discretization of the phase space is finite elements in space, spherical harmonics in angle, multi-group in energy and implicit two level discretization in time. Formulations for applying finite elements to steady-state and time dependent radiation transport problems have been quite extensively explored see e.g. (Ack-

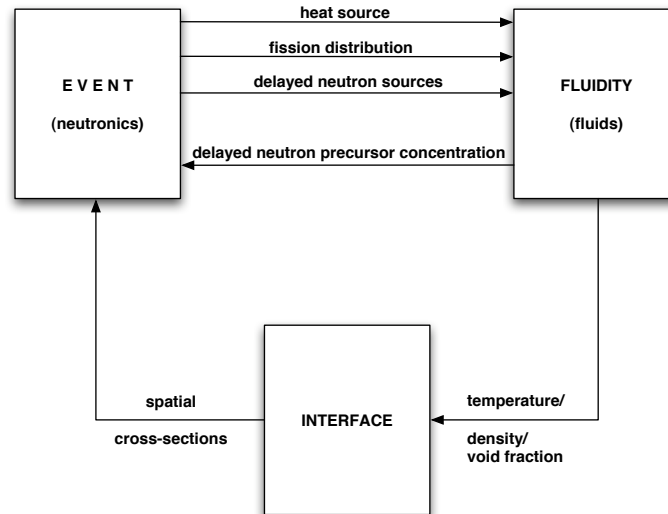


Figure 5.1. An outline of the FETCH code, representing the flow of information among different modules.

royd, 1981, 1995). The finite element method of solving the Boltzman transport equation in the EVENT code is described by De Oliveira (1986).

In the CFD code FLUIDITY, the momentum equations are discretized using a non-linear Petrov-Galerkin method to reduce oscillations in the velocity fields. Other conservation equations are solved using an implicit high resolution method which is second-order accurate in space and time. The interphase coupling is treated implicitly through pressure (Pain *et al.*, 2001c). The FLUIDITY code also incorporates an automatic time-stepping method to improve efficiency of the code. This method produces time step sizes that are dictated by acoustic waves in the particle phase, resulting in time steps between $10^{-5} - 10^{-3}$ seconds.

Some validations of the criticality models have been extensively performed and compared to the experimental results. For example, FETCH has been used to simulate the transient criticality of the SILENE reactor and the results have predicted the fission rates for prompt supercritical step reactivity insertion within acceptable accuracy (Pain *et al.*, 2001a). The robustness of the fluidization model incorporated in FLUIDITY has been investigated for example in bubbling and slugging fluidized beds. The behavior of particles and a number of phenomenon such as formation, elongation and eruption of bubbles obtained from the simulations are consistent with the results of experiments (Pain *et al.*, 2001b; Gomes, 2004). These studies have given enough confidence to investigate the dynamics of FLUBER using the FETCH code.

5.3. Governing equations

5.3.1. Neutronics model

The time-dependent transport equation of neutrons having energy E can be written as

$$\frac{1}{v} \frac{\partial \Psi(\mathbf{r}, \boldsymbol{\Omega}, E, t)}{\partial t} + \boldsymbol{\Omega} \cdot \nabla \Psi(\mathbf{r}, \boldsymbol{\Omega}, E, t) + \mathcal{H}\Psi(\mathbf{r}, \boldsymbol{\Omega}, E, t) = \mathbf{S}(\mathbf{r}, \boldsymbol{\Omega}, E, t) \quad (5.1)$$

where $\Psi(\mathbf{r}, \boldsymbol{\Omega}, E, t)$ is the neutron angular flux, \mathcal{H} is the interaction operator and \mathbf{S} is the effective source. The operator, \mathcal{H} , is defined in terms of the total cross-section, $\Sigma_t(\mathbf{r}, E)$, and the scattering cross-section, $\Sigma_s(\mathbf{r}, \boldsymbol{\Omega}' \cdot \boldsymbol{\Omega}, E' \rightarrow E)$, and is given by the following form

$$\mathcal{H}\Psi(\mathbf{r}, \boldsymbol{\Omega}, E, t) = \Sigma_t(\mathbf{r}, E)\Psi(\mathbf{r}, \boldsymbol{\Omega}, E, t) - \int_{4\pi} \int_0^\infty \Sigma_s(\mathbf{r}, \boldsymbol{\Omega}' \cdot \boldsymbol{\Omega}, E' \rightarrow E, t)\Psi(\mathbf{r}, \boldsymbol{\Omega}', E', t) dE' d\boldsymbol{\Omega}' \quad (5.2)$$

The differential scattering cross-section can be expanded in a series of Legendre polynomials (Duderstadt and Martin, 1979) as

$$\Sigma_s(\mathbf{r}, \boldsymbol{\Omega}' \cdot \boldsymbol{\Omega}) = \sum_{l=0}^L \left(\frac{2l+1}{4\pi} \right) \Sigma_{sl} P_l(\mu_0) \quad (5.3)$$

where $\mu_0 = \boldsymbol{\Omega}' \cdot \boldsymbol{\Omega}$ and

$$\Sigma_{sl} = 2\pi \int_{-1}^{+1} \Sigma_s P_l(\mu_0) d\mu_0 \quad (5.4)$$

The interaction operator, \mathcal{H} , can now be written in a different form

$$\mathcal{H}\Psi(\mathbf{r}, \boldsymbol{\Omega}, E, t) = \sum_{l=0}^L \left(\frac{2l+1}{4\pi} \right) (\Sigma_t - \Sigma_{sl}) \int_0^\infty \int_{4\pi} P_l(\mu_0) \Psi(\mathbf{r}, E', \boldsymbol{\Omega}', t) d\boldsymbol{\Omega}' dE' \quad (5.5)$$

The effective source, \mathbf{S} , has contributions from external sources, fission neutron within energy E to $E + dE$ and delayed neutrons. It can be written as

$$\mathbf{S} \equiv \mathbf{S}_{ext}(\mathbf{r}, \boldsymbol{\Omega}, E, t) + \frac{1-\beta}{4\pi} \chi_p(E) \int_{4\pi} \int_0^\infty \nu \Sigma_f(E') \Psi(\mathbf{r}, \boldsymbol{\Omega}', E', t) d\boldsymbol{\Omega}' dE' + \sum_n \lambda_n \chi_n^d(E) C_n \quad (5.6)$$

In a numerical scheme, the time-dependent equation (Eq. (5.1)) can be cast into a steady-state-like equation by using e.g. backward Euler time-differencing, resulting in

$$\boldsymbol{\Omega} \cdot \nabla \Psi(\mathbf{r}, \boldsymbol{\Omega}, E, t + \Delta t) + \mathcal{H}^* \Psi(\mathbf{r}, \boldsymbol{\Omega}, E, t + \Delta t) = \mathbf{S}^*(\mathbf{r}, \boldsymbol{\Omega}, E, t + \Delta t) \quad (5.7)$$

where

$$\mathcal{H}^* \Psi(\mathbf{r}, \boldsymbol{\Omega}, E, t + \Delta t) = \mathcal{H} \Psi(\mathbf{r}, \boldsymbol{\Omega}, E, t) + \frac{\Psi(\mathbf{r}, \boldsymbol{\Omega}, E, t)}{v \Delta t} \quad (5.8)$$

$$\mathbf{S}^*(\mathbf{r}, \boldsymbol{\Omega}, E, t + \Delta t) = \mathbf{S}^*(\mathbf{r}, \boldsymbol{\Omega}, E, t) + \frac{\Psi(\mathbf{r}, \boldsymbol{\Omega}, E, t)}{v \Delta t} \quad (5.9)$$

Instead of using the angular flux, Ψ , the neutron transport equation can be cast in the even-parity component of the angular flux (Ackroyd, 1978). The even- and odd-parity component can be written as

$$\begin{aligned} \psi^+(\mathbf{r}, \boldsymbol{\Omega}) &= \frac{1}{2} [\Psi(\mathbf{r}, \boldsymbol{\Omega}) + \Psi(\mathbf{r}, -\boldsymbol{\Omega})] \\ \psi^-(\mathbf{r}, \boldsymbol{\Omega}) &= \frac{1}{2} [\Psi(\mathbf{r}, \boldsymbol{\Omega}) - \Psi(\mathbf{r}, -\boldsymbol{\Omega})] \end{aligned} \quad (5.10)$$

and they satisfy the following identities

$$\begin{aligned} \psi^+(\mathbf{r}, \boldsymbol{\Omega}) &= \psi^+(\mathbf{r}, -\boldsymbol{\Omega}) \\ \psi^-(\mathbf{r}, \boldsymbol{\Omega}) &= -\psi^-(\mathbf{r}, -\boldsymbol{\Omega}) \end{aligned} \quad (5.11)$$

Note that the symbols of energy and time in the flux are omitted for simplicity.

Adding Eq. (5.7) written for $-\boldsymbol{\Omega}$ to the same equation written for $\boldsymbol{\Omega}$ and using Eq. (5.10) yields

$$\boldsymbol{\Omega} \cdot \nabla \psi^-(\mathbf{r}, \boldsymbol{\Omega}) + \mathbf{C} \psi^+(\mathbf{r}, \boldsymbol{\Omega}) = \mathbf{S}^+(\mathbf{r}, \boldsymbol{\Omega}) \quad (5.12)$$

and subtracting the same two equations yields

$$\boldsymbol{\Omega} \cdot \nabla \psi^+(\mathbf{r}, \boldsymbol{\Omega}) + \mathbf{G}^{-1} \psi^-(\mathbf{r}, \boldsymbol{\Omega}) = \mathbf{S}^-(\mathbf{r}, \boldsymbol{\Omega}) \quad (5.13)$$

where the even-parity effective source, \mathbf{S}^+ , and the odd-parity effective source, \mathbf{S}^- , are defined by

$$\mathbf{S}^\pm(\mathbf{r}, \boldsymbol{\Omega}) = \frac{1}{2} [\mathbf{S}(\mathbf{r}, \boldsymbol{\Omega}) \pm \mathbf{S}(\mathbf{r}, -\boldsymbol{\Omega})] \quad (5.14)$$

and the even- and odd-parity components of the interaction operator, \mathcal{H} , can be written as

$$\mathbf{C}\psi^+(\mathbf{r}, \boldsymbol{\Omega}) = \sum_{l \text{ even}} \left(\frac{2l+1}{4\pi} \right) (\Sigma_t - \Sigma_{sl}) \int_0^\infty \int_{4\pi} P_l(\mu_0) \psi^+(\mathbf{r}, E', \boldsymbol{\Omega}') d\boldsymbol{\Omega}' dE' \quad (5.15a)$$

$$\mathbf{G}^{-1}\psi^-(\mathbf{r}, \boldsymbol{\Omega}) = \sum_{l \text{ odd}} \left(\frac{2l+1}{4\pi} \right) (\Sigma_t - \Sigma_{sl}) \int_0^\infty \int_{4\pi} P_l(\mu_0) \psi^-(\mathbf{r}, E', \boldsymbol{\Omega}') d\boldsymbol{\Omega}' dE' \quad (5.15b)$$

Combining the two parity equations (Eqs. 5.10 and 5.12) gives rise to the second-order or even-parity form of the transport equation

$$-\boldsymbol{\Omega} \cdot \nabla \mathbf{G} [\boldsymbol{\Omega} \cdot \nabla \psi^+] + \mathbf{C}\psi^+ = \mathbf{S}^+ - \boldsymbol{\Omega} \cdot \nabla \mathbf{G} \mathbf{S}^- \quad (5.16)$$

On the external boundaries of the problem domain, a vacuum boundary condition may be imposed as

$$\Psi(\mathbf{r}, \boldsymbol{\Omega}) = 0, \quad \text{for } \boldsymbol{\Omega} \cdot \hat{\mathbf{n}} < 0 \quad (5.17)$$

and the solution of Eq. (5.16) subject to the aforementioned boundary condition is equivalent to finding the function which minimizes the quadratic variational function (De Oliveira, 1997)

$$\begin{aligned} \mathbf{F}(\psi^+) = & (\boldsymbol{\Omega} \cdot \nabla \psi^+, \mathbf{G}\boldsymbol{\Omega} \cdot \nabla \psi^+) + (\psi^+, \mathbf{C}\psi^+) \\ & + \langle \psi^+, \psi^+ \rangle - 2(\psi^+, \mathbf{S}^+) - 2(\boldsymbol{\Omega} \cdot \nabla \psi^+, \mathbf{G}\mathbf{S}^-) \end{aligned} \quad (5.18)$$

where $\langle \cdot, \cdot \rangle \equiv \int dV \int d\boldsymbol{\Omega}$ and $\langle \cdot, \cdot \rangle \equiv \int dA \int d\boldsymbol{\Omega} |\boldsymbol{\Omega} \cdot \hat{\mathbf{n}}|$. Approximate solutions are then obtained by the well-known Ritz-Galerkin procedure.

Eq. (5.18) can be minimized for a given set of trial functions, φ^+ . Subdividing the spatial domain into E non-overlapping sub-domains or elements, connected at N nodal points, the trial function for the even-parity flux is given in the following form:

$$\varphi^+(\mathbf{r}, \boldsymbol{\Omega}) = \sum_{e=1}^E \sum_{j=1}^{N_e} \sum_{k=1}^M \mathbf{B}_j^e(\mathbf{r}) Q_k(\boldsymbol{\Omega}) \varphi_{jk}^{+e} \quad (5.19)$$

where $Q_k(\boldsymbol{\Omega})$ are the normalized spherical harmonics functions given by

$$Q_{k(lm)} = \sqrt{\frac{(2l+1)}{4\pi} (2 - \delta_{m,0}) \frac{(l-m)!}{(l+m)!}} P_l^m(\mu_0) \left\{ \begin{array}{l} \cos m\chi \\ \sin m\chi \end{array} \right\} \quad (5.20)$$

for l even and $m = 0, 1, \dots, l$. The series is truncated at $l = N - 1$ and the approximation is denoted by P_N .

The source term, Eq. (5.6), includes the contribution of delayed neutrons. The equation for the n th delayed neutron group precursor concentration is written as

$$\frac{\partial C_n(\mathbf{r}, t)}{\partial t} + \nabla \cdot \mathbf{v}_s C_n(\mathbf{r}, t) = -\lambda_n C_n(\mathbf{r}, t) + \beta_n \int_0^\infty \nu \Sigma_f \phi(\mathbf{r}, E, t) dE \quad (5.21)$$

The delayed neutron equation applied in this model is rather different from the commonly used space-dependent equation (see e.g. Ott and Neuhold (1985)). The second term in the LHS of Eq. (5.21) appears as the delayed neutron precursors are advected by the fluidizing coolant.

5.3.2. Multiphase model

Modeling strategy and numerical approach for the prediction of hydrodynamics of gas-solid fluidized beds can be performed in various levels depending on the scale of the phenomena to be investigated (Bokkers, 2005). In the lowest level with the number of particles less than one hundred, the Lattice Boltzman Model (LBM) has been employed (Van der Hoef *et al.*, 2005) where the effective drag force on the particle can be computed. Another model is the Discrete Particle Model (DPM) which is suitable for small scale fluidized beds with the number of particles less than one million (Tsuiji and Kawaguchi, 1993; Van Wachem, 2000). DPM, or Eulerian-Lagrangian model, calculates the path of each individual particle with the second law of Newton, while the gas flow field is computed from the volume-averaged Navier-Stokes equation. If the number of particles exceeds one million, the DPM is not practical anymore since the computational time to compute motion of all individual particles is too much. In such a case, a continuum model, or Eulerian-Eulerian model, is employed. The Two Fluid Model (TFM) is the most widely used continuum model where the particulate and gas phases are assumed to form two inter-penetrating continua, and the equations of continuity, momentum and energy are written for both phases. Many literature contributions have been published describing the hydrodynamic phenomena in fluidized beds using TFM, e.g. by Kuipers *et al.* (1993); Enwald *et al.* (1997); Gera *et al.* (1998) and Goldschmidt (2001). The solid phase rheology is described with the kinetic theory of granular flows to obtain closure equations for the solid phase viscosity and pressure as a function of the random fluctuating particle velocity, i.e. the granular temperature (Ding and Gidaspow, 1990). In FLUIDITY the two fluid granular temperature model is applied (Pain *et al.*, 2001b,c; Gomes, 2004) and the governing equations are described as follows.

Continuity equation

The continuity equation for phase k , where $k = g$ denotes gas and $k = p$ denotes solid particles, is

$$\frac{\partial}{\partial t} (\alpha_k \rho_k) + \nabla \cdot (\alpha_k \rho_k \mathbf{v}_k) = 0 \quad (5.22)$$

where ρ_k is the density of phase k , α_k is the volume fraction of phase k and \mathbf{v}_k is the velocity vector of phase k .

Momentum equation

The corresponding momentum equation is given as,

$$\frac{\partial}{\partial t} (\alpha_k \rho_k \mathbf{v}_k) + \nabla \cdot (\alpha_k \rho_k \mathbf{v}_k \mathbf{v}_k) = -\alpha_k \nabla \cdot (p_g \mathbf{I}) + \alpha_k \rho_k \mathbf{g} + \beta (\mathbf{v}_{k'} - \mathbf{v}_k) + \nabla \cdot \boldsymbol{\tau}_k \quad (5.23)$$

where \mathbf{g} is the gravitational acceleration vector, \mathbf{I} is the unit tensor, k' is the opposite phase, p_g is the shared pressure, β is the gas-solid friction coefficient and is obtained from a modified form of Ergun equation (Pain *et al.*, 2002) as follows:

$$\beta = \begin{cases} \frac{3}{4} C_D \frac{(1 - \alpha_p) \alpha_p \rho_g |v_g - v_p|}{d_p} (1 - \alpha_p)^{-2.65}, & \text{for } \alpha_p \leq 0.175 \\ 20(0.225 - \alpha_p) \left[150 \frac{\alpha_p^2 \mu_s}{(1 - \alpha_p) d_p^2} + \frac{7}{4} \frac{\alpha_p \rho_g |v_g - v_p|}{d_p} \right] + \\ 15(\alpha_p - 0.175) C_D \frac{\alpha_p \rho_g |v_g - v_p|}{d_p} (1 - \alpha_p)^{-1.65}, & \text{for } 0.175 < \alpha_p \leq 0.225 \\ 150 \frac{\alpha_p^2 \mu_p}{(1 - \alpha_p) d_p^2} + \frac{7}{4} \frac{\alpha_p \rho_g |v_g - v_p|}{d_p}, & \text{for } \alpha_p > 0.225 \end{cases} \quad (5.24)$$

and the drag coefficient, C_D , is given as a function of Reynolds number of the particle (Rowe, 1961),

$$C_D = \begin{cases} \frac{24}{Re_p(1 - \alpha_p)} (1 + 0.15[(1 - \alpha_p)Re_p]^{0.687}), & \text{for } Re_p < 1000 \\ 0.44, & \text{for } Re_p \geq 1000 \end{cases} \quad (5.25)$$

The stress tensor, $\boldsymbol{\tau}_k$, in Eq. (5.23) for the gas phase g is (Enwald *et al.*, 1997)

$$\boldsymbol{\tau}_g = \alpha_g \mu_g \left[(\nabla \mathbf{v}_g + (\nabla \mathbf{v}_g)^T) - \frac{2}{3} (\nabla \cdot \mathbf{v}_g) \mathbf{I} \right] \quad (5.26)$$

Here the gas-phase turbulence is neglected because it is strongly suppressed in the densely packed beds.

In the solid phase, the stress tensor is

$$\boldsymbol{\tau}_p = (-p_p + \alpha_p \zeta_p \nabla \cdot \mathbf{v}_p) \mathbf{I} + \alpha_p \mu_p \left[(\mathbf{v}_p + (\mathbf{v}_p)^T) - \frac{2}{3} \nabla \cdot \mathbf{v}_p \mathbf{I} \right] \quad (5.27)$$

where p_p is the solid-phase pressure given as

$$p_p = \alpha_p \rho_p [1 + 2(1 + e) \alpha_p g_0] \Theta \quad (5.28)$$

Here e is the particle-particle restitution coefficient, Θ is the granular temperature and is defined by $\frac{3}{2} \Theta = \frac{1}{2} \bar{C^2}$, where $\bar{C^2}$ is the mean square velocity deviation from the average velocity v_p of the solid phase, and g_0 is the particle radial distribution function (Hunt, 1997; Van Wachem, 2000)

$$g_0 = \frac{3}{5} \left[1 - \left(\frac{\alpha_p}{\alpha_{p,max}} \right)^{1/3} \right]^{-1} \quad (5.29)$$

where $\alpha_{p,max}$ is the maximum particle volume fraction (=0.6).

The solid shear viscosity, μ_p , is given by (Van Wachem, 2000)

$$\mu_p = \frac{4}{5} \alpha_p \rho_p d_p g_0 (1 + e) \left(\frac{\Theta}{\pi} \right)^{1/2} \quad (5.30)$$

and the solid-phase bulk viscosity is given by (Lun *et al.*, 1984)

$$\zeta_p = \frac{4}{3} \alpha_p \rho_p d_p g_0 (1 + e) \left(\frac{\Theta}{\pi} \right)^{1/2} \quad (5.31)$$

Energy equation

The thermal energy equations for gas and solid phases are respectively,

$$\alpha_g \rho_g C_{p,g} \frac{DT_g}{Dt} = -p_g \nabla \cdot (\alpha_g \mathbf{v}_g) + \nabla \cdot (\alpha_g \lambda_g \nabla T_g) + h_{pg}(T_p - T_g) \quad (5.32)$$

$$\alpha_p \rho_p C_{p,p} \frac{DT_p}{Dt} = \nabla \cdot (\alpha_p \lambda_p \nabla T_p) + h_{pg}(T_g - T_p) + S_f \quad (5.33)$$

where T_g and T_p are the gas and solid phase temperature, respectively, λ_g and λ_p are the conductive coefficients, h_{pg} is the interphase volumetric heat transfer coefficient, and S_f is the heat source from fission.

The interphase volumetric heat transfer coefficient, h_{pg} , is computed from

$$h_{pg} = \frac{6\alpha_g}{d_p^2} \lambda_g \text{Nu} \quad (5.34)$$

where the corresponding Nusselt number is given by (Gunn, 1978)

$$\text{Nu} = (7 - 10\alpha_g + 5\alpha_g^2)(1 + 0.7\text{Re}_p^{1/5}\text{Pr}^{1/3}) + (1.33 - 2.4\alpha_g + 1.2\alpha_g^2)\text{Re}_p^{7/10}\text{Pr}^{1/3} \quad (5.35)$$

The effective conductive heat transfer coefficients for the gas and solid phase (Kuipers *et al.*, 1992; Hunt, 1997) are given by

$$\alpha_g \lambda_g = (1 - \sqrt{1 - \alpha_g}) \lambda_{gas} \quad (5.36)$$

$$\alpha_p \lambda_p = \alpha_p \rho_p C_{p,p} d_p \frac{\sqrt{\pi^3 \Theta}}{32g'_0} \quad (5.37)$$

where λ_{gas} is the conductivity of pure gas and g'_0 is given by

$$g'_0 = \frac{16 - 7\alpha_p}{16(1 - \alpha_p)^2} \quad (5.38)$$

Some assumptions are made for the thermal calculation, which reduce the computation time. First, thermal radiation heat transfer is neglected since it tends to increase the homogeneity of the temperature distribution. In the event of loss-of-flow transient when

the bed becomes packed and temperature difference is large, the radiative heat transfer should be taken into account as will be discussed in Chapter 6. Another assumption applied to the current model is that within the time frame of simulation the conductive heat transfer in the graphite reflector is neglected. Also we are interested in the dynamics of the system here.

The granular energy equation can be written as,

$$\frac{3}{2} \left[\frac{\partial(\alpha_p \rho_p \Theta)}{\partial t} + \nabla \cdot (\alpha_p \rho_p \mathbf{v}_p \Theta) \right] = \boldsymbol{\tau}_p : \nabla \mathbf{v}_p - \nabla \cdot \mathbf{q}_\Theta - \gamma - 3\beta\Theta \quad (5.39)$$

The term $-3\beta\Theta$ represents the loss of particle kinetic energy to the gas phase due to particle-gas drag forces. The source term due to turbulence velocity fluctuations of the gas phase has been ignored because of the absence of a gas-phase turbulence model.

The collisional energy dissipation, γ , is given by (Jenkins and Savage, 1983)

$$\gamma = 3(1 - e^2) \alpha_p^2 \rho_p g_0 \Theta \left[\frac{4}{d_p} \sqrt{\frac{\Theta}{\pi}} - \nabla \mathbf{v}_p \right] \quad (5.40)$$

and the flux of fluctuating energy is given by

$$\mathbf{q}_\Theta = -\kappa \nabla \Theta \quad (5.41)$$

with a granular conductivity, κ , is defined as

$$\kappa = 2\rho_p \alpha_p^2 g_0 d_p \left(\frac{\Theta}{\pi} \right)^{1/2} \quad (5.42)$$

5.4. Implementation

The geometry of the reactor used in subsequent calculations is shown in Fig. 5.2(a). The reactor is modeled as a 2D axisymmetrical cylinder and discretized using quadrilateral finite elements. Fig. 5.2(b) shows the finite element mesh of the reactor. The computational domain consists of 2800 volume elements with 2961 nodes.

The geometry is divided into two zones: (i) a solid region (graphite reflector) and (ii) a fluid region (the cavity enclosed by the reflector). Neutronic calculations performed by EVENT consider both the solid and fluid regions while for fluid dynamics calculations (FLUIDITY code) only the fluid region is of interest.

The material cross-section libraries are processed using the WIMS8A code (WIMS8A, 1999) and the resulting cross-section libraries are subsequently converted into a special FETCH-readable format using the WIMS8AFETCH code. Taking into account the temperature and resonance self-shielding, the database is condensed from the original 69 energy groups into 6 energy groups. The energy boundaries and their corresponding WIMS8A partition are given in Table 5.1.

For the purpose of transient calculations, several sets of cross-sections corresponding to different temperatures are written in one library file. The fuel temperature is set at various values (i.e. 500, 550, 600, 650, 700, 750, 800, 850, 900, 950, 1200, 1600, 2200 K), while the gas and reflector temperature are set at 1000 K and 500 K, respectively.

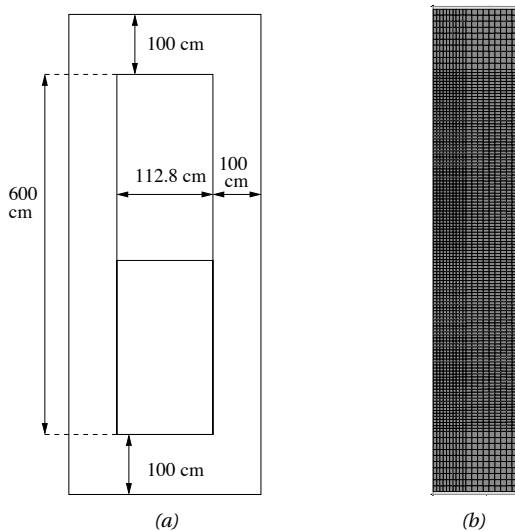


Figure 5.2. (a) The 2D schematic and (b) the finite element mesh for FLUBER used for the time-dependent simulation, the left boundary is the central axis.

A drawback of using WIMS8A library is that it does not provide helium cross-section data, which is very essential in the FLUBER design. Hence, for the purpose of providing nuclear cross-section data of the fluidization gas, nitrogen is used instead.

In terms of the angular flux of neutron, a low order of expansion (P_1) is applied for both the static calculations and the time-dependent simulations.

In the neutronic calculation, 6 groups of delayed neutrons (Hetrick, 1993) are incorporated but only in the solid phase. Fission product poisoning is neglected. The data obtained from FLUIDITY in terms of temperature, density and void fraction are forwarded to EVENT through an interface code which is used to interpolate temperature and gas con-

Table 5.1. Structure of energy groups and their corresponding group collapsing in WIMS and AMPX libraries.

Group number	Energy Boundary (eV)	WIMS Partition	AMPX Groups
1	$8.2085 \times 10^5 - 10^7$	1 – 5	1 – 22
2	$9.1180 \times 10^3 - 8.2085 \times 10^5$	6 – 14	23 – 45
3	$4.0 - 9.1180 \times 10^3$	15 – 27	46 – 92
4	$0.625 - 4.0$	28 – 45	93 – 135
5	$0.14 - 0.625$	46 – 55	136 – 152
6	$1.1 \times 10^{-4} - 0.14$	56 – 69	153 – 172

tent in the cross-section database and then updates the spatial distribution of multigroup neutron cross-sections.

A neutron source of 1000 neutrons/(cm³ s) is applied for the time-dependent simulations.

The thermal properties of particles and helium are given in Table 5.2. The thermal conductivity, heat capacity and dynamic viscosity are temperature-independent. Several boundary conditions are applied such as the inlet condition (velocity, pressure and temperature) and adiabatic condition at the vertical graphite wall. Also no normal flow conditions on the walls are considered. Table 5.3 shows the initial and boundary conditions applied to the simulations.

Several detectors are located in various positions in the bed to monitor calculated data such as volume fraction and temperature of the gas and particles. For our simulations, fourteen detectors are implemented in the bed and their respective positions are given in Table 5.4.

The simulations were performed for two different uranium inventories, i.e. 120 kg and 152 kg. An important parameter to determine how much power can be generated is the superficial velocity (u_g). As a first estimation, the superficial velocity is predicted from the minimum fluidization velocity (u_{mf}). Several correlations have been established, but for our purpose the following correlations are used (Wen and Yu, 1966; Chitester *et al.*, 1984).

$$Re_{p,mf} = \begin{cases} \sqrt{33.7^2 + 0.0408Ar} - 33.7, & \text{for fine particles} \\ \sqrt{28.7^2 + 0.0494Ar} - 28.7, & \text{for coarse particles} \end{cases} \quad (5.43)$$

where $Re_{p,mf}$ is the Reynolds number of the particles at minimum fluidization condition and Ar is the Archimedes number.

Based on Eq. (5.43), the minimum fluidization spans from 23.7 cm/s for fine particles to 28.7 cm/s for coarse particles. For our simulation, superficial velocity of 120 cm/s and 180 cm/s are used for each uranium inventory.

5.5. Static calculations

Static calculations were performed by setting the EVENT code to calculate the criticality eigenvalue. Figure 5.3 shows the effective multiplication factor (k_{eff}) as a function of the particle bed for 120 kg of uranium inventory. The results obtained from running KENO-V.a are presented in the same figure. The EVENT calculations show that the reactor is always subcritical, which is not similar to the results of KENO-V.a. However, the maximum value of k_{eff} is reached approximately at the same bed height, i.e. ≈ 300 cm. The discrepancy between the two results might be caused by the difference in modeling (cell calculations, energy structure, deterministic vs. stochastic transport) or by the lack of helium cross-section in EVENT calculations or a combination of both factors.

To assess this discrepancy, an attempt to include the helium cross-section from AMPX into EVENT has been performed. A 172-group AMPX master library based on JEF-2.2 was processed by using CSAS and XSDRNPM to obtain 6-group zone-weighted libraries at various temperatures (as mentioned in Sec. 5.4) containing either helium or nitrogen. The

Table 5.2. *Physical properties of particles and gas for the simulations.*

	Particles	Fluidization gas
Density (kg m^{-3})	1.92×10^3	Ideal gas
Thermal conductivity ($\text{W m}^{-1} \text{K}^{-1}$)	1.0	2.15×10^{-1}
Heat capacity ($\text{J kg}^{-1} \text{K}^{-1}$)	1.4×10^3	5.24×10^3
Particle diameter (m)	1.00×10^{-3}	–
Dynamic viscosity ($\text{kg m}^{-1} \text{s}^{-1}$)	–	2.7×10^{-5}

Table 5.3. *The initial and boundary conditions for the simulations.*

Initial particle volume fraction	0.6
Inlet gas velocity	1.2 and 1.8 m/s
Inlet gas temperature	226.85 °C
Initial gas and particle velocities	0.0 m/s
Initial gas and particle temperatures	226.85 °C
Particle flow at top boundary	0.0 m/s
Particle stress at top boundary	0.0 N/m ²
Particle-particle restitution coefficient	0.97
Wall-particle restitution coefficient	0.9
Friction coefficient	0.3

Table 5.4. *Position of the fourteen detectors in the bed.*

Detector	<i>r</i> (cm)	<i>z</i> (cm)
01	56.00	100.00
02	56.00	200.00
03	56.00	300.00
04	56.00	400.00
05	56.00	500.00
06	56.00	600.00
07	28.00	100.00
08	28.00	200.00
09	0.00	100.00
10	0.00	200.00
11	0.00	300.00
12	0.00	400.00
13	0.00	500.00
14	0.00	600.00

equivalent group structure of the AMPX library is shown in Table 5.1. The cell model is the same as used for KENO-V.a calculations. The weighted libraries were merged into one by using WAX (Greene, 2000b) and the resulting library was further processed by ALPO (Greene, 2000b) to produce an ANISN library. An in-house PERL script was further developed to finally convert the ANISN library into a FETCH-readable macroscopic cross-section library.

The AMPX-converted libraries were subsequently used in EVENT calculations. Fig. 5.4(a) shows the difference in multiplication factor when nitrogen is used in both WIMS8A library and AMPX-converted library ($\Delta k_{eff} = k_{EVENT,AMPX} - k_{EVENT,WIMS}$). The figure shows that the differences are small, less than 30 pcm, implying that there is no significant difference in the cell modeling between WIMS8A and CSAS-XSDRNP.

Based on this experience, the helium cross-section is then applied for the eigenvalue calculations. The results are then compared to those of KENO-V.a as shown in Fig. 5.4(b) ($\Delta k_{eff} = k_{EVENT} - k_{KENO}$). For large bed expansions the differences are small but for small expansions the differences are large (up to -2000 pcm). The influence of different cell models can be ruled out, hence the differences in group structure (172 vs. 6 groups) and kind of transport method (stochastic vs. deterministic) may cause the discrepancy. The P_1 expansion for the angular flux apparently is not suitable, especially for lower bed heights, due to the presence of a low density region (i.e. the helium cavity) and strong anisotropic neutron streaming. Nevertheless, the multiplication factor is higher and it is even larger than unity at a certain interval. We have tried to include the AMPX-converted library for the dynamic (time-dependent) simulation, but it is not very successful for some unknown reasons. The WIMS8A library with nitrogen is thus used for subsequent calculations.

Figure 5.5 shows the effective multiplication factor of the same reactor geometry but having a larger uranium inventory (152 kg), calculated by EVENT with the WIMS8A library. The collapsed bed is 172 cm. The multiplication factor increases up to a maximum of 0.9945. No KENO-V.a calculations have been made so far for comparison, but based on the results of calculation using 120 kg of uranium, the multiplication factor of KENO-V.a may be larger than unity for all bed expansion.

5.6. Dynamic simulations

Case 1: Uranium inventory = 120 kg, inlet gas velocity = 120 cm/s

A step input in gas velocity of 120 cm/s, corresponding to a coolant mass flow rate of 6.9 kg/s, is given while other initial and boundary conditions are presented in Table 5.3. The time evolution of several variables is shown in Fig. 5.6 and the time-averaged as well as the minimum and maximum values of power, mean gas temperature and maximum particle temperature are given in Table 5.5. Here it is shown that the time-averaged power is 4.4 MW.

Fig. 5.6(a) shows the power generated in the fuel (calculated from the fission rate with a conversion factor of 3.2×10^{-11} J per fission). Although the static calculations show that the reactor is always subcritical, this is not the case in the dynamic simulation. The reactor produces power of the order of megawatts and the average gas temperature increases to about 333 °C. This happens because inhomogeneities in fuel particles distribution influ-

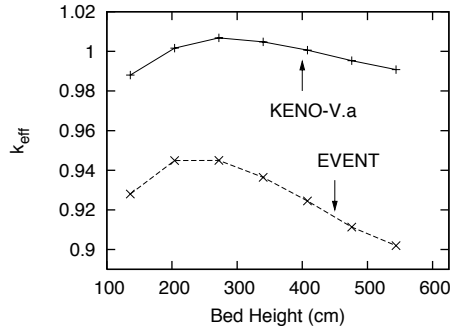


Figure 5.3. The effective multiplication factor as a function of expanded bed. The inventory of uranium is 120 kg. The lower curve represents the results from running EVENT with 6 energy groups libraries obtained from WIMS8A. The upper curve represents the results from running KENO-V. a with 172 energy groups libraries obtained from AMPX.

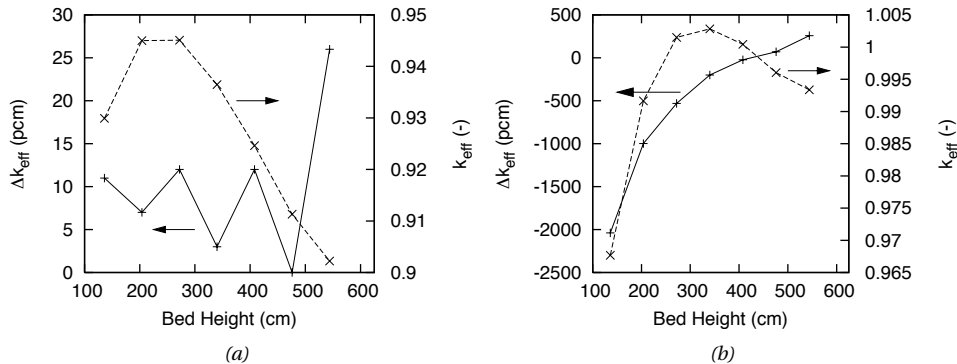


Figure 5.4. (a) The difference in multiplication factor between EVENT with WIMS8A library and EVENT with AMPX-converted library (solid line) and the effective multiplication factor (dashed line) as a function of expanded bed. Nitrogen is included in the library. All calculations were performed using 6 energy groups. (b) The difference in multiplication factor between EVENT with AMPX-converted library and KENO-V. a (solid line) and the effective multiplication factor (dashed line). Helium is included in the library. For EVENT calculations a 6-group library is used while for KENO-V. a a 172-groups library.

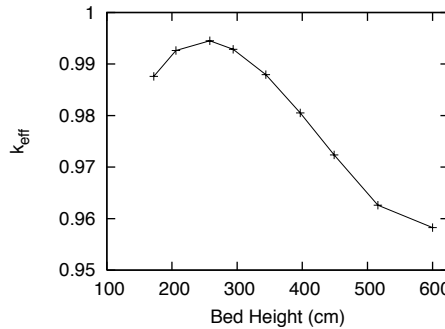


Figure 5.5. The effective multiplication factor as a function of expansion, calculated by EVENT with the 6-group WIMS8A library. The inventory of uranium is 152 kg.

Table 5.5. Time-averaged, minimum and maximum values of power and temperature, excluding the first 20 seconds after initial transient, for a uranium inventory of 120 kg and an input gas velocity of 120 cm/s.

	Power (MW)	Mean Gas Temp. (°C)	Max Particle Temp. (°C)
Time-averaged	4.4	333.3	544.8
Min	0.7	296.8	393.9
Max	26.8	410.9	838.6

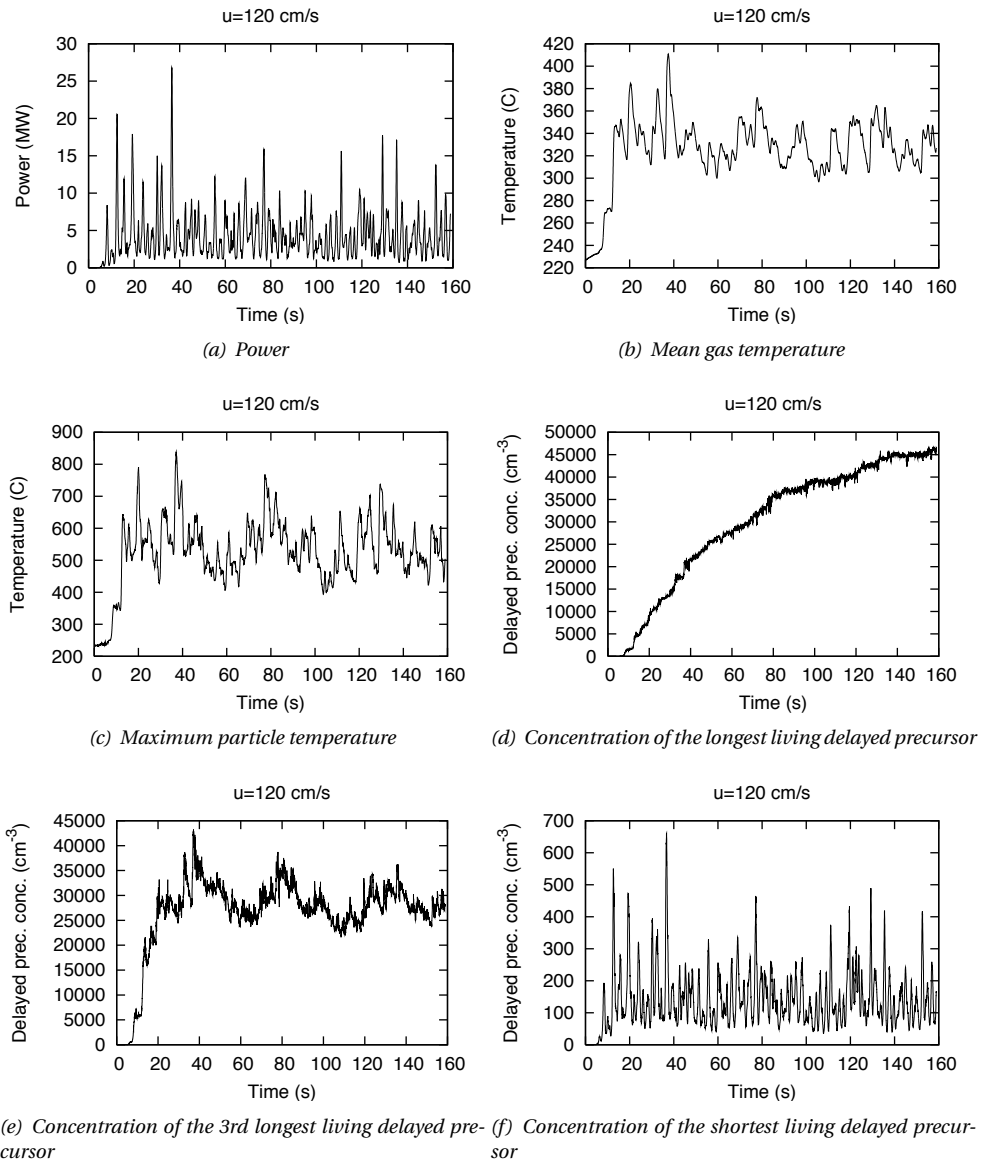


Figure 5.6. Power, mean gas temperature, maximum particle temperature, concentration of the longest, 3rd longest and shortest living delayed neutron precursors for a uranium inventory of 120 kg and an input gas velocity of 120 cm/s.

ence the reactivity as already discussed in Sec. 3.3–3.4 (although the magnitude might be different due to differences in modeling).

Within less than 10 seconds after the initial transient, the reactor produces power up to 7 MW and increases the temperature to ≈ 270 °C (Fig. 5.6(b)). As the temperature coefficient of reactivity is negative, the power goes down and inhibits further increase in temperature. A strong relation between power and temperature can be found in several occasions. For example at ≈ 35 seconds after the initial transient, the power level increases from 2.5 MW to 27 MW, causing the temperature to increase from 320 °C to 410 °C. Such a large temperature surge reduces the power back to ≈ 2 MW.

The mean gas temperature in Fig. 5.6(b) is obtained by averaging the gas temperature over the whole fluid domain. The mean particle temperature (not shown) is very close to the gas temperature due to the good heat transfer between the particles and the gas. This figure is also a good representation of the gas power output. In fact, the gas power output should be calculated as $P_{gas} = \int_{A_{out}} \rho_g u_z C_{p,g} \Delta T_g dA$, where A_{out} is the area of the reactor outlet, ρ_g is the density of the gas, u_z is the normal velocity of the gas at the reactor outlet, $C_{p,g}$ is the specific heat capacity of the gas and ΔT_g is the gas temperature difference between outlet and inlet of the reactor. As the fluidization process tends to homogenize the temperature, the mean value of the gas temperature may be a good estimator for the gas power output. Comparing Fig. 5.6(a) and 5.6(b), we may say that the gas power output is less oscillatory, meaning that the thermal energy to be converted to the turbogenerator for electricity production is more steady than the reactor power despite large oscillations in the fission rate. Assuming that the mass flow rate of the gas is constant and taking the data interval between 50 seconds and 160 seconds after the initial transient to represent a quasi-steady situation, the gas power output may vary between 1.3 MW and 3.3 MW.

An estimate of the maximum particle temperature that may be achieved during the operation time is shown in Fig. 5.6(c). These data are important as the fuel temperature should be limited below 1600 °C for a safe operation (IAEA, 1997a). As shown in the figure, the particle temperature during the operation time is still far below the maximum permissible limit. The result shown in Fig. 5.6(c) does not belong to a single particle and is not at a specific location, but it is representing the maximum value occurring in the domain in a specific time. For example, at 50 seconds after the initial transient, the hottest particle can be found at the lower part of the bed close to the reflector wall (Fig. 5.8(b)).

Figs. 5.6(d), 5.6(e) and 5.6(f) present, respectively, the maximum concentration of the longest (half life = 55 seconds), the third longest (half life = 6.2 seconds) and the shortest (half life = 0.22 seconds) living delayed neutron precursors. Until the end of the simulation time, the concentration of the longest living neutron precursors is still increasing, while the third longest and the shortest living delayed precursors are already quasi-stationary. We may expect a slight increase in power as the concentration of the delayed neutron precursor is approximately proportional to the fission rate.

Fig. 5.7(a) shows the gas temperature at the bottom right of the cavity. The time-averaged value does not deviate much from the initial condition, implying the influence of the “cold” inlet gas. The temperature at the top center of the cavity is shown in Fig. 5.7(b), with a time-averaged value of 326.3 °C. By examining these data and the time-averaged temperature at the top left of the cavity (Detector 06, data are not presented) of 336.5 °C, the use of the mean gas temperature (Table 5.5) to calculate the gas power output can

be justified. Furthermore, by comparing to Fig. 5.6(c), Fig. 5.7(b) shows that in Case 1 the upper part of the cavity (outlet of the reactor) is not the hottest part of the reactor.

Figure 5.8 shows several fields at 50 seconds after the initial transient. Particles are accumulated mostly around the central axis (see Fig. 5.8(a)) and large bubbles have developed. The experimental results obtained by Van der Hagen *et al.* (1997) using a gamma tomography technique show a large particle accumulation close to the wall. The use of an axisymmetric model in the simulation causes this contrast, which can be eliminated by the use of a 3D model or a 2D cartesian coordinate system to break the symmetry (Pain *et al.*, 2001b).

The inhomogeneous “bed height” is slightly less than half of the cavity height. The effective multiplication factor of the corresponding homogeneous bed height (Fig. 5.3) lies in the peak of the curve and movements of the particles within the bed from low-importance zone to high-importance zone (and vice versa) keep the reactor critical at several occasions.

The gas temperature is presented in Fig. 5.8(b). The temperature at the lower part of the bed is low due to the incoming cold gas. As heat is transferred from the particles to the gas, the gas becomes hotter along its way to the outlet. Observe that the maximum gas temperature lies in the lower part of the cavity close to the wall.

Fig. 5.8(d) shows the concentration of the shortest living delayed neutron precursors. It gives an indication of the time-averaged heat source. As the half life of this precursor group is about 0.22 seconds, it is quite a good approximation of the instantaneous power distribution from fission. The maximum value can be found in the region near the graphite wall. Significant amounts of thermal neutrons can be found in this region, producing a large thermal fission rate.

The concentration of the longest living delayed neutron precursors with half time of 55 seconds (Fig. 5.8(c)) is distributed very similar to the concentration of particles. This similarity indicates that the particles, thanks to the good mixing, have been subject to the same heat source from fission over a time scale of 55 seconds.

Case 2: Uranium inventory = 120 kg, inlet gas velocity = 180 cm/s

In the second case, the superficial flow rate is increased to 180 cm/s (corresponding to 10.37 kg/s). Figure 5.9 shows the time-evolution of several variables, while Table 5.6 shows the time-averaged, minimum and maximum values of power, mean gas temperature and maximum particle temperature.

The power generated during the course of operation is small (Fig. 5.9(a)) and the mean temperature increases up to 233 °C only (Fig. 5.9(b)). Fig. 5.10(a) shows that the “bed height” is obviously higher than that of 120 cm/s, approximately three-quarters of the cavity height. Fuel particles are blown upward too strongly, reaching the overmoderated region (Fig. 5.3) and the system settles down in an equilibrium at low power. Fission in this situation is only maintained by the neutron source. Fig. 5.10(b) clearly presents that the temperatures at the bottom and at the top of the cavity are almost the same.

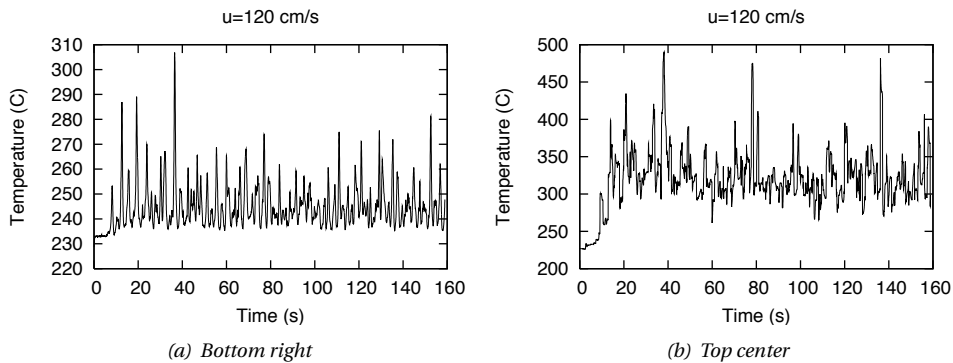


Figure 5.7. Gas temperature at bottom right (Detector 1) and top center (Detector 14) of the cavity for a uranium inventory of 120 kg and an input gas velocity of 120 cm/s.

Table 5.6. Time-averaged, minimum and maximum value of power and temperature, excluding the first 20 seconds after initial transient, for a uranium inventory of 120 kg and an input gas velocity of 180 cm/s.

	Power (MW)	Mean Gas Temp. (°C)	Max Particle Temp. (°C)
Time-averaged	71.2×10^{-6}	233.1	238.1
Min	18.6×10^{-6}	232.8	234.5
Max	265.6×10^{-6}	233.4	246.9

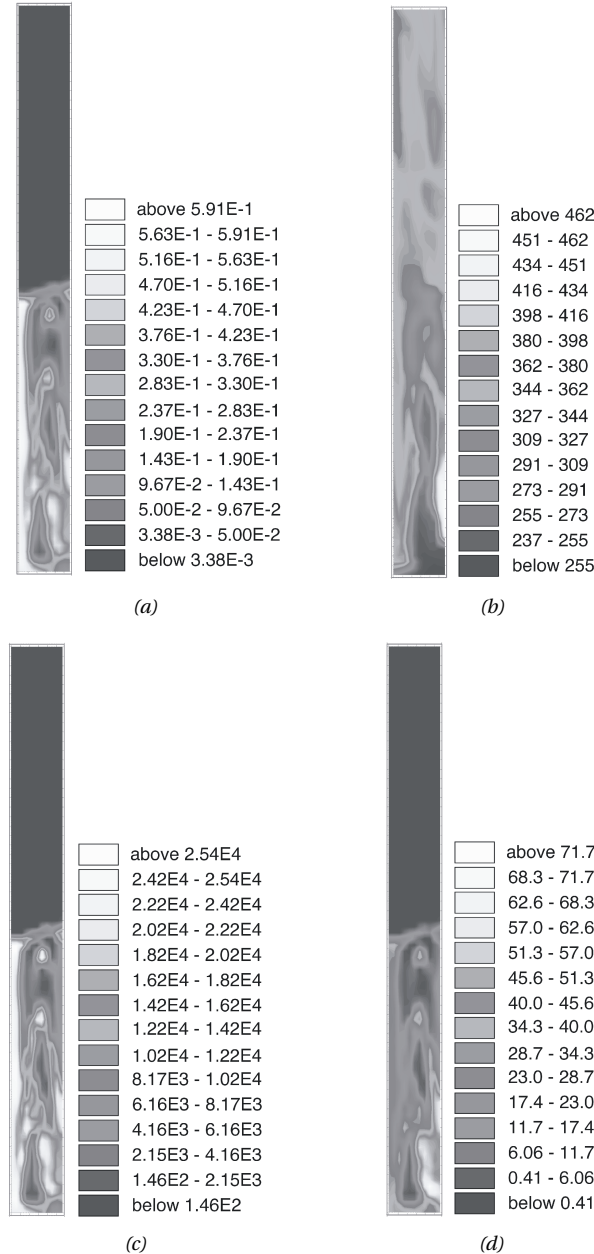


Figure 5.8. (a) Particle volume fraction, (b) gas temperature (°C), (c) the longest living delayed neutron precursor concentration (cm^{-3}), (d) the shortest living delayed neutron precursor concentration (cm^{-3}), for a uranium inventory of 120 kg and an input gas velocity of 120 cm/s at 50 seconds after the initial transient. The left boundary in these figures is the central axis.

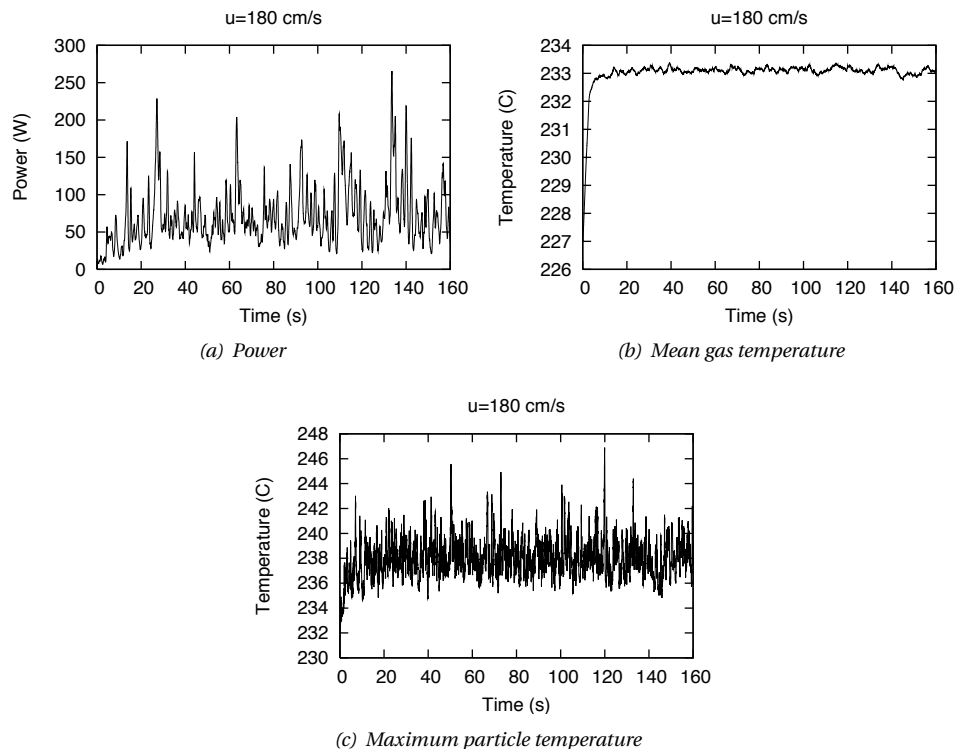


Figure 5.9. Power, mean gas temperature and maximum particle temperature for a uranium inventory of 120 kg and an input gas velocity of 180 cm/s.

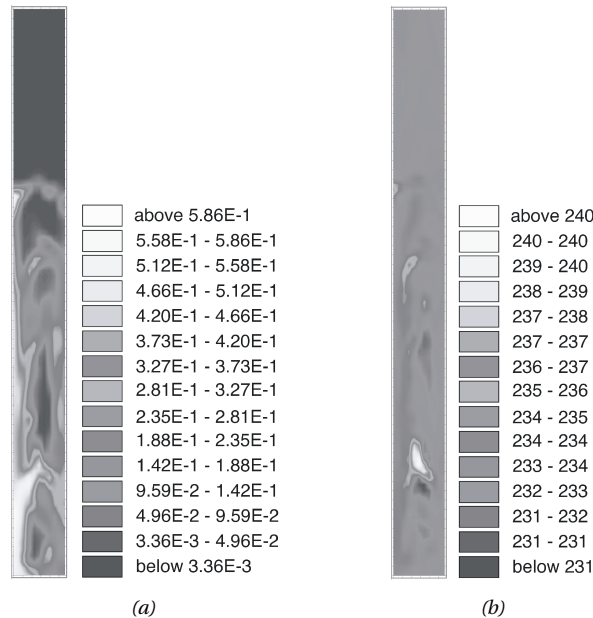


Figure 5.10. (a) Particle volume fraction and (b) gas temperature ($^{\circ}\text{C}$) for a uranium inventory of 120 kg and an input gas velocity of 180 cm/s at 50 seconds after the initial transient.

Case 3: Uranium inventory = 152 kg, inlet gas velocity = 120 cm/s

In Case 3, the inventory has been increased to 152 kg and an increase in both power and temperature can be expected as the reactivity of the homogenous bed is larger than that of 120 kg (see Fig. 5.5). Table 5.7 shows that the time-averaged generated power is now 22.6 MW with a maximum value of 120.1 MW, while the time-averaged gas power output is 16.1 MW (based on the time-averaged mean gas temperature of 672.5 °C). This result seems encouraging as the reactor is able to produce power at high temperature. However, Fig. 5.11(c) shows that the maximum particle temperature oscillates beyond the maximum permissible value. The lower graph in Fig. 5.11(c) represents the particle temperature at the top center of the cavity (Detector 14). Most of the time this temperature is lower than the maximum temperature (except at \approx 66 and 93 seconds), indicating that the hottest position is mostly not at the top of the cavity.

The distribution of particles at various time levels during the initial transient is presented in Fig. 5.12. After 0.5 second, a bubble of 60 cm in size has developed at the bottom of the bed. After 1 second, a second bubble appears and pushes the particles to move upward. After 1.5 seconds, the two bubbles coalesce. After 2.5 seconds the bubble elongates and some particles are moving downward. After 3 seconds the bubble breach occurs. In Section 3.4 an estimation of the influence of bubbles on reactivity has been performed. In the one-bubble model, a spherical bubble of size one-tenth of the bed height may cause change in reactivity of about 250 pcm. In the present situation, the size of the bubble is about half of the initial bed height, hence the magnitude of the reactivity change is quite considerable. This particular change in reactivity will in turn increase the fission rate. Examining Fig. 5.12(g), it is clear that the power increases to \approx 55 MW within 2.5 seconds, which corresponds to the situation just before bubble breach. Thereafter, a subsequent increase in temperature and a possible bubble breach decrease the fission rate.

Fig. 5.13 presents the distribution of particles from 50 seconds to 52.5 seconds after the initial transient. In terms of flow regime, the current situation can be regarded as turbulent (Kunii and Levenspiel, 1991) as the upper surface of the bed disappears and, instead of bubbles, a turbulent motion of solid clusters and voids of gas of various sizes and shapes is observable. Examining Fig. 5.13(g) (solid line), the fission rate between 50 seconds and 51 seconds after the initial transient starts to increase and then later decreases until 52.5 seconds. The temperature (Fig. 5.13(g), dashed line) increases starting at 50.5 seconds to 51.5 seconds and then decreases until 52.5 seconds. Here a strong connection between fission rate and temperature through a negative reactivity feedback is noticeable. On the other hand, although inhomogeneous distribution of particles does affect the magnitude of reactivity, a strong correlation between those two parameters cannot be perceived easily from Fig. 5.13.

Case 4: Uranium inventory = 152 kg, inlet gas velocity = 180 cm/s

The time-averaged power and temperature are smaller than in Case 3. However, unlike Case 2 where the time-averaged power is small, the power in Case 4 is of the order of megawatts. Table 5.8 shows that the time-averaged generated power is 19.4 MW while the mean gas temperature is 463.5 °C. An initial power spike (Fig. 5.14(a)) occurs within the first 6 seconds (3 seconds in Case 3), followed by an increase in temperature (Fig. 5.14(b)).

Table 5.7. Time-averaged, minimum and maximum value of power and temperature, excluding the first 20 seconds after initial transient, for a uranium inventory of 152 kg and an input gas velocity of 120 cm/s.

	Power (MW)	Mean Gas Temp. (°C)	Max Particle Temp. (°C)
Time-averaged	22.6	672.5	1803.3
Min	2.8	539.2	1038.2
Max	120.6	836.8	3305.8

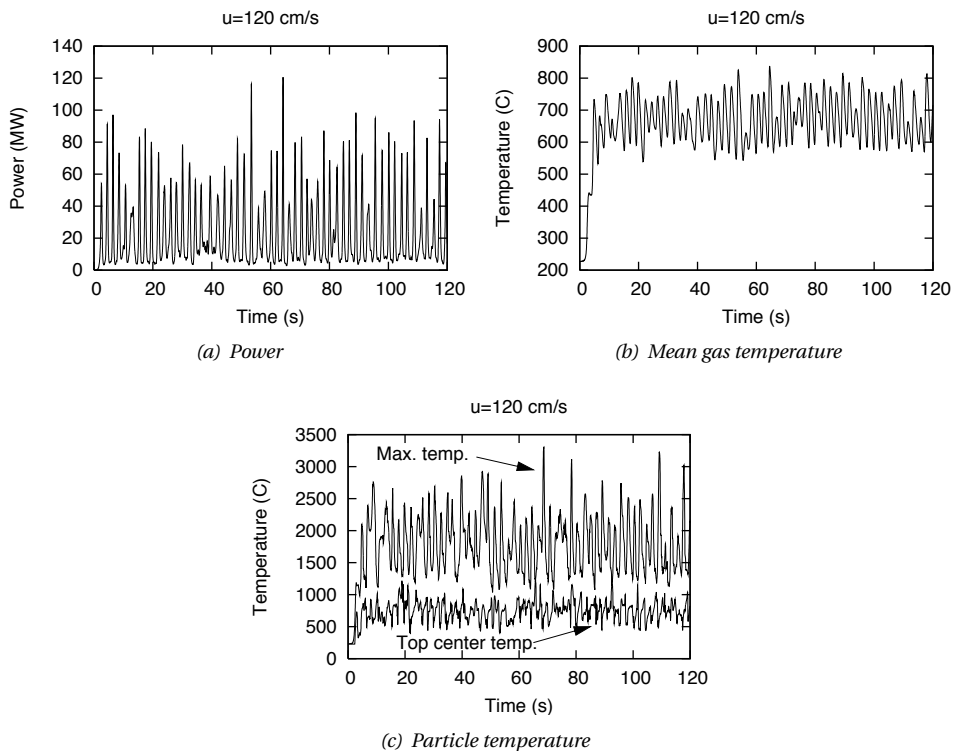


Figure 5.11. Power, mean gas temperature and particle temperature for uranium inventory of 152 kg and input gas velocity of 120 cm/s.

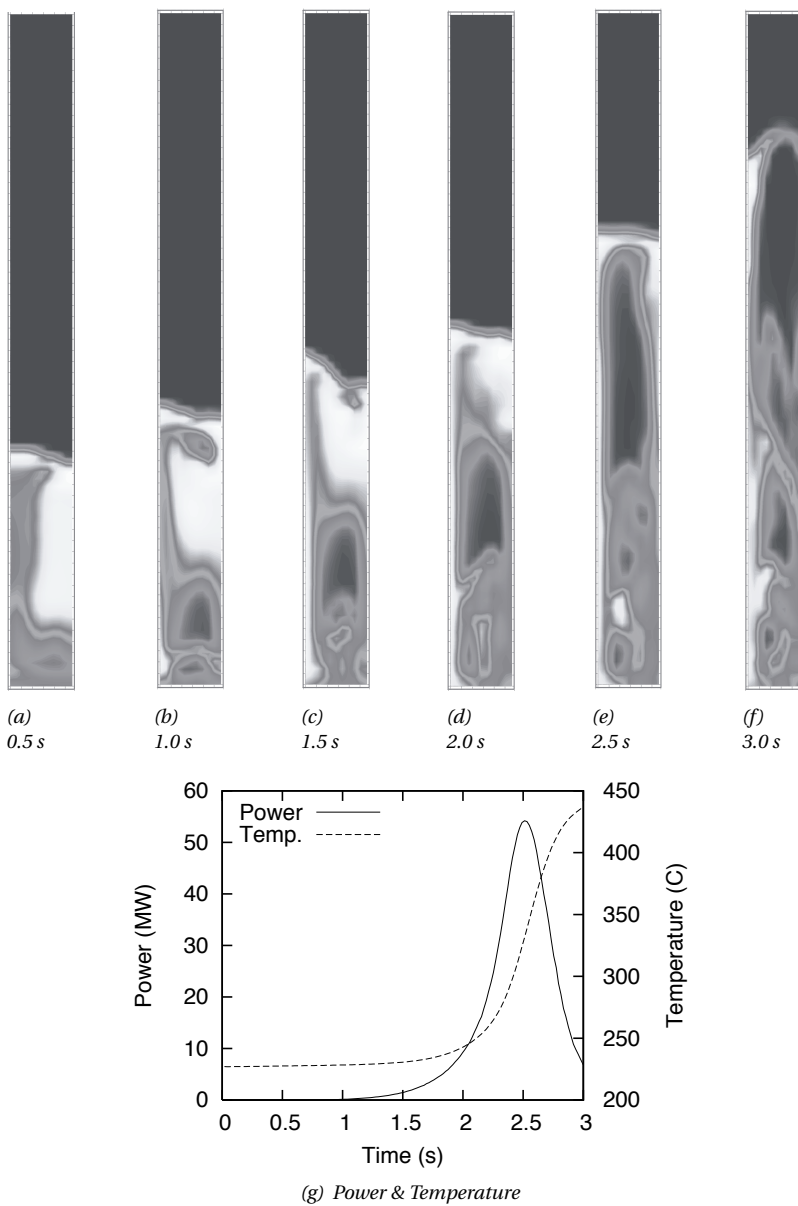


Figure 5.12. The particle volume fraction at various time level after start-up for a uranium inventory of 152 kg and an input gas velocity of 120 cm/s and their corresponding power and temperature.

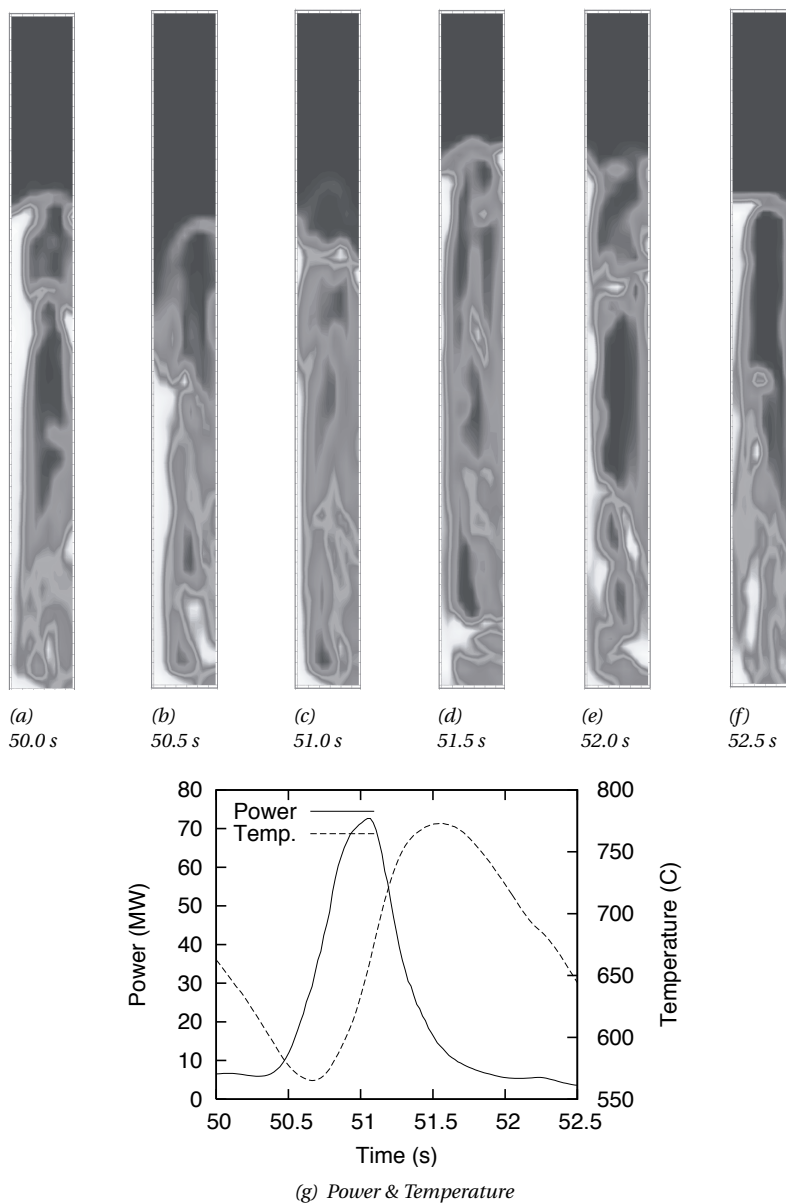


Figure 5.13. The particle volume fraction at various time level for a uranium inventory of 152 kg and an input gas velocity of 120 cm/s and their corresponding power and temperature.

However, this power surge causes the maximum fuel temperature, as shown in Fig. 5.14(c), to increase exceeding the permissible limit. This peak occurs during 3 seconds only and then the temperature becomes quasi-stationary afterwards below the permissible limit. The dashed line in Fig. 5.14(c) shows the particle temperature at the top center of the cavity. At several occasions, this line coincides with the solid line (the maximum particle temperature), indicating that the maximum temperature sometimes occurs around the top of the cavity.

Fig. 5.15 presents the distribution of the particle volume fraction up to 14 seconds after the initial transient along with the associated power and mean temperature. A large bubble is developed during the first 2 seconds, pushing the bed upward and then followed by a bubble breach in the bed surface after 3 seconds. Up to this time, the generated power is of the order of tens of watts. However at 5 and 6 seconds, some particles accumulate near the graphite wall, inducing more thermal fission, which cause the power to rise significantly, followed by a temperature increase. The flow rate is also so high that some particles are suspended in the top part of the cavity and produce local heat generation. Figs. 5.15(e) and 5.15(f) show an accumulation of particles in the top part of the cavity which corresponds to the second and the third power peak (see Fig. 5.15(g)).

Various fields at 50 seconds after the initial transient are shown in Fig. 5.16. Accumulation of particles can be found at the top of the cavity in this situation, leading to an increase in power. Fig. 5.16(b) presents the distribution of gas temperature, which is almost homogeneous at the top part of the cavity. In the bottom part of the bed, a large portion of cold gas can be found, while at the position near to the wall the temperature is quite high. Fig. 5.16(c) shows the distribution of the longest living delayed neutron precursors, which is quite similar to the distribution of particles, implying a good mixing of particles in the bed. The distribution of the shortest living delayed neutron precursors is shown in Fig. 5.16(d), which is also indicating an instantaneous heat generation. Here, we can see a large concentration at the top of the cavity, indicating heat is generated around the top reflector due to the suspended particles in this region.

Table 5.8. Time-averaged, minimum and maximum value of power and temperature, excluding the first 20 seconds after initial transient, for a uranium inventory of 152 kg and an input gas velocity of 180 cm/s.

	Power (MW)	Mean Gas Temp. (°C)	Max Particle Temp. (°C)
Time-averaged	19.4	463.5	959.3
Min	6.1	386.7	653.1
Max	57.7	576.1	1383.5

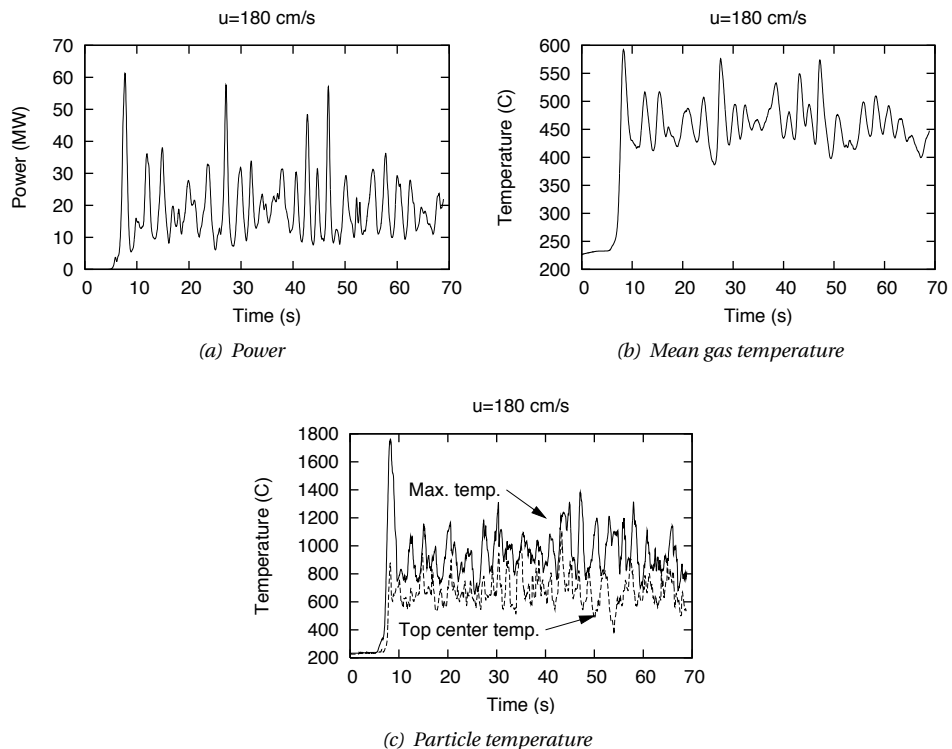


Figure 5.14. Power, mean gas temperature and particle temperature for a uranium inventory of 152 kg and an input gas velocity of 180 cm/s.

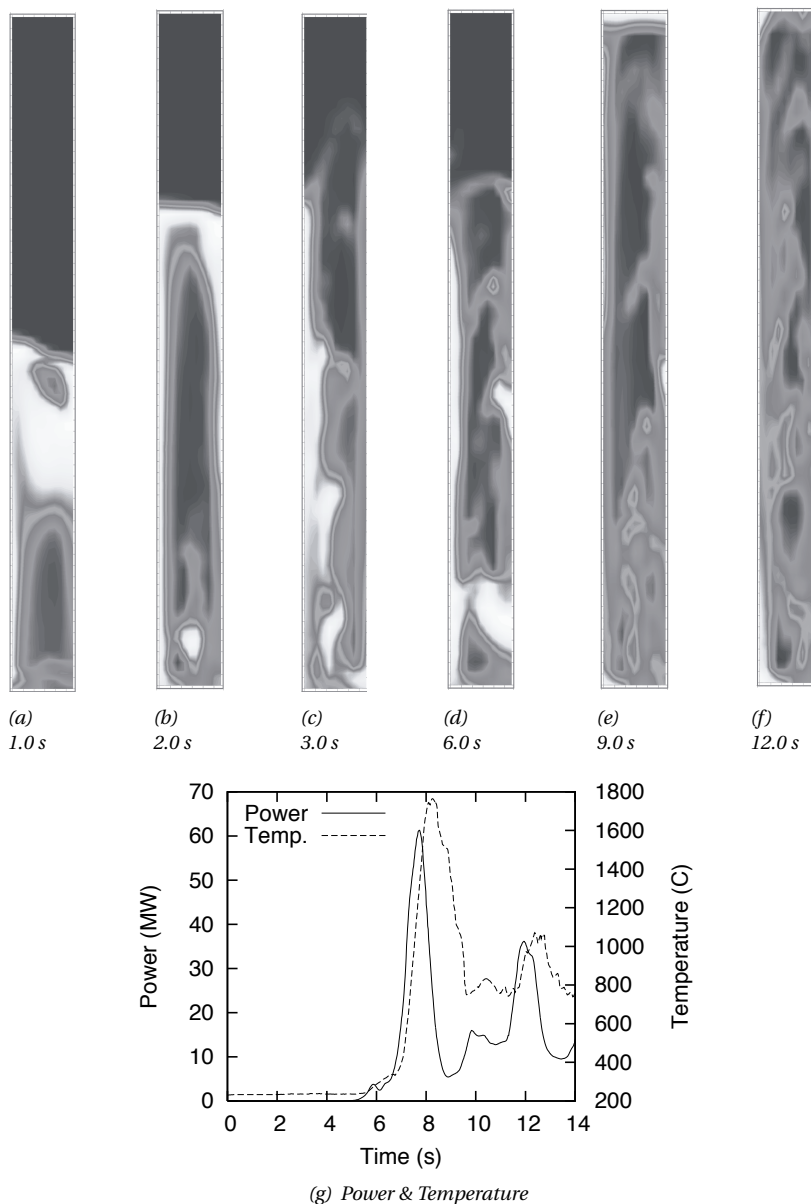


Figure 5.15. The particle volume fraction at various time level after start-up for a uranium inventory of 152 kg and an input gas velocity of 180 cm/s and their corresponding power and temperature.

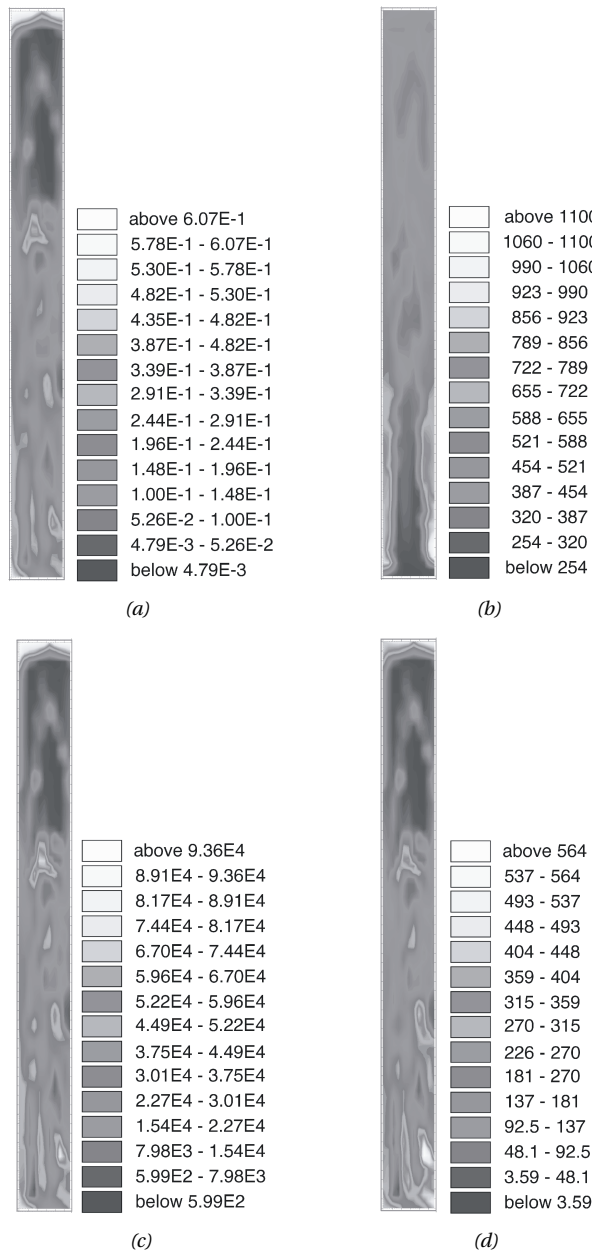


Figure 5.16. (a) Particle volume fraction, (b) gas temperature (°C), (c) the longest living delayed neutron precursor concentration (cm^{-3}), (d) the shortest living delayed neutron precursor concentration (cm^{-3}) for a uranium inventory of 152 kg and an input gas velocity of 180 cm/s at 50 seconds after the initial transient.

5.7. Comparison with the point dynamic model

In Chapter 4 the influence of particle distribution has been included in the point dynamics model as a noise term. For a comparison, we will refer to the results obtained in (Lathouwers *et al.*, 2003). The point dynamics model used here is the same as in Chapter 4 but the parameters have been adjusted to the corresponding geometry, which is quite similar to the geometry used in the current chapter. The reactor is loaded with 170 kg of uranium and is subject to 11 kg/s in mass flow rate. Such a configuration is similar to Case 4 (152 kg of uranium, 10.37 kg/s in mass flow rate) in the current chapter. Fig. 5.17 shows the total power and fuel temperature obtained by using the point dynamics code, reproduced from (Lathouwers *et al.*, 2003).

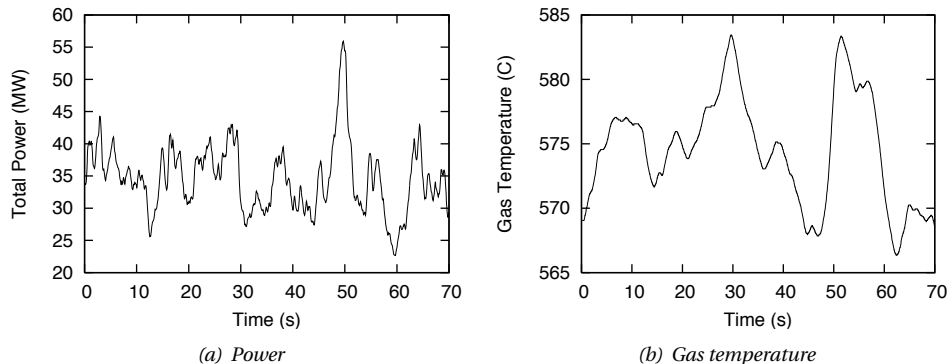


Figure 5.17. Total power and fuel temperature as a function of time calculated using the point dynamics code. Uranium inventory is 170 kg and mass flow rate is 11 kg/s. The graphs are reproduced from (Lathouwers *et al.*, 2003).

The total power and the gas temperature obtained by using the point dynamics have a great resemblance to that obtained with a fully coupled multidimensional calculation, in a sense that the power is highly fluctuating while the response of gas and fuel temperature is relatively steady. Table 5.9 shows the averaged power and gas temperature obtained from the point and multidimensional dynamics models. The data for the latter model are obtained from an extrapolation of the results of Case 2 and Case 4. Here, the power and the gas temperature calculated by using the point dynamics model differs only by less than 10% from the multidimensional model.

As the point dynamics code runs much faster than the multidimensional dynamics code, the point dynamics code –in combination with a detailed 3D Monte Carlo model for preparing the necessary parameters– can be used for a quick and good estimation of power level in FLUBER. On the other hand, the point dynamics code handles the temperature as an average value only, hence it cannot predict the spatially-dependent maximum temperature which is important from the safety point-of-view. For such purpose, the use of multidimensional dynamics code is necessary.

Table 5.9. Time-averaged power and gas temperature for a uranium inventory of 170 kg and a mass flow rate of 11 kg/s calculated by the point dynamics and multidimensional dynamics model. For the multidimensional model, the data are obtained from an extrapolation of the results of Case 2 and Case 4.

	Point dynamics	Multidimensional dynamics
Power (MW)	32.3	30.3
Gas temperature (°C)	572.8	593.1

5.8. Summary

Simulations using time- and space-dependent dynamics with a coupled neutronics and multiphase flow have been performed. The following findings are reported:

1. Variation in fuel inventory causes a change in the averaged bed height that can be achieved, which in turns affects the fission power and the temperature generated.
2. The fission power fluctuations are large, but the gas temperature is relatively steady after the initial transient. Moreover, the temperature tends to be uniform due to rapid mixing of particles.
3. The use of the P_1 (diffusion) model may cause inaccurate results in the neutronics as large bubbles (with small density) are continuously present in the bed. The remedy for such a situation is by using a higher order of expansion for the angular flux.
4. Although the temperature is relatively steady, the initial temperature rise in some cases is quite high due to the use of a step input of the coolant flow rate. Thorough investigations should be performed especially for the startup of the reactor. One example is by introducing a ramp input instead of a step input. In such a case, a high peak of temperature after startup may be prevented.
5. The use of the 2D axisymmetric model gives a discrepancy from experimental results in terms of particle distribution in the bed. This may be resolved by using a 3D model where the particles may move across the center axis.
6. The results of the point dynamics model have a great resemblance to that obtained by using the multidimensional model. The average power level of the reactor can be estimated from the point dynamics model with a good degree of accuracy. The use of both models is thus recommended.

CHAPTER 6

Passive removal of post-shutdown decay heat*

6.1. Introduction

When the flow of helium through the core is reduced either intentionally or by pump failure, the bed of fuel particles forms a packed state and the fission power production stops. However, decay heat is still being produced and has to be removed safely. In the worst-case scenario where no pump is available, heat has to be removed by passive means. As the initial total output power is relatively high, the decay heat after reactor shutdown is significant.

Figure 6.1 shows the percentage of decay heat of the total power up to 1 hour after shutdown. In the case of operation at full bed expansion, for instance, the maximum total power can reach 120 MW with a maximum fuel temperature of 1165 K and after shutting down the reactor (by not introducing helium into the reactor), the bed becomes packed at about 2.5 m^3 of core volume. Initially the decay power is about 7% of the total power, resulting in a decay power density of around 3.4 MW/m^3 .

A hypothetical shutdown of the reactor has been simulated using the point-dynamics code (DYNFLUB) described in Chapter 4. The reactor is assumed to be in steady operation at about 80 MW and the coolant flow rate is then suddenly stopped. The evolution of fuel

*This chapter is adapted from the following papers:

Agung, A., Lathouwers, D., van der Hagen, T.H.J.J., van Dam, H., Pain, C.C., de Oliveira, C.R.E., Goddard, A.J.H., Eaton, M.D., Gomes, J.L.M.A., and Miles, B. (2004). Passive Decay Heat Removal in a Fluidized Bed Nuclear Reactor. *Proc. PHYSOR-2004*, in CD-ROM paper 97543, Chicago, USA.

Agung, A., Lathouwers, D., van der Hagen, T.H.J.J., and van Dam, H. (2005). On The Use of P_N and S_N Methods for Radiative Heat Transfer in a Fluidized Bed Nuclear Reactor: A Case Study for Passive Decay Heat Removal. (in Bahasa Indonesia). *Proc. The 11th National Seminar on Technology and Safety of Nuclear Power Plants and Nuclear Facilities*, pp. 705–720, Malang, Indonesia.

temperature over time is shown in Figure 6.2. After the coolant flow has stopped, the fuel heats up due to the decay heat. The increase in fuel temperature continues and in the end of the transient time, the fuel temperature is already beyond the recommended maximum permissible value. Although this code is adequate for other purposes, the multimode heat transfer (i.e. conduction, convection and radiation) occurred in the reactor is not included. Hence another computational tool is required.

In this chapter a two-dimensional multimode heat transfer model is developed and then using this model it is investigated what the maximum power level can be without compromising the safety of the reactor. For coated fuel particles, IAEA recommends a value of 1873 K as a conservative limit on peak fuel temperature under accident conditions (IAEA, 1997a). The discussion starts with the description of the governing equations in Section 6.2. In this section, the mathematical models are described. Section 6.3 describes the thermal and radiative properties of the material involved in the reactor. The numerical treatment to solve the governing equations is outlined in Section 6.4. The results are then discussed in Section 6.5 and finally Section 6.6 summarizes this chapter and gives some recommendations.

6.2. The mathematical model

During operation, the particles are fluidized and are constantly in motion. The governing equations for the flow model are written for both gas phase and solid phase. However, when the fluidizing gas is stopped, the particles collapse and form a packed bed. Although there is no fission, decay heat is still being generated in the particles. In the packed bed, the generated decay heat is transferred to the gas and the surrounding reflector through conduction, convection and radiation. The gas near the bed surface is heated and due to buoyancy it moves upward and transfers the energy to the reflector. The system is modeled as being closed, hence gas is contained in the system. Moreover, it is assumed that the system has no forced convection through it. In the reflector, no heat source is present and the thermal energy is transferred to the atmosphere.

The governing equations for fluid flow are based on the Reynolds-Averaged Navier-Stokes (RANS) equations which are time-averaged equations of motion. The two-fluid model is applied but as the motion of particles is neglected, the continuity and momentum equations are written only for the fluid phase.

6.2.1. Continuity equation

The continuity equation for the gas phase is

$$\frac{\partial}{\partial t}(\alpha_g \rho_g) + \nabla \cdot (\alpha_g \rho_g \mathbf{u}) = 0 \quad (6.1)$$

where α is the volume fraction, ρ is the density, \mathbf{u} is the averaged velocity vector and the index g represents the gas phase.

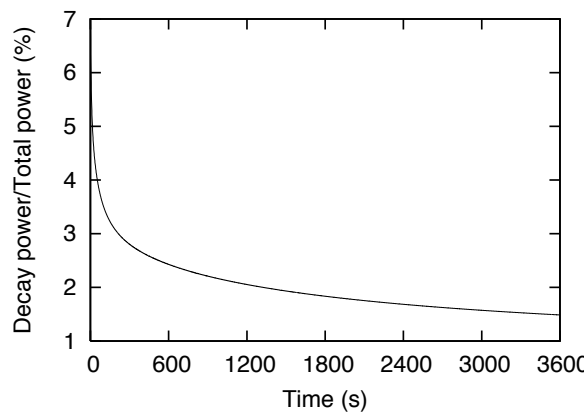


Figure 6.1. Percentage of decay power to the initial total power after shutdown of the reactor as a function of time.

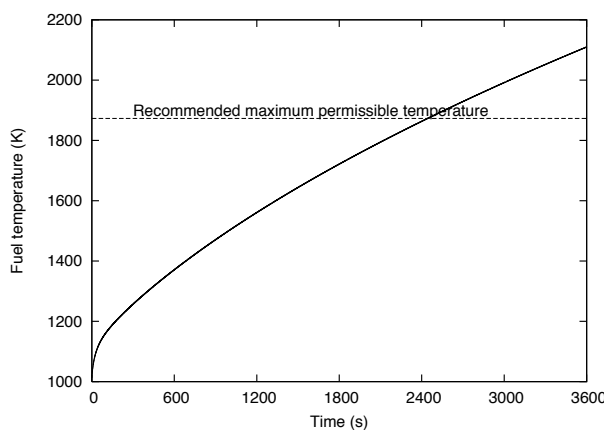


Figure 6.2. Fuel temperature during a loss of mass flow rate from 33 kg/s to 0.01 kg/s. This simulation was performed using the point dynamics model, that does not take into account the multimode heat transfer (i.e. conduction, convection and radiation) in the bed, cavity and reflector.

6.2.2. Momentum equation

The momentum equation for the gas phase can be written as

$$\frac{\partial(\alpha_g \rho_g \mathbf{u})}{\partial t} + \nabla \cdot (\alpha_g \rho_g \mathbf{u} \mathbf{u}) = \alpha_g \nabla \cdot \left(-p \mathbf{I} + \mathbf{T} - \rho_g \overline{\mathbf{u}' \mathbf{u}'} \right) + \alpha_g \rho_g g - \frac{\alpha_p \rho_p}{\tau_{12}} \mathbf{u} \quad (6.2)$$

where p is the static pressure, \mathbf{I} is the unit tensor, \mathbf{T} is the stress tensor, the index p represents the solid phase and g is the gravitational acceleration, τ_{12} is the gas-particle interaction time scale.

The left hand side of this equation represents the change in momentum of fluid due to the unsteadiness in the average flow and the convection by the average flow. This change is balanced by the isotropic stress due to the pressure field, the viscous stresses, the stress due to the fluctuating velocity field, the gravitational force and the friction drag force caused by the particles.

The interaction time, τ_{12} , is calculated from the classical Ergun relation, and can be written as (Lathouwers and Bellan, 2001)

$$\frac{1}{\tau_{12}} = \frac{\rho_g}{\rho_f} \left[150 \frac{\alpha_p}{\text{Re}_p} + 1.75 \right] \frac{u}{d_p} \quad (6.3)$$

where d_p is the diameter of the particle. The particle Reynolds number, Re_p , is calculated based on the velocity of the gas,

$$\text{Re}_p = \alpha_g \frac{\rho_g d_p u}{\mu} \quad (6.4)$$

For Newtonian fluids, the viscous stress tensor, \mathbf{T} , is written as

$$\mathbf{T} = 2\mu \left[\mathbf{S} - \frac{1}{3} (\nabla \cdot \mathbf{u}) \mathbf{I} \right] \quad (6.5)$$

where μ is the dynamic viscosity and the strain-rate tensor, \mathbf{S} , is defined by

$$\mathbf{S} = \frac{1}{2} (\nabla \mathbf{u} + (\nabla \mathbf{u})^T) \quad (6.6)$$

The quantity $-\rho_g \overline{\mathbf{u}' \mathbf{u}'}$ is known as the Reynolds stress tensor, obtained as a direct consequence of the nonlinearity of the convection terms. The presence of Reynolds stress tensor unfortunately produces more unknowns than the number of the available equations. This means that the averaged equations are not closed and require additional equations.

6.2.3. Energy equations

The energy equation is written for both the gas and solid phase. For the gas phase the energy equation is

$$\alpha_g \rho_g C_{p,g} \left[\frac{\partial T_g}{\partial t} + (\mathbf{u} \cdot \nabla) T_g \right] = \nabla \cdot \alpha_g \left(\lambda_g \nabla T_g - \rho_g C_{p,g} \overline{\mathbf{u}' T'_g} \right) + h_{pg} a_{pg} (T_p - T_g) \quad (6.7)$$

where C_p is the heat capacity, T is the temperature, λ is the thermal conductivity, h_{pg} is the heat transfer coefficient between gas and solid phase and a_{pg} is the interfacial area per unit volume of the solid particles.

The first term in the right hand side of the Eq. (6.7) represents heat flux due to conduction. The second term, $-\rho_g C_{p,g} \overline{\mathbf{u}' T'_g}$, is again obtained from the nonlinearity of the convection terms. This quantity is known as the turbulent heat flux. The last term represents transfer of energy between particles and gas.

The heat transfer coefficient, h_{pg} is obtained from the following Ranz correlation

$$\text{Nu} = 2 + 0.66 \text{Re}_p^{1/2} \text{Pr}_g^{1/3} \quad (6.8)$$

where the Prandtl number for helium is taken as 0.72 and the particle Reynolds number is given by Eq. (6.4).

The gas is assumed compressible and is modeled by the ideal gas equation of state. Gas density is calculated by

$$\rho_g = \frac{p_g W_g}{R_u T_g} \quad (6.9)$$

where W_g is the molecular weight of the gas and R_u is the universal gas constant.

The particles are stationary and thus the convective term in the energy equation for the particles is discarded. However, additional terms are included, i.e. (i) the heat flux due to radiative transfer and (ii) the source term resulted from the decay heat. The energy equation for the particles is

$$\alpha_p \rho_p C_{p,p} \frac{\partial T_p}{\partial t} = \nabla \cdot (\alpha_p \lambda_p \nabla T_p) - h_{pg} a_{pg} (T_p - T_g) - \nabla \cdot \mathbf{q}_{rad} + P_d''' \quad (6.10)$$

where P_d''' is the volumetric decay heat source and \mathbf{q}_{rad} is the heat flux from radiation.

The reflector is composed of only one phase, i.e. graphite, and it is assumed that no heat source present in the reflector. The energy equation for the reflector is thus simple as

$$\rho_r C_{p,r} \frac{\partial T_r}{\partial t} = \nabla \cdot (\lambda_r \nabla T_r) \quad (6.11)$$

where the index r represents the reflector part.

6.2.4. Turbulent kinetic energy and dissipation-rate equations

The RANS equations describe an open set of equations due to two additional terms in Eqs. (6.2) and (6.7), i.e. the Reynolds stress tensor, $\rho_g \overline{\mathbf{u}' \mathbf{u}'}$, and the turbulent-heat-flux vector, $\rho_g C_{p,g} \overline{\mathbf{u}' T'_g}$, which is a result of the nonlinearity of the convection terms. Hence, additional equations are required to model the new unknowns. Many models have been proposed, depending on the complexity of the problem, but they can be categorized into two groups, i.e. (i) first order models and (ii) second order models. The first order models are based on the analogy between laminar and turbulent flow, which is referred to as the Boussinesq hypothesis. Members of this group are the zero-equation models, one-equation models and two-equation models (see e.g. (Wilcox, 1993)). The second order

models use the governing equations for the second order moments (i.e. Reynolds stresses and turbulent fluxes) instead of the Boussinesq hypothesis. This group consists of the Algebraic Stress model and Reynolds Stress Model (Budi, 2003).

In this research, we are going to use the $k - \epsilon$ model which falls into the group of two-equation models. The $k - \epsilon$ model is chosen because it performs quite well in confined flows (Versteeg and Malalasekera, 1995) which is applicable to our system. In this model, two PDEs are developed, i.e. for the turbulent kinetic energy (k) and for the turbulent dissipation rate (ϵ). The kinetic energy of the turbulent fluctuations can be expressed as

$$k = \frac{1}{2} \overline{\mathbf{u}' \cdot \mathbf{u}'} \quad (6.12)$$

The transport equation for the turbulent kinetic energy is

$$\frac{\partial}{\partial t} (\alpha_g \rho_g k) + \nabla \cdot (\alpha_g \rho_g \mathbf{u} k) = \alpha_g P_k + G_k + \nabla \cdot \alpha_g \left[\left(\frac{\mu_t}{\sigma_k} + \mu \right) \nabla k \right] - \alpha_g \rho_g \epsilon \quad (6.13)$$

where $P_k = -\rho_g \overline{\mathbf{u}' \mathbf{u}'} : \nabla \overline{\mathbf{u}}$ and $G_k = -\rho_g \beta \mathbf{g} \cdot \overline{\mathbf{u}' T_g'}$.

The two terms in the left hand side are the unsteady and convection term, while in the right hand side are the production rate of k due to gradients of the mean velocity, the buoyancy generation rate of k , the rate of diffusion and the dissipation rate of k converted into internal thermal energy.

The coefficient of thermal expansion, β , is defined as

$$\beta = -\frac{1}{\rho_g} \left(\frac{\partial \rho_g}{\partial T_g} \right)_p \quad (6.14)$$

and the Reynolds stress tensor and the turbulent heat flux are defined as

$$-\rho_g \overline{\mathbf{u}' \mathbf{u}'} = 2\mu_t \mathbf{S} - \frac{2}{3} [\mu_t (\nabla \cdot \mathbf{u}) - \rho_g k] \mathbf{I} \quad (6.15)$$

$$-\rho_g \overline{\mathbf{u}' T_g'} = \frac{\mu_t}{\sigma_k} \nabla T_g \quad (6.16)$$

where σ_k is the turbulent Prandtl number for the turbulent kinetic energy and μ_t is the turbulent viscosity, which is modeled as

$$\mu_t = \rho C_\mu \frac{k^2}{\epsilon} \quad (6.17)$$

where C_μ is a closure constant.

The transport equation for the dissipation rate is

$$\frac{\partial}{\partial t} (\alpha_g \rho_g \epsilon) + \nabla \cdot (\alpha_g \rho_g \mathbf{u} \epsilon) = C_{\epsilon 1} (\alpha_g P_k + C_{\epsilon 3} G_k) \frac{\epsilon}{k} + \nabla \cdot \alpha_g \left[\left(\frac{\mu_t}{\sigma_\epsilon} + \mu \right) \nabla \epsilon \right] - C_{\epsilon 2} \alpha_g \rho_g \frac{\epsilon^2}{k} \quad (6.18)$$

where σ_ϵ are the turbulent Prandtl number for the dissipation rate of k . $C_{\epsilon 1}$, $C_{\epsilon 2}$ and $C_{\epsilon 3}$ are the closure constants. In the standard $k - \epsilon$ model, these constants have the following value (Versteeg and Malalasekera, 1995):

$$\sigma_k = 1.00; \quad \sigma_\epsilon = 1.30; \quad C_{\epsilon 1} = 1.44; \quad C_{\epsilon 2} = 1.92; \quad C_{\epsilon 3} = 1.0; \quad C_\mu = 0.09$$

6.2.5. Radiative transfer equation

The radiative transfer theory describes the interaction of radiation with matter that absorbs, emits and scatters radiant energy, i.e. participating media. In this theory the wave nature of radiation is ignored and instead it is described in terms of photons.

Several authors, e.g. Modest (2003a), Siegel and Howell (2001), and Özışık (1985), have discussed the derivation of the RTE in participating media. The equation is a mathematical statement of the conservation principle applied to a monochromatic pencil (bundle) of radiation. The equation of transfer can be written as

$$\frac{1}{c} \frac{\partial I(\mathbf{r}, \boldsymbol{\Omega}, t)}{\partial t} + \boldsymbol{\Omega} \cdot \nabla I = \Sigma_a I_b(\mathbf{r}, t) - \Sigma_a I(\mathbf{r}, \boldsymbol{\Omega}, t) - \Sigma_s I(\mathbf{r}, \boldsymbol{\Omega}, t) + \frac{\Sigma_s}{4\pi} \int_{4\pi} I(\boldsymbol{\Omega}) \Xi(\boldsymbol{\Omega}' \cdot \boldsymbol{\Omega}) d\Omega' \quad (6.19)$$

where I is the intensity of radiation, defined as the radiation energy passing through an area per unit time, per unit of the projected area and per unit solid angle, I_b is the blackbody radiation intensity, Σ_s is the scattering coefficient, Σ_a is the absorption coefficient and $\boldsymbol{\Omega}$ is the direction vector. The function $\Xi(\boldsymbol{\Omega}' \cdot \boldsymbol{\Omega})$ is called the scattering phase function, describing the probability that a ray from direction $\boldsymbol{\Omega}'$ will be scattered into direction $\boldsymbol{\Omega}$.

The first term on the RHS represents the gain by emission, the second and the third term are the attenuation by absorption and out-scattering, respectively, and the last term represents the gain by in-scattering.

In most applications, the time dependence is small compared to other terms in the equation due to the large magnitude of the speed of propagation, c . Hence Eq. (6.19) can be simplified and by introducing the extinction coefficient, $\Sigma_t = \Sigma_a + \Sigma_s$, one can write

$$\nabla \cdot \boldsymbol{\Omega} I + \Sigma_t I = \Sigma_a I_b + \frac{\Sigma_s}{4\pi} \int_{4\pi} I(\boldsymbol{\Omega}) \Xi(\boldsymbol{\Omega}' \cdot \boldsymbol{\Omega}) d\Omega' \quad (6.20)$$

The blackbody radiation intensity, I_b , can be calculated from

$$I_b = \frac{E_b}{\pi} = \frac{\sigma T^4}{\pi} \quad (6.21)$$

where E_b is the blackbody emissive power and σ is the Stefan-Boltzmann constant ($5.6696 \times 10^{-8} \text{ W m}^{-2} \text{ K}^{-4}$).

If we integrate the radiation intensity over all directions, we obtain the total incident radiation:

$$G(\mathbf{r}) = \int_{4\pi} I(\boldsymbol{\Omega}) d\Omega \quad (6.22)$$

To calculate how much energy is transferred to a physical surface with normal vector $\hat{\mathbf{n}}$ by means of radiation, we are interested in the radiative heat flux which can be written as

$$\mathbf{q} \cdot \hat{\mathbf{n}} = \int_{4\pi} I(\boldsymbol{\Omega}) \hat{\mathbf{n}} \cdot \boldsymbol{\Omega} d\Omega \quad (6.23)$$

In the meantime, for the energy balance of the solid phase in Eq. (6.10), a heat source in terms of the radiative heat flux is required. We can obtain this by integrating the radiative transfer equation (Eq. (6.20)) over all solid angles and the divergence can then be written as

$$\nabla \cdot \mathbf{q} = \Sigma_a \left(4\pi I_b - \int_{4\pi} I(\Omega) d\Omega \right) = \Sigma_a (4\sigma T^4 - G) \quad (6.24)$$

The phase function can be approximated in terms of Legendre polynomials. For spherical particles and independent scattering, the phase function can be written as (Kaviany, 1991)

$$\Xi(\Omega' \cdot \Omega) = \sum_{l=0}^N (2l+1) A_l P_l(\Omega' \cdot \Omega) \quad (6.25)$$

For an isotropic scattering, which is applied for our calculations, the phase function is

$$\Xi(\Omega' \cdot \Omega) = 1 \quad (6.26)$$

6.2.6. Decay heat model

Contribution of the decay power to the total power can be expressed in the form of a set of differential equations as already discussed in Chapter 4. Rewriting Eq. (4.25) here, the change rate of decay power is given as

$$\frac{dP_{d,n}}{dt} = \frac{\gamma_n}{Q_f} P_{pr} - \lambda_n P_{d,n} \quad (6.27)$$

where $P_{d,n}$ is the decay heat power of group n , Q_f is the prompt recoverable energy per fission, γ_n is the decay heat yield (given in MeV/fission/s) and λ_n is the decay heat time constant, respectively. In the present chapter, we use the original data of 23 groups from DIN-25485 (1990), instead of the compressed 15 groups structure as in Chapter 4.

The total power is obviously the sum of prompt fission power and decay power (see Eq. (4.28)),

$$P_{tot} = P_{pr} + \sum_{n=1}^{N_d} P_{d,n} \quad (6.28)$$

where N_d is number of decay heat groups.

The reactor is assumed to have been in operation long enough before shutdown so that the decay power has achieved steady state and consequently Eq. (6.27) can be expressed as

$$P_{d,n} = \frac{\gamma_n}{Q_f \lambda_n} P_{pr} \quad (6.29)$$

After shutdown the fission power can be assumed zero due to large shutdown margin, thus the post-shutdown decay power, P_d , in terms of total power can then be expressed in the following form:

$$P_d = \frac{P_{tot}}{Q_f + \sum_{n=1}^{N_d} \frac{\gamma_n}{\lambda_n}} \sum_{n=1}^{N_d} \frac{\gamma_n}{\lambda_n} e^{-\lambda_n t} = P_{d0} \sum_{n=1}^{N_d} \frac{\gamma_n}{\lambda_n} e^{-\lambda_n t} \quad (6.30)$$

where P_{d0} is the decay power at the initial shutdown time.

The volumetric decay heat source in the energy equation (Eq. (6.10)) is then given as

$$P_d''' = P_d / V_{core} \quad (6.31)$$

where V_{core} is the core volume. Note that the decay heat source is generated homogeneously in the packed bed as a result of the homogeneous burn-up of the fuel during the fluidization process owing to the excellent mixing associated with fluidization.

6.2.7. Boundary conditions

At the outer wall of the graphite reflector, the boundary condition is obtained by a combination of the convective heat flux and radiative transfer,

$$\mathbf{q}_{out} = \mathbf{q}_{conv} + \mathbf{q}_{rad} = h_w(T_w - T_\infty) + \sigma\epsilon_w(T_w^4 - T_\infty^4) \quad (6.32)$$

where T_w and ϵ_w are the temperature and the emissivity of the outer wall and T_∞ is the temperature of the environment. The convective heat transfer coefficient, h_w , is obtained from the following Nusselt number (Janssen and Warmoeskerken, 1997),

$$Nu_w = \begin{cases} 0.13 Ra^{1/3}, & \text{for the side of cylinder} \\ 0.16 Ra^{1/4}, & \text{for the top of cylinder} \end{cases} \quad (6.33)$$

Here, the Rayleigh number, Ra, defined as

$$Ra = g\beta_{air}(T_w - T_\infty)L^{*3} \Pr_{air}/\nu_{air}^2 \quad (6.34)$$

where β_{air} is the coefficient of thermal expansion of air, ν_{air} is the kinematic viscosity of air and L^* is the characteristic length, described as

$$L^* = \begin{cases} H_r; & \text{for the side of cylinder} \\ 2R_r; & \text{for the top of cylinder} \end{cases} \quad (6.35)$$

where H_r is the total height of the side reflector and R_r is the radius of the top reflector.

At the inner wall of the reflector, the boundary condition is obtained from the presence of a multi-layered structure of the near wall turbulent boundary layer. Adjacent to the wall there is an extremely thin viscous sub-layer followed by the buffer layer and the turbulent core. Based on this phenomenon the boundary condition is given in terms of 'wall functions', and the wall drag force is described as

$$\tau_w = \rho_g C_\mu^{1/4} \kappa k^{1/2} \frac{U}{\ln(Ey^+)} \quad (6.36)$$

where C_μ is a turbulent constant, κ is von Karman's constant ($\simeq 0.41$), k is the turbulent kinetic energy, E is an integration constant that depends on roughness of the wall and y^+ is the dimensionless distance to the wall of the reflector, given by

$$y^+ = \rho_g C_\mu^{1/4} k^{1/2} \frac{y_p}{\mu} \quad (6.37)$$

where y_p is the distance to the wall of the reflector.

The heat transfer coefficient at the inner wall of the reflector can also be expressed in terms of the wall function as

$$\lambda_w = \alpha_g y_p \frac{(\tau_w / \rho_g)^{1/2}}{\gamma^+ \mu \text{Pr}_t} \rho_g C_{p,g} \mu_t \quad (6.38)$$

where Pr_t is the turbulent Prandtl number (≈ 0.9) and μ_t is the turbulent viscosity.

At the inner wall of the reflector, the boundary condition in terms of radiative transfer is described as follows. For a surface that emits and reflects diffusely, the intensity is independent of direction. Hence the intensity at a point \mathbf{r}_w on the surface can be written as (Modest, 2003a):

$$\begin{aligned} I(\mathbf{r}_w, \Omega) &= \text{emitted component} + \text{diffusely reflected component} \\ &= \epsilon(\mathbf{r}_w) I_b(\mathbf{r}_w) + \frac{\rho(\mathbf{r}_w)}{\pi} \int_{\hat{\mathbf{n}} \cdot \Omega' < 0} I(\mathbf{r}_w, \Omega') |\hat{\mathbf{n}} \cdot \Omega'| d\Omega' \end{aligned} \quad (6.39)$$

where ϵ and ρ are the emissivity and reflectivity, respectively.

6.3. Material properties

6.3.1. Thermal properties

The conductivity of graphite is influenced by the fast neutron fluence. For unirradiated (fresh) graphite, the corresponding equation for the thermal conductivity is (IAEA, 2001)

$$\lambda_{un} = 115 (1 - 1.084 t_c + 0.743 t_c^2 - 0.213 t_c^3) \quad (6.40)$$

where $t_c = T/1000$ with T is the graphite temperature in °C.

The thermal conductivity of irradiated graphite can be expressed as

$$\lambda_{irr} = 115 F_a [1.5648 - 0.3162 \ln(t_c + 100)] \quad (6.41)$$

where

$$\begin{aligned} F_a &= \frac{F_1}{Y_d - F_2} + F_3 \\ F_1 &= -5.4705 \cdot 10^{-3} + 3.8214 \cdot 10^{-4} t_c + 1.3487 \cdot 10^{-1} t_c^2 \\ F_2 &= -1.3951 \cdot 10^{-2} + 1.2064 \cdot 10^{-1} t_c - 3.2955 \cdot 10^{-1} t_c^2 \\ F_3 &= -7.2640 \cdot 10^{-2} + 4.1459 \cdot 10^{-1} t_c + 2.3149 \cdot 10^{-1} t_c^2 \\ Y_d &= \frac{F_d}{10} \end{aligned}$$

and F_d is the fast neutron fluence (10^{21} n/cm^2).

These equations are plotted in Fig. 6.3 where the left figure represents the conductivity of unirradiated graphite while the right figure shows the conductivity of irradiated

graphite as a function of graphite temperature for various fast fluence doses. For unirradiated graphite, the increasing temperature decreases the conductivity while the opposite behavior is observed for irradiated graphite. Within the range of normal operation temperature (< 1873 K), the conductivity of irradiated graphite is smaller than that of fresh graphite, although at high temperature the difference becomes smaller. The magnitude of the fast fluence dose determines the conductivity. The larger the dose of fast fluence, the smaller the conductivity of graphite, but at high temperature the difference is quite small.

Other properties of the gas and solid phase have been mentioned in Eq. (4.33) – (4.36).

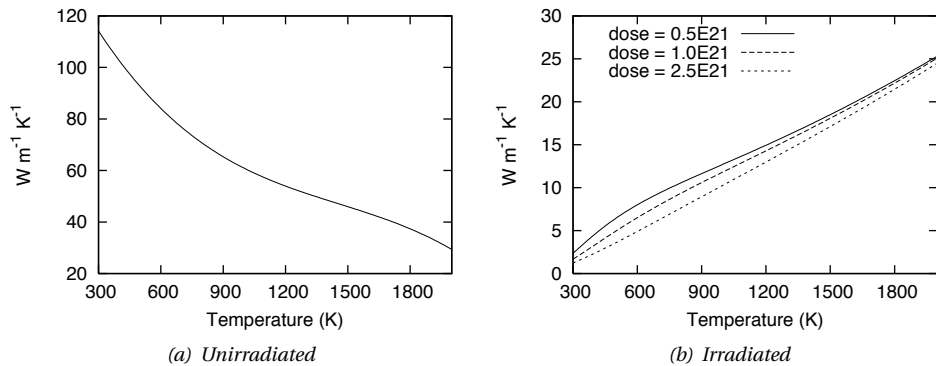


Figure 6.3. Thermal conductivity of unirradiated graphite (left) and irradiated graphite (right). The conductivity of irradiated graphite is given for various level of fast fluence (in neutron/cm²).

6.3.2. Radiative properties of particles

The radiative properties of particles in the bed can be distinguished into two categories, i.e. *dependent* and *independent* properties. The scattering and absorption are independent if the absorption and scattering characteristics of a particle is not influenced by its neighboring particles. Thus the scattering and extinction of energy is expressed by a simple algebraic addition of the extinguished and scattered energy by each particle (Tien and Vafai, 1989). Tien and Drolen (1987) developed a map of independent-dependent scattering for packed beds and suspensions of spherical particles based on experimental results and it was shown that for high temperatures the scattering of thermal radiation in most packed beds can be regarded as independent.

Using the number of the scatterers per unit volume N_s (particle/m³) and assuming independent scattering from each scatterer, the scattering coefficient for uniformly distributed monosize scatterers is defined as

$$\Sigma_s = N_s \sigma_s \quad (6.42)$$

where σ_s is the (per particle) scattering cross-section.

For large spheres where the particle size parameter $\alpha_R = \pi d_p / \lambda \gg 1$ (λ being the wavelength), the scattering, absorption and extinction coefficient are

$$\Sigma_s = \Sigma_a = \frac{3}{2} \frac{\alpha_p}{d_p} \quad (6.43a)$$

$$\Sigma_t = 3 \frac{\alpha_p}{d_p} \quad (6.43b)$$

6.4. Numerical treatment

The model described in previous sections is implemented in an in-house code, called DECFLOB. The code discretizes the spatial and angular domains and solves the associated integro-differential equations.

6.4.1. Discretization and solution method for the flow model

The set of partial differential equations was solved using the finite volume method with a staggered grid for a two-dimensional axisymmetric cylinder. This method ensures integral conservation of mass, momentum and energy over any group of control volumes and over the whole solution domain.

The solution domain is divided into a finite number of non-overlapping control volumes based on structured grids. The grids for the radial coordinate have been generated through the sinusoidal relation while the grids for the axial coordinate are homogeneous.

Scalar variables such as temperature, pressure and turbulence properties are defined at the center of the grid cells. The boundaries of a grid are located midway between the grid centers. Storage of vector variables such as velocity components is staggered 'half a cell' in the direction they represent. The staggered grid arrangement is suitable for a coupling of pressure and velocity and avoids some type of convergence problems and oscillations in the pressure field (Ranade, 2002).

To perform the integration on a computational cell, one has to perform two level of approximations: (i) approximation of surface and volume integrals based on the variable values at one or more locations on the cell face within the control volume, and (ii) approximation of the variable values at the cell face from the values at the cell centers. Approximations for the surface and volume integrals is described in e.g. (Ferziger and Perić, 2002). The second level of approximation concerns estimating the values of variables and gradients of variables at locations other than cell centers. In our calculations, all convective fluxes are approximated with a second-order bounded Total Variation Diminishing (TVD) scheme with the Van Leer flux limiting function (Wesseling, 2000). This scheme preserves monotonicity which prevents the divergence of the algorithm due to oscillations in the solution of the equations. The time discretization is based on a backward Euler scheme in combination with a pressure-correction technique.

The discretization procedure imposed to the partial differential equations leads to a set of algebraic equations, which can be solved by either a direct method or an iterative method. The latter has advantages over the other method if the matrices are not sparse.

Several methods have been proposed to perform such task. In our calculation the Conjugate Gradient (CG) and the Generalized Minimum RESidual (GMRES) are applied. The CG method is excellent for symmetric positive definite (SPD) matrices, such as in the pressure equation. On the other hand, the GMRES method is applicable for non-symmetric matrices. Hence for other transport equations, the GMRES method is applied. Preconditioning of these linear solvers was based on ILU factorization. Further discussions about these solvers and their algorithm can be found in e.g. (Wesseling, 2000; Barrett *et al.*, 1994).

6.4.2. Numerical treatment for the RTE

The RTE is an integro-differential equation and its solution is quite difficult even for a one-dimensional, gray medium. Most engineering systems, on the other hand, are multidimensional, therefore it is necessary to introduce some simplifying assumptions for each application before attempting to solve the RTE in its general form. Several numerical methods for solving the RTE have been developed over the years. Some of the commonly used ones are: (i) Monte Carlo method (Howell, 1998), (ii) zonal method (Larsen and Howell, 1986), (iii) Spherical harmonics or P_1 approximation method (Ratzell III and Howell, 1983), (iv) discrete ordinates method (Truelove, 1987) and (v) Finite volume methods (Raithby and Chiu, 1990). A detailed discussion of all these methods is obviously beyond the scope of this thesis. A review of these methods has been written e.g. by Viskanta and Mengüç (1987).

The problem in choosing an appropriate model of radiative transfer for FLUBER lies in the fact that it is a multimode heat transfer, combining conduction, convection and radiation. The solution method of the RTE has to be compatible with the numerical treatment of conduction and convective model. For this research we have chosen the P_N and S_N methods.

Spherical Harmonics Approximation

In the P_N model the radiation intensity is expanded in orthogonal series of spherical harmonics, with the series are truncated into N finite terms. Retaining the series up to $N = 1$ gives the P_1 approximation, retaining up to $N = 3$ gives the P_3 approximation and so forth. Further in this model the integro-differential radiative transfer equation can be converted into differential equations by the use of moment equations which can be obtained by multiplying the transfer equation by powers of the cosine of the direction vectors.

The radiation intensity can be written as

$$I(\mathbf{r}, \boldsymbol{\Omega}) = \frac{1}{4\pi} [G(\mathbf{r}) + 3\mathbf{q}(\mathbf{r}) \cdot \boldsymbol{\Omega}] \quad (6.44)$$

where the incident radiation and the radiative heat flux can be obtained as the zeroth and the first moments, respectively

$$G(\mathbf{r}) = \int_{4\pi} I(\mathbf{r}, \boldsymbol{\Omega}) d\Omega \quad (6.45)$$

$$\mathbf{q}(\mathbf{r}) = \int_{4\pi} I(\mathbf{r}, \boldsymbol{\Omega}) \boldsymbol{\Omega} d\Omega \quad (6.46)$$

Assuming isotropic scatterings, the moment equations can be written as

$$\nabla \cdot \mathbf{q} = \Sigma_a (4\sigma T^4 - G) \quad (6.47)$$

$$\nabla G = -3\Sigma_t \mathbf{q} \quad (6.48)$$

These two equations can be combined leading to a diffusion equation as

$$D \nabla \cdot \nabla G(\mathbf{r}) + \Sigma_a G(\mathbf{r}) = 4\Sigma_a \pi I_b \quad (6.49)$$

where $D = -1/3\Sigma_t$ is the diffusion coefficient.

It is quite obvious now how the energy equation and the radiative transfer equation are interconnected. Once the incident radiation field is determined from the RTE, it can then be coupled to the energy equation (Eq. (6.10)) through the divergence of the radiative heat flux, i.e. Eq. (6.47). On the other hand, to determine the incident radiation field, the temperature field should be given in the diffusion equation.

Expanding the P_N model into higher order is possible but the formulation becomes complicated and the computational time increases without substantial gain in accuracy (Bayazitoglu and Higenyi, 1979).

The boundary condition of radiative transfer equation (see Eq. (6.39)) cannot be longer satisfied by the P_N approximation as the orthogonal series of the intensity are truncated after a finite number. In this thesis, the Marshak's boundary condition is applied for the radiative model.

The Marshak's boundary condition can be written as:

$$\int_{\hat{\mathbf{n}} \cdot \mathbf{\Omega} > 0} I(\mathbf{r}_w, \mathbf{\Omega}) Y_{2i-1}^m(\mathbf{\Omega}) d\Omega = \int_{\hat{\mathbf{n}} \cdot \mathbf{\Omega} > 0} I_w(\mathbf{\Omega}) Y_{2i-1}^m(\mathbf{\Omega}) d\Omega \quad (6.50)$$

$$i = 1, 2, \dots, \frac{1}{2}(N+1), \text{ all relevant } m$$

and for P_1 , $i = 1$ and $m = 0$ in the weight function of Eq. (6.50).

For an opaque, diffusely emitting and reflecting wall, the intensity on the wall is given in Eq. (6.39). This leads to

$$I_w(\mathbf{\Omega}) = \epsilon_w I_b(T_w) + \frac{\rho_w}{4\pi} (G - 2q_n) \quad (6.51)$$

and

$$\mathbf{q} \cdot \hat{\mathbf{n}} = \frac{\epsilon_w}{2(2 - \epsilon_w)} (4\sigma T_w^4 - G) \quad (6.52)$$

where T_w is the temperature of the wall.

Discrete-Ordinates Method

The discrete-ordinates method (DOM) was suggested originally in the field of astrophysics by Chandrasekhar (1960). The method of discrete ordinates first transforms the integro-differential equation into a set of simultaneous partial differential equations and these are further transformed into algebraic equations which can be solved numerically.

The 4π solid angle is divided into a finite number of ordinate directions with corresponding weight factors. The integro-differential equation is written for each ordinate and the integrals over solid angles are replaced by the sums over the ordinate directions and its corresponding weight factors:

$$\int_{4\pi} f(\Omega) d\Omega = \sum_m w_m f(\Omega_m) \quad (6.53)$$

The choice of quadrature sets in the general DOM is quite arbitrary and the choice of different sets of ordinates may give different levels of accuracy, as has been observed by Truelove (1987) and Fiveland (1987). A simpler version of the DOM is called the S_N method and it was originally developed and extensively applied in neutron transport (Lathrop, 1966; Carlson and Lathrop, 1968). This method discretizes the direction cosines into N discrete values by considering symmetry (invariant to 90° rotation) in such a way to satisfy the following relation:

$$\zeta_m^2 + \eta_m^2 + \mu_m^2 = 1 \quad (6.54)$$

The set of ordinates and weights in the S_N method should also satisfy the following zeroth, first and second moments:

$$\int_{4\pi} d\Omega = \sum_{m=1}^n w_m = 4\pi \quad (6.55a)$$

$$\int_{4\pi} \Omega d\Omega = \sum_{m=1}^n w_m \Omega_m = 0 \quad (6.55b)$$

$$\int_{4\pi} \Omega \Omega d\Omega = \sum_{m=1}^n w_m \Omega_m \Omega_m = \frac{4\pi}{3} \mathbf{I} \quad (6.55c)$$

where \mathbf{I} is the unit tensor, and the half-moment equation

$$\int_{\hat{\mathbf{n}} \cdot \Omega < 0} |\hat{\mathbf{n}} \cdot \Omega| d\Omega = \int_{\hat{\mathbf{n}} \cdot \Omega > 0} \hat{\mathbf{n}} \cdot \Omega d\Omega = \sum_{\hat{\mathbf{n}} \cdot \Omega_m > 0} w_m \hat{\mathbf{n}} \cdot \Omega_m = \pi \quad (6.56)$$

A set of ordinates and weights that satisfy the aforementioned requirements (Modest, 2003a) is used in our subsequent calculations.

Derivation and the use of S_N method for the radiative transfer is similar to the method applied for the neutron transport. The radiative transfer equation for direction m in a 2D axisymmetric cylinder is

$$\frac{\mu_m}{r} \left[\frac{\partial(r I_m)}{\partial r} \right] - \frac{1}{r} \left[\frac{\partial(\eta_m I_m)}{\partial \phi} \right] + \zeta_m \frac{\partial I_m}{\partial z} + \Sigma_t I_m = \Sigma_a I_b + \frac{\Sigma_s}{4\pi} \sum_j P(\Omega_j \rightarrow \Omega_m) w_j I_j \quad (6.57)$$

where $m = 1, 2, \dots, (N+2)N/2$.

Equation (6.57) becomes complicated because of the angular derivative. The way to handle this kind of derivative is by using the *direct-differencing technique* as described by Lewis and Miller (1984), while to handle the intensity at the edges of the angular range, the so-called *weighted method* is used (Rhoades and Simpson, 1997; Greene and Petrie, 2000) to prevent negative values of intensity.

The incident radiation, Eq. (6.22), and the radiative heat flux, Eq. (6.23), can also be written as follows:

$$G(\mathbf{r}) \simeq \sum_{m=1}^N w_m I_m(\mathbf{r}) \quad (6.58)$$

$$\mathbf{q}(\mathbf{r}) \simeq \sum_{m=1}^N w_m I_m(\mathbf{r}) \mathbf{\Omega}_m \quad (6.59)$$

The boundary condition is quite straightforward. Introducing Eq. (6.53) into Eq. (6.39) gives the intensity at the wall as

$$I_m(\mathbf{r}_w) = \epsilon(\mathbf{r}_w) I_b(\mathbf{r}_w) + \frac{\rho(\mathbf{r}_w)}{\pi} \sum_{\hat{\mathbf{n}} \cdot \mathbf{\Omega}_j < 0} w_j I_j(\mathbf{r}_w) |\hat{\mathbf{n}} \cdot \mathbf{\Omega}_j|, \quad \hat{\mathbf{n}} \cdot \mathbf{\Omega}_m > 0 \quad (6.60)$$

The solution algorithm entails sweeping through the grid in the direction where the rays travel. The sweeping procedure has to be performed for every direction of the rays. Hence, for an axisymmetric cylindrical geometry, there will be $N(N+2)/2$ number of sweeping steps. By the end of one sweeping step, the value of I_m within the spatial domain \mathbf{r} is obtained. This step is repeated until the values of I_m converge.

Having found the I_m , the total incident radiation (i.e. Eq. (6.58)) can be computed easily and the divergence of the radiation heat flux (i.e. Eq. (6.24)) can be computed straightforward.

In the same manner, the surface heat flux can be obtained from the energy balance at the surface, giving the following relation.

$$\mathbf{q} \cdot \hat{\mathbf{n}}(\mathbf{r}_w) = \epsilon \left(\pi I_b(\mathbf{r}_w) - \sum_{\hat{\mathbf{n}} \cdot \mathbf{\Omega}_m < 0} w_m I_m |\hat{\mathbf{n}} \cdot \mathbf{\Omega}_m| \right) \quad (6.61)$$

6.4.3. Implementation

The geometry of the reactor is discretized in a 2D axisymmetric cylindrical coordinate with an inhomogeneous mesh as already described in the preceding section. The core is discretized into 20 (radial) by 120 (axial) cells, 26 of which are for the packed bed. The reflectors are meshed with 20 additional control volumes in radial and axial directions. Some parametric studies were performed to check the influence of mesh size to the stability of numerical calculations and it has been found that the results are insensitive to the size of the mesh.

The initial temperature of particles and helium is uniform throughout the bed and the cavity in accordance with the good mixing mentioned in the earlier chapter. The initial values of the temperatures are obtained from preceding calculations using a point dynamics code (see Chapter 4) and are listed in Table 6.1. The initial value of the reflector temperature is obtained from a separate steady-state 2D calculation with the outer wall boundary set to 298 K and the temperature of the inner wall depends on the case. The initial velocity of the gas is set to zero.

The boundary condition for the temperature at the side and top outer walls is obtained from the natural convective and gray body radiation to the atmosphere while the

temperature of the bottom reflector wall is assumed constant at 500 K. The atmospheric temperature in this case is 298 K.

The fuel volume fraction is constant at 0.6 in the bed and 10^{-15} in the cavity. The emissivity of the fuel is assumed to be 0.8. The same value is also applied for the inner and outer surface of the reflector.

Table 6.1. *Initial values of the temperatures.*

Total Power (MW)	Fuel Temperature (K)	Gas Temperature (K)
50	875	874
60	922	920
70	967	966
80	1012	1010

6.5. Results and discussions

6.5.1. Assessment of the numerical methods for the RTE

It is shown that the P_1 and S_N methods are compatible with the numerical schemes of the flow and energy equations. An assessment of these two methods has been performed to determine whether they are accurate and efficient.

For a test case, a single-mode heat transfer calculation has been performed, i.e. only radiation. The reactor is modeled as a 2D axisymmetrical cylinder with the packed bed of 130 cm in height and the cavity of 470 cm in height. The bed is 1000 K with a particle volume fraction of 0.6. The surface of the reflector is set 800 K. For this test, the particle volume fraction in the cavity is set at two different values, i.e. 10^{-3} and 10^{-12} .

Fig. 6.4 shows the heat transferred to the surface of the bottom reflector which is in direct contact with the fuel particles having volume fraction of 0.6. The results show that the difference is only less than 1%, indicating that there is no significant differences between the two methods.

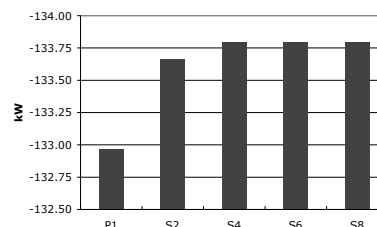


Figure 6.4. *Heat transferred to the surface of the bottom reflector, calculated by using P_1 and S_N methods with a particle volume fraction in the bed of 0.6.*

Estimates for the heat transferred to the surface of the top reflector are shown in Fig. 6.5. The left figure represents the condition where α_p in the cavity is 10^{-3} while the right figure α_p is 10^{-12} . In each figure the results of calculation using P_1 , S_2 , S_4 , S_6 and S_8 are presented. The View Factor (VF) method (Modest, 2003b) is used for a comparison as this method is more accurate on transparent medium. Fig. 6.5(a) clearly shows that all the approximation methods (P_1 and S_N) give significantly different results than the VF method. Hence, the particle volume fraction of 10^{-3} is not transparent enough so that the medium in the cavity becomes participating. Fig. 6.5(b) clearly shows that the flow direction of the heat transfer in the surface using P_1 method is not correct, meaning that heat is transferred from the cooler reflector surface to the hotter surface of the particle bed. The P_1 method is thus not valid for very low particle volume fraction. In this case the extinction coefficient is too small so that the diffusion coefficient ($D = 1/\Sigma_t$, for an isotropic scattering) becomes very large.

Contrary to the P_1 method, heat is transferred into a correct direction in the S_N method and it is in the order of magnitude as compared to the VF method. The higher the order of S_N , the smaller the differences to the results of VF method. The S_2 method over-predicts the heat transferred due to small number of ordinates. In analogy to the neutron transport, this is caused by the ray effect.

Now the radiation methods are included for the multi-mode heat transfer calculations. These calculations were performed for 3 hours real-time with the initial conditions already described in Section 6.4.3.

The maximum fuel temperature as a function of time calculated using different methods is presented in Fig. 6.6. In general the transient behavior is similar. Thermal transient in the active core shows an increase in the fuel temperature up to a maximum value within less than two hours after shutdown, followed by a slow cooling down. The core at first becomes hot as the decay heat generation exceeds the rate of heat removal. The heat removal later becomes larger than the heat generation and since then the average core temperature decreases as heat is transferred to the reflector and the atmosphere.

The maximum fuel temperature calculated using the P_1 method is very high and even exceeds the permissible limit (1873 K). The particle volume fraction in the cavity is 10^{-12} , leading to incorrect heat flow at the surface of the reflector. Instead of heat transferred from

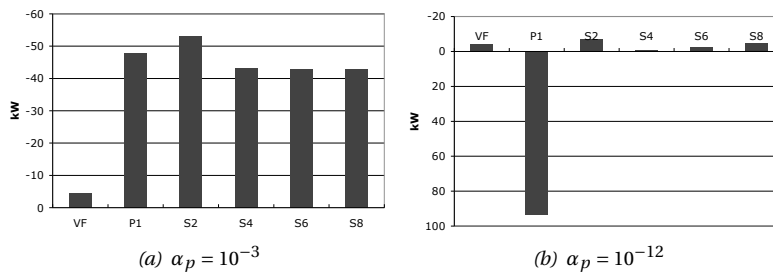


Figure 6.5. Heat transferred to the surface of the top reflector, calculated by using P_1 , S_N and VF (as comparison) with a particle volume fraction in the cavity of 10^{-3} and 10^{-12} .

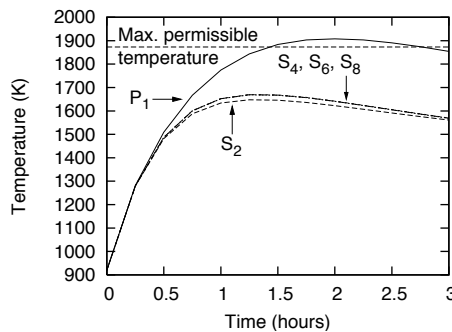


Figure 6.6. The maximum fuel temperature as a function of time calculated by different methods. Multimode heat transfer is applied in these simulations.

the fuel to the reactor, the fuel particles is heated up due to thermal radiation from the reflector.

The S_2 method produces an over-predicted radiative heat transfer as compared to higher order S_N method (see Fig. 6.5(b)). The fuel particles are thus cooling down faster. It can be seen in Fig. 6.6 that the maximum fuel temperature for the S_2 method is lower than the other higher order S_N methods, although the difference is not more than 30 K. The S_4 , S_6 , and S_8 results show insignificant differences (less than 1 K). But as shown in Fig. 6.5(b), the results of the S_4 method still differ significantly compared to the VF method. The higher the order, the closer the results to the VF method, and it is shown that the results of S_8 is close enough to the VF method.

Although the S_8 method looks promising, a big constraint exists for using this method. Table 6.2 shows the CPU time for 3-hour real-time simulations performed by using AMD64 2800+. The S_8 method is about 6 times slower than the S_4 method. The running time is long due to the sweeping procedure for each ordinate in every mesh-point until the radiation intensity converges. Another reason is that the calculation for the flow and the radiation problem is performed in the same time-step. As the *time disadvantage ratio* (i.e. the ratio between the CPU time and the real time) is high for S_8 method (~ 9), the use of S_8 method is not economical for simulating the condition of the reactor long after shutdown. For this reason, our subsequent calculations will be using the S_6 method as a compromise between accuracy and time.

6.5.2. Results for different cases

Four different cases were considered, i.e. (A) pressurized, fresh graphite system, (B) pressurized, irradiated graphite system, (C) depressurized, fresh graphite system and (D) depressurized, irradiated graphite system. In a pressurized system, the pressure of the system remains constant at an operational setting of 60 bar while in a depressurized system, the pressure of the system is assumed constant at 1 bar. In a fresh graphite system, the influence of fast neutron fluence is assumed negligible and hence the thermal conductivity of graphite follows the curve as shown in Fig. 6.3(a). In an irradiated graphite system, the

Table 6.2. The CPU time and the time-disadvantage factor for simulating 3-hour real time using various methods.

Method	P ₁	S ₂	S ₄	S ₆	S ₈
CPU Time (hours)	1.53	2.29	4.78	11.56	26.69
Time-disadvantage factor	0.51	0.76	1.59	3.85	8.90

calculations are performed at fast neutron fluence of 10^{21} cm^{-2} and the thermal conductivity of graphite is obtained from Eq. (6.41). Various initial power levels are simulated for each case, starting from 50 MW up to 80 MW.

All calculations were performed with a time step of 0.25 seconds, with the capability to save the results and to restart the problem every 900 seconds of real time. The simulations were run for 24 hours of real time. Such calculations demand approximately 4 days of CPU time, running on an AMD64 2800+.

Case A: Pressurized, fresh graphite system

The time evolution of the maximum fuel temperature is shown in Fig. 6.7 for several initial total powers. The thermal transient in the active core shows an increase of the fuel temperature within less than 2 hours to reach peak temperature followed by a gradual cool down. The core initially heats up relatively fast as the decay heat generation exceeds the heat removal rate. Later the active core heat removal rate exceeds the decay heat generation rate and from then on the average core temperature decreases slowly as heat is transferred to the reflector and the atmosphere. Figure 6.7 also clearly shows that at an operating power of 80 MW the peak fuel temperature exceeds the recommended maximum permissible temperature.

The percentage of heat transferred from the core to the surface of the reflector is shown in Fig. 6.8. The percentage is calculated from the amount of heat transferred by a particular heat transfer mode against the total heat transferred through that particular reflector surface. Near the core (see Figs. 6.8(a) and 6.8(b)), the dominant heat transfer mechanism is conduction. The conductivity of the particles is in fact a function of temperature and its value decreases quite significantly at higher temperatures. Hence at higher heat production rate, the particles becomes less efficient in transferring energy and consequently the percentage of conductive transfer becomes smaller. During the first hours, as the heat production increases, the temperature of the bed also increases. As the heat flux by radiation increases by the power of four of the temperature, the contribution of radiation at the first few hours becomes larger. However, about two hours after shutdown and beyond the bed cools down and hence the contribution of radiative transfer becomes smaller and conductive transfer becomes larger. The figures also show that convection does not contribute much near the bed.

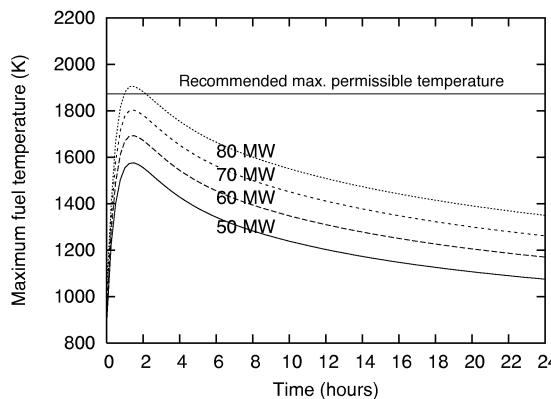


Figure 6.7. The time evolution of the maximum fuel temperature for different initial operating power using the S_6 model for the pressurized, fresh graphite system.

Figs. 6.8(c) and 6.8(d) indicate that convection is the most dominant mechanism in transferring energy in the cavity. Conduction is very poor due to low conductivity of helium. These two figures are also an indication that the model for radiative transfer, i.e. the S_6 method, is successfully applied even at a very small particle volume fraction in the cavity (i.e. 10^{-15}).

Combining all balances, the decay heat generated in the bed is transferred to the reflector mostly by conduction (see Fig. 6.8(e)). The thermal conductivity of graphite is quite high, even at the highest achievable temperature (still $> 40 \text{ W/m}^2 \text{ K}$). The contribution of radiation is still considerable, between 10 to 20%. As the temperature in the bed decreases during a later stage, the contribution of radiation becomes smaller and at the same time as the graphite conductivity increases as the temperature decreases, the contribution of conductive heat transfer becomes larger.

Figure 6.9 visualizes the combined temperature fields (i.e. fuel temperature in the bed, gas temperature in the cavity and graphite temperature in the reflector) for an initial operating power of 60 MW. Initially, the fuel and helium temperatures are uniform as a result of perfect mixing of the particles during the fluidization process. Up to 2 hours after shutdown, the core heats up as the decay heat is still dominant. It can be seen as well that at the top of the particle bed the temperature gradient is quite large, which is caused by the flow of hotter helium running over it. Large temperature gradients can also be seen in the interface of bed and the bottom/side reflector and in this case the presence of conductive/radiative transfer is the main cause. After the peak temperature is reached at about 2 hours after shutdown, the core experiences a slow cooling down. The figures also show how the reflector heats up through conductive transfer. The temperature of the outer surface of the reflector near the packed bed increases from an initial value of 293 K up to $\sim 600\text{--}700 \text{ K}$.

Figure 6.10(a) shows the helium flow field inside the reactor at 2 hours after shutdown for an initial operating power of 60 MW. Note that some grid points are omitted in this graph for clarity reason. The flow inside the packed region is virtually absent due to the

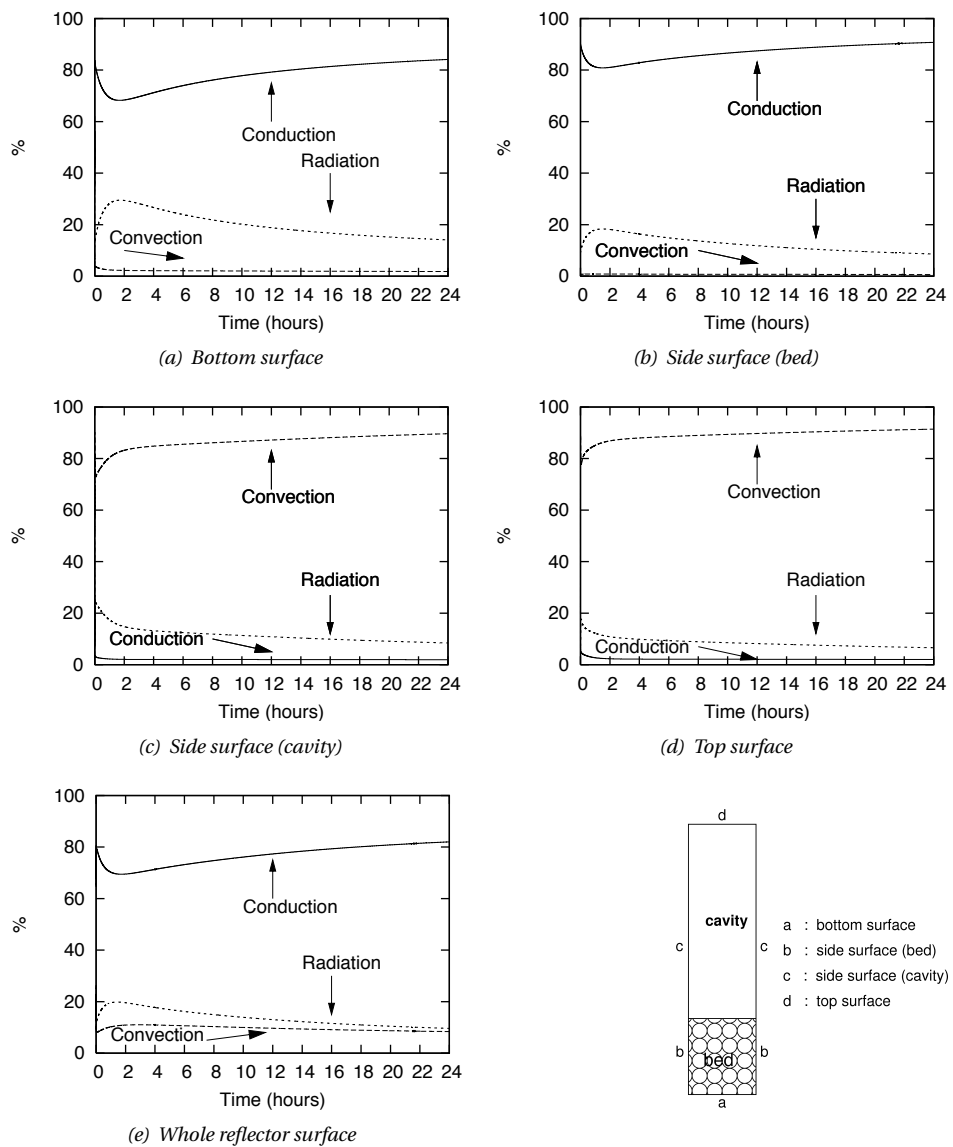


Figure 6.8. Percentage of heat transferred at various surface locations of interface between the core and reflector in a pressurized system. The initial power of the reactor before shutdown is 60 MW.

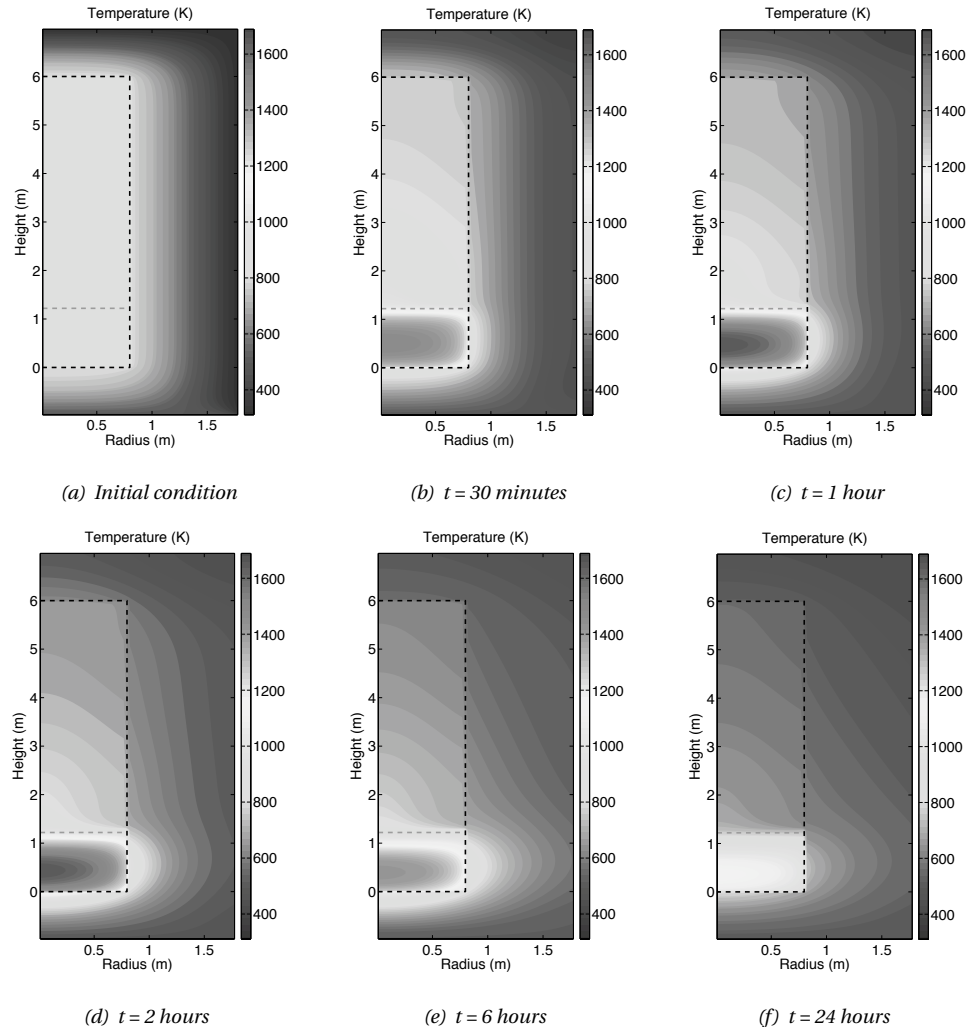


Figure 6.9. The fuel temperature in the bed, the helium gas temperature in the cavity and the graphite temperature in the reflector at different time after shutdown for an initial operating power of 60 MW.

high associated flow resistance in this region and the heat transfer from the particles toward the gas is strictly diffusional. Having received thermal energy from the bed surface, the hot gas moves upward in center of the cavity, and later moves downward close to the reflector surface.

The ratio of the turbulent viscosity to the laminar viscosity is shown in Fig. 6.10(b). The value of turbulent viscosity is obviously larger than the laminar viscosity by several orders of magnitude, justifying the use of a high Reynolds number turbulence model.

Case B: Pressurized, irradiated graphite system

The maximum fuel temperature in a pressurized, irradiated graphite system as a function of time after shutdown is presented in Fig. 6.11. The graphite in such system is assumed to have been exposed by fast neutrons and as already shown in Fig. 6.3 the thermal conductivity of graphite deteriorates. Consequently heat generated in the bed is not effectively transferred by mean of conduction. As shown in the previous section that conduction is the main heat transfer mechanism in the bed (in the case of fresh graphite), we might expect that the maximum fuel temperature in the irradiated graphite system will be higher than that in the fresh graphite system. In this case, the decay heat production rate is not balanced well by the removal rate by means of conduction. At 70 MW the maximum fuel temperature already reaches the recommended permissible value.

In contrast to the results in Case A, Figs. 6.12(a) and 6.12(b) show that conduction is no longer the dominant transfer mechanism in the bed. In such a system, radiation gives the largest contribution to the total transferred heat. The emissivity of the irradiated graphite is assumed the same as that of the fresh one, hence in this case energy transfer by means of radiation is not affected. A similar situation applies to convection, having its percentage still very low.

Figs. 6.12(c) and 6.12(d) show that convection remains the most dominant mechanism and the results are similar to those of Case A. Although for numerical reasons we use very small particle volume fraction in the cavity (i.e. 10^{-15}), the contribution of the particles in conducting energy is negligible. The conduction in the cavity thus comes mainly from the gas.

For the whole reactor surface, radiation gives the largest contribution (Fig 6.12(e)), followed by convection and conduction. As the bed cools down, radiation becomes less dominant. In contrast to a fresh graphite system, the conductivity of irradiated graphite is smaller when the temperature decreases. Hence, the contribution of conduction will not rise significantly. This situation leads to an increase in the contribution of convection. If the increase rate of convection and the decrease rate of radiation is constant, the curve of convection may intercept the one of radiation at longer times, making convection the dominant mode.

Case C: Depressurized, fresh graphite system

The pressure in the depressurized system is assumed constant at 1 bar instead of 60 bar. This influences the transport properties of helium, so we might expect that energy transfer by means of convection will be affected. In Fig. 6.13 it is shown that the maximum permissible temperature is exceeded when the total power is 70 MW. Comparing

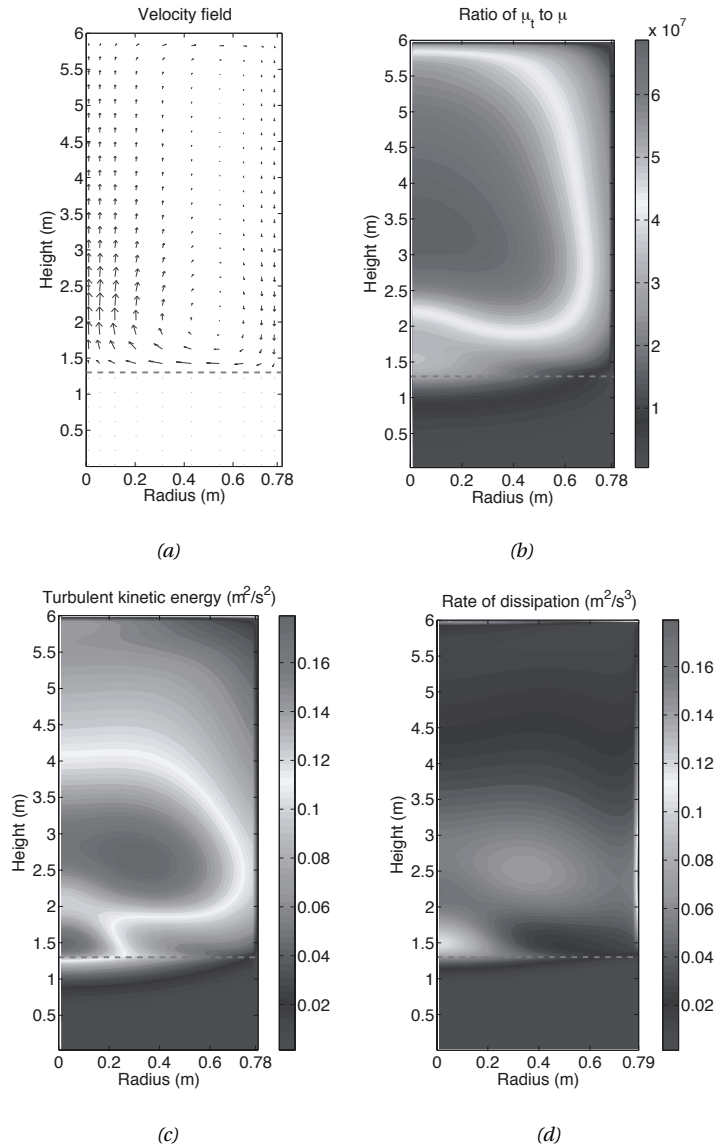


Figure 6.10. (a) The velocity field, (b) the ratio of the turbulent viscosity (μ_t) to the laminar viscosity (μ), (c) the turbulent kinetic energy (k) and (d) the dissipation rate of the turbulent kinetic energy (ϵ) in the core. All calculations were performed for 2 hours after shutdown at initial operating power of 60 MW. Note that some grid points in the velocity field are omitted for clarity reason. Here the discretization is shown only for 10 (radial) x 30 (axial) from the actual 20 (radial) x 120 (axial).

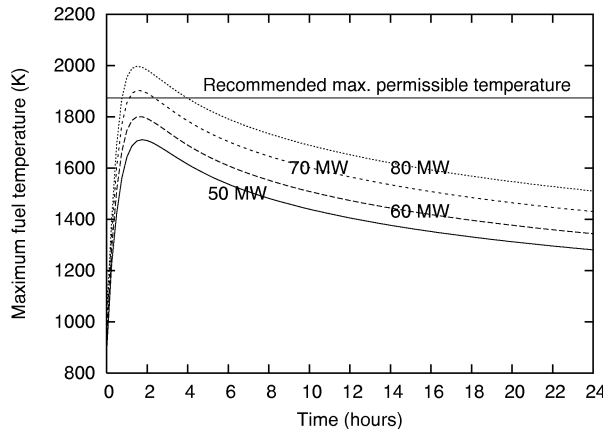


Figure 6.11. The time evolution of the maximum fuel temperature for different initial operating power using S_6 model for the pressurized, irradiated graphite system.

Comparing this graph to Fig. 6.7 we see that the maximum fuel temperature in Case C is larger than in Case A. As the conductive properties of fuel and graphite do not change, we can immediately see that the contribution of convective transfer in the cavity decreases quite significantly.

Fig. 6.14 shows the percentage of heat surface at various locations for Case C. Heat transfer in the cavity (see Fig. 6.14(c) and 6.14(d)) is now dominated by radiation. In the longer term, however, the contribution of radiation is becoming less and less as the bed is cooling down and convection will take over. For the whole surface, conduction remains the most significant mechanism in transferring energy (see Fig. 6.14(e)). The trend is quite similar to the one in Case A though convection is slightly smaller.

Case D: Depressurized, irradiated graphite system

Case D represents a possible severe situation of post-shutdown of the reactor, in which transfer of heat by means of conduction and convection does not occur efficiently. The maximum fuel temperature in the bed for a specific operating power level in this case is thus the highest among all cases. This is shown in Fig. 6.15. At 60 MW the maximum fuel temperature has exceeded its maximum permissible value and at 50 MW the fuel temperature is close to the maximum permissible value. The slope of the fuel temperature curve after reaching its peak is very lean.

As conductive and convective transport do not occur effectively, radiation will be dominant in transferring heat to the reflector (see Figs. 6.16(a)–6.16(e)).

6.5.3. Discussion

The results of calculations indicate that it is possible to remove the decay heat of the fluidized bed reactor by passive means. In the case of a severe situation where the system

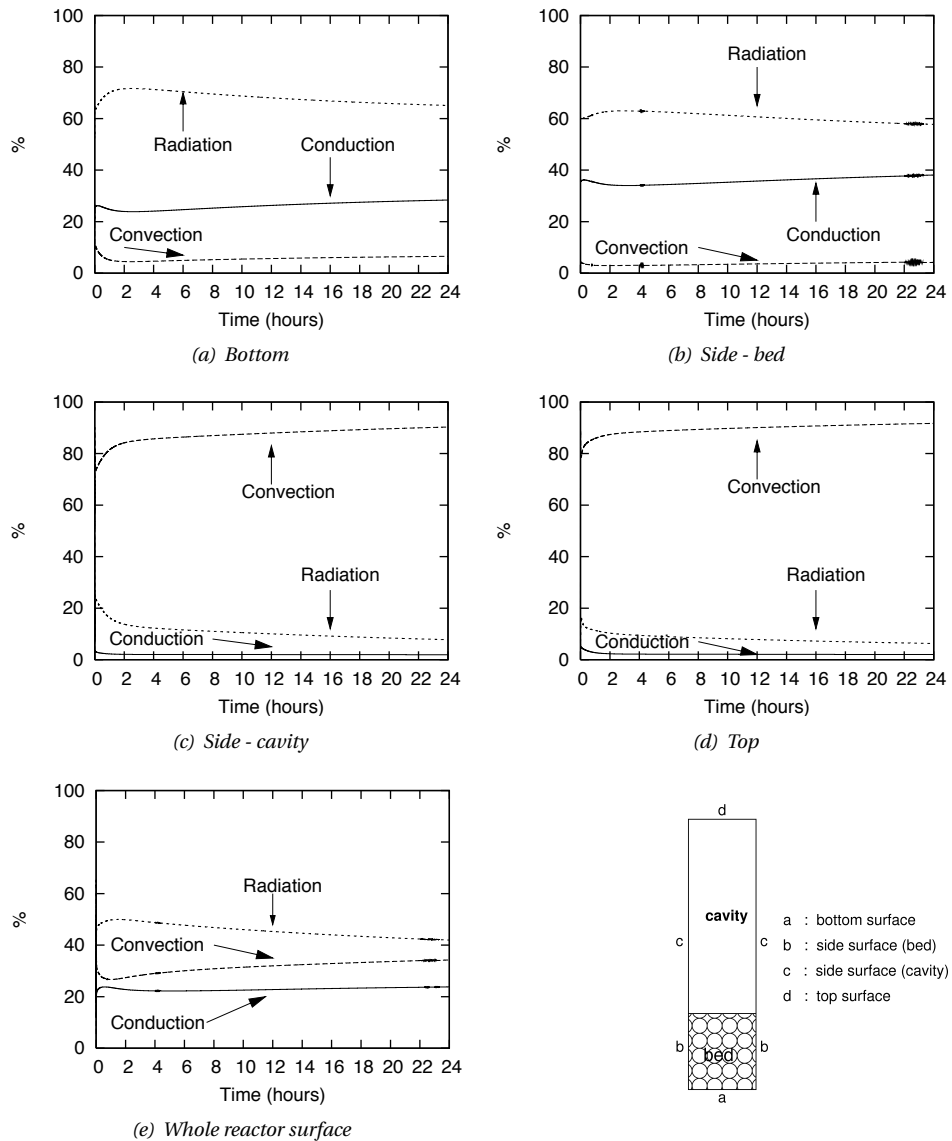


Figure 6.12. Percentage of heat transferred at various surface locations of interface between the core and reflector for a pressurized, irradiated graphite system. The initial power of the reactor before shutdown is 60 MW.

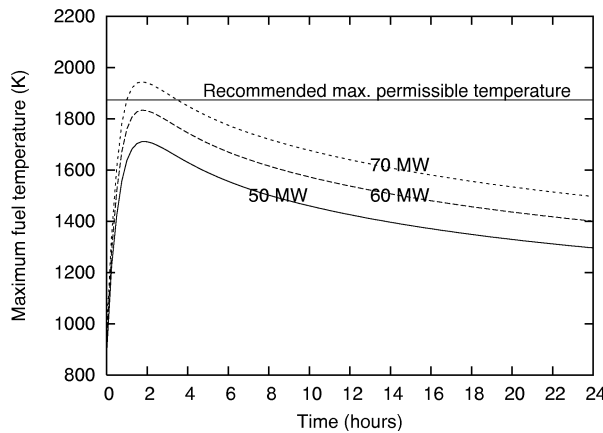


Figure 6.13. The time evolution of the maximum fuel temperature for different initial operating power using S_6 model for the depressurized, fresh graphite system.

is depressurized and the thermal conductivity of graphite has deteriorated due to neutron irradiation, the maximum operating power level of which its associated decay heat can be removed safely by passive means is slightly above 50 MW. This power level is rather low if we consider that the maximum attainable power level for this design of reactor is about 120 MW.

The model used in these calculations is conservative because the reactor is assumed as a closed system in which no coolant (helium) coming into and taking decay heat out of the core. In such a condition, the hot helium is circulated only inside the cavity. Should a mechanism exist to extract hot helium out of the core and replace it with cooler helium coming in from the bottom reflector, the decay heat removal will be enhanced and the maximum fuel temperature will be lower. However, the procedure to remove heat by introducing helium from the bottom should be performed carefully. The flow rate of the cool helium should be low (less than the minimum fluidization velocity) that the bed is not fluidized to avoid recriticality of the reactor.

Another possibility to enhance heat transfer is by installing coolant channels in the side reflector. The heat transferred to the side reflector by means of conduction is then transferred by natural or forced convection in the coolant channels.

Another option is by implementing a directing funnel in the lower part of the reactor by which the particles are collected in a cooling pool once the fluidizing gas is stopped. Removal of the decay heat is then performed in this pool. To enhance safety, borated water is used as the cooling agent, ensuring a negative reactivity during the cooling period.

6.6. Summary

Mathematical models have been derived and a computer code (i.e. DECFLUB) has been developed to simulate the removal of post-shutdown decay heat by passive means. All heat

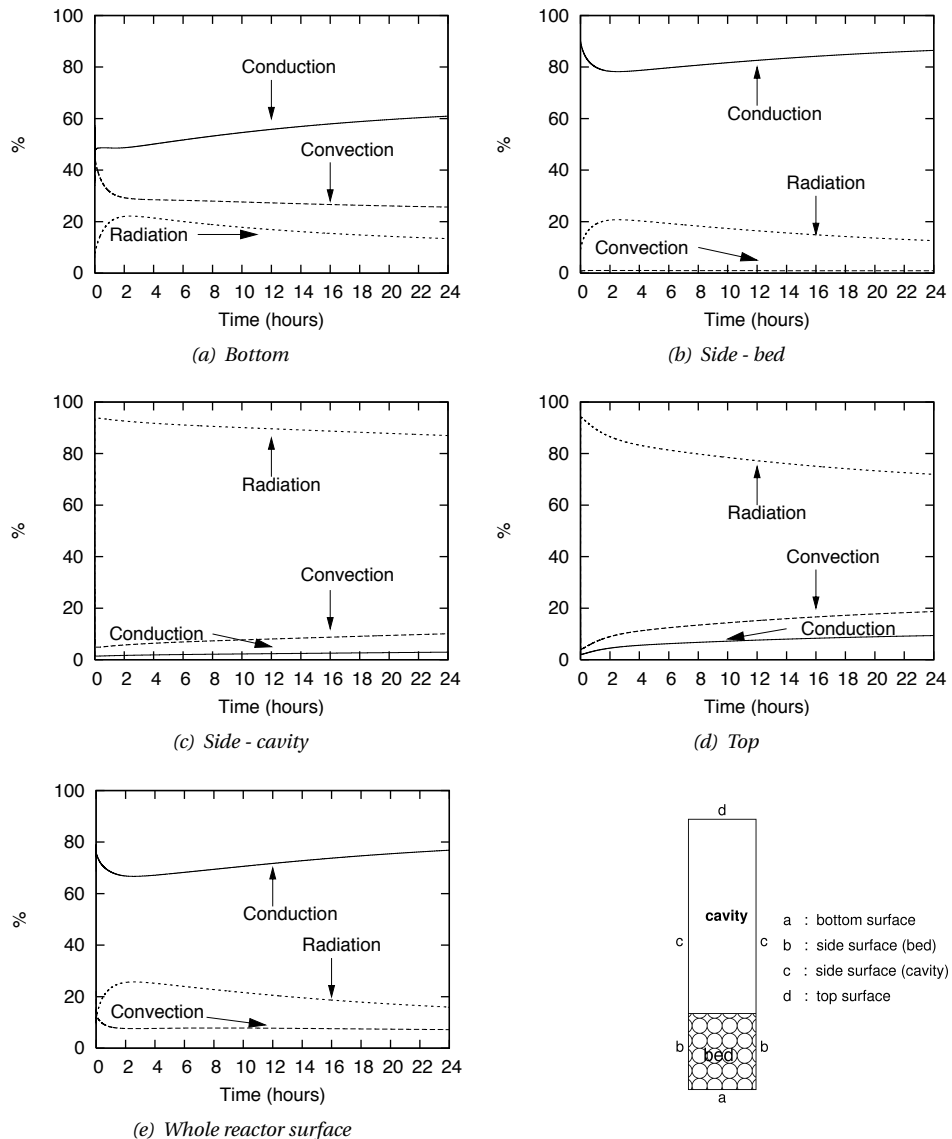


Figure 6.14. Percentage of heat transferred at various surface locations of interface between the core and reflector for a depressurized, fresh graphite system. The initial power of the reactor before shutdown is 60 MW.

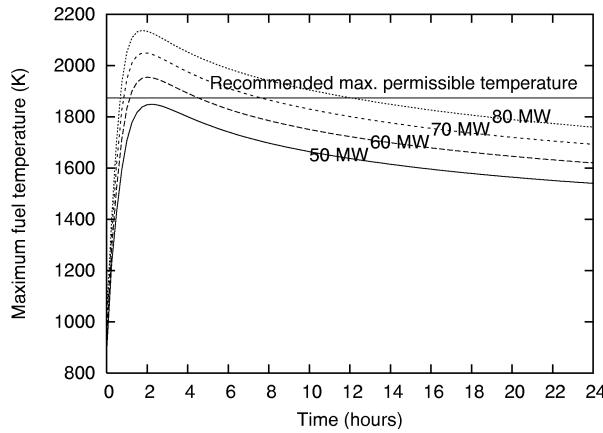


Figure 6.15. The time evolution of the maximum fuel temperature for different initial operating power using S_6 model for the depressurized, irradiated graphite system.

transfer mechanisms, i.e. conduction, convection and radiation, are included in the model. The system is modeled as a two dimensional axisymmetric cylinder and being closed. The numerical scheme incorporates the standard $k - \epsilon$ model for turbulent flow and the S_N model for radiative transfer.

Different cases are simulated, being a combination of the pressure of the system and the thermal properties of graphite. In terms of pressure of the system, two situations are considered, i.e. a fully pressurized system where the system remains at its operational pressure of 60 bar and a fully depressurized system where the pressure in the system drops to 1 bar. The thermal properties of graphite being considered are fresh graphite where the influence of neutron irradiation to the thermal conductivity is negligible and irradiated graphite where the thermal conductivity of graphite becomes worse due to neutron fluence.

In general the following findings are reported:

1. The use of the discrete ordinate S_N method for modeling radiative transfer is satisfying, especially when applied to the cavity. The use of this method is a real improvement to the P_1 model which is incapable to simulate radiative transfer with a very low particle volume fraction in the cavity.
2. The flow of helium occurs mainly in the cavity while in the bed it is negligible due to the high associated flow resistance in this region. The heat transfer from the particles toward the gas is strictly diffusional.
3. The peak of the maximum fuel temperature is reached at 1 to 2 hours after shutdown.
4. In the pressurized, fresh graphite system, the decay heat can be removed by passive means for reactor power up to 75 MW.

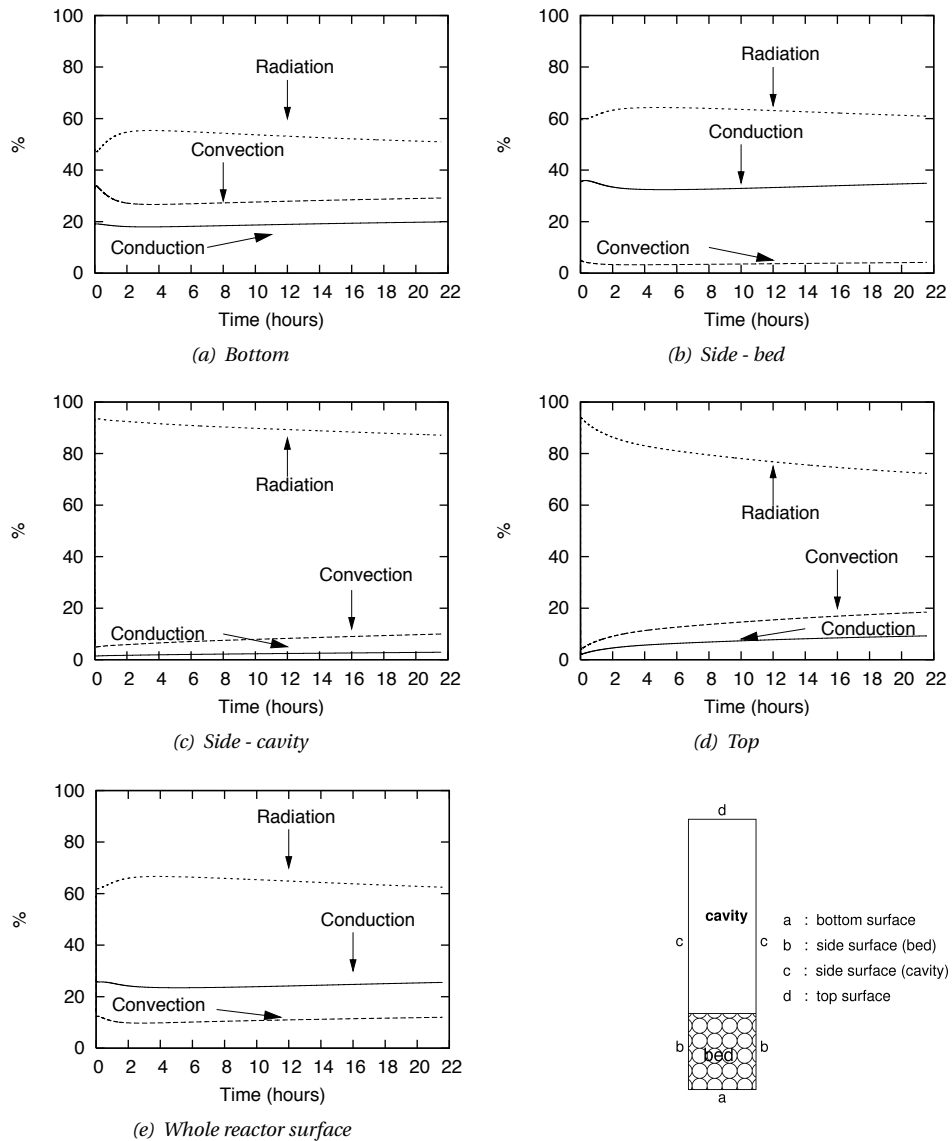


Figure 6.16. Percentage of heat transferred at various surface locations of interface between the core and reflector for a depressurized, irradiated graphite system. The initial power of the reactor before shutdown is 60 MW.

In this system, conduction is the dominant mechanism in the bed while in the cavity the transfer of heat is dominated by convection.

5. In the depressurized, irradiated graphite system (representing the worst case), the decay heat can be removed by passive means for reactor power up to 50 MW. As the thermal conductivity of graphite has deteriorated due to irradiation and the transport properties of helium is influenced by depressurization, the dominant heat transfer mechanism is thus radiation.
6. It is recommended to enhance heat transfer. This might include installing coolant channels/ring to remove heat by means of natural convection in the side reflector or by collecting the particles in a borated-water cooling pool.

CHAPTER 7

Concluding remarks

7.1. General discussion

This research project has dealt with a conceptual design of an innovative high temperature reactor based on the fluidization principle. The main findings are summarized below.

Some modifications to the FLUBER design available at the time of starting this PhD project have been performed. These include enlarging the core cross-section, modifying the fuel kernel diameter, increasing the fuel inventory and adding boron absorber in the bottom part of the side absorber. By doing so, the desired cold shutdown margin of -4% and the excess reactivity of 4% can be achieved. Static calculations (without feedback effects from fluidization or heat transfer process) further show that the maximum fuel temperature where FLUBER can still achieve criticality is about 1200 K. The core temperature coefficient is found to be ≈ -7 pcm/K while the total temperature coefficient is ≈ -4 pcm/K. This gives an additional subcriticality level when the reactor is shutdown from a hot operation. For example, after being operated at 850 K, the reactor is shutdown and it forms a packed bed with an additional -2% of reactivity to the shutdown margin. This will ensure a safe shutdown in the case of loss of the coolant flow.

Static calculations also show that the reactivity is strongly dependent on the particle position and it has been shown that radial redistribution of particles can cause a large change in reactivity. The presence of large bubbles strongly perturb the reactivity. Static calculations have predicted a change in reactivity of the order of 300 pcm due to bubble formation. This estimation is based on a single large bubble of 1 m in diameter. In reality, larger bubbles as well as bubble elongation or bubble coalescence may occur, thus the reactivity change could be underpredicted. Most important here is the fact that the bubble formation has a significant influence on reactivity. Particle redistribution from a low

importance zone to a high importance zone, or vice versa, is the cause of this reactivity change.

The steady state and transient behavior of FLUBER are investigated by using a point dynamics model. The maximum steady state power produced by this new design is 120 MW with a maximum steady state fuel temperature of 1163 K. The specific power of FLUBER is ≈ 3.5 MW per kg U^{235} when it is being operated at full power. This value is 3.5 times the specific power of more conventional reactors. Even when FLUBER is being operated at half of its maximum power, this figure is still about 2.25. Having a larger specific power, FLUBER demonstrates a prospect of economic competitiveness against conventional nuclear reactors.

Transient simulations show that the total power might experience a large overshoot when the reactor is subjected to a step input, while the fuel temperature, thanks to the negative reactivity feedback, stays still far below the maximum permissible limit. Furthermore, the feedback in FLUBER is fast acting. Hence, an increase in power is almost immediately followed by a counteraction of the feedback. Adjusting the helium flow through the core can be used to control the power level of the reactor, thus no active control mechanisms are required for this purpose. This in fact reduces the complexity of control mechanism and the economic cost as well. The reactor becomes more simple in design. The absence of the active systems for removing decay heat also reduces the cost of the reactor.

The stability of the system has been investigated by a root-locus analysis as a function of the coolant flow rate and it is shown that all loci have negative real parts. The stability analysis has been performed as well for sinusoidal disturbances. The results show that the reactor is stable for all frequencies. Thus in terms of linear system analysis, the reactor is stable.

A multidimensional dynamic code has been used to study the influence of bubbles and their consequences to the reactor power and temperature. Bubbles of different sizes occur in the reactor and at higher input velocity bubbles elongate and sometimes create a column-like structure. This continuous formation of bubble implies a continuous movement of particles and induces reactivity and power changes. Oscillation in power and temperature is observed. However as this reactor has a negative reactivity feedback, any excessive increase in the power is restrained. The fission power fluctuations are large, but the gas temperature is relatively steady after the initial transient.

The gas temperature across the bed to a certain extent is uniform as a result of excellent mixing. All in all this leads to a uniform burnup of the fuel. The difference of temperature between the fuel and the gas is almost negligible due to the size of the particles and the good thermal conductivity of the coated particles.

Although the reactor is stable, an initial sharp increase in power and temperature occurs in the reactor as a result of incorporating a step input of the coolant flow rate. In practice a step input is not realistic considering the inertia of the pumps. Introducing a ramp input instead of a step input may prevent a high peak of temperature after startup.

Investigations have been performed on the possibility of passive removal of the decay heat in FLUBER. When operated at the maximum power of 120 MW, the power density of FLUBER is about 10 MW/m 3 and when the reactor is shutdown the initial decay power density ($\sim 7\%$ of the total power) in a packed bed condition is 3.4 MW/m 3 . These figures are below the power density of the conventional reactors (100 MW/m 3 during operation

and 7 MW/m^3 of the initial decay power density). The results of the calculations show that to be able to remove the decay heat by passive means, the reactor should be operated at about 50 MW with an output temperature of approximately 900 K. At this power level, the initial decay power density is 1.4 MW/m^3 . This result is based on the maximum fuel particle temperature of a depressurized system with irradiated graphite, representing the worst accidental condition. The temperature peak occurs within 2 hours after the reactor is shutdown. This figure is far below that in a typical HTGR where the peak occurs within tens of hours (Kugeler, 1992).

7.2. Remarks on computational tools

FLUBER has unconventional aspects which require special attention in terms of neutronic calculations, such as the variation of geometry under operational conditions, the presence of a large void volume above the core, and a strong spectral variation in the core. The use of a diffusion code need a special treatment to handle the diffusion coefficient of the cavity. The use of discrete-ordinates code also does not result better accuracies mostly due to the ray effects in the cavity. For such a reason, the Monte Carlo code has been used for static calculations to obtain accurate results.

In terms of thermalhydraulic calculations, the nature of fluidization poses difficulty as the available thermalhydraulics codes will not be sufficient. Two levels of approach have been performed:

- A zero-dimensional dynamics (or point dynamics) model comprising coupled neutronics, heat transfer and fluidization has been used to estimate the time-dependent behavior of the system. The real system is in fact more complicated due to moving of particles and the occurrences of bubbles in the bed. These phenomena cannot be captured accurately by the point dynamics model. The results of the 3D Monte Carlo static calculations are then adopted to the point dynamics model and the presence of bubbles is included in the model as a noise term. By doing so the results are thus expected to be close to the real system.
- A multidimensional dynamics code comprising a deterministic transport code coupled with a fluidization dynamics code has been used. Movement of the particles and the occurrence of bubbles can be depicted more accurately. Hence the evolution of power and temperature occurs naturally.

The results of the point dynamics model have shown a great resemblance to that obtained by using the multidimensional model.

For an assessment of the decay heat removal, we have incorporated the $k - \epsilon$ turbulence model and a radiative transfer model. For the radiative transfer model, we have considered to use either the P_1 or S_N methods. Preliminary tests show the use of the discrete ordinate S_N method for modeling the radiative transfer is better, especially when applied to the cavity. The use of this method is an improvement to the P_1 model which is incapable to simulate radiative transfer with a very low particle volume fraction in the cavity. The drawback of using the S_N method, especially for higher orders, is its long computation

time. The running time is long due to the sweeping procedure for each ordinate in every mesh-point until the radiation intensity converges. Another reason is that the calculation for the flow and the radiation problem is performed in the same time-step. A proposal to reduce the computation time is by freezing the radiation field after several “flow mechanics” time steps.

7.3. Future work

Several issues are not covered in this project and to actually deploy such a reactor the following issues are recommended for future work.

- *Material issues*

This research project deals with the neutronics and fluidization of the reactor using the fuel developed for the HTGR. Up to this moment we have assumed that these particles are suitable for FLUBER. However, the strength of TRISO particles under various fluidization regimes must be verified. An important issue is related to the fission gas release. The coated particle fuel has low defect fractions during fabrication and a high degree of leak tightness with respect to fission products. However, experimental data were obtained from irradiated coated particles in a *fixed* position. In a fluidized bed where particle-particle and particle-wall collisions occur, integrity of the particles must be maintained and failure probability of the particles should be kept as low as possible. For this reason, a small-scale graphite-walled fluidized bed with dummy (non-fisile fuel) TRISO particles is suggested to study the effect of fluidization to the attrition and erosion of the materials.

Another option is to use ZrC instead of SiC for the coating material of TRISO. The melting point of ZrC is higher than that of SiC and it has better performance under irradiation conditions (Minato *et al.*, 2000). ZrC is also mechanically more stable (Petti and Homann, 2002), thus it may constitute better choices with respect to attrition. The principle presented in this thesis and the computational procedure, however, will still be applicable with such alternatives.

- *Nonlinear stability analysis*

For the stability analysis we have used a linear approach, meaning that the system is subject to a small perturbation. However, the neutronics and fluidization are nonlinear. To investigate the stability of the system subject to large perturbations in a wider range of operation, an analysis based on a nonlinear approach is necessary.

- *Enhanced passive safety*

We have presented that a passive system can be applied in the reactor to remove the decay heat. This system can be further enhanced by installing coolant channels or rings in the side reflector or by collecting the particles in a borated-water cooling pool. By doing so the fuel particles can be further cooled while maintaining the subcriticality level of the reactor. Our current decay heat code (DECFLUB) is limited to a simple geometry only and thus it is not able to simulate such situation. Further modeling and tool development is necessary in this case.

Bibliography

Ackroyd, R. T. (1978). A Finite Element Method for Neutron Transport – I. Some Theoretical Considerations. *Annals of Nuclear Energy*, 5:75–94.

Ackroyd, R. T. (1981). The Why and How of Finite Elements. *Annals of Nuclear Energy*, 8:539–566.

Ackroyd, R. T. (1995). Foundations of Finite Element Applications to Neutron Transport. *Progress in Nuclear Energy*, 29:43–56.

Ahlf, J., Conrad, R., Cundy, M., and Scheurer, H. (1990). Irradiation Experiments on High Temperature Gas-Cooled Reactor Fuels and Graphites at the High Flux Reactor Petten. *Journal of Nuclear Materials*, 171:31–36.

Anderson, E., Bai, Z., Bischof, C., Blackford, L. S., Demmel, J., Dongara, J., Croz, J. D., Greenbaum, A., Hammarling, S., McKenney, A., and Sorensen, D. (2000). *LAPACK Users' Guide*. Society for Industrial & Applied Mathematics.

Ansolabehere, S., Deutch, J. J., Driscoll, M., Gray, P. E., Holden, J. P., Joskow, P. L., Lester, R. K., Moniz, E. J., and Todreas, N. E. (2003). *The Future of Nuclear Power: An Interdisciplinary MIT Study*. Massachusetts Institute of Technology.

Babu, S. P., Shah, B., and Talwalker, A. (1978). Fluidization Correlations for Coal Gasification Materials: Minimum Fluidization Velocity and Fluidized Bed Expansion Ratio. *AICHE Symposium Series*, 74:176.

Barrett, R., Berry, M., Chan, T. F., Demmel, J., Donato, J., Dongarra, J., Eijkhout, V., Pozo, R., Romine, C., and der Vorst, H. V. (1994). *Templates for the Solution of Linear Systems: Building Blocks for Iterative Methods*, 2nd Edition. SIAM, Philadelphia, PA.

Bayazitoglu, Y. and Higenyi, J. (1979). Higher-Order Differential Equations of Radiative Transfer: P_3 Approximation. *AIAA Journal*, 17:424–431.

Bokkers, G. A. (2005). *Multi-Level Modelling of The Hydrodynamics in Gas Phase Polymerisation Reactors*. PhD thesis, Twente University, The Netherlands.

Brandau, E. (2002). Microsphere of UO_2 , ThO_2 and PuO_2 for the High Temperature Reactor. In *Transactions of the 1st International Topical Meeting on High Temperature Reactor Technology (HTR)*, Petten, The Netherlands. European Nuclear Society and International Atomic Energy Agency.

Brown, P. N., Byrne, G. D., and Hindmarch, A. C. (1989). VODE: a Variable Coefficient ODE Solver. *SIAM Journal on Scientific and Statistical Computing*, 10:1038–1051.

Budi, G. S. (2003). *Contribution to Advanced Modelling of Turbulent Natural and Mixed Convection*. PhD thesis, Delft University of Technology, The Netherlands.

Carbajo, J. J., Yoder, G. L., Popov, S. G., and Ivanov, V. K. (2001). A Review of The Thermo-physical Properties of MOX and UO_2 Fuels. *Journal of Nuclear Materials*, 299:181–198.

Carlson, B. G. and Lathrop, K. D. (1968). Transport Theory – The Method of Discrete Ordinates. In Greenspan, H., Kelber, C. N., and Okrent, D., editors, *Computing Methods in Reactor Physics*. Cordon and Breach Science Publishers, New York.

Chandrasekhar, S. (1960). *Radiative Transfer*. Dover Publications, New York.

Chapelot, P., Langueille, A., Raepsaet, X., and Hittner, D. (2001). Requirements for High Temperature Fuel Particle Design Assessment. *Progress in Nuclear Energy*, 38:415–418.

Chatfield, C. (1996). *The Analysis of Time Series*. Chapman & Hall, London, fifth edition.

Cheremisinoff, N. and Cheremisinoff, P. (1984). *Hydrodynamics of Gas-Solids Fluidization*. Gulf Publishing Company, Houston.

Chitester, D. C., Kornosky, R. M., Fan, L. S., and Dankoo, J. P. (1984). Characteristics of Fluidization at High Pressure. *Chemical Engineering Science*, 39:253–261.

Cumberland, D. J. and Crawford, R. J. (1987). *The Packing of Particles*. Elsevier, Amsterdam, The Netherlands.

de Leege, P. F. A. (1994). NSLINK: Preparing AMPX MASTER (SCALE) Library from NJOY Output. In Ganesan, S., editor, *Preparation of Processed Nuclear Data Libraries for Thermal, Fast and Fusion Research and Power Reactor Applications*, pages 41–48. International Atomic Energy Agency, Vienna, Austria.

De Oliveira, C. R. E. (1997). Multidimensional Deterministic Radiation Transport: Review and Status. In *CEA Frederic Joliot Summer School*, pages 113–128. CEA, Cadarache, France.

De Oliveira, C. R. E. (1986). An Arbitrary Geometry Finite Element Method for Multi-group Neutron Transport with Anisotropic Scattering. *Progress in Nuclear Energy*, 18:227–236.

Deutch, J. M. and Moniz, E. J. (2006). The Nuclear Option. *Scientific American*, September:76–83.

DIN-25485 (1990). Berechnung der Nachzerfallsleitung der Kernbrennstoffe von Hochtemperaturreaktoren mit kugelförmigen Brennelementen. Technical Report DIN 25 485, Deutsches Institut für Normung e.V.

Ding, J. and Gidaspow, D. (1990). A bubbling Fluidization Model Using Kinetic Theory of Gas Flow. *AIChE Journal*, 36:525–538.

Dinsdale, A. T. (1991). SGTE Data for Pure Elements. *CALPHAD*, 15:317–425.

Duderstadt, J. and Hamilton, L. (1976). *Nuclear Reactor Analysis*. John Wiley & Sons, New York.

Duderstadt, J. J. and Martin, W. R. (1979). *Transport Theory*. John Wiley & Sons, Inc., New York.

Enwald, H., Peirano, E., and Almstedt, A. E. (1997). Eulerian Two-Phase Flow Theory Applied to Fluidization. *International Journal of Multiphase Flow*, 22:21–66.

Ergun, S. (1952). Fluid Flow Through Packed Columns. *Chemical Engineering Progress*, 48:89–94.

Fan, L. S. and Zhu, C. (1998). *Principles of Gas-Solids Flows*. Cambridge University Press, Cambridge, UK.

Feher, S., Hoogenboom, J. E., de Leege, P. F. A., and Valko, J. (1994). Monte Carlo Calculation of Dancoff Factors in Irregular Geometries. *Nuclear Science and Engineering*, 117:227–238.

Ferziger, J. H. and Perić, M. (2002). *Computational Methods for Fluid Dynamics*. Springer-Verlag, Berlin, 3rd edition.

Fink, J. K. (2000). Thermophysical Properties of Uranium Dioxide. *Journal of Nuclear Materials*, 271:1–18.

Fink, J. K., Chasanov, M. G., and Leibowitz, L. (1981). Thermophysical Properties of Uranium Dioxide. *Journal of Nuclear Materials*, 102:17–25.

Fiveland, W. A. (1987). Discrete Ordinate Methods for Radiative Heat Transfer in Isotropically and Anisotropically Scattering Media. *Journal of Heat Transfer*, 109:809–812.

Formisani, B., Girimonte, R., and Mancuso, L. (1998). Analysis of the Fluidization Process of Particle Beds at High Temperature. *Chemical Engineering Science*, 53:951–961.

Geldart, D. (1972). The Effect of Particle Size and Size Distribution on The Behaviour of Gas-Fluidized Beds. *Powder Technology*, 6:201–215.

Gera, D., Gautam, M., Tsuji, Y., Kawaguchi, T., and Tanaka, T. (1998). Computer Simulation of Bubbles in Large-Particle Fluidized Beds. *Powder Technology*, 98:38–47.

Gerwin, H. and Scherer, W. (1987). Treatment of the Upper Cavity in a Pebble-Bed High-Temperature Gas-Cooled Reactor by Diffusion Theory. *Nuclear Science and Engineering*, 97:9–19.

Goldschmidt, M. (2001). *Hydrodynamic Modelling of Fluidised Bed Spray Granulation*. PhD thesis, Twente University, The Netherlands.

Golubev, I., Kadarmetov, I., and Makarov, V. (2002). Mathematical Model and Computer Code for Coated Particles Performance at Normal Operating Conditions. In *Transactions of the 1st International Topical Meeting on High Temperature Reactor Technology (HTR)*, Petten, The Netherlands. European Nuclear Society and International Atomic Energy Agency.

Gomes, J. L. M. A. (2004). *Modelling Heat and Mass Transfer in Gas-Solid Fluidized Beds Using the Two-Fluid Granular Temperature Approach*. PhD thesis, Imperial College London and University of London, U. K.

Grace, J. R. (1982). Fluidized-Bed Hydrodynamics. In Hetsroni, G., editor, *Handbook of Multiphase Systems*, Washington D.C. Hemisphere.

Greene, N. M. (2000a). BONAMI: Resonance Self-Shielding by The Bondarenko Method. Technical Report ORNL/NUREG/CSD-2/V2/R6, Volume 2, Section F1, Oak Ridge National Laboratory, Oak Ridge, Tennessee.

Greene, N. M. (2000b). User's Guide for AMPX Utility Modules. Technical Report ORNL/NUREG/CSD-2/V3/R6, Volume 3, Section M15, Oak Ridge National Laboratory, Oak Ridge, Tennessee.

Greene, N. M. and Petrie, L. M. (2000). XSDRNPM: A One-Dimensional Discrete Ordinates Code for Transport Analysis. Technical Report ORNL/NUREG/CSD-2/V2/R6, Volume 2, Section F3, Oak Ridge National Laboratory, Oak Ridge, Tennessee.

Greene, N. M., Petrie, L. M., and Westfall, R. M. (2000). NITAWL-II: SCALE System Module for Performing Resonance Shielding and Working Library Production. Technical Report ORNL/NUREG/CSD-2/V2/R6, Volume 2, Section F2, Oak Ridge National Laboratory, Oak Ridge, Tennessee.

Gunn, D. J. (1978). Transfer of Heat or Mass to Particles in Fixed and Fluidized Beds. *International Journal of Heat and Mass Transfer*, 21:467–476.

Harms, A. A. and Kingdon, D. R. (1994). A Gravity-Removable Suspended Fuel Core for Passive Coolability of a Reactor. *ANS Transactions*, 71:329.

Hetrick, D. L. (1993). *Dynamics of Nuclear Reactors*. American Nuclear Society, Inc., La Grange Park, Illinois.

Howell, J. R. (1998). The Monte Carlo Method in Radiative Heat Transfer. *Journal of Heat Transfer*, 120:547–560.

Hunt, M. L. (1997). Discrete Element Simulations for Granular Material Flows: Effective Thermal Conductivity and Self-Difusity. *International Journal of Heat Mass Transfer*, 40:3059–3068.

IAEA (1997a). Fuel Performance and Fission Product Behaviour in Gas-Cooled Reactors. Technical Report IAEA-TECDOC-978, International Atomic Energy Agency, Vienna, Austria.

IAEA (1997b). Terms for Describing New, Advanced Nuclear Power Plants. Technical Report IAEA-TECDOC-936, International Atomic Energy Agency, Vienna, Austria.

IAEA (1997c). Thermophysical Properties of Materials for Water Cooled Reactors. Technical Report IAEA-TECDOC-949, International Atomic Energy, Vienna, Austria.

IAEA (2000). Irradiation Damage in Graphite Due to Fast Neutrons in Fission and Fussion Systems. Technical Report IAEA-TECDOC-1154, International Atomic Energy Agency, Vienna, Austria.

IAEA (2001). Heat Transport and Afterheat Removal for Gas Cooled Reactors Under Accident Conditions. Technical Report IAEA-TECDOC-1163, International Atomic Energy Agency, Vienna, Austria.

Janssen, L. P. B. M. and Warmoeskerken, M. M. C. G. (1997). *Transport Phenomena Data Companion*. Delftse Universitaire Pers, Delft, The Netherlands.

Jenkins, J. T. and Savage, S. B. (1983). A Theory for The Rapid Flow of identical, Smooth, Nearly Elastic, Spherical Particles. *Journal of Fluid Mechanics*, 130:187–202.

Kaviany, M. (1991). *Principles of Heat Transfer in Porous Media*. Springer, New York.

Kendal, M. and Ord, J. K. (1990). *Time Series*. Edward Arnold, London, third edition.

Kingdon, D. R. (1998). *Safety Characteristics of a Suspended Pellet Fission Reactor System*. PhD thesis, McMaster University, Hamilton, Ontario.

Kloosterman, J. L., Golovko, V. V., van Dam, H., and van der Hagen, T. H. J. J. (1999). Neutronic Design of a Fluidized Bed Reactor. In *Proc. GLOBAL '99*, Wyoming.

Kloosterman, J. L., Golovko, V. V., van Dam, H., and van der Hagen, T. H. J. J. (2001). Conceptual Design of a Fluidized Bed Nuclear Reactor. *Nuclear Science and Engineering*, 139:118–137.

Kugeler, K. (1992). Principles of Decay Heat Removal in Reactor Technology – Present Status and Future Prospects. In *IAEA-TECDOC-757: Decay Heat Removal and Heat Transfer Under Normal and Accident Conditions in Gas Cooled Reactors*, Vienna, Austria. International Atomic Energy Agency.

Kugeler, K. and Phlippen, P. W. (1996). The Potential of the Self-Acting Safety Features of High Temperature Reactors. *Kerntechnik*, 61:239.

Kuipers, J. A. M., Prins, W., and van Swaaij, W. P. M. (1992). Numerical Calculation of Wall-to-Bed Heat Transfer Coefficients in Gas-Fluidized Beds. *AIChE Journal*, 38:1079–1091.

Kuipers, J. A. M., van Duin, K. J., van Beckum, F. P. H., and van Swaaij, W. P. M. (1993). Computer Simulation of The Hydrodynamics of a Two-Dimensional Gas-Fluidized Bed. *Computers and Chemical Engineering*, 17:839–858.

Kunii, D. and Levenspiel, O. (1991). *Fluidization Engineering*. Series in Chemical Engineering. Butterworth-Heinemann, Stoneham, second edition.

Landers, N. and Petrie, L. (2000). CSAS: Control Module for Enhanced Criticality Safety Analysis Sequences. Technical Report ORNL/NUREG/CSD-2/V2/R6, Volume 1, Section C4, Oak Ridge National Laboratory, Oak Ridge, Tennessee.

Larsen, M. E. and Howell, J. R. (1986). Least-Squares Smoothing of Direct-Exchange Areas in Zonal Analysis. *Journal of Heat Transfer*, 108:239–242.

Lathouwers, D., Agung, A., van der Hagen, T. H. J. J., van Dam, H., Pain, C. C., de Oliveira, C. R. E., and Goddard, A. J. H. (2003). Dynamics Modeling and Stability Analysis of a Fluidized Bed Nuclear Reactor. *Progress in Nuclear Energy*, 43:437–443.

Lathouwers, D. and Bellan, J. (2001). Modeling of Dense Gas-Solid Reactive Mixtures Applied to Biomass Pyrolysis in a Fluidized Bed. *International Journal of Multiphase Flow*, 27:2155–2187.

Lathrop, K. D. (1966). Use of Discrete-Ordinates Methods in Solution of Photon Transport Problems. *Nuclear Science and Engineering*, 24:381–388.

Lemmon, E. W., McLinden, M. O., and Friend, D. G. (2003). Thermophysical Properties of Fluid Systems. In Linstrom, P. J. and Mallard, W. G., editors, *NIST Chemistry Webbook, NIST Standard Reference Database Number 69*. National Institute of Standards and Technology, Gaithersburg MD, 20899.

Lewis, E. E. and Miller, W. F. (1984). *Computational Methods of Neutron Transport*. John Wiley & Sons, New York.

Lun, C. K. K., Savager, S. B., Jefferey, D. J., and Chepurniy, N. (1984). Kinetic Theories for Granular Flow: Inelastic Particles in Couette Flow and Slightly Inelastic Particles in a General Flowfield. *Journal of Fluid Mechanics*, 140:223–256.

Mansoorzadeh, S., Pain, C. C., de Oliveira, C. R. E., and Goddard, A. J. H. (1998). Finite Element Simulations of Incompressible Flow Past a Heated/Cooled Sphere. *International Journal of Numerical Methods in Fluids*, 28:903–915.

Massimo, L. (1976). *Physics of High-Temperature Reactors*. Pergamon Press, Oxford, U.K.

Matzke, H., Lucuta, P. G., Verrall, R. A., and Henderson, J. (1997). Specific Heat of UO₂-based SIMFUEL. *Journal of Nuclear Materials*, 247:121–126.

Melese, G. and Katz, R. (1984). *Thermal and Flow Design of Helium-Cooled Reactors*. American Nuclear Society, La Grange Park, Illinois.

Miller, G. K., Petti, D. A., Varacalle, D. J., and Maki, J. T. (2001). Consideration of the Effects of Fuel Particle Behavior From Shrinkage Cracks in the Inner Pyrocarbon Layer. *Journal of Nuclear Materials*, 295:205–212.

Minato, K., Ogawa, T., Fukuda, K., Sekino, H., Miyanishi, H., Kado, S., and Takahashi, I. (1993). Release Behavior of Metallic Fission Products From HTGR Fuel Particles at 1600 to 1900 °C. *Journal of Nuclear Materials*, 202:47–57.

Minato, K., Ogawa, T., Fukuda, K., Shimizu, M., Tayama, Y., and Takahashi, I. (1994). Fission Product Behavior in TRISO Coated UO₂ Fuel Particles. *Journal of Nuclear Materials*, 208:266–281.

Minato, K., Ogawa, T., Sawa, K., Ishikawa, A., Tomita, T., Iida, S., and Sekino, H. (2000). Irradiation Experiment on ZrC-Coated Fuel Particles for Hight Temperature Gas-Cooled Reactors. *Nuclear Technology*, 130:272–281.

Mizuno, T., Ito, T., and Ohta, K. (1990). The Inherently-Safe Fluidized Bed Boiling Water Reactor Concept. *Annals of Nuclear Energy*, 17:487–492.

Modest, M. F. (2003a). *Radiative Heat Transfer*. Academic Press, Massachussets, second edition.

Modest, M. F. (2003b). Thermal Radiation. In Bejan, A. and Kraus, A. D., editors, *Heat Transfer Handbook*, pages 573–633. John Wiley & Sons, Inc.

Mori, S. and Wen, C. Y. (1975). Estimation of Bubble Diameter in Gaseous Fluidized Beds. *AICHE Journal*, 21:109–115.

Mourogov, K., Fukuda, K., and Kagramanian, V. (2002). The Need for Innovative Nuclear Reactor and Fuel Cycle Systems: Strategy for Development and Future Prospects. *Progress in Nuclear Energy*, 40:285–299.

Mudde, R. F., Harteveld, W. K., van den Akker, H. E. A., van der Hagen, T. H. J. J., and van Dam, H. (1999). Gamma Radiation Densitometry for Studying The Dynamics of Fluidized Beds. *Chemical Engineering Science*, 54:2047–2054.

Nickel, H., Nabielek, H., Pott, G., and Mehner, A. W. (2002). Long Time Experience with the Development of HTR Fuel Elements in Germany. *Nuclear Engineering and Design*, 217:141–151.

Ogawa, T., Fukuda, K., Sekino, H., Numata, M., and Ikawa, K. (1985). Release of Metal Fission Products from UO₂ Kernel of Coated Fuel Particle. *Journal of Nuclear Materials*, 135:18–31.

Ohashi, K., Okamoto, F., and Hayakawa, H. (2000). Modular High Temperature Reactor (Modular HTR) Contributing the Global Environment Protection. *Progress in Nuclear Energy*, 37:253–258.

ORNL (1989). Bold-Venture IV: A Reactor Analysis Code System. Technical report, Oak Ridge National Laboratory.

Ott, K. O. and Neuhold, R. J. (1985). *Introductory Nuclear Reactor Dynamics*. American Nuclear Society, La Grange Park, Illinois.

Özişik, M. N. (1985). *Radiative Transfer and Interaction with Conduction and Convection*. Werbel and Peck.

Pain, C. C., de Oliveira, C. R. E., and Goddard, A. J. H. (2001a). Non-Linear Space-Dependent Kinetics for Criticality Assessment of Fissile Solutions. *Progress in Nuclear Energy*, 39:53–114.

Pain, C. C., Mansoorzadeh, S., and de Oliveira, C. R. E. (2001b). A Study of Bubbling and Slugging Fluidized Beds Using The Two-Fluid Granular Temperature Model. *International Journal of Multiphase Flow*, 27:527–551.

Pain, C. C., Mansoorzadeh, S., de Oliveira, C. R. E., and Goddard, A. J. H. (2001c). Numerical Modelling of Gas-Solid Fluidized Beds Using the Two-Fluid Approach. *International Journal of Numerical Methods in Fluids*, 36:91–124.

Pain, C. C., Mansoorzadeh, S., Gomes, J. L. M., and de Oliveira, C. R. E. (2002). A Numerical Investigation of Bubbling Gas-Solid Fluidized Bed Dynamics in 2-D Geometries. *Powder Technology*, 128:56–77.

Petrie, L. (2001). Dancoff Factor: Black or Grey. SCALE Notebook page 349.
URL:<http://www-rsicc.ornl.gov/cgi-bin/enote.pl?nb=scale&action=view&page=349>.

Petrie, L. and Landers, N. (2000). KENO-Va: An Improved Monte Carlo Criticality Program with Supergrouping. Technical Report ORNL/NUREG/CSD-2/R6, Volume 2, Section F11, Oak Ridge National Laboratory, Oak Ridge, Tennessee.

Petti, D. A. and Homan, F. J. (2002). Coated Particle Fuel Behavior Under Irradiation. In *Proc. HTR-ECS 2002*, High Temperature Reactor School, Cadarache, France.

Porta, J., Pinto, P. L., Bonnet, M., Kugeler, K., Alkan, Z., Heuss, R., and von Lensa, W. (2001). Coated Particle Fuel to Improve Safety, Design, Economics in Water-Cooled and Gas-Cooled Reactors. *Progress in Nuclear Energy*, 38:407–410.

Raithby, G. D. and Chiu, E. H. (1990). A Finite-Volume Method for Predicting Radiant Heat Transfer in Enclosures with Participating Media. *Journal of Heat Transfer*, 112:415–423.

Ranade, V. R. (2002). *Computational Flow Modeling for Chemical Reactor Engineering*. Academic Press, San Diego.

Ratzell III, A. C. and Howell, J. R. (1983). Two-Dimensional Radiation in Absorbing-Emitting Media Using the P-N Approximation. *ASME Journal of Heat Transfer*, 105:333–340.

Rhoades, W. A. and Childs, R. L. (1988). The DORT Two-Dimensional Discrete Ordinates Transport Code. *Nuclear Science and Engineering*, 99(1):88.

Rhoades, W. A. and Simpson, D. B. (1997). The TORT Three-Dimensional Discrete Ordinates Neutron/Photon Transport Code. Technical Report ORNL/TM-13221, Oak Ridge National Laboratory.

Ronchi, C., Sheindlin, M., Musella, M., and Hyland, G. J. (1999). Thermal Conductivity of Uranium Dioxide up to 2900 K from Simultaneous Measurement of the Heat Capacity and Thermal Diffusivity. *Journal of Applied Physics*, 85:776–789.

Rowe, P. N. (1961). Drag Forces in a Hydraulic Model of a Fluidized Bed, Part II. *Transactions of Institutional Chemical Engineers*, 39:175–186.

Sawa, K., Minato, K., Tobita, T., and Fukuda, K. (1997). An Investigation of Cesium Release from Coated Particle Fuel of the High-Temperature Gas-Cooled Reactor. *Nuclear Technology*, 118:123–131.

Sawa, K., Suzuki, S., and Shiozawa, S. (2001). Safety Criteria and Quality Control of HTTR Fuel. *Nuclear Engineering and Design*, 208:305–313.

SCDAP/RELAP5 (1997). SCDAP/RELAP5/MOD3.2 Code Manual, Volume IV: MATPRO - A Library of Materials Properties for Light-Water Reactor Accident Analysis. Technical Report NUREG/CR-6150, vol. IV (INEL-96/0422), Rev.1., Idaho National Engineering and Environmental Laboratory.

Sefidvash, F. (1985). A Fluidized-Bed Nuclear Reactor Concept. *Nuclear Technology*, 71:527–534.

Sefidvash, F. (1996). Status of the Small Modular Fluidized Bed Light Water Nuclear Reactor Concept. *Nuclear Engineering and Design*, 167:203–214.

Sefidvash, F. (2002). Fluidized Bed Nuclear Reactor as a IV Generation Reactor. In *Proc. PHYSOR 2002*, Seoul, Korea.

Siegel, R. and Howell, J. R. (2001). *Thermal Radiation Heat Transfer*. Taylor and Francis, New York.

Stacey, W. M. (2001). *Nuclear Reactor Physics*. John Wiley & Sons, Inc.

Taube, M., Lanfranchi, M., von Weissenfluh, T., Ligou, J., Yadigaroglu, G., and Taube, P. (1986). The Inherently-Safe Power Reactor Dyonisos (DYnamic Nuclear Inherently-Safe Reactor Operating with Spheres). *Annals of Nuclear Energy*, 13:641–648.

Tien, C.-L. and Drolen, B. L. (1987). Thermal Radiation in Particulate Media with Dependent and Independent Scattering. *Annual Review of Numerical Fluid Mechanics and Heat Transfer*, 1:1–32.

Tien, C.-L. and Vafai, K. (1989). Convective and Radiative Heat Transfer in Porous Media. *Advances in Applied Mechanics*, 27:225–282.

Truelove, J. S. (1987). Discrete-Ordinate Solutions of The Radiation Transport Equation. *Journal of Heat Transfer*, 109:1048–1051.

Tsuchie, Y. (2000). Desirability of Small Reactor, HTGR in Particular. *Progress in Nuclear Energy*, 37:253–258.

Tsuji, Y. and Kawaguchi, T. (1993). Discrete Particle Simulation of Two Dimensional Fluidized Bed. *Powder Technology*, 77:78–87.

U.S. DOE and GIF (2002). A Technology Roadmap for Generation IV Nuclear Energy System. Technical Report GIF-002-00, U. S. DOE Nuclear Energy Research Advisory Committee and the Generation IV International Forum.

Van Dam, H., van der Hagen, T. H. J. J., and Hoogenboom, J. E. (1996). Neutronics and Thermal Aspects of a Fluidized Bed Fission Reactor. In *Proc. Int. Conf. on Emerging Nuclear Energy System*, page 196, Obninsk, Russia.

Van der Hagen, T. H. J. J., van Dam, H., Harteveld, W., Hoogenboom, J. E., Khotylev, V. A., and Mudde, R. F. (1997). Studies on the Inhomogeneous Core Density of a Fluidized Bed Nuclear Reactor. In *Proc. GLOBAL '97*, page 1050, Yokohama, Japan.

Van der Hoef, M. A., Beetstra, R., and Kuipers, J. A. M. (2005). Lattice Boltzman Simulations of Low-Reynolds-Number Flow Past Mono- And Bidisperse Arrays of Sphere: Results for The Permeability And Drag Force. *Journal of Fluid Mechanics*, 528:233–254.

Van der Stappen, M. L. M. (1996). *Chaotic Hydrodynamics of Fluidized Beds*. PhD thesis, Delft University of Technology, The Netherlands.

Van Wachem, B. (2000). *Derivation, Implementation and Validation of Computer Simulation Models for Gas-Solid Fluidized Beds*. PhD thesis, Delft University of Technology, The Netherlands.

Versteeg, H. K. and Malalasekera, W. (1995). *An Introduction to Computational Fluid Dynamics: The Finite Volume Method*. Pearson Education Ltd., Essex, England.

Viskanta, R. and Mengüç, M. P. (1987). Radiation Heat Transfer in Combustion Systems. *Progress in Energy and Combustion Science*, 13:97–160.

Wen, C. Y. and Yu, Y. H. (1966). Mechanics of Fluidization. *Chem. Eng. Progr. Symp. Ser.*, 62:100.

Wesseling, P. (2000). *Principles of Computational Fluid Dynamics*. Springer, Berlin.

Wilcox, D. C. (1993). *Turbulence Modeling for CFD*. DCW Industries, Inc., La Cañada, California.

WIMS8A (1999). User Guide for Version 8. Technical Report ANSWERS/WIMS (99)9, AEA Technology.

Yan, X. (1990). *Dynamics Analysis and Control System Design for an Advanced Nuclear Gas Turbine Power Plant*. PhD thesis, MIT, Cambridge, USA.

Nomenclature

Roman symbols

<i>Symbol</i>	<i>Quantity</i>	<i>Unit</i>
A_b	bed cross-sectional area	m^2
A_i	total interfacial area	m^2
a_{pg}	interfacial area per unit volume of the solid particles	m^{-1}
C_D	drag coefficient	-
C_i	delayed neutron precursor concentration	m^{-3}
C_p	specific heat capacity	$\text{J kg}^{-1} \text{K}^{-1}$
$C_{\epsilon 1}, C_{\epsilon 2}, C_{\epsilon 3}$	turbulent closure constant	-
C_{μ}	turbulent closure constant	-
D	bed diameter	m
D	diffusion coefficient	m
d_b	bubble diameter	m
d_p	particle diameter	m
d_{bm}	maximum bubble diameter	m
d_{b0}	initial bubble diameter	m
E	energy	J
e	coefficient of particle-particle restitution	-
E_b	blackbody emissive power	W m^{-2}
F_d	drag force	m kg s^{-2}
F_g	gravity force	m kg s^{-2}
\mathbf{g}	vector of the independent input variables	consistent units
G	mass flow rate	kg s^{-1}
G	total radiation intensity	W m^{-2}
g	gravitational acceleration	m s^{-2}
G_{ij}	gain of the transfer function	consistent units
G_k	buoyancy generation rate of turbulent kinetic energy	$\text{kg m}^{-1} \text{s}^{-3}$
g_0	radial distribution function	-
H	bed height	m
h	enthalpy	J kg^{-1}

H_0	height of the packed bed	m
H_j	transfer function of the system	consistent units
h_{pg}	heat transfer coefficient between gas and solid phase	$\text{W m}^{-2} \text{K}^{-1}$
\mathbf{I}	unit vector or tensor	-
I	intensity of radiation	$\text{W m}^{-2} \text{sr}^{-1}$
I_b	blackbody radiation intensity	$\text{W m}^{-2} \text{sr}^{-1}$
J_x, J_g	Jacobian matrices	consistent units
k	kinetic energy of the turbulent fluctuation	$\text{m}^2 \text{s}^{-2}$
L^*	characteristic length	m
m	mass	kg
N_d	number of the decay heat groups	-
N_{pc}	number of the delayed neutron precursor groups	-
N_s	concentration of scatterer particles	particles m^{-3}
p	pressure	Pa
P_{pr}	prompt power	W
P_t	total power	W
P_{d0}	decay power at the initial shutdown time	W
P_d	decay power	W
P_k	production rate of the turbulent kinetic energy	$\text{kg m}^{-1} \text{s}^{-3}$
\mathbf{q}_Θ	flux of fluctuating energy	kg m^{-3}
\mathbf{q}	heat flux	W m^{-2}
Q	interfacial heat transfer	W
Q_f	prompt recoverable energy release per fission	J fission^{-1}
S	neutron source	consistent units
\mathbf{T}	viscous stress tensor	$\text{m}^{-1} \text{kg s}^{-2}$
T	temperature	K
t	time	s
T_i	temperature at the initial time of the transient	K
u	superficial velocity	m s^{-1}
u_{mb}	minimum bubbling velocity	m s^{-1}
u_{mf}	minimum fluidization velocity	m s^{-1}
u_t	terminal velocity	m s^{-1}
\mathbf{u}	velocity vector	m s^{-1}
\mathbf{v}	velocity vector	m s^{-1}
V	volume	m^{-3}
\mathbf{x}	vector of the state variables	consistent units
y_p	distance to the wall of the reflector	m
y_+	dimensionless distance to the wall of the reflector	-
z	height	m

Greek symbols

Symbol	Quantity	Unit
α	volume fraction	-

$\alpha_{d,t}$	total temperature coefficient of reactivity	K^{-1}
$\alpha_{g,0}$	void fraction of the packed bed	-
$\alpha_{d,c}$	core temperature coefficient of reactivity	K^{-1}
β	coefficient of thermal expansion	K^{-1}
β	gas-solid friction coefficient	$\text{kg m}^{-3} \text{s}^{-1}$
β	total delayed neutron fraction	-
β_i	fraction of the i th delayed neutron group	-
χ_p	prompt fission neutron spectra	-
ϵ	emissivity	-
ϵ	dissipation rate of turbulent kinetic energy	$\text{m}^2 \text{s}^{-3}$
γ	collisional energy dissipation	$\text{kg m}^{-1} \text{s}^{-3}$
γ_n	decay heat yield for fission product of group n	$\text{J fission}^{-1} \text{s}^{-1}$
κ	granular conductivity	$\text{kg m}^{-1} \text{s}^{-1}$
Λ	effective neutron generation time	s
λ	thermal conductivity	$\text{W m}^{-1} \text{K}^{-1}$
λ_i	decay constant of the i th group delayed neutron precursor	s^{-1}
λ_n	decay constant for fission product of group n	s^{-1}
λ_{gas}	thermal conductivity of pure gas	$\text{W m}^{-1} \text{K}^{-1}$
μ	dynamic viscosity	Pas
μ_t	turbulent viscosity	$\text{kg m}^{-1} \text{s}^{-1}$
ν	number of neutron generated per fission	-
Ω	directional solid angle	sr
ϕ_s	sphericity of the particles	-
Ψ	fission rate	fission s^{-1}
ψ^\pm	even- and odd-parity neutron flux	$\text{neutron cm}^{-2} \text{sr}^{-1} \text{s}^{-1}$
Ψ	neutron angular flux	$\text{neutron cm}^{-2} \text{sr}^{-1} \text{s}^{-1}$
ρ	reactivity	-
ρ	reflectivity	-
ρ_g	density of gas	kg m^{-3}
ρ_p	density of particle	kg m^{-3}
Σ_a	absorption cross-section / coefficient	m^{-1}
σ_c	turbulent Prandtl number for the dissipation rate of k	-
Σ_f	macroscopic fission cross-section	m^{-1}
σ_k	turbulent Prandtl number for the turbulent kinetic energy	-
Σ_s	scattering cross-section / coefficient	m^{-1}
σ_s	per particle scattering cross-section	m^2
Σ_t	total cross-section / extinction coefficient	m^{-1}
τ	time constant	s
τ_{12}	gas-particle interaction time-scale	s
τ	stress tensor	$\text{m}^{-1} \text{kg s}^{-2}$
Θ	granular temperature	$\text{m}^2 \text{s}^{-2}$
ω	frequency	rad s^{-1}
ζ_p	solid-phase bulk viscosity	$\text{kg m}^{-1} \text{s}^{-1}$

Subscripts

<i>Symbol</i>	<i>Description</i>
<i>air</i>	pertaining to the air
<i>conv</i>	convection
<i>core</i>	pertaining to the core
<i>ex</i>	excess
<i>ext</i>	external
<i>g</i>	gas phase
<i>hom</i>	pertaining to the homogeneous particle distribution
<i>in</i>	inlet
<i>jet</i>	pertaining to the jet model of particle distribution
<i>k</i>	phase index
<i>m</i>	angular coordinate direction
<i>mf</i>	pertaining to minimum fluidization condition
<i>max</i>	maximum
<i>out</i>	outlet
<i>p</i>	solid (particle) phase
<i>r</i>	reflector
<i>rad</i>	radiation
<i>ref</i>	reference
<i>sm</i>	shutdown margin
<i>tr</i>	transient
<i>w</i>	pertaining to the wall

Superscripts

<i>Symbol</i>	<i>Description</i>
$''$	volumetric

Abbreviations

<i>Abbreviation</i>	<i>Description</i>
AR	Auto Regression
BWR	Boiling Water Reactor
CFD	Computational Fluid Dynamics
CG	Conjugate Gradient
DOM	Discrete Ordinates Method
DPM	Discrete Particle Model
DR	Decay Ratio
ECCS	Emergency Core Cooling System
FLUBER	Fluidized Bed Nuclear Reactor
GMRES	Generalized Minimum RESidual
HTGR	High Temperature Gas-cooled Reactor

LOCA	Loss-of-Coolant Accident
LOFA	Loss-of-Flow Accident
LBM	Lattice Boltzman Model
LHS	Left Hand Side
LWR	Light Water Reactor
MFR	Moderator-to-Fuel Ratio
NIST	National Institute of Standards and Technology
ODE	Ordinary Differential Equation
PHWR	Pressurized Heavy Water Reactor
PWR	Pressurized Water Reactor
RANS	Reynolds-Averaged Navier-Stokes
RHS	Right Hand Side
RTE	Radiative Transfer Equation
SPD	Symmetric Positive Definite
SVR	Surface-to-Volume Ratio
TFM	Two Fluid Model
TVD	Total Variation Diminishing
VF	View Factor

Summary

In this thesis a conceptual design of an innovative high temperature reactor based on the fluidization principle (FLUBER) is proposed. The reactor should satisfy the following requirements: (a) modular and low power, (b) large shutdown margin, (c) able to produce power when the bed of particles expands and stop as soon as the coolant flow is lost, (d) stable from the reactivity point of view, (e) resistant to inherent fluctuations in the fluidization regime, and (f) able to remove post-shutdown decay heat by passive means without compromising the safety margin.

The research has been conducted in three parts. The first part is concerned with the static behavior of the reactor. This includes setting the design targets and parameters, upon which a preliminary design is then proposed. The reactor should have a large cold shutdown margin so that the reactor remains subcritical if the coolant does not flow. The other design target is that the reactor has ample excess reactivity to compensate for the negative reactivity feedback from the fuel temperature. The calculations were performed by using a Monte Carlo code, KENO-V.a, with nuclear data libraries based on the JEF-2.2 data file. The results show that the maximum fuel temperature at which FLUBER can still achieve criticality is around 1200 K. The behavior of the reactor at low and high void fraction and with a nonuniform distribution of fuel particles is further investigated. It is shown that radial redistribution of particles and the presence of large bubbles in the bed cause a large change in reactivity.

The subject of the second part is related to the behavior of the reactor under dynamic conditions. A first approach to understand the behavior of the system is to use a zero-dimensional dynamics (or point dynamics) model comprising coupled neutronics, heat transfer and fluidization. This model is implemented in the DYNFLUB code. Since the real system is more complicated due to the movement of particles and the occurrence of bubbles in the bed, the point-dynamics model is supported by incorporating the results of three-dimensional static calculations in terms of a time-dependent stochastic external reactivity. The results show that power is produced only when a specific coolant flow rate has been reached and the bed has expanded. Increasing the flow rate further increases the power generated. However, as soon as the coolant is stopped, the bed becomes strongly

subcritical and the fission process stops. The reactor is able to produce power at maximum 120 MW and has a specific power of ≈ 3.5 MW per kg U²³⁵ and a power density of ≈ 10 MW/m³.

The stability of the proposed system under various flow rate conditions has been investigated by using a root-locus analysis. The resulting eigenvalues are found to have negative real parts for all mass flow rates within the operational range of the reactor. The stability analysis has also been performed for sinusoidal disturbances and shows that the reactor is stable for all frequencies. These results indicate that, in terms of linear system, the reactor is stable.

The presence of bubbles and their consequences to the reactivity change are difficult to capture in the point-dynamics code. For this reason, a multidimensional dynamics code is used to study this phenomenon. The simulations of time- and space-dependent dynamics have been performed by using the FETCH code system of Imperial College. The fission power fluctuations are large, but the gas temperature is relatively steady after an initial transient. The difference between the temperatures of the fuel and the gas is almost negligible due to the size of the particles and the good thermal conductivity of the coated particles. The temperature of the bed is near uniform due to rapid mixing of particles.

The third part of this research deals with the decay heat removal in absence of a forced cooling system. A two-dimensional multimode heat transfer model that includes convection, conduction and thermal radiation has been developed and implemented in the DECFLUB code. With this tool it is investigated what the maximum power level can be without the fuel temperature exceeding a predetermined limit, here chosen as 1873 K.

Several different cases have been considered and the results of the calculations indicate that to a certain extent it is possible to remove the decay heat of the fluidized bed reactor by passive means. The worst case scenario has been studied when the system is depressurized and the thermal conductivity of the graphite reflector has decreased due to neutron irradiation. The maximum operating power level of which its associated decay heat can be removed in this case is slightly above 50 MW.

In conclusion, by tailoring the design of the fuel particles and the geometry of the reactor the proposed system can satisfy all of the predetermined requirements. By using specialized tools such as the FETCH code system, the dynamic behavior of the reactor can be well understood. However, several issues remain open such as (i) the strength and durability of TRISO materials under fluidization conditions and (ii) an enhanced passive system to further cool down the particles after the reactor has been shutdown.

Samenvatting

In dit proefschrift wordt een concept van een innovatieve hoge-temperatuur reactor voorgesteld op basis van het fluidisatie principe (FLUBER). De reactor dient aan de volgende eisen te voldoen: (a) modulair en laag vermogen , (b) grote afschakelmarge, (c) in staat om vermogen te produceren in opgeblazen toestand en hiermee te stoppen wanneer de koelmiddelstroom uitvalt, (d) stabiel uit reactiviteitoogpunt (e) bestand tegen inherent fluctuaties in het fluidisatiegebied, en (f) in staat om vervalwarmte op passieve manier af te voeren zonder de veiligheid aan te tasten.

Het project is opgedeeld in drie delen. Het eerste deel betreft het statische gedrag van de reactor alsmede het stellen van doelen en randvoorwaarden waarop het voorlopig ontwerp is gebaseerd. De reactor dient een grote afschakelmarge te hebben en dient subkritiek te blijven als de koelmiddelstroom stopt. Een andere eis aan de reactor is dat er voldoende overreactiviteit aanwezig is om de negatieve terugkoppeling afkomstig van de verhoogde temperatuur te compenseren. De berekeningen zijn uitgevoerd met de Monte Carlo code, KENO-V. a, met databibliotheken gebaseerd op de JEF-2.2 bestanden. De resultaten tonen aan dat de maximum temperatuur van de brandstof bij een kritiek systeem maximaal 1200 K kan bedragen. Het gedrag van de reactor is onderzocht bij lage en hoge gasfracties en in geval van een inhomogene verdeling van de brandstofdeeltjes in het bed. Aangetoond is dat radiale herdistributie van deeltjes en de aanwezigheid van bellen in het bed een grote invloed hebben op de reactiviteit.

Het tweede deel van het project betreft het gedrag van de reactor onder dynamische condities. Een eerste aanzet tot modellering van het systeem is gebruik van een nuldimensionaal model bestaande uit modules voor neutronica, warmteoverdracht en fluidisatie. Dit model is geïmplementeerd in de zogenaamde DYNFLUB code. In werkelijkheid is het systeem een stuk gecompliceerder door de beweging van de deeltjes in het bed. Hierom zijn de puntdynamische berekeningen uitgebreid met stochastische tijdafhankelijke reactiviteitstermen die gespecificeerd zijn op basis van 3-dimensionale statische berekeningen.

De resultaten tonen aan dat de reactor alleen dan vermogen produceert wanneer een zekere koelmiddelstroom wordt overschreden en het bed tot bepaalde hoogte is opgeblazen. Het verhogen van het koelmiddeldebit verhoogt het vermogen van de reactor.

Het splijtingsproces stopt wanneer de koelmiddelstroom wordt afgeschakeld omdat de reactor sterk subkritiek wordt. De reactor heeft een maximaal vermogen van 120 MW en heeft een specifiek vermogen van ≈ 3.5 MW per kg U²³⁵ en een vermogensdichtheid van ≈ 10 MW/m³.

De stabiliteit van het voorgestelde reactorontwerp is onderzocht met een eigenwaarde-analyse. De berekende eigenwaarden hebben een negatief reëel deel voor alle relevante waarden van de koelmiddelstroom. Een stabiliteitsanalyse is ook uitgevoerd voor sinusvormige verstoringen en heeft aangetoond dat de reactor stabiel is tegen verstoringen van alle frequenties. Deze resultaten tonen aan dat de reactor lineair stabiel is.

De aanwezigheid van bellen in het bed en de resulterende reactiviteiteffecten is moeilijk te verdisconteren in het puntdynamisch model. Hierom is voor deze doeleinden tevens een multidimensionale dynamische code gebruikt. De ruimte- en tijdafhankelijke simulaties zijn uitgevoerd met het FETCH codesysteem van Imperial College. Hieruit blijkt dat de vermogensfluctuaties groot zijn maar dat de gastemperatuur vrijwel constant blijft na een initiële transient. Het verschil in temperatuur tussen de deeltjes en het omringende gas is verwaarloosbaar vanwege de kleine diameter van de deeltjes en de hoge thermische geleiding van de deeltjes. De temperatuur van het bed is vrijwel uniform vanwege de goede menging van de deeltjes.

Het derde deel van het project betreft de afvoer van vervalwarmte na afschakeling van de reactor in afwezigheid van een actief koelsysteem. Een tweedimensionaal model gebaseerd op de incorporatie van convectie, geleiding en stralingstransport is ontwikkeld en geïmplementeerd in de DECFLUB code. Op basis van dit model is bepaald wat het maximum vermogen van de reactor mag zijn om de resulterende vervalwarmte af te voeren zonder een temperatuurlimiet van de brandstof te overschrijden (1873 K).

Diverse scenario's zijn bestudeerd en de resultaten van de berekeningen geven aan dat de vervalwarmte tot op zekere hoogte passief kan worden afgevoerd. Het meest ongunstige geval is als uitgangspunt genomen waar het systeem van druk af is en waar de geleiding binnen het grafiet is afgenomen door een lange periode van bestraling. Het maximale vermogen waarvan de vervalwarmte passief kan worden afgevoerd bedraagt iets boven 50 MW.

Concluderend kan een reactor ontworpen worden die aan alle vooropgestelde eisen voldoet door zowel het ontwerp van de brandstofdeeltjes en de reactorgeometrie aan te passen. Dor gebruik van specialistische codeystemen zoals FETCH kan het dynamische gedrag van de reactor goed worden beschreven en begrepen. Een aantal kwesties blijven op dit moment echter open zoals (i) de sterkte en duurzaamheid van de TRISO deeltjes onder fluidisatiecondities en (ii) een verbeterd passief systeem om de deeltjes te koelen na afschakeling van de reactor.

Ringkasan

Pada disertasi ini diajukan rancangan konseptual reaktor nuklir inovatif bersuhu tinggi yang dioperasikan berdasarkan prinsip fluidisasi. Reaktor tersebut harus memenuhi persyaratan-persyaratan sebagai berikut: (a) berbentuk modular dan mempunyai daya yang kecil, (b) mempunyai batas pemadaman yang besar, (c) mampu menghasilkan daya ketika hamparan partikel mengalami ekspansi dan berhenti beroperasi ketika aliran pendingin hilang, (d) stabil dari sudut pandang reaktivitas, (e) tahan terhadap fluktuasi inheren pada rejim fluidisasi, dan (f) mampu mengambil kalor peluruhan pasca pemadaman secara pasif tanpa membahayakan batas-batas keselamatan.

Penelitian ini dilakukan dalam tiga bagian. Bagian pertama terkait dengan perilaku reaktor pada keadaan statis. Termasuk di dalamnya adalah penentuan sasaran dan parameter yang mendasari rancangan awal. Reaktor harus mempunyai batas pemadaman keadaan dingin yang besar sehingga reaktor tetap berada pada kondisi subkritis apabila pendingin tidak mengalir. Sasaran perancangan yang lain adalah bahwa reaktor mempunyai nilai reaktivitas lebih yang memadai untuk mengkompensasi umpan balik reaktivitas negatif dari suhu bahan bakar. Perhitungan dilakukan menggunakan kode Monte Carlo, KENO-V.a, dengan pustaka data nuklir diambil dari JEF-2.2. Hasil menunjukkan bahwa suhu bahan bakar maksimum apabila FLUBER masih kritis adalah sekitar 1200 K. Selanjutnya dipelajari juga perilaku reaktor ini ketika berada pada fraksi hampa yang rendah maupun tinggi serta ketika partikel bahan bakar terdistribusi secara tidak merata. Hasil menunjukkan bahwa pendistribusian partikel ke arah radial serta adanya gelembung besar pada hamparan menyebabkan perubahan reaktivitas yang besar.

Tema dari bagian kedua terkait dengan perilaku reaktor pada kondisi dinamis. Pendekatan awal untuk memahami perilaku reaktor adalah dengan menggunakan model dinamika titik yang terdiri dari pengkopelan neutronika, perpindahan kalor dan fluidisasi. Model ini diimplementasikan pada kode DYNFLUB. Mengingat sistem yang sesungguhnya bersifat lebih rumit dikarenakan adanya gerakan partikel-partikel dan adanya gelembung-gelembung pada hamparan, model dinamika titik kemudian dibantu dengan menyeretkan hasil-hasil perhitungan statis tiga dimensi sebagai reaktivitas eksternal stokastis ga- yut waktu. Hasil menunjukkan bahwa daya reaktor dapat dihasilkan apabila besar laju

aliran pendingin tertentu telah tercapai dan hamparan partikel telah terekspansi. Dengan memperbesar laju aliran massa, daya yang dihasilkan juga semakin meningkat. Akan tetapi, begitu pendingin dihentikan, hamparan partikel menjadi subkritis dan daya fisi tidak lagi dihasilkan. Reaktor mampu menghasilkan daya maksimum sebesar 120 MW dan mempunyai daya spesifik sebesar ≈ 3.5 MW per kg U²³⁵ serta rapat daya sebesar ≈ 10 MW/m³.

Permasalahan stabilitas sistem telah dipelajari menggunakan analisis *root-locus* sebagai fungsi laju aliran pendingin. Nilai-nilai diri yang dihasilkan mempunyai bagian real yang negatif untuk semua laju aliran pendingin yang berada pada rentang operasi reaktor. Analisis stabilitas juga telah dilakukan untuk gangguan bersifat sinusoid dan reaktor ternyata stabil untuk semua rentang frekuensi. Hasil-hasil ini menunjukkan bahwa reaktor stabil dalam kaitannya dengan sistem linear.

Adanya gelembung-gelembung beserta pengaruhnya terhadap perubahan reaktivitas sulit untuk dijabarkan pada kode dinamika titik. Untuk alasan ini kode dinamika banyak dimensi digunakan untuk mempelajari fenomena tersebut. Simulasi dinamika gayut waktu dan ruang telah dilakukan menggunakan kode FETCH dari *Imperial College*. Fluktuasi daya fisi cukup besar akan tetapi suhu gas relatif ajeg setelah keadaan fana awal. Perbedaan antara suhu bahan bakar dengan suhu gas hampir dapat diabaikan dikarenakan ukuran partikel yang kecil dan nilai konduktivitas termal partikel yang bagus. Suhu hamparan hampir seragam dikarenakan pengadukan partikel secara cepat.

Bagian ketiga dari penelitian ini terkait dengan pengambilan kalor peluruhan tanpa sistem pendinginan paksa. Model perpindahan kalor banyak mode dua dimensi yang menyertakan konveksi, konduksi dan radiasi telah disusun dan diimplementasikan pada kode DECFLUB. Kode tersebut kemudian digunakan untuk mempelajari seberapa besar daya maksimum yang mungkin dicapai tanpa harus melebihi suhu bahan bakar maksimum yang telah ditetapkan sebesar 1873 K.

Perhitungan dilakukan untuk beberapa kasus yang berbeda dan hasil menunjukkan bahwa pengambilan kalor peluruhan secara pasif pada reaktor nuklir fluidisasi dapat dilakukan dalam batas-batas tertentu. Telah dipelajari pula proses pengambilan kalor pada kondisi terparah yaitu ketika sistem mengalami penurunan tekanan dan konduktivitas termal grafit menjadi buruk akibat iradiasi neutron. Tingkat daya operasi maksimal yang mana kalor peluruhan dapat diambil secara pasif pada kasus ini adalah sedikit di atas 50 MW.

Kesimpulannya, dengan mengubah desain partikel bahan bakar dan geometri reaktor, sistem yang diusulkan memenuhi persyaratan-persyaratan yang telah ditetapkan. Dengan menggunakan alat khusus seperti sistem kode FETCH, perilaku dinamis reaktor dapat dipahami. Meskipun demikian beberapa masalah masih perlu dikaji misalnya (i) kekuatan dan ketahanan bahan TRISO pada kondisi fluidisasi dan (ii) sistem pasif yang lebih mendalam untuk mendinginkan partikel ketika reaktor sudah padam.

List of relevant publications

Agung, A., Lathouwers, D., van der Hagen, T. H. J. J., van Dam, H., Pain, C. C., Goddard, A. J. H., Eaton, M. D., Gomes, J. L. M. A., Miles, B., and de Oliveira, C. R. E. (2006). On an improved design of a fluidized bed nuclear reactor. Part I: design modifications and steady state features. *Nuclear Technology*, 153:117.

Lathouwers, D., Agung, A., van der Hagen, T. H. J. J., van Dam, H., Pain, C. C., de Oliveira, C. R. E., and Goddard, A. J. H. (2003). Dynamics modeling and stability analysis of a fluidized bed nuclear reactor. *Progress in Nuclear Energy*, 43:437.

Agung, A., Lathouwers, D., van der Hagen, T. H. J. J., van Dam, H., Pain, C. C., Goddard, A. J. H., Miles, B., Ziver, K. A., Eaton, M. D., and de Oliveira, C. R. E. (2007). On an improved design of a fluidized bed nuclear reactor. Part II: linear stability and transient analysis. Submitted to *Nuclear Technology*.

Agung, A., Lathouwers, D., van der Hagen, T.H.J.J., and van Dam, H. (2005). On the use of P_N and S_N methods for radiative heat transfer in a fluidized bed nuclear reactor: A case study for passive decay heat removal. (in Bahasa Indonesia), *Proc. The 11th National Seminar on Technology and Safety of Nuclear Power Plants and Nuclear Facilities*, pp. 705–720, Malang, Indonesia.

Agung, A., Lathouwers, D., van der Hagen, T.H.J.J., van Dam, H., Pain, C.C., de Oliveira, C.R.E., Goddard, A.J.H., Eaton, M.D., Gomes, J.L.M.A., and Miles, B. (2004). Passive decay heat removal in a fluidized bed nuclear reactor. *Proc. PHYSOR-2004*, on CD-ROM paper 97543, Chicago, USA.

Agung, A., Lathouwers, D., van der Hagen, T.H.J.J., and van Dam, H. (2003). On a new design of a fluidized bed nuclear reactor. *Proc. 8th Indonesian Students Scientific Meeting*, in CD-ROM, Delft, The Netherlands.

Agung, A., Lathouwers, D., van der Hagen, T. H. J. J., van Dam, H., Pain, C. C., de Oliveira, C. R. E., and Goddard, A. J. H. (2003). Influence of bubbles on reactivity and power in a fluidized bed nuclear reactor. *Proc. GENES4/ANP-2003*, in CD-ROM paper 1122, Kyoto, Japan.

Lathouwers, D., Agung, A., van der Hagen, T. H. J. J., van Dam, H., Pain, C. C., de Oliveira, C. R. E., and Goddard, A. J. H. (2002). Dynamics modeling and stability analysis of a fluidized bed nuclear reactor. *Proc. SMORN-VIII*, in CD-ROM paper 45, Göteborg, Sweden.

Agung, A., Lathouwers, D., van der Hagen, T.H.J.J., van Dam, H., Pain, C.C., De Oliveira, C.R.E., and Goddard, A.J.H. (2002). Analysis of operational transients in a fluidized bed nuclear reactor. *Transaction of the 1st International Topical Meeting on High Temperature Reactor Technology (HTR)*, pp. 292–296, Petten, The Netherlands.

Acknowledgments

Eindelijk is het klaar. This thesis would have not been ready without the support of many people who have helped me directly as well as indirectly. I would like to convey my gratitude to some of them for their efforts and best wishes.

First of all, I would like to express my gratitude to my promotores, Prof. Hugo van Dam and Prof. Tim van der Hagen for giving me the possibility to perform the PhD research at PNR group and for their valuable support, advice, encouragement and help about the project until the last period of writing this thesis.

I am indebted to Danny Lathouwers, my daily supervisor, for his continuous assistance, constructive critics, patience and more important for providing me with an ideal environment to carry out my work.

I wish to express my thanks to Riny Purmer for her attention and caring when I arrived at the group; Ine Olsthoorn for her caring especially during the last period of writing this thesis; Piet de Leege for his invaluable support related to the codes and for being my office mate during the last two months. I would like also to thank all people in the PNR group for the support, aid and fruitful environment.

Thanks are also due to people at the AMCG group of the Imperial College London. Especially I would like to thank Prof. Chris Pain, Kemal Ziver, Matthew Eaton, Bryan Miles and Jefferson Gomes. Without them I will not be able to finish Chapter 5.

I wish to thank all my Indonesian friends in the Netherlands for their unlimited moral support. A special appreciation goes to Dobson Simanjuntak in Eindhoven and his family in Bandung. I would like also to express my thank and prayer for my best friend, the late Waris Santosa, who passed away during the big earthquake in Yogyakarta.

One word of special thanks goes to all my colleagues and faculty members of the Department of Engineering Physics at Universitas Gadjah Mada for their encouragement, support and understanding. I also take this opportunity to thank Susetyo Hario Putero for always helping me when I was in a bad mood and for our joyful discussions during lunch; Rachmawan Budiarto for always encouraging me and giving moral support to finish this thesis.

I would like to thank my former students and housemates: Donny Hartanto, Nur Ahmadi and Hendra Firnadi, for our friendship and joyful moments at C-190. To my friends: Aries Adinugroho, Fitri Wulandari, Filian Arbiyani, Suwondho Arie Prayudha, Teddy Ardiansyah, Wahyuni, M. Kunta Biddinika and all members of KSR2N research group; thank you very much. Life would not be so exciting without all of you.

In this occasion I would like to express my gratitude to my parents for the support, for the love, and for the prayers. Thanks for always encouraging and supporting me to pursue higher education far away from home.

Finally, a very special appreciation is due to my beloved wife, Nur Abidah, and my sons, Naufal Urfi Dhiya'ulhaq and Adrian Isna Izzulhaq, to whom this thesis is dedicated. Thanks for your constant encouragement and support and also for your enduring love and sacrifice.

Curriculum Vitae



ALEXANDER AGUNG was born in September 16, 1972 in Pekalongan, Central Java, Indonesia. He attended his elementary school at *SD Negeri Kedungwuni I* from 1979 to 1985. His next three-year secondary education was obtained from *SMP Negeri Wonopringgo*. Afterwards, he spent another three years at *SMA Negeri 1 Pekalongan*. In 1991 he obtained his high-school certificate in physical sciences with distinction and subsequently he was admitted to the Department of Nuclear Engineering, *Universitas Gadjah Mada* in Yogyakarta. In 1996 he received his bachelor's degree *Sarjana Teknik* with honor (*cum laude*).

The topic of his graduation project was modeling and calculating the pressure transient in the containment of AP-600 nuclear power plant (which was proposed for the first nuclear power plant in Indonesia at that time) after a loss-of-coolant accident and its consequence to the accumulated iodine dose in the human thyroid. In 1997 he became a faculty member of the Department of Engineering Physics, *Universitas Gadjah Mada*. In 1998 he received a STINT (*stiftelsen för internationalisering av högre utbildning och forskning*) scholarship from the Swedish government to continue his education at the Department of Energy Technology, *Kungliga Tekniska Högskolan* in Stockholm. In 2000 he received his Master of Science degree and the topic of his master thesis was performing exergoeconomic evaluations of a co-generation plant in an Indonesian sugar cane factory. Since February 2001 until January 2005 he was on leave from his duty in Indonesia to become a PhD student at the Department of Radiation, Radionuclides and Reactors, Faculty of Applied Sciences, Delft University of Technology. Currently he is an assistant professor at the Nuclear Engineering and Engineering Physics program of *Universitas Gadjah Mada* and is actively engaged in nuclear and energy related research.

Alexander Agung
Department of Engineering Physics
Universitas Gadjah Mada
Jl. Grafika 2, Yogyakarta 55281, INDONESIA
e-mail : a_agung@ugm.ac.id

